NNT : 2025AIXM0087

THÈSE DE DOCTORAT

Soutenue à AMU — Aix-Marseille Université
le 24 avril 2025 par

Soufiane SAÏDI

Nano-mechanical properties of ZnO piezoelectric semiconductor nanowires

Discipline
Physique et Sciences de la Matière

Spécialité
Matière Condensée et Nanosciences

École doctorale
ED 352

Laboratoire/Partenaires de recherche
IM2NP-UMR 7334 CNRS

Composition du jury

Damien FAURIE LSPM, Université Sorbonne Paris Nord, Professeur	Rapporteur
Jean-Michel CHAUVEAU GEMAC, Université Versailles St Quentin, Professeur	Rapporteur
Marie-Ingrid RICHARD IRIG, CEA, DR-CEA	Examinatrice Présidente du jury
Frederic LEROY IM2NP, Université de Aix-Marseille, Professeur	Examinateur
Thomas W. Cornelius IM2NP, Université de Aix-Marseille, DR-CNRS	Directeur de thèse
Michaël TEXIER IM2NP, Université de Aix-Marseille, Professeur	Co-directeur de thèse
Cristian MOCUTA Soleil Synchrotron, Scientifique de ligne	Membre invité

Affidavit

I, undersigned, Soufiane SAÏDI, hereby declare that the work presented in this manuscript is my own work, carried out under the scientific supervision of Thomas W. Cornelius et Michaël TEXIER, in accordance with the principles of honesty, integrity and responsibility inherent to the research mission. The research work and the writing of this manuscript have been carried out in compliance with both the french national charter for Research Integrity and AMU charter on the fight against plagiarism.

This work has not been submitted previously either in this country or in another country in the same or in a similar version to any other examination body.

Marseille 19/02/2025

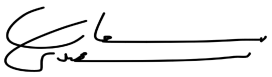

This work is licensed under Creative Commons Attribution-NonCommercial-NoDerivatives 4.0 International Public License

Liste de publications et participation aux conférences

Liste des publications et/ou brevets réalisées dans le cadre du projet de thèse :

1. Three-point bending behavior of individual ZnO nanowires studied by in situ Laue microdiffraction. Soumise à (*J.Appl.Crystallogr.*)

   Soufiane Saidi*, Michael Texier, Shruti Sharma, Gustavo Ardila, Céline Ternon, Jean-Sébastien Micha, Stéphanie Escoubas, Olivier Thomas and Thomas Cornelius

Participation aux conférences et écoles d'été au cours de la période de thèse :

1. European School for Young Scientists on Microscopy and Materials Characterization *Dresden, Germany* (contribution orale)
2. Mecanano Summer School 2023 *Rome, Italy* (poster)
3. ESRF User Meeting 2023 *Grenoble, France* (poster)
4. RXM 2023 *Bordeaux, France* (poster)
5. XTOP Conference 2024 *Carry-le-Rouet, France* (poster)
6. Journées de la Matière Condensée *Marseille, France* (contribution orale)

Résumé et mots clés

Cette thèse étudie les propriétés structurelles, mécaniques et électromécaniques des nanofils de ZnO à l'aide de techniques avancées de rayons X synchrotron. Des tests de flexion à trois points in situ révèlent que les nanofils présentent une résistance à la rupture et une déformation élastique élevée par rapport au bulk, les désalignements lors de l'application de la charge induisant à la fois une flexion et une torsion. Des simulations par éléments finis étayent les résultats expérimentaux en détaillant l'interaction complexe entre la déformation élastique et plastique dans ces systèmes quasi-unidimensionnels. Des méthodes avancées telles que la microdiffraction Laue, la TEM haute résolution (HR-TEM) et l'imagerie cohérente par diffraction de Bragg (BCDI) ont été utilisées pour caractériser la contrainte intrinsèque et la formation de défauts. L'étude examine également les effets d'une exposition prolongée aux rayons X, mettant en évidence les dommages et la dégradation de la surface, tout en intégrant des tests électromécaniques avec la cartographie par fluorescence X (XRF) pour élucider les réponses piézoélectriques. Ces résultats soulignent le potentiel mécanique des nanofils de ZnO pour des applications dans l'électronique flexible et les dispositifs de récupération d'énergie.

Mots-clés : ZnO, nanofils, piézoélectricité, comportement électromécanique, flexion à trois points, rayons X synchrotron, microdiffraction Laue, BCDI.

Abstract and keywords

This thesis investigates the structural, mechanical, and electromechanical properties of ZnO nanowires using advanced synchrotron X-ray techniques. *In situ* three-point bending tests reveal that the nanowires exhibit enhanced fracture strength and elastic strain, with loading misalignments inducing both bending and torsion. Finite element simulations support the experimental findings by detailing the complex interplay of elastic and plastic deformation in these quasi-one-dimensional systems. Advanced methods such as Laue microdiffraction, HR-TEM, and Bragg coherent diffraction imaging were employed to characterize intrinsic strain and defect formation. The study also examines the effects of prolonged X-ray exposure, highlighting surface damage and degradation, while integrating electromechanical testing with XRF mapping to elucidate piezoelectric responses. These results underscore the mechanical potential of ZnO nanowires for flexible electronics and energy-harvesting devices.

Keywords: ZnO, nanowires, piezoelectricity, electromechanical behavior, three-point bending, synchrotron X-ray, Laue microdiffraction, BCDI

Acknowledgments

I extend my deepest gratitude to DR Thomas W. Cornelius and Professor Michaël Texier for their unwavering support, invaluable guidance, and encouragement throughout the entire process of completing this thesis. Their expertise, patience, and insightful feedback have been instrumental in shaping this work. Their mentorship and constructive criticism have challenged me to grow both intellectually and personally, and I am truly appreciative of the time and effort they invested in guiding me towards excellence. I absolutely owe them for all what I have learned and achieved during these last three years.

I express my extreme gratitude to DR. Marie-Ingrid RICHARD, Pr. Frederic LEROY, Pr.Jean-Michel CHAUVEAU and Pr.Damien FAURIE for accepting to take part in my evaluation board. I was honored to be reviewed by such excellent scientists.

I want to express my profound gratitude to the entire research team (MNO team), including Olivier THOMAS, Marc GAILHANOU, Stéphane LABAT, Stéphanie ESCOUBAS, Jonathan AMODEO, Solène DASSONNEVILLE and Jean-Marc Roussel who contributed greatly to the positive atmosphere within the team.

All the PhD students, and post-doctorates with whom I shared many good moments : Anassya RAAD, Mehdi Yacine MEDJKOUNE, Thomas FERNANDES, Abdelrahman ZAKARIA, Marcelo DEMETRIO DE MAGALHÂES, Sara Maria DE ALBUQUERQUE SOUSA, Serine HOUAM, Chaymaa BOUJROUF, Nawal FERDI and Torkia BRAIK. Each one of you has played an integral role in making this thesis memorable. I am grateful for the invaluable friendships and the knowledge we've exchanged during this thesis.

I would like to thank our collaborators Gustavo ARDILA, Celine TERNON, Jean-Sebastien MICHA and Cristian MOCUTA for interesting scientific discussions about this thesis work.

Special tank to my former Professors Bruno METTOUT, Robert BOUZERAR and Claire MEYER at University of Picardie Jules Vernes (UPJV) who believed in me and supported me throughout my years of study.

I want to extend my deepest thanks to my family, mom and dad, Souhayla, Mohammed Amine and Ismael for their unwavering support, love, and encouragement throughout these years of thesis. Their constant belief in me has been a pillar of strength, and their sacrifices have paved the way for my success. Words are not enough to express my love and gratitude, I couldn't have done it without you. THANK YOU !

يفنى الناس و لا تفنى صنائعهم
فاختر لنفسك ما يحلو به الأثر

Résumé étendu

Cette thèse présente une étude des propriétés mécaniques, électromécanique et microstructurales des nanofils de ZnO en utilisant des techniques de caractérisation avancées.

Le premier chapitre présente les propriétés physiques en lien avec la structure cristallographique de l'oxyde de zinc (ZnO) et introduit ses principaux domaines d'applications. Après un rappel historique et une brève synthèse des ressources et applications initiales du ZnO, une partie importante du chapitre est consacrée à la structure cristalline du ZnO, en mettant l'accent sur sa forme la plus stable : la structure hexagonale wurtzite (Figure. 1). Cette structure, caractérisée par une disposition non-centrosymétrique, est au cœur du comportement piézoélectrique du ZnO. Le texte détaille l'arrangement des ions Zn^{2+} et O^{2-}, l'importance des surfaces polaires, ainsi que la manière dont la nature directionnelle des liaisons donne lieu à une polarisation spontanée le long de l'axe-c. Ces caractéristiques sont non seulement essentielles pour comprendre les propriétés optiques et électriques du ZnO, mais aussi pour expliquer sa réponse mécanique sous contrainte.

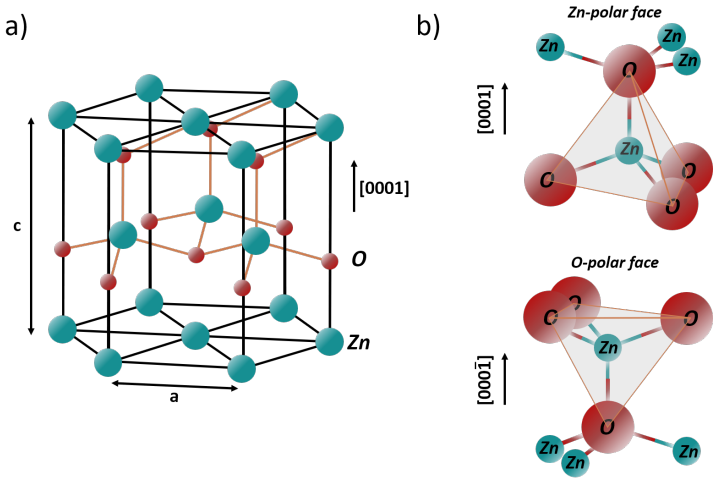

Figure 1: a) Structure cristalline wurtzite du ZnO b) Les deux faces polaires du ZnO.

En plus de ses caractéristiques structurales, ce chapitre aborde les propriétés mécaniques du ZnO. Des concepts fondamentaux tels que la contrainte, la déformation et l'élasticité y sont introduits, incluant la formulation de la loi de Hooke ainsi que la définition du module de Young, du module de cisaillement et du coefficient de Poisson. La discussion

s'étend à la déformation plastique et à la rupture, en examinant des notions telles que le point d'écoulement, la résistance à la rupture et la ténacité à la fracture. Le chapitre détaille également le rôle des dislocations en incluant les concepts de vecteur de Burgers, de caractère (coin ou vis) et de systèmes de glissement dans le processus de déformation, illustrant comment ces défauts influent sur le comportement mécanique macroscopique du matériau. Les propriétés électriques du ZnO sont ensuite présentées, mettant en lumière sa nature de semi-conducteur II–VI à large bande interdite, d'environ 3,37 eV. Le texte décrit les raisons de la conductivité de type-n intrinsèque du ZnO, principalement due aux lacunes en oxygène, et aborde les défis liés à l'obtention d'un dopage de type-p stable. L'interaction entre les métaux et le ZnO est également explorée, clarifiant les conditions dans lesquelles se forment des contacts ohmiques ou des contacts Schottky. Cette discussion est cruciale pour comprendre les propriétés d'interface qui influent sur la performance des dispositifs à base de ZnO. De plus, le chapitre aborde les formes nanostructurées du ZnO, en particulier les nanofils, et examine comment les effets de taille finie peuvent conduire à une amélioration tant des propriétés mécaniques que piézoélectriques par rapport au ZnO. Il passe en revue diverses techniques de synthèse, telles que la croissance hydrothermale et la déposition en phase vapeur, et présente les applications potentielles des nanostructures de ZnO dans des domaines tels que la nanoélectronique, les capteurs et la récupération d'énergie.

Le deuxième chapitre présente un aperçu complet des méthodologies employées pour étudier les nanofils de ZnO à l'échelle nanométrique. Il commence par exposer les principes fondamentaux de la diffraction des rayons-X, en détaillant comment ces derniers interagissent avec la matière et en présentant la théorie sous-jacente à la diffusion par un cristal. Des concepts-clefs tels que la loi de Bragg et la géométrie de la sphère d'Ewald y sont abordés afin d'établir le cadre théorique nécessaire à l'interprétation des figures de diffraction expérimentales. Ce fondement théorique s'avère essentiel puisqu'il sous-tend les différentes techniques basées sur l'utilisation du rayonnement synchrotron qui sont décrites par la suite. Le chapitre se poursuit ensuite par une description détaillée des dispositifs expérimentaux utilisés dans l'étude. Y sont décrits les optiques de focalisation, telles que les mirroirs Kirkpatrick–Baez (KB), les lentilles de Fresnel et les lentilles de Beryllium, qui permettent à focaliser des faisceaux des rayons X à une taille de quelques centaines

de nanomètre. La discussion inclut également les défis liés à l'obtention d'une intensité élevée tout en assurant une focalisation précise du faisceau, éléments essentiels à la réussite des expériences rapportées dans les chapitres suivants. Une des techniques centrales présentées est la microdiffraction Laue qui permet d'accéder à l'orientation cristalline des nanofils de ZnO avec une très haute précision. Le chapitre détaille comment un faisceau de rayons-X polychromatique est utilisé pour éclairer l'échantillon, produisant ainsi des motifs de diffraction sensibles aux contraintes, à l'orientation et aux structures de défauts à l'intérieur des nanofils. La sensibilité de la microdiffraction Laue aux variations subtiles des paramètres du réseau cristallin en fait un outil indispensable pour la cartographie des distributions de contraintes et l'identification de zones de déformation localisée. Par la suite, le chapitre propose une discussion approfondie sur la technique d'imagerie cohérente en condition de diffraction de Bragg (BCDI). La BCDI est présentée comme une technique d'imagerie basée sur la reconstruction de la phase, permettant de calculer les champs de contraintes tridimensionnels au sein d'un nanocristal. Le chapitre détaille la configuration expérimentale pour la BCDI, incluant des informations sur le positionnement du détecteur, les protocoles de balayage et les algorithmes itératifs utilisés pour récupérer l'information de phase à partir des intensités de diffraction mesurées. Il met également en lumière les difficultés rencontrées lors de l'application de la BCDI aux petits nanofils de ZnO, telles que le faible volume diffusant et les problèmes associés à la reconstruction de phase en présence de bruit. En complément des méthodes basées sur les rayons-X, le chapitre passe en revue des techniques de caractérisation complémentaires, notamment la microscopie électronique à balayage (SEM) et la microscopie électronique en transmission (TEM). La SEM est utilisée pour évaluer la morphologie générale et les caractéristiques de surface des nanofils de ZnO, fournissant des images à haute résolution qui révèlent les changements de géométrie des nanofils avant et après les tests mécaniques. La TEM, quant à elle, permet d'étudier la microstructure interne, telles que la présence de défauts étendus, avec une résolution atomique. Le couplage de ces techniques de microscopie électronique avec les méthodes de diffraction par rayons-X permet d'obtenir une compréhension plus complète des caractéristiques structurelles externes et internes des nanofils.

Le chapitre décrit également l'utilisation de la microscopie à force atomique (AFM), et plus précisément du système SFINX, qui est utilisé pour les tests mécaniques *in situ*. Le

système AFM SFINX permet l'acquisition simultanée de données topographiques et de la réponse mécanique sous forces appliquées, reliant ainsi la morphologie de surface au comportement mécanique. Cette technique revêt une importance particulière pour établir la corrélation entre les motifs de diffraction observés et la déformation réelle des nanofils lors des tests de flexion.

Le troisième chapitre, consacré aux tests *in situ* de flexion à trois points sur des nanofils de ZnO, présente une étude détaillée du comportement mécanique de nanofils individuels soumis à des conditions de chargement contrôlées. La procédure expérimentale débute par une préparation minutieuse des échantillons, où les nanofils de ZnO sont déposés sur un substrat en silicium microstructuré comportant des tranchées micrométriques. Cette géométrie de substrat permet de suspendre une partie des nanofils, garantissant ainsi une mise en charge efficace lors des tests de flexion. Une attention particulière est portée à l'alignement des nanofils par rapport à la surface du substrat ainsi qu'à la pointe SFINX utilisée pour appliquer la charge, car de légers désalignements peuvent induire non seulement une flexion, mais aussi des déformations en torsion (Figure. 3.8).

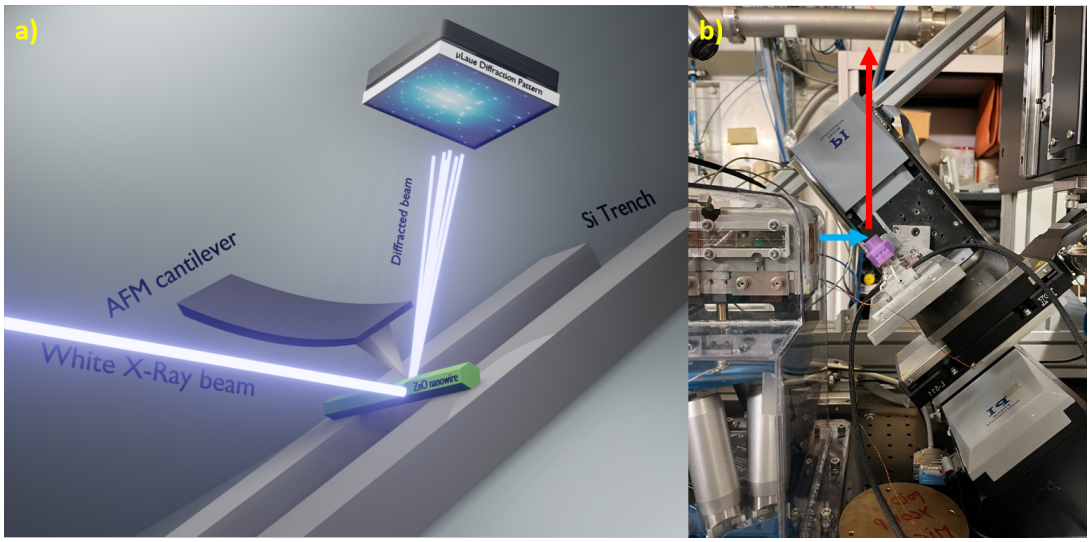

Figure 2: a) Illustration schématique de l'installation expérimentale pour les tests in situ de flexion à trois points en combinaison avec la microdiffraction Laue. b) Photographie illustrant le montage de l'échantillon ainsi que le faisceau incident et le faisceau diffracté dans la cabine expérimentale BM32.

Avant l'application du chargement mécanique, une cartographie par microdiffraction Laue est réalisée afin de caractériser l'orientation cristallographique initiale et d'évaluer les contraintes résiduelles préexistantes dans les nanofils. Cette étape est cruciale puisqu'elle établit une référence permettant de comprendre l'évolution de la structure du réseau sous l'effet du stress mécanique appliqué. Dès le début des tests de flexion, une force calibrée est appliquée via un microscope à force atomique compatible avec les goniomètres des lignes de lumière utilisés dans le cadre des études sous rayonnement synchrotron. La déflexion des nanofils est suivie en temps réel en utilisant la microdiffraction de Laue. La calibration de la force imposée est effectuée avec une grande précision, en reliant le déplacement du nanopositionneur piézoélectrique à la force effectivement appliquée sur le nanofil. Au cours du chargement, les nanofils montrent non seulement une déformation par flexion, mais également une composante de torsion notable. Cette torsion peut être attribuée à un désalignement entre la pointe SFINX et les facettes latérales du nanofil, ainsi qu'à l'orientation du nanofil par rapport aux micro-tranchées traversées par les nanofils. Des simulations par la méthode des éléments finis (FEM) corroborent cette hypothèse en démontrant que l'angle auquel un nanofil traverse une tranchée joue un rôle crucial dans la distribution inhomogène de la contrainte qui peut générer un moment de rotation autour de l'axe c. Le chapitre aborde ensuite l'analyse quantitative de la réponse mécanique. Les données expérimentales de déflexion sont comparées aux calculs effectués dans le cadre de la théorie classique des poutres d'Euler-Bernoulli ainsi qu'à des simulations numériques par FEM. Pour de faibles déflexions, les valeurs théoriques et simulées sont en bon accord ; toutefois, des écarts apparaissent à des charges plus élevées, suggérant l'apparition d'un comportement non linéaire et d'une déformation plastique localisée. Les expériences révèlent que les nanofils de ZnO peuvent supporter des contraintes élastiques maximales d'environ 1,9% et présenter des résistances à la rupture pouvant atteindre 3 GPa des valeurs nettement supérieures à celles mesurées dans le ZnO massif. Ces propriétés remarquables soulignent l'importance des effets de taille sur l'amélioration de la résistance mécanique. À l'issue des tests mécaniques, des analyses post-mortem sont réalisées à l'aide de la microscopie électronique à balayage (MEB) et de la microscopie électronique en transmission (MET). Les images obtenues par MEB fournissent des évidences d'une déformation irréversible, incluant à la fois la flexion et la torsion, tandis que la MET offre

un aperçu des modifications microstructurales à l'intérieur des nanofils. Les études en MET révèlent la formation de boucles de dislocation localisées notamment dans les régions ayant subi les contraintes les plus élevées. De façon surprenante, le système de glissement observé présente un facteur de Schmidt très faible dans les conditions de déformation des nanofils mais la présence de ces dislocations peut contribuer à la torsion macroscopique observée par microdiffraction Laue. Par ailleurs, la présence de taches de diffraction Laue fendue ou étirée pendant les tests de flexion indique que des rotations locales du réseau et l'accumulation de dislocations géométriquement nécessaires contribuent à la déformation observée.

Dans l'ensemble, ce chapitre offre une vision globale de l'interaction complexe entre la flexion élastique, la déformation plastique et les effets torsionnels dans les nanofils de ZnO soumis à des tests de flexion à trois points *in situ*. En intégrant la microdiffraction Laue en temps réel avec un chargement mécanique précis et une microscopie post-mortem approfondie, l'étude fournit des informations précieuses sur l'évolution des contraintes et la dynamique des défauts dans ces nanostructures. Les résultats enrichissent notre compréhension des propriétés mécaniques fondamentales des nanofils de ZnO et présentent des implications significatives pour leur utilisation dans des dispositifs électromécaniques à l'échelle nanométrique, où une haute résistance à la rupture et une conversion efficace de l'énergie via l'effet piézoélectrique sont essentielles.

Le quatrième chapitre explore les effets de l'exposition aux rayons-X sur les nanofils de ZnO lors des investigations expérimentales. Il commence par décrire les conditions expérimentales auxquelles les échantillons ont été soumis à l'irradiation par rayons-X, en soulignant la nécessité de contrôler soigneusement l'intensité du faisceau et la durée d'exposition. L'étude met en évidence que l'exposition prolongée à des rayons-X de haute intensité peut entraîner des modifications structurales susceptibles d'impacter la précision des mesures mécaniques et électromécaniques. Un des points centraux de ce chapitre est l'observation de la dégradation des échantillons, avec des preuves recueillies par imagerie par fluorescence des rayons-X, microscopie électronique à balayage (MEB) et microscopie à force atomique (AFM). Les résultats montrent qu'après une exposition prolongée, les nanofils de ZnO présentent des modifications notables, incluant des dommages en surface conduisant à une rupture éventuelle. Ces altérations sont corrélées à l'évolution progressive

des tâches de diffraction Laue, qui sont sensibles à l'accumulation de contraintes et au désordre structurel induit par le faisceau (Figure 4.4). Des analyses comparatives entre différents dispositifs expérimentaux révèlent des différences significatives dans le degré de détérioration des échantillons. Le chapitre souligne ainsi la nécessité d'optimiser les paramètres du faisceau pour atténuer l'endommagement tout en obtenant des données de diffraction fiables. La discussion s'étend également aux implications des défauts induits par le faisceau sur les tests mécaniques, ces défauts pouvant influencer l'interprétation des relations contrainte-déformation et des effets de couplage électromécanique.

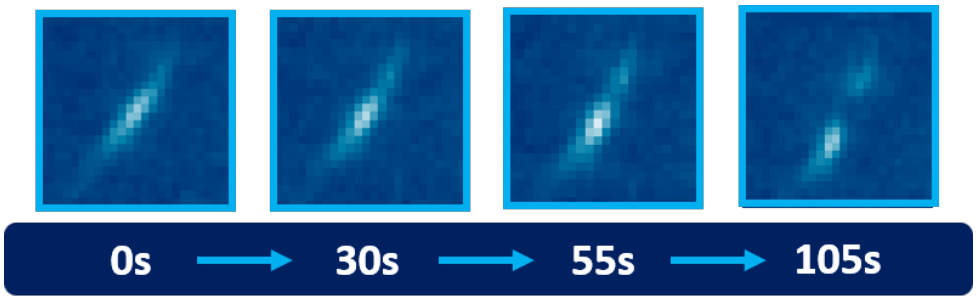

Figure 3: Le spot Laue du nanofil de ZnO se divise avec le temps.

Le dernier chapitre se penche sur l'étude simultanée des comportements électriques et mécaniques des nanofils de ZnO en utilisant des techniques avancées basées sur le synchrotron. Il débute en décrivant la mise en œuvre de l'imagerie cohérente de diffraction de Bragg (BCDI) sur des nanofils électriquement contactés. Le texte détaille minutieusement comment les échantillons sont préparés, alignés et dimensionnés afin d'optimiser le processus d'imagerie. La microscopie à diffraction des rayons-X à balayage est employée pour cartographier avec précision les nanofils démontrant la déformation des nanofils déposé sur le substrat. La BCDI appliquée aux nanofils de ZnO déposés de manière aléatoire montre que presque tous les nanofils étudiés présentent une contrainte ou courbature interne. Les motifs de diffraction reconstruits montrent des champs de déplacement non uniformes, indiquant que, même en l'absence de charge mécanique externe, les nanofils maintiennent un état de contrainte intrinsèque. Cette contrainte est probablement due aux contraintes résiduelles issues du processus de croissance ou aux effets de surface pendant le processus de la déposition sur le substrat.

Par la suite, le chapitre présente une approche complémentaire impliquant la cartographie *in situ* par fluorescence des rayons-X (XRF). Cette technique est intégrée aux tests électromécaniques pour suivre en temps a localisation du nanofil en sélectionnant une raie de fluorescence caractéristique de cet élément sous tension appliquée.

Contents

Introduction **1**

1 Context **4**

1.1 **Properties of bulk Zinc Oxide (ZnO)** 4

1.1.1 History and general information 5

1.1.2 Crystal structure 6

1.1.3 Mechanical properties 7

1.1.4 Electrical properties 17

1.1.5 Piezoelectric properties 19

1.2 **ZnO Nanostructures** 25

1.2.1 Nanomechanics 25

1.2.2 Nano-piezoelectric testing methods 35

1.2.3 Growth of ZnO nanowires 39

1.2.4 ZnO nanowires applications 41

2 Experimental techniques **45**

2.1 **Basic principles of X-ray diffraction** 45

2.1.1 X-ray interaction with matter 46

2.1.2 Scattering by a crystal 52

2.2 **Experimental Techniques** 64

2.2.1 Focusing optics 64

2.2.2 Laue microdiffraction 67

2.2.3 Bragg coherent X-ray diffraction imaging 79

2.2.4 Electron microscopy techniques 86

2.2.5 AFM SFINX 92

3 In situ three-point bending tests on ZnO NWs **101**

3.1 Sample preparation 101

3.2 Sample alignment 103

3.3 Laue microdiffraction mapping of as deposited ZnO NWs 106

3.4 In-situ three-point bending tests 109

3.4.1 Force calibration 109

3.4.2 Three-point bending 112

3.4.3 Comparison of calculations using classical Euler-Bernoulli beam theory and finite-element method simulations 113

3.4.4 Fracture 115

3.4.5 Plasticity 118

3.5 **TEM Analysis** 121

3.5.1 Sample preparation 122

3.5.2 Defects observation 123

3.6 Appendix 129

3.7 Discussion 133

4 Influence of X-ray beam and beam damage **137**

4.1 **Experimental conditions** 138

4.2 **Sample damage** 139

4.3 **Discussion** 145

5 In-situ electro-mechanical experiments **147**

5.1 **Bragg Coherent Diffraction Imaging of ZnO NWs** 148

5.1.1 Sample preparation 148

5.1.2 Experimental conditions 150

5.1.3 Sample size 151

5.1.4 Scanning X-Ray Diffraction Microscopy mapping 153

5.1.5 BCDI on ZnO nanowires 155

5.2 **Electromechanical testing by in-situ XRF** 163

5.2.1 Sample preparation and alignment 163
5.2.2 Experimental conditions 164
5.3 **X-Ray fluorescence mapping** 165
5.4 **Discussion** 166

General discussion **169**

List of Figures

1 a) Structure cristalline wurtzite du ZnO b) Les deux faces polaires du ZnO.

2 a) Illustration schématique de l'installation expérimentale pour les tests in situ de flexion à trois points en combinaison avec la microdiffraction Laue. b) Photographie illustrant le montage de l'échantillon ainsi que le faisceau incident et le faisceau diffracté dans la cabine expérimentale BM32. . . . .

3 Le spot Laue du nanofil de ZnO se divise avec le temps. . . . . .

1.1 a) ZnO crystalline wurtzite structure. b) The two polar faces of ZnO . . . 7

1.2 Diagram explaining the stress tensor. 8

1.3 A typical stress–strain curve showcasing the elastic and plastic deformation regions in a material.[1] 10

1.4 The models of (a) edge, (b) screw and (c) mixed dislocations in a simple cubic structure. Black arrows indicate dislocation line. Burgers circuit is marked in green (S-start and F-finish positions of atom-to-atom counting). The Burgers vector $\vec{b}$ is shown in red.[2] 14

1.5 a) When the metal (ϕ_m) is smaller than the semiconductor (ϕ_s) in an n-type semiconductor, the bands bend downwards, forming an Ohmic contact that allows current to flow from the metal to the semiconductor's conduction band. b) When ϕ_m is larger than ϕ_s, the bands bend upwards, creating a Schottky contact. Here, current can only flow from the semiconductor to the metal via electrons. For p-type semiconductors, the opposite conditions apply. 18

1.6 Schematic illustrations of a) direct and b) inverse piezoelectric effect 19

1.7 Schematic representation of ZnO structure showing the Zn^{2+} and O^{2-} atoms polarization 20

1.8 Schematic representation of a force-displacement curve obtained during nanoindentation of an elastoplastic solid. 27

1.9 a) A push-to-pull device for in-situ nanomechanical testing[3] b) A MEMS-based testing platform for in situ TEM, enabling compressive and tensile testing on nanostructures.[4][5] 28

1.10 Free body diagram, shear force diagram, and bending moment diagram for a beam fixed at both ends and loaded with a point load at its center. . . . 31

1.11 The measured value of the Young's modulus for ZnO nanowires according to different studies [6]. 34

1.12 a) Schematic of the 3-point bending test of a single ZnO NW with AFM. b)Young's modulus measured for ZnO NWs of different diameters [7]. . . . 35

1.13 Piezoelectric coefficient of ZnO nanobelts as a function of the nanobelt's lateral dimension.[8] 37

1.14 a–d) The principle of the piezoelectric nanogenerator. e-f) metal–semiconductor Schottky contact between the AFM tip and the semiconductor ZnO NB at at reverse and forward bias[9] 38

1.15 SEM image of as-grown ZnO nanowires on Si substrate by hydrothermal method 40

1.16 schematic of generating electricity by deforming single ZnO NWs using a conductive AFM tip. In this setup, the AFM operates in contact mode and scans over the NW arrays[10] 42

1.17 Finite element simulation (left) shows the piezoelectric potential distribution in a PZT nanowire. The schematic (right) illustrates the structure of a multilayered nanogenerator made from same nanowires. [11] 43

2.1 Schematic representation of the different interactions between incident X-rays and a sample. 47

2.2 elastic scattering of x-ray by an atom 49

2.3 a) Schematic representation of the electron excitation and de-excitation processes. b) Energy level diagram illustrating absorption, non-radiative transitions, and fluorescence, where an excited electron returns to a lower energy state, emitting a photon with energy corresponding to the energy difference between the two levels. 51

2.4 Scattering of a monochromatic beam with wavelength λ by two atoms, A and B, within an infinitesimal volume element d^3r. 52

2.5 Schematic representation of a hexagonal crystal lattice system, showing the lattice parameters and orientations. The coordinate axes (x_1, x_2, x_3) are shown, where (x_1, x_2) form a 120° angle, characteristic of the hexagonal symmetry. Both (x_1, x_3) and (x_2, x_3) are orthogonal, forming 90° angles. . 56

2.6 Schematic of the Bragg's law 57

2.7 Schematic illustration of the Ewald sphere 59

2.8 simulated diffraction patterns for three strain-free crystals. The recorded fringe pattern depends on the particle shape, with fringes seen in the directions of any surface facets.[12] 61

2.9 Diagram illustrating coherence lengths: (a) longitudinal coherence length and (b) transverse coherence length. 62

2.10 a) Picture and a schematic view of a Kirkpatrick-Baez (KB) system[13] b) Schematic of a Fresnel zone plate (FZP) setup which consists of the FZP itself, an order sorting aperture (OSA) for selecting one particular diffraction order, and a central beam stop (CBS)[14] c) Schematics of a biconcave lens with radius R and the arrangement of several lenses as compound refractive lens.[15] 67

2.11 A 2D representation of the Ewald sphere is shown for a white beam, defined by two wavelength limits, the minimum and the maximum. 68

2.12 a) Example of a Laue diffraction pattern showing ZnO and Si diffraction spots. b) Diagram of the Laue microdiffraction setup at the BM32 beamline of the ESRF. 69

2.13 Laue diffraction sensitivity to deviatoric strain[16] 70

2.14 (a) Cartesian coordinate system representing the reciprocal lattice of the sample. (b) Cartesian coordinate system representing the real-space unit cell. 71
2.15 Schematic of Laue diffraction for a grain with (111) orientation. Incident X-rays interact with the crystal, diffracting different zone axis and projected onto a 2D detector. 74
2.16 The coordinate system in reciprocal space is obtained by orthonormalizing the X, Y, and Z axes. 75
2.17 a) Schematic illustration of the experimental setup for in-situ three-point bending tests in combination with Laue microdiffraction. b) Photograph illustrating the sample mount and the incident and diffracted beam at the BM32 experimental hutch 76
2.18 Illustration of the measured position in reciprocal space for a rocking scan 80
2.19 General functioning of the inversion algorithm 83
2.20 Simplified schematic of the Bragg coherent diffraction imaging setup 85
2.21 Schematic illustrating the FEI titan 80-300 components 88
2.22 a) ZnO Crystal structure created in atomsk serves as an object model for the JEMS simulation. b) The solid is sliced into thin sub-slices [17]. c) Example image of a HRTEM image simulation of the ZnO crystal model with a dislocation loop at the center 92
2.23 Diagram showing the basic working principle of an Atomic Force Microscope (AFM). 93
2.24 Contact mode AFM continuously operates in the repulsive force regime, where the tip of the AFM remains in physical contact with the sample. In amplitude modulation (AM) mode, the AFM lever oscillates with large amplitudes, sweeping across a wide range of distances, including both attractive and repulsive regimes. Conversely, frequency modulation (FM) mode typically uses small oscillation amplitudes, focusing on detecting force gradients, particularly in the attractive range near the sample surface. . . . 97
2.25 Parts of the SFINX AFM tool[18] 98
2.26 a) Oscillation amplitude and b) phase during a frequency sweep of ±400 Hz, measured before and after adjusting the parasitic capacitance.[19] . . . 100

3.1 Scanning electron microscopy image of the cross-section of a sample containing a dense forest of ZnO NWs on top of a Si substrate. 102

3.2 a) Optical microscope image of a drop-casted suspended ZnO NW across a Si microtrench. b) SEM image of a suspended ZnO NW embedded by Pt at the extremities. 103

3.3 a) Optical microscopy image of the microstructured Si substrate with ZnO NWs and the AFM-tip close to the sample surface. b) Laue microdiffraction pattern of a ZnO nanowire on the Si substrate partially shadowed by the AFM-head. The Laue spots corresponding to the ZnO NW and the Si substrate are highlighted by orange and by blue circles, respectively. 104

3.4 a) Side profile SEM image of the Akiyama probe tip [20]. b) X-Ray transmission mapping of the AFM cantilever side profile showing a high transmission at the tip [21] 105

3.5 a) SEM image, b) AFM topography image, and c) fluorescence map of a ZnO NW. The arrows in part (c) mark the areas related to the $Zn-K_{\alpha}$ and $Pt-L_{III}$ fluorescence. 106

3.6 Laue diffraction pattern of a suspended ZnO NW on a Si substrate, showing Laue diffraction spots. 107

3.7 a) SEM image of a suspended ZnO NW before nanomechanical testing superposed with a grid representing the measurement steps during the mapping of the NW using the $Zn-K_{\alpha}$ fluorescence and Laue microdiffraction. b) Fluorescence mapping of a suspended ZnO NW c) Laue microdiffraction mapping of the $\mathbf{1\bar{1}01}$ diffraction spot of the same ZnO NW 108

3.8 Applied force as a function of the displacement of the piezoelectric stage carrying the Si cantilever inferred from the rotation angle of the Si lattice planes of the SFINX-tip. 112

3.9 a) Rotation angles the three orthogonal lattice planes (0002) (□), $(0\bar{1}10)$ (△), and $(2\bar{1}\,\bar{1}0)$ (◯) in ZnO NW I during three-point bending. The inset shows the crystalline orientation of the NW with its growth direction along [0001] lying flat on one of its $(0\bar{1}10)$ side facets. b) The ZnO $(0\bar{1}10)$ Laue spot before and after the three-point bending test demonstrating that no plasticity was actually induced within the probed volume. 113

3.10 a) Theoretical calculation of the NWs deflection using Euler-Bernoulli beam equation b) FEM simulation in COMSOL showing the deflection value of a NW with same parameters 114

3.11 Comparison of FEM simulation and theoretical calculations using the Euler-Bernoulli beam deflection equation for an applied force of 25 µN. The theoretical model closely matches the FEM results for small deflections, after which it starts to diverge. 115

3.12 a) Rotation angle of the three orthogonal lattice planes (0002) (□), $(0\bar{1}10)$ (△), and $(2\bar{1}\,\bar{1}0)$ (◯) during three-point bending of a ZnO NW with a diameter of 200 nm and a suspended length of 2.5 µm until failure. The inset shows a *post-mortem* scanning electron microscopy image confirming NW fracture. b) Strain ε_{zz} and c) stress σ_x, σ_y, σ_z (of the lower NW facet) in the ZnO NW at highest applied load of 5.79 µN calculated by finite-element method simulations considering identical loading and positioning configuration as in the experiment. The z direction shows a high stress of 3 GPa at the loading point, while the x and y directions are clearly affected by the positioning of the NW along the trenches, where the stress near the embedded parts are highest in the opposite part of each region. 117

3.13 Rotation angle of the three orthogonal lattice planes (0002) (□), $(0\bar{1}10)$ (△), and $(2\bar{1}\,\bar{1}0)$ (◯), during three-point bending of ZnO NW III 118

3.14 *Post-mortem* scanning electron micrograph of the ZnO NW III after three-point bending testing demonstrating irreversible deformation. The $[5\,\bar{4}\,\bar{1}\,2]$ Laue spot measured all along the NW after mechanical testing is exemplarily shown below the SEM image. A splitting of the Laue spot is apparent in the clamped area on the left-hand side of the NW while the Laue spot of the suspended NW part shows a pronounced streaking. Open circles indicate the simulation of the position of the same Laue spot considering a rotation of the crystal around the [0001] axis. In the case of the split Laue spot a rotation of 0.20° reproduces the splitting. 119

3.15 Rotation angle of the three orthogonal lattice planes (0002) (□), $(0\bar{1}10)$ (△), and $(2\bar{1}\,\bar{1}0)$ (◯) measured along the length of ZnO NW III in steps of 200 nm after complete unloading. 121

3.16 Scanning electron microscopy image a) of the plastically deformed ZnO NW III observed from the top and b) of a TEM lamella of the same NW prepared by FIB micromachining. Platinum was deposited prior to the milling process to avoid any damaging of the NW. 123

3.17 Left : Assembly of bright field (BF) TEM images of plastically deformed ZnO NW, observed in cross-section. Right: Higher magnification BF image of the area marked by a square in the left image. This zone, located at the edge of the trench, contains numerous extended defects. 124

3.18 Left: HRTEM image filtered using the average background subtraction filtering (ABSF) method showing two differently-oriented crystalline parts of the NW separated by a disordered transition zone. Right: Schematic drawing of the spots observed in the FFT. The two crystalline parts are parallel to the $[2\bar{1}\bar{1}0]$ crystallographic axis and rotated by an angle of 3.8° with respect to each other. 125

3.19 Average background subtraction filtered HRTEM image and the corresponding FFT of the area located at the corner of the trench. Numerous dislocations extend in the (0001) planes. 126

3.20 Left: ABSF-filtered HRTEM image and the corresponding FFT of a region containing an isolated dislocation loop. Right: image filtered using the $1\bar{1}00$ symmetrical reflections. A scheme showing the approximate positions of the two opposing 60° segments of the dislocation is superimposed on the image. 126

3.21 **Top**: Detail of a HRTEM image showing two small dislocation loops in close basal planes. The local thickness of the sample, derived from image simulation of a defect-free region of the sample close to the observed region (see Fig. 3.23), is estimated to be 17.2 nm. **Botttom**: Multislice simulation showing the local contrast variations produced by two dislocation loops with Burgers vectors $\vec{b} = 1/3[11\bar{2}0]$ in a similar configuration to that observed in the experimental image (t: 17.2nm, C1: -12nm, C3: -7μm). Note that the simulation does not take into account the slight misorientation of the sample with respect to the <$11\bar{2}0$> crystallographic axis as seen in the experimental image. 127

3.22 Rotation angle of the three orthogonal lattice planes (0002) (□), $(0\bar{1}10)$ (△), and $(2\bar{1}\,\bar{1}0)$ (◯) measured along the length of ZnO NW III in steps of 200 nm after complete unloading. 128

3.23 Experimental (left) and simulated (right) HRTEM images of the wurtzite structure observed along the <$2\bar{1}\bar{1}0$> crystallographic axis. The thickness of the sample is estimated to 17.2 nm in this region (C1: -23nm, C3: -7μm). The atomic positions of Zn (blue) and O (red) atoms are superimposed to the right-part of the simulated image. 128

3.24 Scanning electron microscopy image a) of ZnO nanowires grown on a Si substrate b) of a single suspended ZnO nanowire. 129

3.25 Scanning electron microscopy image a) of the electrically connected e-chip holding b) a single suspended ZnO NW between two electrodes. 130

3.26 TEM images showing the morphology of a nanowire before biasing experiment (left), and after biasing experiments with V=2V (center) or 3V (right). 130

3.27 TEM images of the NW shown in Figure 3.26 performed at higher magnification before biasing experiment (left) and after (right). The partial melting of the NW is clearly visible on the right image. 131

3.28 TEM images showing the damaging of a nanowire submitted to various voltages: a) 0V, b) 2V, c) 30V, d) 40V. 132

3.29 HRTEM images of the NW shown in Figure 3.28 showing the microstructure of the NW in the vicinity of the melted part. 133

3.30 2D FEM simulation of the electric potential distribution for a ZnO nanowire of a rectangular form with $D = 50nm$ and $L = 600nm$ at a lateral bending force of $F = 80nN$ [22] 134

3.31 Electric potential profile of our ZnO NW extracted from equation 3.9. . . . 135

4.1 Diffraction pattern of a suspended ZnO NW on Si substrate of the old (left) and the new "LAUEMAX" (right) setup, showcasing a notable difference in clarity and background intensity 139

4.2 a) Fluorescence image of a ZnO NW before focusing the X-ray beam on it b) Fluorescence image of the same NW after focusing the beam for some seconds c) AFM image of the NW after breakage 140

4.3 a) SEM image of the suspended ZnO NW before the beam damage b) SEM image of the same ZnO NW after the beam damage 141

4.4 The Laue spot of the ZnO NW under the beam experiences a splitting in the course of time 142

4.5 SEM images of the suspended ZnO nanowire a) before and b) after the Laue microdiffraction experiment at the LaueMAX end-station using a reduced incident flux. 142

4.6 SEM images of a GaAs NW a) before and b) after exposure of 4 hours [23] 145

5.1 a) SEM images of the sample surface for in-situ electromechanical tests on ZnO NWs showing interdigitated Al contacts that were prepared by UV lithography. b) Schematic illustration of the Al electrical contacts including an Al_2O_3 insulating layer and a suspended ZnO NW. 149

5.2 Scanning electron microscopy image of the sample studied using BCDI, showing a single connected ZnO NW. 149

5.3 Image of the Maxipix detector positioned at δ=86° for the ZnO 3000 peak. 150

5.4 Top left : Superposition of 200 scans of the ZnO 3000 Bragg peak measured using BCDI, with vertical and horizontal lines showing the direction of the scan. Top right & Bottom left : Normalized intensity profiles along the horizontal and vertical directions, with detected peaks (red crosses) and analysis regions (yellow shading). Bottom right : Peak spacing as a function of distance from the pattern center, showing variations in fringe periodicity along both directions. 151

5.5 a) SXDM map of ZnO nanowires showing Bragg intensity distribution across the mapped area, highlighting several distinct diffraction spots corresponding to individual nanowires. b) Zoomed-in SXDM map focusing on a single nanowire. c) Mapping of the rocking angle as a function of the detector ν angle, demonstrating irregularities and significant twisting of the ZnO nanowire, resulting in the movement of the Bragg spot across the detector. 154

5.6 Bragg diffraction maps of ZnO nanowires, where the x-axis represents the detector position (ν angle) and the y-axis corresponds to the rocking scan range of $\eta - 1.5°$ to $\eta + 1.5°$. Movement along the x-axis corresponds to torsional deformation of the nanowire(s), while shifts along the y-axis indicate bending. 155

5.7 4 examples of raw integrated diffraction patterns of full scans around different ZnO NWs. 156

5.8 The stacking of all Bragg diffraction peaks of the 200-step rocking curve and creation of a signal clean of noise and dead regions. (X is the maximum intensity and X is the center of mass 157

5.9 FFT of the original diffraction patterns during the phase retrieval step that display intensity distributions in reciprocal space. 158

5.10 Post processing of a BCDI measurement showing the phase, the displacement, and the strain in the reconstructed object. 159

5.11 3D representation of the reconstructed nanowire showing a) The distribution of the phase in the nanowire. b) The distribution of strain in the nanowire 160
5.12 A diffraction pattern showing a part of the Al **222** Debye-Scherrer ring . . 161
5.13 a) SXDM mapping of the Al showing the electrodes b) SXDM mapping of the ZnO showing some NWs that are in the diffraction conditions. 162
5.14 The superposition of an SXDM and a SEM map allowing us to correlate the positioning of our nanowires. 162
5.15 SXDM mapping before and after soldering the contacts on the sample, showing the disappearing of our last connected ZnO NW. 163
5.16 a) A schematic of the sample positioned on a stub while connected to a Keithley sourcemeter b) photo of the sample at the P10 beamline 164
5.17 a) Diffraction mapping of the Al showing the electrodes b) XRF mapping of the Zn (K_α) line showing several nanowires. 165
5.18 The superposition of a XRF and a SEM map allowing us to correlate the positioning of our nanowires. 165
5.19 XRF map of an area containing a connected nanowire and its evolution when applying the electrical field from 0 to 6V. 166

List of Tables

1.1 Zinc production by country in the year 2023[24] 5
1.2 Bulk ZnO Elastic constants (in GPa)[25]. 11
1.3 Different mechanical parameters of Bulk ZnO in literature[26, 27] 12
1.4 Types of contacts formed based on the work function differences. 18
1.5 Comparison of piezoelectric coefficients (d_{33}) for different semiconducting materials [25, 28] 24

2.1 Zn and O Cromer-Mann coefficients 50
2.2 Fluorescence Energies of Zinc and Oxygen (in eV) [29][30] 52

3.1 The studied ZnO nanowires in this work and their parameters 109

Introduction

Zinc oxide (ZnO) is a fascinating material that has garnered significant attention in the fields of nanotechnology and materials science. Known for its wide band-gap and high exciton binding energy, ZnO exhibits remarkable piezoelectric and semiconducting properties. These features make it an ideal candidate for applications in sensors, actuators, energy harvesting devices, and nanogenerators. The quasi one-dimensional form of ZnO nanowires offers a unique platform to explore the interplay between electrical and mechanical phenomena at the nanoscale.

Motives :

ZnO is a promising material for sensing and energy conversion applications. However, this material and in particular, its piezoelectric behavior is less investigated at the nanoscale. Despite the extensive potential of ZnO, there remains a significant gap in understanding the influence of size effects on its mechanical and piezoelectric behavior, particularly in one-dimensional structures such as nanowires. Theoretical studies suggest that the Young modulus and piezoelectric coefficients of ZnO nanowires may increase as their diameters decrease, potentially enhancing their performance in nanoscale devices. However, this hypothesis has yet to be experimentally validated. Addressing this gap is essential for advancing both fundamental knowledge and the practical utilization of ZnO in cutting-edge applications.

Objectives :

The primary goal of this work is to investigate the nano-mechanical behavior and the piezoelectric properties of ZnO nanowires, focusing on the impact of size effects on their behavior. To achieve this, advanced experimental techniques are employed, many of which are applied in situ, allowing real-time observation of the material's response to external

stimuli. These experiments aim to provide direct evidence of how nanowire diameter influences the mechanical and piezoelectric behavior.

The study involves two key experimental approaches. First, nano-mechanical experiments, more precisely three-point bending, are performed to assess the structural and mechanical responses of ZnO nanowires. Second, electro-mechanical experiments are conducted, wherein an external electric field is applied to the nanowires while their diffraction signals are monitored. This approach enables the direct observation of any coupling between mechanical deformation and electrical fields at the nanoscale, with a focus on changes in the diffraction patterns that could signify piezoelectric behavior.

Means of this research :

This thesis was performed within the framework of the ANR LATINO (ANR-21-CE50-0026) project in the MNO research group at the IM2NP in Marseille. This thesis relies on a comprehensive suite of cutting-edge techniques and tools. Synchrotron X-ray diffraction (XRD) is a cornerstone of this study, providing precise measurements of strain and mechanical deformation evolution during in-situ experiments. And a custom-built atomic force microscope (AFM) system, known as the SFINX, which allows precise mechanical testing in combination of Synchrotron XRD. Post-mortem high-resolution transmission electron microscopy (HRTEM) is used to analyze the atomic structure and mechanical deformation/dislocations at the nanoscale. Focused ion beam (FIB) is employed for sample preparation. Additional characterization tools include scanning electron microscopy (SEM) for the observation of our nano-meter sized samples enabling a complete understanding of the evolution of our samples. The ZnO nanowires were synthesized using a hydrothermal method by the group of *C. Ternon* at the LMGP in Grenoble, ensuring high-quality samples for the experiments. Over the course of this study, seven synchrotron experiments were conducted, complemented by extensive measurements using the other techniques mentioned.

Thesis structure and general approach :

The first chapter serves as an introduction to the context of this thesis, including the material of interest (ZnO). It details the material's crystal structure, piezo-mechanical behavior, and electrical characteristics. It further presents the synthesis techniques and the potential applications of ZnO nanostructures. This chapter also underlines the influence

of finite size effects on the mechanical and piezoelectric behavior of ZnO nanowires.

As for the second Chapter, it details the experimental techniques used to study ZnO nanowires, including synchrotron X-ray diffraction methods like Laue microdiffraction and Bragg coherent X-ray diffraction imaging, alongside with SEM, TEM, and the AFM "SFINX". Synchrotron techniques provided insights into strain, orientation, and displacement fields, while electron microscopy characterized morphology and structure. These methods enabled a thorough understanding of ZnO nanowires structural and electromechanical behavior for future applications.

The third Chapter explores the nano-mechanical properties of ZnO nanowires using in-situ three-point bending experiments, revealing their elevated limit of elasticity and fracture strength. Advanced methods like Laue microdiffraction and HRTEM identified deformation mechanisms and defect structures at the nanoscale. Simulations and post-mortem analyses confirmed the interplay of bending, torsion, and plasticity.

The fourth Chapter addresses the challenges such as X-ray-induced damage, emphasizing the need for controlled experimental environments.

The fifth and last chapter focuses on in-situ electromechanical studies of electrically contacted ZnO nanowires using in-situ Bragg coherent X-ray diffraction imaging (BCDI) and in-situ X-ray fluorescence. We explore the tests carried out using the Bragg Coherent Diffraction Imaging (BCDI) technique on electrically connected ZnO nanowires samples. These type of tests gave us a first look at the possibility of imagining connected thin ZnO nanowires with BCDI technique. Fluorescence mappings were also used during electrical actuation which has showed that these kind of tests are possible in this configuration with the correct beam intensity.

The manuscript ends with a general Conclusion and perspectives for In-situ electromechanical experiments on Zinc Oxide nanowires in combination with Synchrotron XRD techniques.

Chapter 1

Context

1.1 Properties of bulk Zinc Oxide (ZnO)

Zinc oxide (ZnO) is a versatile inorganic compound that exhibits a distinctive combination of properties, which has led to its extensive usage in a multitude of applications. It is a transparent crystalline material with a stable hexagonal wurtzite crystalline structure. It can also crystallize in a Zinc Blende or a Rock salt cubic structure under certain conditions such as high pressure. ZnO is a II-VI semiconductor exhibiting a wide bandgap of approximately 3.37 eV. It is highly valued for its excellent optical transparency, strong ultraviolet absorption, and significant piezoelectricity. Additionally, it exhibits remarkable chemical stability, biocompatibility, and antibacterial properties. These characteristics render ZnO a pivotal material in electronics, optoelectronics, sensors, and biomedical applications. Furthermore, its wide range of different nanostructures formation trough different growth techniques augments its potential in advanced technologies. In particular, it is a highly promising candidate in the development of new devices for renewable energy and environmental applications. This chapter gives a brief historical background followed by the description of the crystalline structure and the various properties (electrical, piezoelectric, and mechanical) of ZnO. It further introduces the influence of size effects on the mechanical behavior and the piezoelectric properties of ZnO NWs and the corresponding methods to study these properties at the nanoscale. The chapter finishes with a short review on the synthesis methods of ZnO NWs and the different areas of their potential

applications.

1.1.1 History and general information

ZnO is a material with a long history. It has been used since ancient times in Egypt and Rome, primarily in ointments for skin treatments [31]. In the 18th and 19th centuries, ZnO began being used as a pigment, first in watercolor and later in oil painting, facilitated by the French process for creating ZnO pigments [32]. Today, it is still widely used in products like rubber, concrete, sunscreens, ointments, and as a colorant in various industries [33, 34]. While it also has a wide range of applications in microelectronics such as transistors[35] or LEDs[36].

ZnO is primarily derived from zinc ores, with zinc sulfide being the most common source. Zinc is relatively abundant in the Earth's crust, where China leads global zinc production, producing 4 million metric tons (MMT) in 2023, followed by Peru (1.4 million MMT) and Australia (1.1 million MMT) [24]. It is estimated that the identified zinc resources of the world are about 1.9 billion tons.

Country	**Production in 2023 (MMT)**	**Reserves (MMT)**
United States	0.750	6.6
Sweden	0.220	4.1
Peru	1.400	21
China	6.200	2
Australia	1.100	64
India	0.860	7.4
Russia	0.310	25
South Africa	0.230	6.2
Other countries	3.310	25

Table 1.1: Zinc production by country in the year 2023[24]

1.1.2 Crystal structure

Zinc oxide exists in three different crystal structures: wurtzite, zinc-blende, and rock salt. Among these, the hexagonal wurtzite structure is the most stable under ambient conditions. This hexagonal wurtzite structure belongs to the $P6_3mc$ space group and has lattice constants of $a = 3.2492$ Å and $c = 5.2054$ Å [37] (Figure 1.1 a). In this structure, Zn^{2+} and O^{2-} ions form two interlocking hexagonal close-packed arrangements. Each Zn^{2+} ion is surrounded by four O^{2-} ions, creating a tetrahedral coordination. The direction along the c-axis from a Zn^{2+} ion towards an O^{2-} ion defines the [0001] direction and Zn-polarity, while the opposite $[000\bar{1}]$ direction indicates O-polarity (Figure 1.1 b). The bonding between Zn^{2+} and O^{2-} ions is ionocovalent, where the two shared electrons are drawn more towards the O^{2-} ion due to its higher electron negativity compared to Zn. According to Pauling, a bond is 50% ionic and 50% covalent when the electron negativity difference between two elements is 1.7 [38]. For ZnO, the electron negativity values for Zn and O are 1.65 and 3.44, respectively, giving a difference of 1.79. On the Philips ionicity scale, the bond between Zn and O has an ionicity degree of 0.616 [39]. This partial ionic character, along with the non-centrosymmetric structure of ZnO, leads to an uneven charge distribution within the crystal, causing spontaneous polarization along the c-axis. Consequently, ZnO exhibits pyroelectric and piezoelectric properties. The (0001) and $(000\bar{1})$ planes, known as c-planes, are polar with opposite charges, while directions perpendicular to the c-axis have no dipole moment. Planes perpendicular to the c-planes, like the $(10\bar{1}0)$ and $(11\bar{2}0)$ planes, are non-polar, while the in-between planes such as $(12\bar{3}2)$ are considered as semi-polar.

The surface energies between two polar surfaces, as well as between the polar and non-polar surfaces, differ significantly[40] per example with a surface energy difference of about 1.14 J/m^2 between Zn-terminated (0001) and O-terminated $(000\bar{1})$[41]. By varying different factors (such as temperature or pressure) during ZnO fabrication, the relative surface energy of these planes can be affected[42]. Thus, it is possible to obtain ZnO nanostructures with various morphologies and to modify their structural, electrical, and piezoelectric properties by controlling the fabrication process conditions since these parameters are intricated with the surface energy of the ZnO crystal[43].

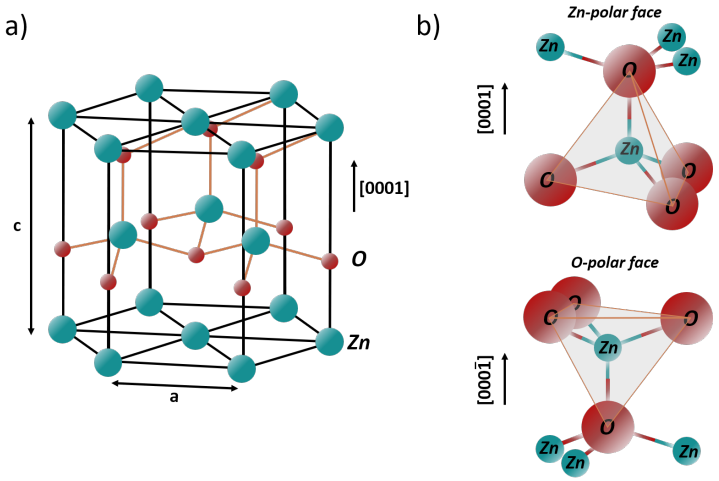

Figure 1.1: a) ZnO crystalline wurtzite structure. b) The two polar faces of ZnO

1.1.3 Mechanical properties

The study of mechanics provides the foundation for understanding how materials and structures respond to external forces, deformations, and other environmental influences. In this section, the fundamental theories and equations describing elasticity and plasticity as well as the conditions leading to material failure by fracture are introduced.

1.1.3.1 Stress

The stress as a parameter is important to understand material failure and deformation under complex loading conditions. Stress measures the internal forces within a material when it is subjected to external forces. It quantifies how these forces are distributed over a given area and helps predict how materials deform or fail under this load. Stress is written as a tensor, meaning it contains both magnitude and direction. For a material, normal stress (σ) acts perpendicular to the surface with

$$\sigma = \frac{F}{A} \tag{1.1}$$

where F represents the applied force and A is the area. ($+\sigma$) represents tensile stress, while ($-\sigma$) is the compressive stress. As for the shear stress, it acts parallel to the surface, and it occurs when forces cause a "sliding" between layers within the material.

$$\sigma = \frac{F_{\text{parallel}}}{A} \tag{1.2}$$

The stress tensor in three dimensions is described by a 3x3 matrix as :

$$\sigma_{ij} = \begin{bmatrix} \sigma_{xx} & \sigma_{xy} & \sigma_{xz} \\ \sigma_{yx} & \sigma_{yy} & \sigma_{yz} \\ \sigma_{zx} & \sigma_{zy} & \sigma_{zz} \end{bmatrix} \tag{1.3}$$

The diagonal components $(\sigma_{xx}, \sigma_{yy}, \sigma_{zz})$ are normal stresses, while the rest of the components (σ_{ij}) are shear stresses.

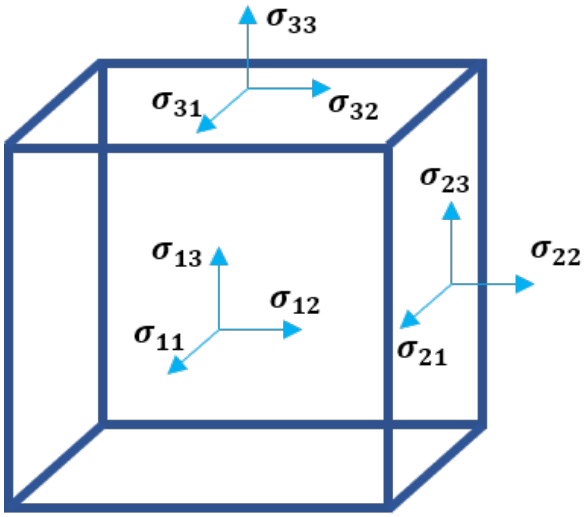

Figure 1.2: Diagram explaining the stress tensor.

1.1.3.2 Strain

Strain describes the deformation of a material in response to applied stress. Unlike stress, strain is a measure of relative change in size or shape and is dimensionless. The measure of the relative change in length along a specific direction is written as :

$$\varepsilon = \frac{\Delta L}{L} \tag{1.4}$$

Where ΔL is the change in length and L is the original length. The shear strain describes angular distortion within a material and is defined as the change in angle between two originally perpendicular lines. The 3D strain tensor is represented as:

$$\varepsilon_{ij} = \frac{1}{2}\left(\frac{\partial u_i}{\partial x_j} + \frac{\partial u_j}{\partial x_i}\right) \tag{1.5}$$

where u_i are displacement components in the i-direction. Strain must satisfy certain conditions to correspond to a physically realistic deformation. These conditions ensure that the strain field is continuous:

$$\varepsilon_{ij,kl} = \varepsilon_{ik,jl} + \varepsilon_{jl,ik} - \varepsilon_{il,jk} \tag{1.6}$$

1.1.3.3 Elasticity

The figure below, illustrates a stress-strain curve, describing the mechanical behavior of a material under applied stress. The curve begins with a linear elastic region, where the material responds entirely reversibly, and the slope corresponds to its elastic modulus or (Young's modulus). Deviation from linearity marks the yield point, indicating the limit of elasticity and the start of a permanent, plastic deformation. In this plastic region, the material deforms irreversibly. The stress peaks at the ultimate strength, which is the maximum the material can withstand, before decreasing due to localized weakening. Finally, the curve ends at a fracture, where the material fails and breaks. This curve is essential for understanding the mechanical behavior of a material including its elasticity, plasticity, as well as fracture.

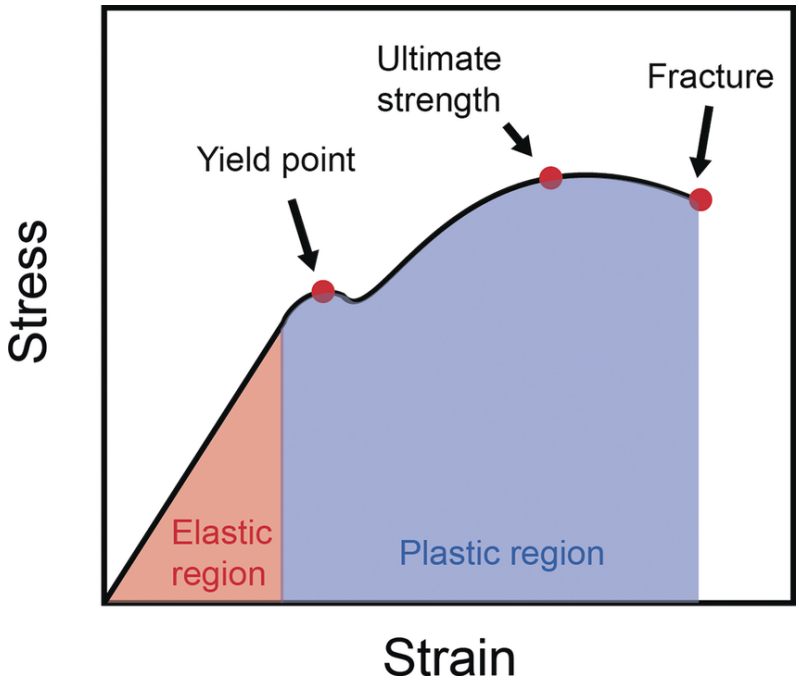

Figure 1.3: A typical stress–strain curve showcasing the elastic and plastic deformation regions in a material.[1]

The figure 1.3 shows a stress-strain curve, which describes how a material responds to an applied force. Initially, the material behaves elastically in what is called the elastic region (region highlighted in red). In this region, the material deforms when stress is applied, but it will return to its original shape when the stress is removed.

The relationship between stress and strain here is linear, meaning they are proportional to each other, which is described by Hooke's Law: $\sigma = E\varepsilon$, where σ is stress, ε is strain, and E is the Young's modulus, a constant that measures the stiffness of the material.

The point labeled *Yield Point* marks the transition from elastic behavior to plastic behavior. After this point, the material enters the plastic region (region highlighted in blue). In this region, the material undergoes permanent deformation, meaning it will not return to its original shape even if the stress is removed. As we move further along the curve, the material reaches its *Ultimate Strength*, which is the maximum stress it can endure. Beyond this peak, the material starts to weaken, even though it continues to deform. And finally, at the *Fracture Point*, the material breaks completely.

The property of materials to return to their original shape and size after an applied

stress is removed is called "Elasticity". This parameter establishes a linear relationship between stress and strain. The relationship between stress (σ_{ij}) and strain (ε_{ij}) for a linear elastic material is described using a fourth-rank tensor, the elasticity tensor, denoted C_{ijkl}. This tensor encapsulates the material's stiffness properties, allowing us to model how it deforms under applied forces in a generalized Hooke's law and it is expressed as:

$$\sigma_{ij} = \sum_{k,l} C_{ijkl}\varepsilon_{kl} \tag{1.7}$$

where i, j, k, l range over the spatial coordinates (1, 2, 3). σ_{ij} is the stress tensor components, ε_{kl} is the strain tensor components, and C_{ijkl} is the elasticity tensor components, describing how stress components relate to strain components. As for materials with hexagonal symmetry, such as ZnO, the symmetry further reduces the number of independent components in C_{ijkl}. Out of 21 possible components in a 6×6 matrix, only five are independent: $C_{11}, C_{12}, C_{13}, C_{33}, C_{44}$. The generalized Hooke's law in Voigt notation for a hexagonal structure is written as :

$$\begin{pmatrix} \sigma_{xx} \\ \sigma_{yy} \\ \sigma_{zz} \\ \sigma_{yz} \\ \sigma_{zx} \\ \sigma_{xy} \end{pmatrix} = \begin{pmatrix} C_{11} & C_{12} & C_{13} & 0 & 0 & 0 \\ C_{12} & C_{11} & C_{13} & 0 & 0 & 0 \\ C_{13} & C_{13} & C_{33} & 0 & 0 & 0 \\ 0 & 0 & 0 & C_{44} & 0 & 0 \\ 0 & 0 & 0 & 0 & C_{44} & 0 \\ 0 & 0 & 0 & 0 & 0 & C_{66} \end{pmatrix} \begin{pmatrix} \varepsilon_{xx} \\ \varepsilon_{yy} \\ \varepsilon_{zz} \\ \varepsilon_{yz} \\ \varepsilon_{zx} \\ \varepsilon_{xy} \end{pmatrix} \tag{1.8}$$

where $C_{66} = \frac{1}{2}(C_{11} - C_{12})$. For bulk ZnO, generally the elastic constants in gigapascals (GPa) are valued at[25] :

C_{11}	C_{12}	C_{13}	C_{33}	C_{44}	C_{66}
209.7	121.1	105.1	210.9	42.47	44.29

Table 1.2: Bulk ZnO Elastic constants (in GPa)[25].

The elastic constants are related to the material's properties such as:

Young's Modulus E:

$$E = \frac{C_{11}C_{33} - C_{13}^2}{C_{11} + C_{33} - 2C_{13}}. \tag{1.9}$$

Shear Modulus μ:

$$\mu = C_{44} \tag{1.10}$$

Poisson's Ratio ν:

$$\nu = \frac{C_{13}}{C_{11} + C_{33} - 2C_{13}} \tag{1.11}$$

Hooke's law states that for isotropic materials, we have :

$$\sigma_{ij} = \lambda \delta_{ij} \varepsilon_{kk} + 2\mu \varepsilon_{ij} \tag{1.12}$$

Where λ and μ are Lamé constants, ε_{kk} is the trace of the strain tensor and δ_{ij} is the Kronecker delta. The elastic constants (E) are the "Young's modulus" which relates stress and strain along one axis, (G) is the shear modulus that describes the material's response to axial stress and (ν) is the Poisson's ratio, which is the ratio of lateral to axial strain in response to axial stress, the table below shows the corresponding values of these parameters for bulk ZnO.

	λ (GPa)	μ (GPa)	E (GPa)	ν
Bulk ZnO	60	25	144	0.34

Table 1.3: Different mechanical parameters of Bulk ZnO in literature[26, 27]

The potential energy stored by elastic deformation is given in the Einstein's notation by :

$$U = \frac{1}{2} \sigma_{ij} \varepsilon_{ij} \tag{1.13}$$

1.1.3.4 Plasticity

While "Elasticity" is the property of materials to return to their original shape, "Plasticity" describes the permanent deformation of materials when stress exceeds the elastic limit, which is also called yield strength. Once the yield point is reached, materials undergo irreversible changes in shape. The "Von Mises Criterion" or the "maximum distortion

energy criterion" is used to determine if a given material will yield or fracture. It is used for ductile materials such as metals. Where we have :

$$\sqrt{\frac{3}{2}s_{ij}s_{ij}} = \sigma_y \tag{1.14}$$

Where s_{ij} are deviatoric stresses, and σ_y is the yield stress. The evolution of plastic strain is governed by the plastic flow rule:

$$\dot{\varepsilon}^p_{ij} = \dot{\lambda}\frac{\partial f}{\partial \sigma_{ij}} \tag{1.15}$$

Where $\dot{\varepsilon}^p_{ij}$ is the plastic strain tensor, f is the yield function, $\dot{\lambda}$ is the plastic multiplier, and $\frac{\partial f}{\partial \sigma_{ij}}$ specifies the direction of plastic strain evolution in the stress space, ensuring that the plastic strain aligns with the yield criterion.

The yield function (f) defines the transition between elastic and plastic behavior in materials. It is a scalar function of the stress tensor (σ_{ij}). When $f < 0$, the material is in the elastic regime, and any deformation is fully recoverable when the load is removed. When $f = 0$, the material has reached the yield surface, meaning the stress state corresponds to the onset of plastic deformation.

1.1.3.5 Dislocations

Beyond the elastic limit deformations in a crystal, distinctive slip lines begin to appear on its surface. These lines are small steps that are caused by the movement of linear defects within the crystal, known as dislocations. There are two fundamental types of straight dislocations: **edge dislocations** and **screw dislocations**. Very often, dislocations exhibit a mix of these two characteristics, forming what are called **mixed dislocations**. These mixed dislocations are not straight but curved, and at any given point, they can be broken down into edge and screw components.

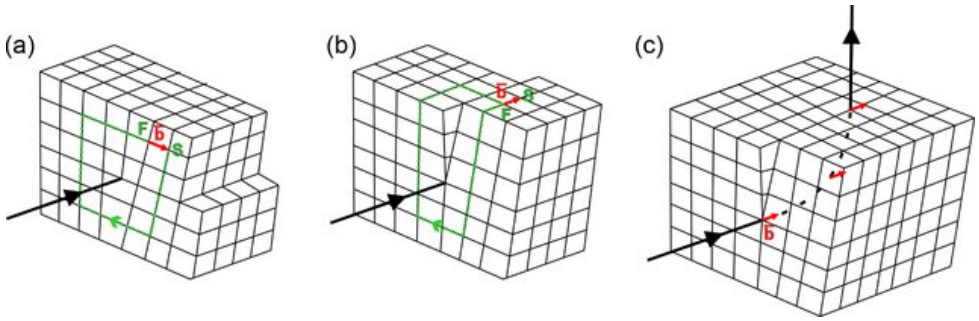

Figure 1.4: The models of (a) edge, (b) screw and (c) mixed dislocations in a simple cubic structure. Black arrows indicate dislocation line. Burgers circuit is marked in green (S-start and F-finish positions of atom-to-atom counting). The Burgers vector $\vec{b}$ is shown in red.[2]

1.1.3.5.1 Edge dislocation

An edge dislocation can be visualized as the result of inserting a half-plane of atoms into a perfect crystal. The position of the dislocation is defined as the boundary where this extra atomic half-plane ends within the otherwise undisturbed crystal structure. The deformation caused by this dislocation is similar to adding an additional layer of atoms to the upper part of the crystal. As a result, atoms in the upper half of the crystal experience compression, while those below the dislocation are subjected to tension (See Fig. 1.4) a).

1.1.3.5.2 Screw dislocation

A screw dislocation can be imagined as a cut made in a crystal, followed by sliding one edge of the cut relative to the other by an atomic-scale distance. This dislocation transforms successive atomic planes into a helical surface, which is why it is referred to as a "screw" dislocation (See Fig. 1.4) b).

1.1.3.5.3 Burgers vector

A dislocation is characterized by its position in the crystal and a vector called the **Burgers vector**. The Burgers vector, denoted as $\vec{b}$ (shown in red in Fig. 1.4), is defined by a loop (the Burgers circuit) connecting neighboring atoms and encircling the dislocation line (shown in green in Fig. 1.4). By convention, the Burgers circuit is constructed in a

clockwise direction. In the case of an edge dislocation, the Burgers vector is perpendicular to the dislocation line. As for a screw dislocation, the Burgers vector is parallel to the dislocation line.

1.1.3.5.4 Shear deformation

A dislocation can move and slide within the atomic plane where its dislocation line lies. This plane is referred to as the slip plane of the dislocation. For an edge dislocation, the slip direction coincides with the Burgers vector. In contrast, for a screw dislocation, the slip direction is perpendicular to the Burgers vector. Hence, a dislocation is fully characterized by its Burgers vector and the orientation of its dislocation line.

However, not all dislocations within a material are mobile. Crystallographic analyses of deformed samples reveal that slip tends to occur along well-defined planes within the crystal lattice. These slip planes correspond to planes of highest atomic density, while the slip directions align with the densest crystallographic directions. Consequently, a slip system is defined by a slip plane—specified by its unit normal—and a slip direction.

In HCP metals, the primary slip system involves the basal plane (0001) due to its low critical resolved shear stress (CRSS), which makes basal slip the most easily activated mechanism. However, under certain loading conditions, shear deformation can extend to prismatic $\{10\bar{1}0\}$ and pyramidal planes $\{10\bar{1}1\}$[44]. For a basal slip, $\langle a\rangle$ type dislocations move in the basal plane, contributing to shear deformation, as for a pyramidal slip, it involves $\langle c+a\rangle$ dislocations, which are crucial for accommodating deformation along the c-axis.

In ZnO, dislocations are typically observed as segments within the crystal. The main types include edge dislocation segments, where the Burgers vector lies within the basal plane ($\vec{b}$), involving extra atomic planes. These segments are often visible due to their slower mobility compared to other types of dislocations. However, dislocations in a crystal are inherently loops unless they terminate at a surface. Screw dislocations, characterized by a Burgers vector along [0001], and mixed dislocations may also form but are less commonly observed if their higher mobility allows them to move out of the observable region. This mobility disparity can explain why edge dislocation segments are more frequently detected in deformed ZnO samples.

1.1.3.6 Fracture

Fracture is the separation or fragmentation of a material into two or more parts under the influence of stress. It marks the ultimate failure of a material and is a critical area of study to prevent catastrophic failures. When a material contains a crack, the stress distribution around the crack tip is not uniform. Instead, the stress intensifies near the crack tip, leading to a phenomenon known as stress concentration. For an elliptical crack in an infinite plate subjected to a nominal stress σ, the stress at the crack tip σ_{tip} can be approximated by:

$$\sigma_{\text{tip}} = \sigma \left(1 + 2\frac{a}{c}\right) \tag{1.16}$$

where a is the half-length of the crack, c is the half-width of the crack. As the crack becomes sharper (i.e., c decreases), the stress concentration increases, making the material more susceptible to fracture. To quantify the effect of a crack on a material's strength, fracture mechanics introduces the concept of the Stress Intensity Factor K. This factor characterizes the stress state near the crack tip and depends on the load, crack size, and geometry of the component. For a crack of length $2a$ in an infinite plate under uniform tensile stress σ, the stress intensity factor is given by:

$$K = Y\sigma\sqrt{\pi a} \tag{1.17}$$

where Y is a dimensionless parameter that depends on the geometry of the specimen, for example :

- **Long strip, central crack, tensile stress :**

$$K_I = Y\sigma\sqrt{\pi a} \tag{1.18}$$

$$Y = cos(\pi a/2)^{\frac{1}{2}} \tag{1.19}$$

- **Long strip, edge crack, tensile stress :**

$$K_I = Y\sigma\sqrt{\pi a} \tag{1.20}$$

$$Y = 1.12 + \alpha(2.91\alpha - 0.64)/(1 - 0.93\alpha) \tag{1.21}$$

Where $\alpha = \frac{a}{w}$ is the normalised crack size, where w is the width of the sample. Each material has a critical stress intensity factor, known as fracture toughness (K_{Ic}). When K reaches K_{Ic}, rapid crack propagation occurs, leading to fracture. For ZnO, K_{1c} has been estimated at values between 2.02 and 2.5 $MPa \cdot m^{1/2}$ [45, 46].

1.1.4 Electrical properties

Zinc oxide is a II-VI semiconductor with a direct bandgap of about 3.37 eV at room temperature, classifying it as a wide-gap semiconductor [47]. The bandgap energy is crucial because it determines the energy an electron needs to move from the valence band to the conduction band. ZnO naturally exhibits n-type electrical conductivity primarily due to the presence of oxygen vacancies which are naturally formed during the growth process [48]. It can also exhibit this n-type doping via other materials such as Al or Ga with a doping range of 1 to 6 at.%, depending on the application and synthesis method [49]. The resistivity of ZnO doped with 1.5% of Al, for example, is around $1.54 \cdot 10^{-4}$ Ω.cm [50]. Achieving stable p-type doping, however is difficult due to ZnO's tendance to exhibit n-type conductivity due to native defects such as oxygen vacancies. Materials like nitrogen are used as dopant and often requires ratios around 1–2 atomic%. However, excess doping can revert the material to n-type due to compensation effects [51]. The reported resistivity of p-type dopant ZnO is 0.6 Ω.cm, using P as a dopant at a concentration of 1% which should be sufficient for LED fabrication [52].

In semiconductor devices, the contact between the metal and the semiconductor is crucial. There are two types of contacts: Ohmic contacts and Schottky contacts. The former is characterized by a linear and symmetric current-voltage (I-V) curve, whereas the latter is non-linear and asymmetric in its I-V characteristics. The type of contact that forms at the metal/semiconductor junction depends on whether the semiconductor is n-type or p-type and the difference in work functions (Φ) between the metal Φ_m and the semiconductor $\Phi_s c$, as shown in the table below.

	n-type Semiconductor	**p-type Semiconductor**
$\Phi_m > \Phi_{sc}$	Schottky	Ohmic
$\Phi_{sc} > \Phi_m$	Ohmic	Schottky

Table 1.4: Types of contacts formed based on the work function differences.

For example, when n-type ZnO (Φ_{ZnO} = 4.53 eV) is in contact with gold (Au, Φ_{Au} = 5.1 eV) or platinum (Pt, Φ_{Pt} = 6.1 eV), a Schottky contact is formed. Conversely, when ZnO is in contact with titanium (Ti, Φ_{Ti} = 3.90 eV), silver (Ag, Φ_{Ag} = 4.26 eV), or aluminum (Al, Φ_{Al} = 4.08 eV), an Ohmic contact is established [53]. The alignment of the conduction band and the valence band of the materials in contact is schematically illustrated in (Fig. 1.5).

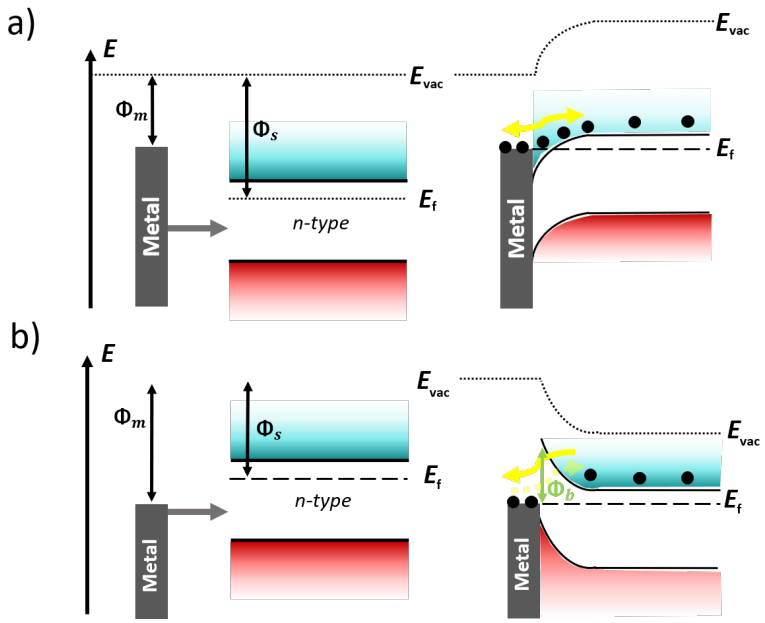

Figure 1.5: a) When the metal (ϕ_m) is smaller than the semiconductor (ϕ_s) in an n-type semiconductor, the bands bend downwards, forming an Ohmic contact that allows current to flow from the metal to the semiconductor's conduction band. b) When ϕ_m is larger than ϕ_s, the bands bend upwards, creating a Schottky contact. Here, current can only flow from the semiconductor to the metal via electrons. For p-type semiconductors, the opposite conditions apply.

1.1.5 Piezoelectric properties

Piezoelectricity was discovered in 1880 by the brothers Jacques Curie (1856-1941) and Pierre Curie (1859-1906) on Quartz and Topaz [54]. They observed an unusual characteristic in certain crystalline minerals such as tourmaline, quartz, topaz, and Rochelle salt. They found that positive and negative charges appeared on certain faces of these materials when they were mechanically stressed. In 1881, Hankel named this phenomenon "Piezoelectricity" where "Piezo" as a term is derived from Greek meaning "to press" [55]. The following year, Lippmann predicted the existence of the inverse piezoelectric effect based on fundamental thermodynamic principles [56]. Since the 1980s, piezoelectric materials have garnered significantly more interest due to their usage in various applications, including robotics, healthcare, sensors, and defense. Piezoelectricity is the property of certain materials to become electrically polarized when subjected to mechanical stress, or conversely, to deform when an electric field is applied to them (Fig. 1.6).

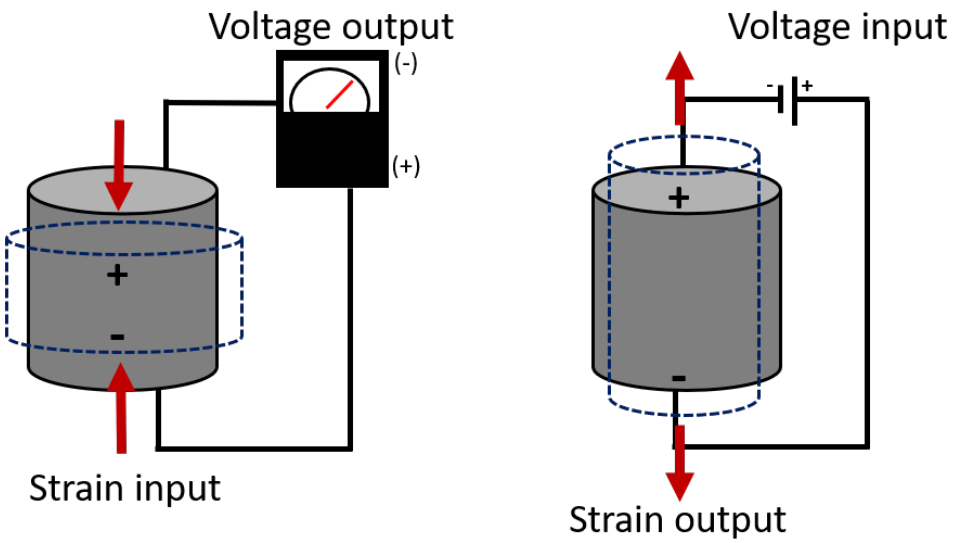

Figure 1.6: Schematic illustrations of a) direct and b) inverse piezoelectric effect

However, the piezoelectric effect is not present in all materials. It is only found in crystals that contain at least two oppositely charged elements and lack a center of symmetry. Of the 32 known crystal classes, 21 are not centrosymmetric, and 20 of these exhibit piezoelectric properties. In a piezoelectric crystal at rest, the centers of mass of the

positive and negative charges in each unit cell coincide. Consequently, the polarization is zero and the material exhibits electrical neutrality. When stress is applied to the material, the crystal lattice is deformed, causing a separation of the centers of mass of the positive and negative charges, thereby generating dipoles (Fig. 1.7).

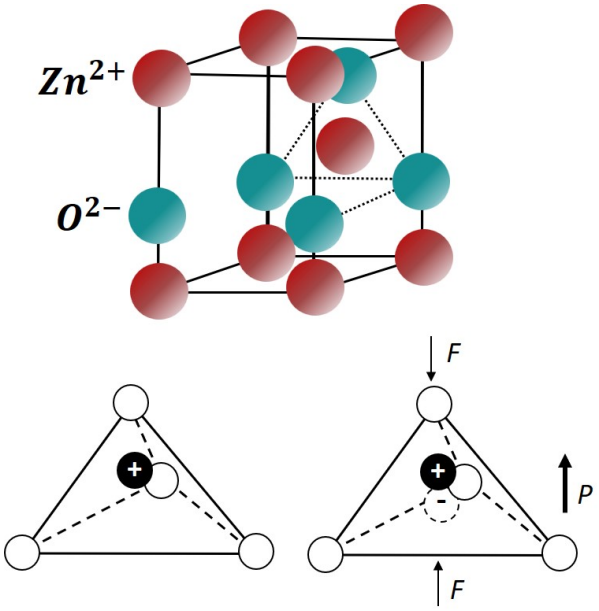

Figure 1.7: Schematic representation of ZnO structure showing the Zn^{2+} and O^{2-} atoms polarization

If the piezoelectric material is connected to an external measurement circuit via electrodes, applying pressure to the material polarizes it, and a charge density appears on the surface in contact with the electrodes. This polarization generates an electric field, which causes free charges to flow in the external circuit. Depending on their sign, the free charge carriers move to compensate for the opposing potential until an equilibrium state is reached. Once equilibrium is reached, the measured voltage returns to zero. Upon the release of the stress, the piezoelectric polarization disappears and the flow of charge carriers reverses direction; the charges accumulated on the surfaces of the material return to the external circuit. In this case, a voltage of opposite sign to that measured during the compression of the piezoelectric material is observed.

The piezoelectric effect can be described using two parameters, which are the mechanical deformation ε and the electric displacement field D. Both of these parameters are functions

of the electric field and the mechanical stress which is written as [57]:

$$\begin{cases} D = \epsilon^{\sigma} E + d^{E} \sigma \\ \varepsilon = d^{\sigma} E + S^{E} \sigma \end{cases} \tag{1.22}$$

The anisotropic permittivity tensor ϵ describes the variation of the electric displacement field D with respect to an applied electric field E. It characterizes the dielectric properties of the material and is dimensionally equivalent to permittivity (ϵ). The direct piezoelectric tensor $\mathbf{d^E}$ relates the variation of D to mechanical stress σ, assuming no external electric field is present. This tensor quantifies the direct piezoelectric effect, where stress induces polarization. The indirect piezoelectric tensor $\mathbf{d}^{\sigma}$, on the other hand, describes the variation of mechanical strain $(\mathbf{S})$ with an applied electric field $\boldsymbol{E}$, under the assumption of no external mechanical stress. This tensor characterizes the inverse piezoelectric effect, where an electric field induces deformation. And, finally, S^E is the compliance matrix or the inverse of the elasticity matrix, relating the variation of strain with mechanical stress. It represents the material's ability to deform under stress in the absence of an electric field.

To describe the direct piezoelectric effect: In the 3D space, σ is a symmetric tensor that can be written as a 3x3 matrix or by symmetry it can be reduced into a vector with 6 components using the Voigt's notation in which :

$$\sigma = \begin{pmatrix} \sigma_{xx} & \sigma_{xy} & \sigma_{xz} \\ \sigma_{yx} & \sigma_{yy} & \sigma_{yz} \\ \sigma_{zx} & \sigma_{zy} & \sigma_{zz} \end{pmatrix} = \begin{pmatrix} \sigma_1 \\ \sigma_2 \\ \sigma_3 \\ \sigma_4 \\ \sigma_5 \\ \sigma_6 \end{pmatrix} \tag{1.23}$$

Where $\sigma_{xx} \rightarrow \sigma_1$, $\sigma_{yy} \rightarrow \sigma_2$, $\sigma_{zz} \rightarrow \sigma_3$, $\sigma_{yz} \rightarrow \sigma_4$, $\sigma_{xz} \rightarrow \sigma_5$, $\sigma_{xy} \rightarrow \sigma_6$. In the spatial reference (x, y, z) the electric field E also has 3 components $E_{xx} \rightarrow E_1$, $E_{yy} \rightarrow E_2$, $E_{zz} \rightarrow E_3$ for which we can note it as:

$$E = \begin{pmatrix} E_1 \\ E_2 \\ E_3 \end{pmatrix} \tag{1.24}$$

and the permittivity matrix is thus written as:

$$\epsilon = \begin{pmatrix} \epsilon_1 & 0 & 0 \\ 0 & \epsilon_2 & 0 \\ 0 & 0 & \epsilon_3 \end{pmatrix} \tag{1.25}$$

In (x, y, z), the coefficient e_{ijk} represents the contribution of the stress component in the direction jk to the i-th component of the electric displacement field. This relationship is a fundamental part of the piezoelectric effect, where mechanical stress induces an electric displacement field in piezoelectric materials. Therefore, the general form is:

$$D_i = \sum_{jk} e_{ijk}\sigma_{jk} + \epsilon_i E_i, \quad \forall\, i \in \{x, y, z\},\, jk \in \{xx, yy, zz, yz, xz, xy\}. \tag{1.26}$$

Which can be simplified in the Voigt notation as:

$$D_i = \sum_{j=1}^{6} e_{ij}\sigma_j + \epsilon_i E_i, \quad \forall\, i \in \{1, 2, 3\}. \tag{1.27}$$

Where d^E is a 3×6 piezoelectric tensor. The contracted notation simplifies the representation of the components. The matrix form of the **direct piezoelectric effect** equation is:

$$\begin{pmatrix} D_1 \\ D_2 \\ D_3 \end{pmatrix} = \begin{pmatrix} e_{11} & e_{12} & e_{13} & e_{14} & e_{15} & e_{16} \\ e_{21} & e_{22} & e_{23} & e_{24} & e_{25} & e_{26} \\ e_{31} & e_{32} & e_{33} & e_{34} & e_{35} & e_{36} \end{pmatrix} \begin{pmatrix} \sigma_1 \\ \sigma_2 \\ \sigma_3 \\ \sigma_4 \\ \sigma_5 \\ \sigma_6 \end{pmatrix} + \begin{pmatrix} \epsilon_1 & 0 & 0 \\ 0 & \epsilon_2 & 0 \\ 0 & 0 & \epsilon_3 \end{pmatrix} \begin{pmatrix} E_1 \\ E_2 \\ E_3 \end{pmatrix}. \tag{1.28}$$

Here, D_i are the electric displacement field components, σ_j are the components of the stress tensor (in Voigt notation), E_i are the components of the electric field, e_{ij} are the piezoelectric coefficients, and ϵ_i are the permittivity components in the material. This

matrix formulation expresses how the electric displacement field D_i is influenced both by an applied stress σ_j and an electric field E_i in piezoelectric materials.

As for the indirect piezoelectric effect: We cleared out the ambiguity around the mechanical stress σ, the electric field E and the coefficient e_{ijk}. Here ε_i is a symmetric strain tensor of size 3×3, which can also be reduced to a vector with six components $(\varepsilon_1, \varepsilon_2, \varepsilon_3, \varepsilon_4, \varepsilon_5, \varepsilon_6)$ using the Voigt notation. Each component of the total electric field E in the directions x, y, z can induce a deformation S_{ij} in the crystal. This deformation can be superimposed with the elastic deformation caused by an applied stress T. Mathematically, the deformation is expressed as:

$$\varepsilon_i = \sum_k d_{ik}^{\sigma} E_k + \sum_j S_{ij}^{E} \sigma_j, \quad k \in \{1,2,3\}, \forall\, i \in [1,6],\ \forall\, j \in [1,6] \tag{1.29}$$

The matrix form of the indirect piezoelectric equation in Voigt notation becomes:

$$\begin{pmatrix} \varepsilon_1 \\ \varepsilon_2 \\ \varepsilon_3 \\ \varepsilon_4 \\ \varepsilon_5 \\ \varepsilon_6 \end{pmatrix} = \begin{pmatrix} d_{11}^{\sigma} & d_{12}^{\sigma} & d_{13}^{\sigma} \\ d_{21}^{\sigma} & d_{22}^{\sigma} & d_{23}^{\sigma} \\ d_{31}^{\sigma} & d_{32}^{\sigma} & d_{33}^{\sigma} \\ d_{41}^{\sigma} & d_{42}^{\sigma} & d_{43}^{\sigma} \\ d_{51}^{\sigma} & d_{52}^{\sigma} & d_{53}^{\sigma} \\ d_{61}^{\sigma} & d_{62}^{\sigma} & d_{63}^{\sigma} \end{pmatrix} \begin{pmatrix} E_1 \\ E_2 \\ E_3 \end{pmatrix} + \begin{pmatrix} S_{11} & S_{12} & S_{13} & S_{14} & S_{15} & S_{16} \\ S_{21} & S_{22} & S_{23} & S_{24} & S_{25} & S_{26} \\ S_{31} & S_{32} & S_{33} & S_{34} & S_{35} & S_{36} \\ S_{41} & S_{42} & S_{43} & S_{44} & S_{45} & S_{46} \\ S_{51} & S_{52} & S_{53} & S_{54} & S_{55} & S_{56} \\ S_{61} & S_{62} & S_{63} & S_{64} & S_{65} & S_{66} \end{pmatrix} \begin{pmatrix} \sigma_1 \\ \sigma_2 \\ \sigma_3 \\ \sigma_4 \\ \sigma_5 \\ \sigma_6 \end{pmatrix} \tag{1.30}$$

In the case of a wurtzite crystal structure, as it is the case for ZnO, only 3 independent coefficients exist in the piezoelectric matrix written in the Voigt notation:

$$\begin{pmatrix} D_1 \\ D_2 \\ D_3 \end{pmatrix} = \begin{pmatrix} 0 & 0 & 0 & 0 & d_{15}^{\sigma} & 0 \\ 0 & 0 & 0 & d_{15}^{\sigma} & 0 & 0 \\ d_{31}^{\sigma} & d_{31}^{\sigma} & d_{33}^{\sigma} & 0 & 0 & 0 \end{pmatrix} \begin{pmatrix} \sigma_1 \\ \sigma_2 \\ \sigma_3 \\ \sigma_4 \\ \sigma_5 \\ \sigma_6 \end{pmatrix} \tag{1.31}$$

The coefficients $d_{31}^{\sigma}, d_{33}^{\sigma}, d_{15}^{\sigma}$ are the longitudinal, transverse and shear operational modes, respectively. For many applications of piezoelectric materials, the d_{33}^{σ} coefficient is the most important one. On the one hand, it is oriented along the c-axis of a wurtzite

structure, which has the largest piezoelectric potential. On the other hand, it is parallel to the applied electric field. It's then the parameter used to compare the piezoelectric potential of different materials.

ZnO has a non-centrosymmetric crystal structure, which grants it piezoelectric properties. Under mechanical stress, the ZnO crystal lattice is deformed, causing the displacement of the center of gravity of positive and negative charges, leading to the emergence of a polarization vector (P) on the surface of the ZnO. Table 1.5 presents the piezoelectric coefficient for ZnO and other piezoelectric semiconducting materials.

Material	**Piezoelectric Coefficient** (d_{33}) [pC/N]
ZnO (Zinc Oxide)	12
InN (Indium Nitride)	7.6
$LiNbO_3$ (Lithium Niobate)	7
AlN (Aluminum Nitride)	5
GaN (Gallium Nitride)	3.1
Quartz	2.3

Table 1.5: Comparison of piezoelectric coefficients (d_{33}) for different semiconducting materials [25, 28]

The table above compares the piezoelectric coefficients (d_{33}) of six materials: Zinc Oxide (ZnO), Aluminum Nitride (AlN), Lithium Niobate ($LiNbO_3$), Quartz, Gallium Nitride (GaN), and Indium Nitride (InN). ZnO stands out with the highest d_{33} value of 12 pC/N, demonstrating its excellent piezoelectric properties.

Flexoelectricity on the other hand, is the generation of electric polarization in a material due to a non-uniform mechanical strain, such as bending or twisting. Unlike piezoelectricity, which requires a non-centrosymmetric crystal structure, flexoelectricity can occur regardless of symmetry. In ZnO nanowires, flexoelectric effects become significant due to their small dimensions and the ease with which they can undergo bending deformations. The combination between piezoelectricity and flexoelectricity can lead to an enhanced electromechanical response since both surface elasticity and flexoelectricity significantly affect the piezoelectric potential [58].

1.2 ZnO Nanostructures

Over the past decades the miniaturization of electronic devices has strongly influenced the technological evolution. Moore's law, for instance, which has been valid for the last sixty years, states that roughly every eighteen months the number of transistors on an integrated circuit doubles [59]. This ongoing process requires a further reduction of feature sizes. However, with the ongoing miniaturization, the object size becomes comparable to intrinsic length scales and the Fermi wavelength leading to classical finite-size effects and quantum size effects, respectively. For instance, when a structure is on the same order as the electron mean-free-path or the diffusion length of defects, the electrical transport properties, respectively, the mechanical properties of the material are altered. On the other hand, when the size of nanostructures is on the order of the Fermi wavelength of charge carriers, the electronic band structure of a material is modified inducing discrete energy levels. This splitting of continuous energy bands into discrete energy levels affects the electrical transport properties and optoelectronic properties of materials. In addition, the surface-to-volume ratio increases significantly when scaling down materials to the nanoscale, which by itself affects charge transfer and surface-related electrical phenomena. In particular, defects are able to diffuse to the free surfaces of nano-objects where they are annihilated leading to defect-scarce nanostructures. The reduced amount of defects improve the alignment of polarization which thereby may increase the piezoelectric effect in piezoelectric nanomaterials. The following two sub-chapters will focus on the mechanical and the piezoelectric properties in nanostructures with a focus on ZnO nano-objects.

1.2.1 Nanomechanics

In the 50s of the last century, S.S. Brenner conducted pioneering works on micro-whiskers demonstrating extraordinary mechanical behaviors on the microscale [60]. Tensile tests on iron, copper, and silver whiskers with diameters ranging from 1.2 to 15 µm and lengths of up to 4 mm demonstrated strengths which were close to the strength of perfect crystals. In addition, Brenner showed that the strength decreased with increasing diameter and length which he attributed to defects formed during the growth process. To study the mechanical behavior of materials, different testing methods including nanoindentation, uniaxial tension

and compression, bending tests as well as dynamic vibration tests exist. In the last few decades, great efforts were undertaken to investigate the mechanical behavior at small scales. In the following sub-chapter, the different nano-mechanical testing techniques for *ex-situ* as well as *in-situ* studies will be introduced.

1.2.1.1 Nano-mechanical testing techniques

1.2.1.1.1 Nanoindentation

Nanoindentation is an instrumented technique used to experimentally study the properties of materials at small scales. The principle of nanoindentation is forcing an indenter tip, typically made out of diamond, into the surface of the sample. These indenter tips can take different shapes and forms from spherical to conical to a Berkovich type etc. Nanoindentation was initially developed for the analysis of different materials. This technique has undergone significant advancements over the past twenty years. It enables the precise determination of local mechanical properties of materials, such as hardness, Young's modulus, and strain hardening. Hardness tests are among the most commonly used methods to determining the mechanical properties of a material. A traditional indentation test measures a material's local resistance to plastic deformation. Hardness is not an intrinsic mechanical property but rather a conventional measure. There are various hardness testing methods that operate on the same basic principle: a known force F is applied to press an indenter into the material, and the punch is removed after a certain period. Once the load is removed, a residual imprint remains in the material. In nanoindentation tests, both the penetration depth h and the applied force F can be measured dynamically during a load-unload cycle, giving a force-displacement curve, commonly referred to as an indentation curve. (Fig. 1.8) illustrates a typical indentation curve for an elastic material indented by a sharp tip.

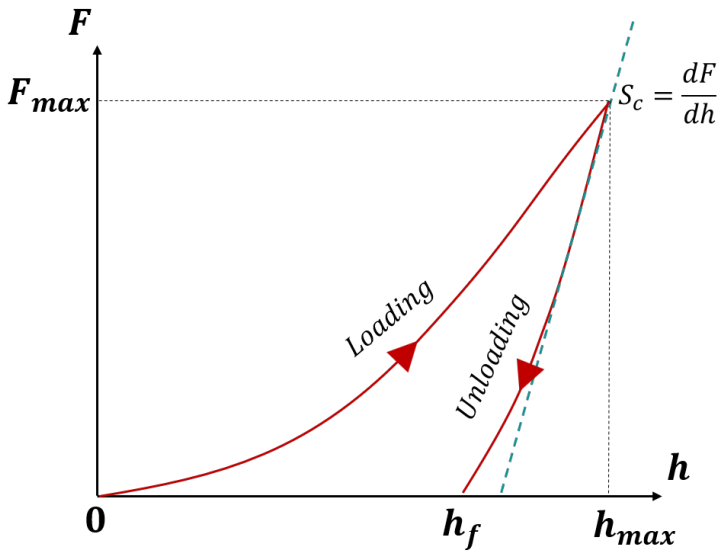

Figure 1.8: Schematic representation of a force-displacement curve obtained during nanoindentation of an elastoplastic solid.

To determine the mechanical properties, it is crucial to calculate the contact area at every indentation depth h. This requires the precise definition of the indenter tip geometry as a function of h. Accurately determining the actual contact area is essential in nanoindentation testing, as it significantly impacts the calculations of hardness and the indentation modulus. The Oliver-Pharr model is the most widely used approach to analyze nanoindentation experiments. This method provides an accurate description of the unloading curve during indentation using the following equation:

$$F = B_{\text{op}}(h - h_r)^{m_{\text{op}}} \tag{1.32}$$

where F is the load, h is the indentation depth, h_r is the residual indentation depth, B_{op} is a constant from experimental data and m_{op} is an exponent determined by fitting the unloading curve.

Another nanoindentation technique that is worth mentioning is the Continuous Stiffness Measurement (CSM). This method has been introduced to simplify the determination of the contact point during nanoindentation. It involves applying rapid, low-amplitude oscillations to the indenter while it is in motion. By monitoring these oscillations throughout the entire loading and unloading cycle, the mechanical properties of the material such as the Young

modulus can be assessed almost continuously. [61] demonstrated a specific application of this technique to identify the exact contact point. Their study highlighted that plotting the evolution of contact stiffness against displacement near the surface reveals a distinct slope change, marking the point where the indenter makes contact with the material.

1.2.1.1.2 Uniaxial compression and tensile testing

This uniaxial testing procedure involves stretching/compressing the material to investigate its mechanical properties, including its tensile strength, Young's modulus, fracture strength, and plasticity. In contrast to nanoindentation, the strain fields are much simpler for uniaxial tensile and compression tests.

In order to perform uniaxial tensile and compression tests on nanostructures, dedicated tools such as push-to-pull devices and micromechanical system (MEMS) based tensile stages have been developed (see Fig. 1.9). The former can be actuated by an atomic force microscope (AFM) inside scanning electron microscopes (SEM) or by using dedicated transmission electron microscope (TEM) holders. The MEMS-based tensile stage works by applying an electrical voltage leading to an electrical current in the bars on the right-hand side of the device which generates Joule heat and thus results in the expansion of these bars and the actuation of the MEMS-based tensile testing stage. This device is very well adapted for tensile tests on nanowires and thin films [4, 5].

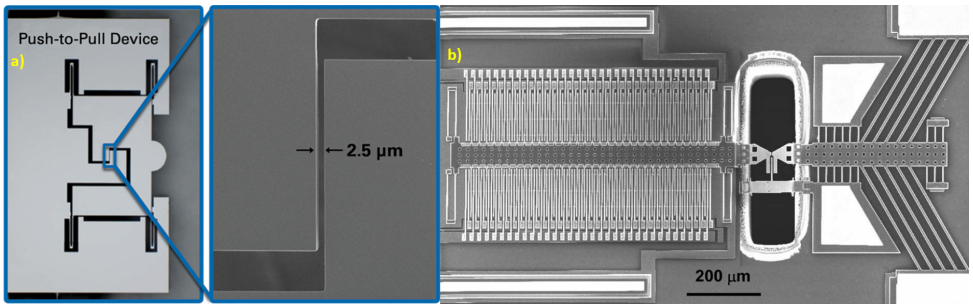

Figure 1.9: a) A push-to-pull device for in-situ nanomechanical testing[3] b) A MEMS-based testing platform for in situ TEM, enabling compressive and tensile testing on nanostructures.[4][5]

These dedicated nano-mechanical instruments in combination with TEM enable high-resolution imaging, precise alignment, and accurate measurement of force and displacement

at the nanoscale.

Uniaxial compression and tensile testing of ZnO nanowires often encounter problems such as alignment challenges, buckling under compression, and gripping difficulties during tension. These issues can result in inaccurate stress measurements and amplify surface effects, complicating the characterization process.

1.2.1.1.3 Three-point bending

Bending experiments can generally be performed in various configurations. The testing structure can be fixed on one end only and the load is applied at its free end resulting in a cantilever-like test. On the other hand, both ends of the specimen can either be simply supported or both be clamped while the load is applied on one or two points along the suspended structure facilitating three-point and four-point bending tests. For the mechanical behavior of the tested structure, the boundary conditions, *i.e.* if the two ends are simply supported or thoroughly clamped, is of prime importance.

The mechanical deformation of a beam tested in bending configuration is well described by the Euler-Bernoulli beam theory [62]. In the following, we will focus on three-point bending tests.

The Free Body Diagram (FBD) is a simple representation of the beam with the forces acting on it. In this case F is the applied load at the center of the beam. R represents the reaction forces at the supports, which are equal and opposite to the load applied to maintain equilibrium. Since the beam is symmetric and the load is applied at the center, the reaction forces R are equal and can be calculated as $R = \frac{F}{2}$. On the other hand, the Shear Force Diagram (SFD) illustrates how the shear force V, which acts parallel to the cross-section of the beam, varies along the length of the beam. For the case of a beam with a central load and fixed ends, the shear force is constant in each segment of the beam. On one side of the beam V is equal to $\frac{F}{2}$. It decreases linearly towards zero approaching the center of the beam and then reverses its direction and amounts to $-\frac{F}{2}$ on the other side. Thirdly, the Bending Moment Diagram (BMD) demonstrates the variation of the bending moment along the length of the beam. The bending moment $M_{\max}$ is a measure of the internal moment that causes the beam to bend. It is maximum at the center of the beam and at the two supports. For a beam with a central load, the maximum bending

moment can be calculated as $M_{\max} = \frac{FL}{8}$ with L being the full length of the beam. The bending moment is zero at the supports and increases to a maximum at the center of the beam. This creates a parabolic distribution of moments along the beam's length.

The deflection Δ_x at any point along the beam is given by the following equation:

$$\Delta_x = \frac{Fx^2}{48EI} \times (3L - 4x) \tag{1.33}$$

where x is the distance from one end of the beam, L is the length of the beam, E is the Young modulus of the material, and I is the moment of inertia of the beam's cross-section. The latter quantifies how the cross-sectional area is distributed about a certain axis and impacts the beam's resistance to bending. For a hexagonal cross-section, I equals to [63]:

$$I = \frac{A}{12}\left[\frac{d^2\left(1 + 2\cos^2 30°\right)}{4\cos^2 30°}\right] = 0.06d^4 \tag{1.34}$$

The maximum deflection $\Delta_{\max}$ occurs at the center of the beam and can be calculated as:

$$\Delta_{\max} = \frac{FL^3}{192EI} \tag{1.35}$$

This tells us how much the beam will bend under the applied load, which is crucial for ensuring that the beam maintains its structural integrity.

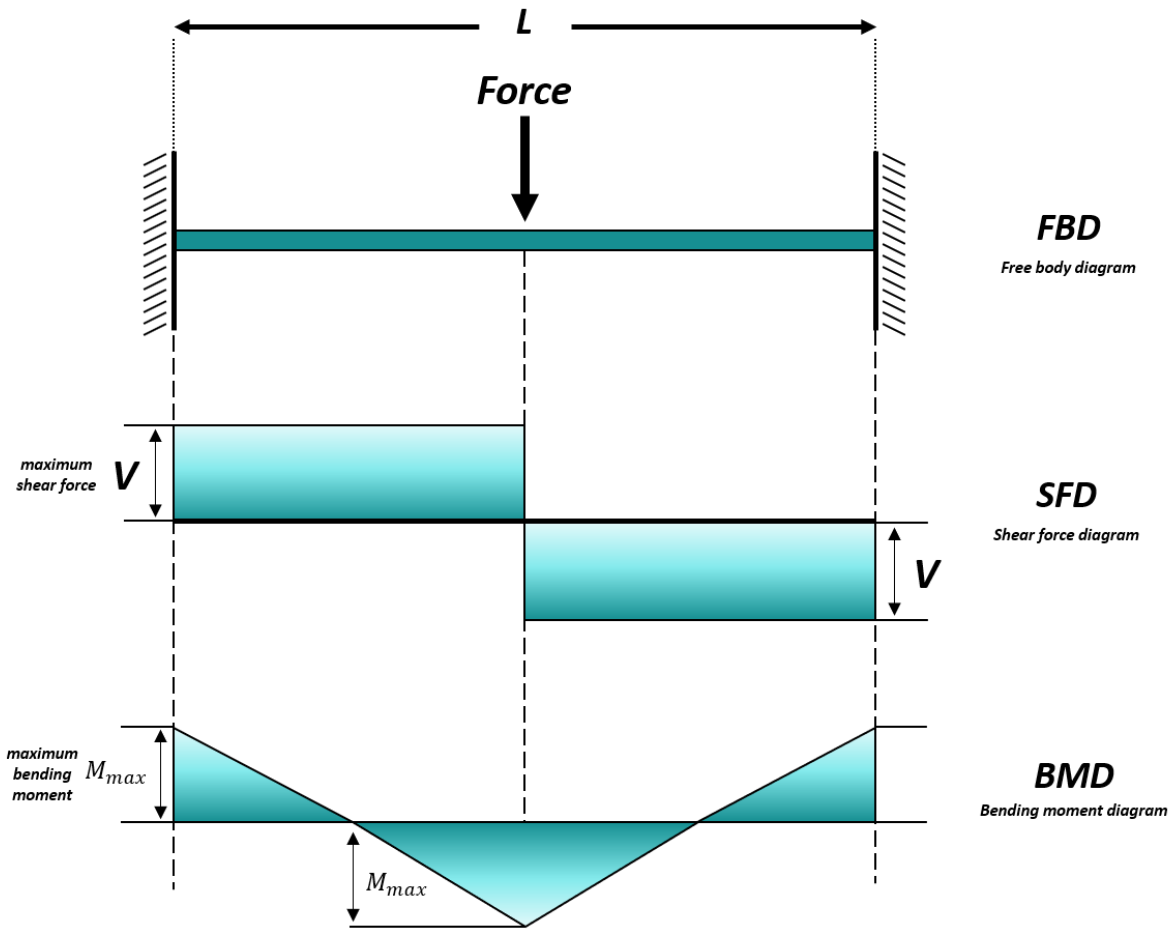

Figure 1.10: Free body diagram, shear force diagram, and bending moment diagram for a beam fixed at both ends and loaded with a point load at its center.

1.2.1.2 Nano-mechanical properties

The mechanical behavior of materials at small scales has been a significant focus of research due to its implications for material design and performance in advanced technologies. *Uchic et al.* pioneered micromechanical testing by compression experiments on metal micro-pillars created by focused ion beam (FIB) micromachining out of a bulk material. This approach avoids the complexities of multi-axial stresses in traditional nanoindentation [64]. FIB milling is crucial in fabricating micro-pillars from bulk materials, facilitating localized mechanical testing. Numerous studies on micro-pillars compression experiments

revealed an increasing yield strength (limit of elasticity) with decreasing object size. This finding is commonly termed in literature as "smaller is stronger"[65, 66, 67]. This effect arises from limited dislocation motion at small scales, because the physical dimensions of the material are comparable to the characteristic length scales of dislocation motion, such as their mean free path. As structures approach nanoscale dimensions, dislocation activity diminishes, and materials can achieve near-ideal strength, particularly evident in defect-free nanowires [68]. The micro-pillar fabrication process by FIB, however, can introduce defects, such as point defects, surface amorphization, or implantation of Ga in surface near regions, which potentially affect test results[69]. In contrast, as-grown nanowires remain pristine, making them ideal for studying near-ideal mechanical behavior under stress, even if it will exclude the possibility to perform micro-compression tests due to the large aspect ratio.

While most of the micropillar compression tests focused on metals showing increased yield strengths, semiconductors like Si, GaAs, GaN, and ZnO typically fail through brittle fracture with stresses well below their yield strength [70]. However, high temperatures provide sufficient thermal energy to activate dislocation mechanisms in semiconductors, transitioning their deformation mode from brittle to ductile [71]. For silicon and gallium arsenide, when reduced below a critical size, brittle-to-ductile transitions can occur even at room temperature, influenced by factors like strain rate and size-dependent stress distribution [72, 73, 74].

Integrating testing setups with XRD, SEM, TEM, or STEM enables real-time observation of deformation and defect evolution, enhancing the understanding of micro-structural effects on mechanics of the material [75]. Some nanoscale materials exhibit reversible plastic deformation, where dislocation structures revert to their initial state upon unloading. This behavior is particularly prominent in metallic nanowires [76] or such as the case of twinning-detwinning of Au NWs [77]. In BCC nanowires, deformation often occurs through twinning and detwinning mechanisms, allowing reversible shape changes under cyclic loading. This unique behavior stems from their high symmetry and reduced defect density [78]. Zinc oxide, known for its brittleness at the macroscale, exhibits enhanced mechanical resilience, making it a subject of extensive testing [79].

1.2.1.3 Nano-mechanical properties of ZnO

Experimental and computational studies on ZnO nanowires (NWs) have revealed their unique nano-mechanical behaviors, significantly influenced by size, structure, and surface effects. Experimental approaches, including in-situ tensile and bending tests in TEM and SEM setups, have shown that ZnO NWs exhibit size-dependent elastic moduli and fracture strengths [80, 81].

Ever since 2005 many experimental mechanical studies were conducted to explore the size effects on ZnO nanowires when measuring the Young's modulus and understanding their elastic properties (See Fig. 1.11). The results show a general behavior of the Young's modulus (E) increasing exponentially at smaller NWs diameters that is more prominent for $d < 200$nm. Several experimental techniques used to assess these properties, each with its own advantages, limitations, and sources of error which can explain the wide range of E values that can go from $15GPa$ to $250GPa$ with most of these values found above $100GPa$. The various experimental techniques for determining the Young's modulus of ZnO nanowires have specific benefits and challenges. Per example, tensile testing provides direct stress-strain measurements but often struggles with alignment, and sample breakage due to the fragile nature of nanowires. Resonance methods are highly sensitive and non-destructive but require controlled conditions to avoid inaccuracies caused by environmental noise and also surface contamination. Three-point bending simplifies preparation and avoids gripping issues, but inaccuracies in modeling the beam geometry can lead to errors. Indentation measures local mechanical properties and is suitable for small-scale studies but is prone to surface and substrate effects, which can distort results. Buckling experiments are effective for slender nanowires, offering insights into their stability, but they are sensitive to geometric imperfections and boundary conditions. Each technique must balance precision and practicality based on the specific application and sample characteristics.

The first experiment evidencing size effects by resonance testing was conducted by Chen et al.[82] on ZnO NWs using tungsten probes that produces an alternating electrical field which vibrates the NWs.

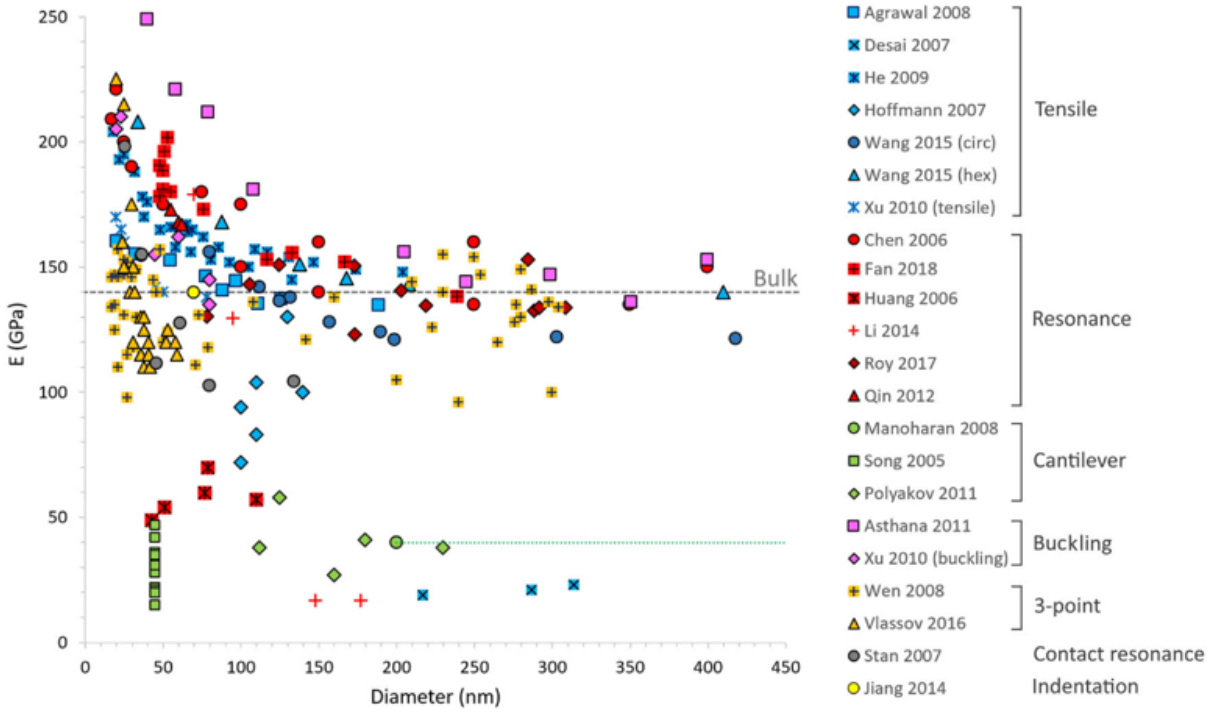

Figure 1.11: The measured value of the Young's modulus for ZnO nanowires according to different studies [6].

Three-point bending experiments on ZnO nanowires suspended across a hole or a gap were performed by applying a force at the midpoint of the nanostructure using either an atomic force microscope or a nanoindenter, causing the nanowire to bend. These experiments can be conducted *ex situ* or *in situ*. In *in situ* setups, real-time observations during bending allow for the direct correlation of structural changes, such as strain distribution or defect formation, with the applied force. The resulting deflection is used to calculate the elastic modulus. The primary challenge is ensuring that the nanowire remains stable and correctly positioned during the experiment, as misalignment can lead to significant errors.

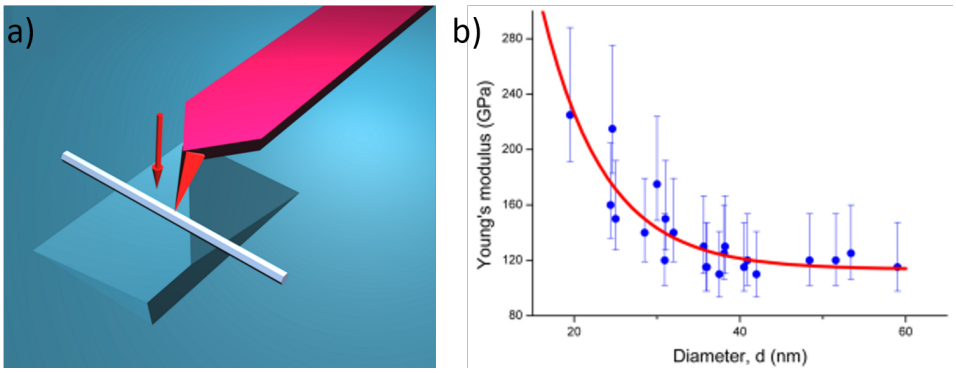

Figure 1.12: a) Schematic of the 3-point bending test of a single ZnO NW with AFM. b)Young's modulus measured for ZnO NWs of different diameters [7].

As demonstrated by Vlassov et al. [7], the Young's modulus increases with decreasing nanowire diameter for diameters smaller than 40 nm (Fig. 1.12). These findings, based on in-situ mechanical testing of ZnO nanowires, were attributed to finite-size effects. The use of in-situ experiments provides crucial advantages, such as real-time observation of deformation mechanisms and minimizing environmental artifacts, which enhance the reliability of the mechanical property measurements at the nanoscale.

1.2.2 Nano-piezoelectric testing methods

The piezoelectric properties of materials at the nanoscale often differ from those observed at the macroscopic scale, making it necessary to employ precise and reliable measurement techniques, such as:

- **Conductive Atomic Force Microscopy (c-AFM)** is used to investigate the electrical response of materials. In this method, a conductive AFM tip is brought into contact with the sample surface. A voltage is applied between the tip and the material and the resulting electrical current is measured. This approach enables simultaneous mapping of the electrical conductivity and piezoelectric response of nanomaterials such as thin films and nanowires, under mechanical stress. For piezoelectric testing, c-AFM can identify local variations in piezoelectric activity by detecting the coupling between applied force and current generation. This is particularly useful for analyzing nanostructured materials like ZnO and GaN nanowires [83, 84]. However, the main

challenges of c-AFM can include tip-induced artifacts and substrate influence, which can distort piezoelectric measurements. For small ZnO nanowires (under 600 nm), the technique is unsuitable due to their fragile structure, weak signal, and the need for a conductive substrate[85].

- **Piezoresponse Force Microscopy (PFM):** Is a mode of AFM where an alternating current (AC) voltage is applied through a conductive tip that makes contact with the piezoelectric material's surface. The material deforms mechanically in response to the applied voltage due to the piezoelectric effect, producing oscillations at the tip. These small deformations are detected through the deflection of the AFM cantilever. PFM allows for both qualitative and quantitative analysis of piezoelectric domains and local piezoelectric coefficients[86]. As for ZnO nanowires, the main challenges of PFM include limited quantitative accuracy due to electrostatic artifacts, as well as potential tip-induced sample damage. PFM is less ideal for us due to small size of NWs that complicate stable tip-sample contact and accurate piezoelectric response measurement[87].

- ***In situ* Transmission Electron Microscopy (TEM)** is also a powerful technique for directly observing the piezoelectric response of materials at the atomic scale. This method combines TEM imaging with the application of an external electrical field or a mechanical stimulus to the sample using special TEM holders[88, 89]. By applying an electric field in real-time, we can observe the structural changes within the material caused by its piezoelectric behavior. TEM provides unmatched spatial resolution, allowing for the visualization of atomic displacements, lattice distortions...etc[90].

- ***In situ* X-Ray diffraction (XRD)** Is also a technique for investigating the piezoelectric properties of nanomaterials under applied electrical stimuli by monitoring changes in diffraction patterns in real-time. In-situ synchrotron XRD has been employed to characterize the longitudinal piezoelectric constant d_{33} of aluminum scandium nitride $Al_{1-x}Sc_xN$ films. This method involves applying an external voltage to the film and observing the resulting lattice spacing variations, thereby quantifying the piezoelectric effect with high precision[91].

1.2.2.1 Nano-piezoelectric properties of ZnO

As it was mentioned before, the piezoelectric effect arises from the electromechanical interaction at the atomic level in crystals with a non-centrosymmetric structure. This condition manifests in two forms, which are the direct piezoelectric effect (i.e. a mechanical stress applied to the crystal generates an internal polarization) and the inverse piezoelectric effect (i.e. an applied electric field induces a mechanical strain that deforms the crystalline structure).

Molecular dynamics simulations of the piezoelectric behavior of ZnO nanobelts with lateral sizes ranging from 10 to 40 Å demonstrated an increasing piezoelectric coefficient with decreasing lateral size. In the study of [8], they created simulation models considering different sizes of ZnO nanobelts, all of which had the same length but varying lateral dimensions. These simulations use classical inter-atomic potentials, specifically the Binks potential which is a type of force field that describes how atoms interact within a material. It accounts for the electrostatic interactions between ions (Zn^2+ and O^2- in ZnO), allowing for accurate predictions of how the atoms respond to external stresses. While bulk ZnO exhibits a piezoelectric coefficient of 1.4 C/m², the nanobelts, depending on their size, showed significantly higher values, up to 2.322 C/m² (See Fig. 1.13).

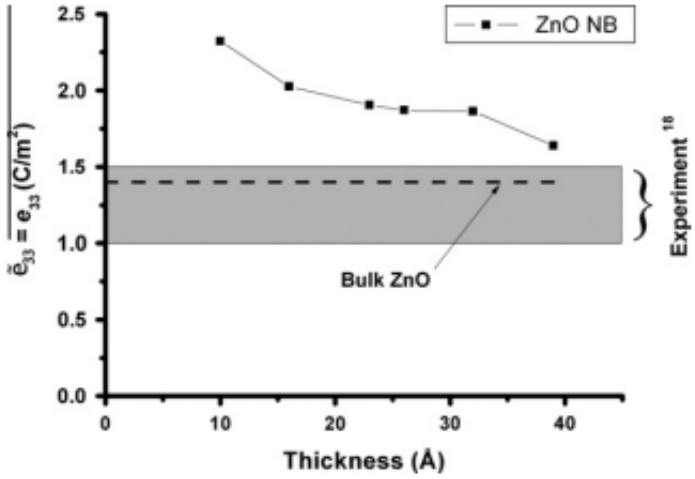

Figure 1.13: Piezoelectric coefficient of ZnO nanobelts as a function of the nanobelt's lateral dimension.[8]

The enhancement of the piezoelectric properties with reducing size is primarily due to the increased surface-to-volume ratio in smaller nanostructures, which leads to a redistribution of surface charges that enhances the piezoelectric effect. However, experimentally, the smallest ZnO nanobelts width are 10 times these values.

In 2006, Zhong Lin Wang and his team conducted a work on the piezoelectric properties of ZnO nanostructures. They used an AFM to measure the piezoelectric output of ZnO nanowires under mechanical deformation. Their findings demonstrated that mechanical stress applied to ZnO nanowires generates an electric potential, laying the foundation for the field of nanopiezotronics[9].

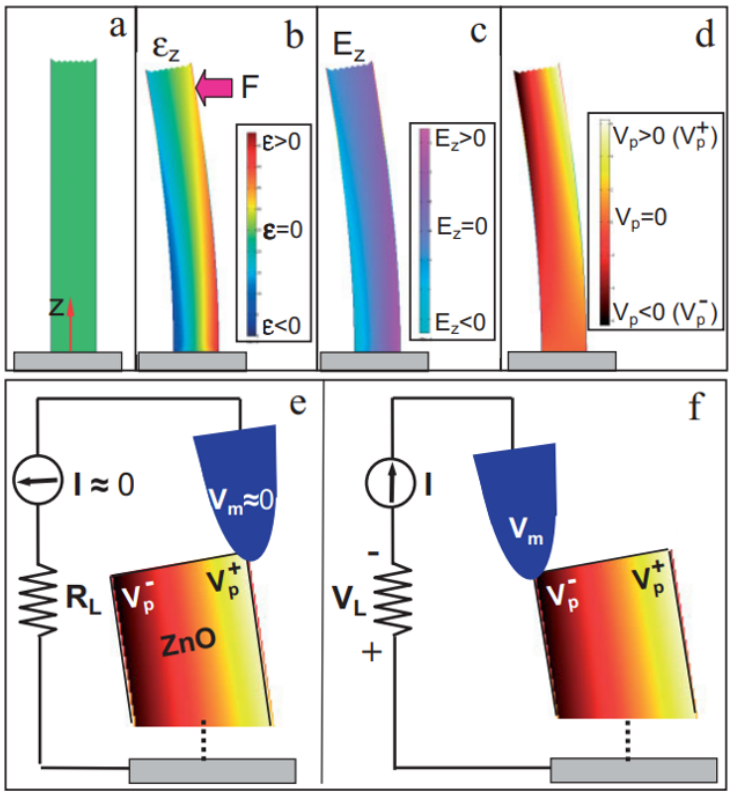

Figure 1.14: a–d) The principle of the piezoelectric nanogenerator. e-f) metal–semiconductor Schottky contact between the AFM tip and the semiconductor ZnO NB at at reverse and forward bias[9]

While for density functional theory (DFT) studies, they have provided significant insights into the piezoelectric properties of ZnO nanostructures, such as putting evidence to size-dependent piezoelectricity, where some works have shown that the piezoelectric prop-

erties of ZnO nanowires are influenced by their size and surface effects. DFT calculations indicate that as the dimensions of ZnO nanowires decrease, there can be notable changes in their piezoelectric coefficients, attributed to surface relaxation and reconstruction at the nanoscale[92]. Some DFT studies also explored the interplay between mechanical strain and electronic properties in ZnO. DFT analyses reveal that applying strain to ZnO nanostructures can modulate their electronic band structure and enhance piezoelectric responses, suggesting potential for strain-engineered piezoelectric devices[93].

1.2.3 Growth of ZnO nanowires

The synthesis of nanostructures can in general be divided into two main approaches - the top-down and the bottom-up approach - which are shortly introduced below.

- **Top-down approach:** This method involves breaking down a bulk material into nanoscale structures. For ZnO NWs, this might mean etching a ZnO thin film to shape it into the desired NW geometry. The top-down approach has been effectively used for other materials; however, it has limitations for ZnO. Due to ZnO's high solubility in acidic and basic solutions, etching processes can be inconsistent and lack reproducibility[94]. Moreover, this method does not allow for precise control over the NW dimensions, making it challenging to achieve specific sizes and shapes. These issues make the top-down approach suboptimal for ZnO NW synthesis.

- **Bottom-up approach :** The bottom-up method assembles nanostructures atom-by-atom or molecule-by-molecule, through different growth processes such as chemical bath deposition or metal-organic chemical vapor deposition (MOCVD) etc[95]. These methods allow for more accurate control over the size, shape, and orientation of ZnO NWs, allowing to tailoring the dimensions to meet specific requirements. Given the challenges of the top-down approach, the bottom-up approach is typically preferred for synthesizing ZnO NWs, providing both reproducibility and control over structural properties.

In the bottom-up approach for ZnO NW synthesis, two primary phases are utilized: vapor phase deposition and liquid phase synthesis [96]. Vapor phase deposition involves

synthesizing ZnO NWs from gaseous precursors with methods such as vapor-liquid-solid (VLS) growth, chemical vapor deposition (CVD), and metal-organic chemical vapor deposition (MOCVD). In VLS growth, a metal catalyst forms a liquid droplet on the substrate, which absorbs vapor-phase precursors, facilitating NW nucleation [97]. This vapor-based approach allows precise control over NW dimensions and crystalline quality by adjusting parameters like temperature and gas flow rates.

On the other hand, liquid-phase synthesis[98] uses a liquid medium for NW growth. Techniques include chemical bath deposition (CBD) and hydrothermal synthesis. In the former case, zinc precursors and a hydroxide source in a solution form ZnO NWs on a substrate. In the latter method, a solution is heated to moderate temperatures enabling NW growth on seeded substrates. Liquid-phase methods are generally less complex and suitable for large-area deposition, making them more energy-efficient.

The ZnO NWs used in the present theses were grown and provided by the FunSurf group at the LMGP in Grenoble (France) using the hydrothermal approach [99, 100]. This method involves two steps which are the formation of a ZnO seed layer and the growth of ZnO NWs in a growth bath.

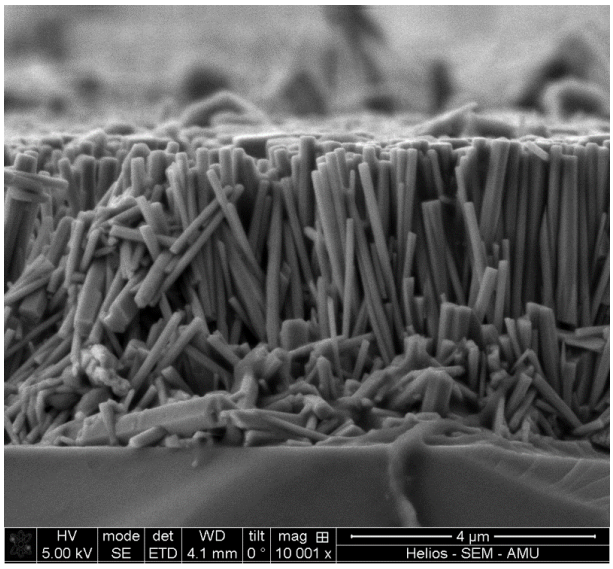

Figure 1.15: SEM image of as-grown ZnO nanowires on Si substrate by hydrothermal method

The hydrothermal growth method is used because it is inexpensive compared to other

methods, the process does not require high temperatures, making it energy-efficient. It can easily be scaled up to produce large quantities of ZnO nanowires, and most importantly, the nanowires produced are usually of high quality, with fewer defects compared to other methods [101].

1.2.4 ZnO nanowires applications

In the realm of sensing, ZnO NWs high surface-to-volume ratio enhances their performance in gas sensors, where they can detect trace amounts of gases like hydrogen, ethanol, and carbon monoxide[102]. This makes them valuable in industrial safety and environmental monitoring. Furthermore, thanks to their piezoelectric properties, ZnO NWs can convert mechanical energy into electrical signals, opening up applications in energy harvesting and self-powered nanoscale devices[103]. These piezoelectric nanogenerators can harness ambient vibrations or biomechanical energy, such as movement, to power small electronics or implantable medical devices. ZnO NWs also hold potential in biomedical fields, where their biocompatibility and antibacterial properties support applications in drug delivery, biosensors, and antimicrobial coatings[104]. Combined, these unique characteristics underline ZnO NWs as a promising material for future technologies in energy, environmental monitoring, health, and advanced electronics. In the following, a variety of applications of ZnO NWs will be highlighted.

1.2.4.1 Piezoelectric generators

As introduced above, the piezoelectric effect is defined by the interaction between mechanical and electrical properties. Thus, it allows for converting mechanical energy into electrical energy and vice versa making piezoelectric materials (like ZnO amongst others) potential candidates for harvesting energy from environmental vibrations, for example[105]. The potential for using ZnO nanowires in piezoelectric generation was first demonstrated by Professor Zhong Lin Wang's research team in 2006 [106]. By bending a ZnO nanowire with a conductive AFM tip (Fig. 1.16), a piezoelectric potential is created within the nanowire. The potential difference generated by this effect, measured between the substrate and the AFM tip, reached 8 mV for a force of 5 nN (with nanowires ranging from 0.2 to 0.5 µm in

length and around 40 nm in diameter). In this experiment, the energy dissipated across a resistive load during the discharge of a single nanowire was estimated at 0.05 fJ. The electrical energy converted by this nanowire amounted to 0.5 pW. [10].

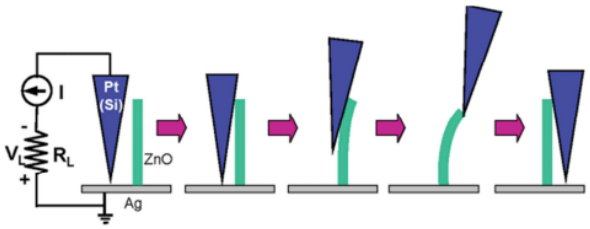

Figure 1.16: schematic of generating electricity by deforming single ZnO NWs using a conductive AFM tip. In this setup, the AFM operates in contact mode and scans over the NW arrays[10]

The first conversion from mechanical energy into electrical energy at the nanoscale using a piezoelectric network of ZnO nanowires was reported by [107]. These nanowires were deformed by a conductive atomic force microscope tip, which generated an electric field. The device achieved an efficiency of 17 to 30%. [48] developed a transparent, flexible nanogenerator using a flexible polydimethylsiloxane (PDMS) substrate on which ZnO nanowires were grown. ZnO nanowires in this study were grown on an Au/Ti-coated polymethylglutarimide (PMGI) layer on a silicon wafer substrate using the hydrothermal method. The PMGI layer acted as a sacrificial layer for later lift-off processes. The fully encapsulated nanogenerator in epoxy resin exhibited good transparency, with a visible light transmittance of 50-60%, for which they can be used as optoelectronic devices. The output voltage and current were 1.8 V and 90 nA/cm^2, respectively, corresponding to a power density of 5.3 mW/cm^3. Comparing this result to a study also by [108] on GaN-based nanogenerators, where they generated a voltage of about 1.2 V and a current of around 38 nA/cm^2. ZnO-based nanogenerators, with power densities up to 5.3 mW/cm^3, are suitable for supplementing low-power wearable and wireless sensors but are insufficient for high-consumption portable electronics[109]. In a study by R. Tao et al.[110] ZnO-based VINGs achieved 85 µW/cm^3 power density (0.29 V) under 5 N compression, surpassing bulk PZT (25 µW/cm^3) despite its 40× higher piezoelectric coefficient. Thinner PMMA layers ($\tilde{1}$.2 µm) and sparser ZnO nanowires (30 mM precursor) tripled output voltage (60

mV) by enhancing charge transfer. Precise perpendicular compression reduced voltage variability by ±30%. The study confirms ZnO as a sustainable, lead-free alternative for energy harvesting applications.

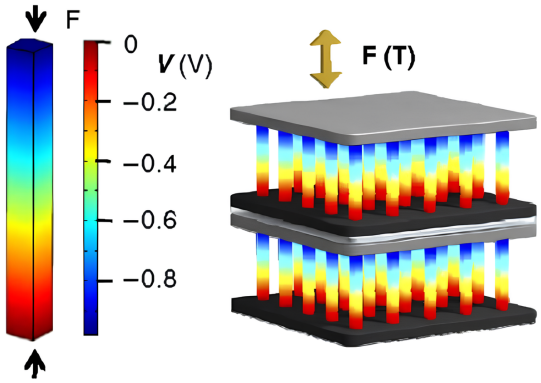

Figure 1.17: Finite element simulation (left) shows the piezoelectric potential distribution in a PZT nanowire. The schematic (right) illustrates the structure of a multilayered nanogenerator made from same nanowires. [11]

1.2.4.2 Other applications

Beyond their utility as piezoelectric nanogenerators, ZnO nanostructures also have significant potential in other applications, particularly as photovoltaic cells and light emitting diodes.

Photovoltaic cells : The basic structure of a photovoltaic cell consists of a p-n junction formed by two semiconductors, one doped p-type and the other n-type. When these two regions come into contact, holes from the p-doped region and electrons from the n-doped region spontaneously diffuse across the junction, creating a depletion zone where the concentration of free carriers is almost zero. Although a doped semiconductor typically has good conductivity, the junction itself allows very little current to pass through. ZnO has been used in the field of photovoltaics, particularly in the production of nanostructured solar cells[111]. The purpose of nanostructuring these cells is to increase the effective surface area of the p-n junction. This can be achieved by using a vertical array of ZnO nanowires as the base structure. Research has shown that the energy conversion efficiency of solar cells by photovoltaic effect increases with the length of the ZnO nanowires. As the

length of the NWs increases, the effective surface area for the absorption of light becomes greater, thus increasing the solar cell efficiency[112].

Light emitting diodes : The role of a light-emitting diode (LED) is to convert electrical energy into light radiation. This process relies on the emission of a photon generated by the recombination of an electron and a hole within a semiconductor. Zinc oxide has also been used in the production of LEDs due to its wide bandgap and high exciton binding energy of around 60 meV [113], which enables it to emit ultraviolet light effectively at room temperature [114].

Chapter 2

Experimental techniques

2.1 Basic principles of X-ray diffraction

X-rays are electromagnetic waves which cover a spectrum of wavelengths ranging from 0.01 to 10 nm corresponding to energies in the range of 100 eV to 100 keV[115]. We distinguish between "soft" and "hard" X-rays depending on their respective energy, thus their penetration depth into materials. Typically, X-rays with energies above 5 keV are regarded as "hard" and below this threshold as "soft". Thanks to the fact that the wavelength of hard X-rays is in the same range as the lattice parameter of solid-state materials, the atomic lattice functions like a diffraction grating leading to interferences.

X-ray diffraction (XRD) by crystals is an important technique in the field of materials science. Since the discovery of X-rays by Wilhelm Conrad Röntgen in 1895, for which he earned the first Nobel prize in physics in 1901, X-rays have become a major tool for investigating and imaging matter. In 1912, Max von Laue presented the first X-ray diffraction pattern of a ZnS crystal, which laid the foundation for the field of X-ray crystallography, which has since provided key insights into the atomic and molecular structure of crystalline solids. Nowadays, X-ray diffraction extends across a large part of scientific domains, from materials characterization and structural properties to biology and geology. It provides access to the crystal structure including lattice parameters and defects within crystalline materials. It further allows for crystal phase identification.

In this chapter, the basic principles of X-ray diffraction are presented. After introducing

the scattering of X-rays by a free electron and a single atom, scattering processes from a crystal will be detailed. The basic notions of reciprocal space will be introduced followed by the description of Bragg's law. After presenting the structure factor of materials and the shape factor, this chapter will finish with a section on the coherence of an X-ray beam.

2.1.1 X-ray interaction with matter

The wavelength λ of X-rays is related to the momentum p of the photons and the Planck constant h by the De Broglie relation:

$$\lambda = \frac{h}{p} \tag{2.1}$$

The energy E of the X-rays can be written as a function of the wavelength λ and the speed of light c through the following equation:

$$E = \frac{hc}{\lambda} \tag{2.2}$$

Several types of interaction between X-rays and matter can occur, each with its own cross-section, which describe the likelihood of that interaction to happen (Fig. 2.4). The main types of interaction of X-rays with matter are Thomson scattering, Compton scattering, and the photoelectric effect.

1. **Thomson Scattering** is the elastic scattering of X-rays by free or loosely bound electrons. In this process, the X-ray photon is elastically scattered without transferring energy to the electron that remains in its initial state. Thomson scattering is dominant at low photon energies and provides valuable information about the electron density within the crystal.

2. **Compton Scattering** is an inelastic scattering process where the X-ray photon transfers part of its energy to a bound electron, resulting in a scattered photon with lower energy and a dispersed electron. Compton scattering is significant at higher photon energies and is an important factor in understanding the attenuation of X-rays in materials.

3. The **Photoelectric Effect** is the transfer of the complete energy of the incident photon to an atom in which a bound electron is then ejected. The energy of the ejected electron is equal to the energy of the incident photon minus the binding energy of the

electron in the atom. The photoelectric effect is more probable at lower photon energies and is highly dependent on the atomic number of the material.

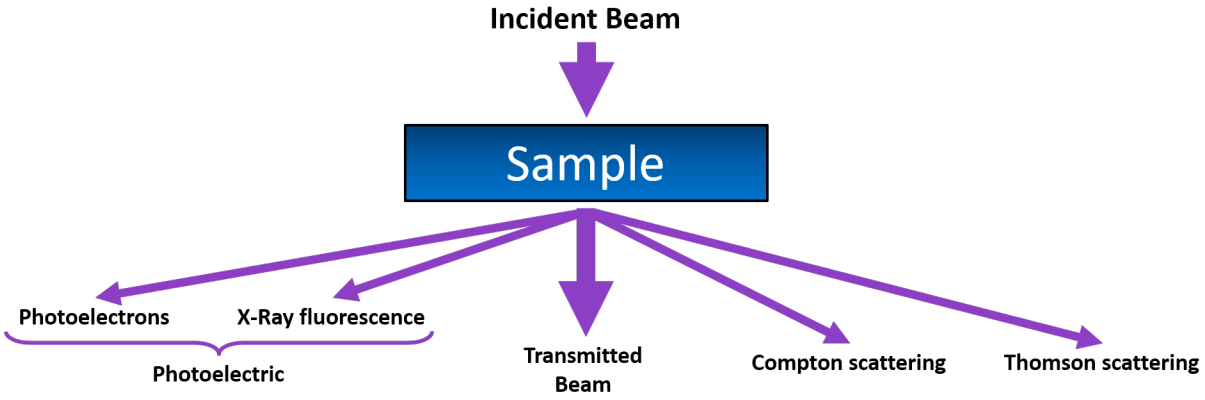

Figure 2.1: Schematic representation of the different interactions between incident X-rays and a sample.

When X-rays interact with an atom they can be attenuated by absorption, reflection, or scattering. In this work, we will concentrate on Thomson scattering to explain the working principles of X-ray diffraction and on the photoelectric effect to explain X-ray fluorescence.

2.1.1.1 Scattering by a free electron

Considering a primary X-ray beam, which is an electromagnetic plane wave with an electric field vector $\vec{E}$ that varies sinusoidally with time and is oriented perpendicular to the direction of propagation of the beam expressed as:

$$\vec{E}(\vec{r},t) = \vec{E}_0 \cdot e^{i\cdot(\omega t - \vec{k}\cdot\vec{r}+\varphi)} \tag{2.3}$$

Here, ω is the angular frequency, $\vec{r}$ is the position vector in space, φ is the phase constant, $\vec{E}_0$ is the amplitude of the electric field, and $\vec{k}$ is the wave vector. The modulus of the latter is defined as :

$$k = \|\vec{k}\| = \frac{2\pi}{\lambda} \tag{2.4}$$

During elastic scattering, the oscillating electric field of the incident X-ray wave exerts an electromagnetic force on the electron, causing it to accelerate and oscillate in the same direction as the incident electric field. During an elastic scattering event, the oscillating electron emits a spherical electromagnetic wave with the same wavelength as the incident wave which we call Thomson scattering. This scattered spherical electromagnetic wave $\vec{E}_d$ is written as :

$$E_d(t, R, \theta) = \frac{e}{R} \frac{1}{4\pi\epsilon_0 c^2} \vec{a_T} \sin\theta \left(t - \frac{R}{c} \right) \tag{2.5}$$

Here, e is the electron charge, R is the distance from the electron to the observation point, ϵ_0 is the vacuum permittivity, c is the speed of light, and $\vec{a_T}$ is the transverse acceleration of the electron that can be written as:

$$\vec{a_T} = -\frac{e}{m_e} \cdot \vec{E}_i \tag{2.6}$$

with m_e being the mass of the electron and $\vec{E}_i$ being the electric field vector of the incident electromagnetic wave.

2.1.1.2 Scattering from a single atom

An atom can be described as an electron cloud volume with a density $\rho_{atom}(\vec{r})$ (Fig. 2.2). An incident electromagnetic wave with an electric field amplitude $\vec{E}_i$ scattered by a small volume $d\tau$ containing an electron density $\rho_{atom}(\vec{r})d\tau$ will therefore take the form of a spherical wave:

$$dE_d = -r_0 \vec{E}_i \frac{\exp\left(i\vec{k} \cdot \vec{R}\right)}{\vec{R'}} \rho_{atom}(\vec{r}) d\tau \tag{2.7}$$

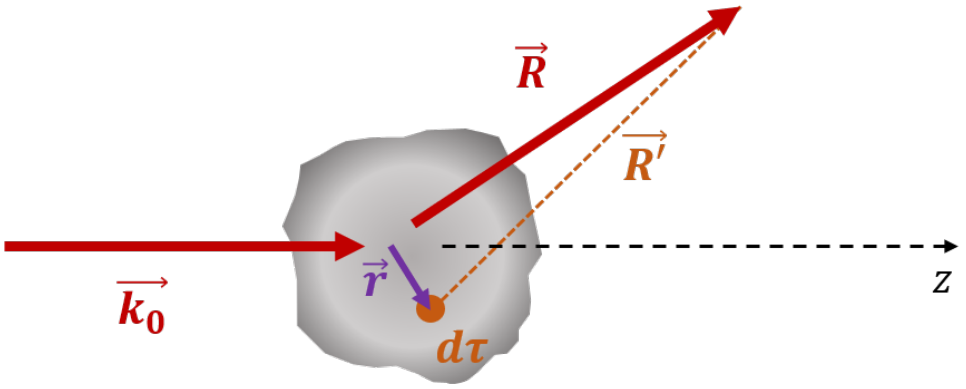

Figure 2.2: elastic scattering of x-ray by an atom

For distances far from the atom, $\vec{r}$ is small compared to $\vec{R}$ and, thus, $\vec{R}' \approx \vec{R}$. This approximation allows for simplifying the expression as follows:

$$dE_d = -r_0 \frac{\vec{E}_i^T}{R} \exp\big(i(\vec{k}_0 \cdot \vec{r} - \omega t)\big) \exp\left(i\left(\vec{k} \cdot \vec{R}\right)\right) \rho_{atom}(\vec{r}) d\tau \tag{2.8}$$

where $\vec{E}_i$ and $\vec{E}_d$ are the amplitudes of the incident electric field and of the scattered electric field, respectively, while $\vec{k}_0$ and $\vec{k}$ are the wave vectors of the incident wave and of the scattered wave, respectively. $d\tau$ is an infinitesimal volume element within the scattering region, which contributes to the overall scattered field, $\vec{R}$ is the vector from the origin of the atom to the observation point P, $\vec{r}$ is the position vector of a point within the scattering volume element $d\tau$ relative to the origin, where the interaction with the incident wave $\vec{k}_0$ occurs and, finally, $\vec{R}'$ is the vector distance between the position of the scatterer at $\vec{r}$ and the observation point P.

Assuming that $\vec{r}$ is small compared to $\vec{R}$, which corresponds to the so-called far-field approximation, this expression can be further simplified:

$$\vec{k}_0 \cdot \vec{r} + \vec{k} \cdot \vec{R}' \approx \vec{k}\vec{R} + \left(\vec{k}_0 - \vec{k}\right) \cdot \vec{r} = \vec{k}\vec{R} + \vec{q} \cdot \vec{r} \tag{2.9}$$

where $\vec{q}$ is the scattering vector $\vec{q} = \vec{k}_0 - \vec{k}$.

Considering the far-field approximation and thus $\vec{R}' \approx \vec{R}$, an integration over the entire volume of the electron cloud results in:

$$E_d = -r_0 \frac{\vec{E_i^T} \exp\big(i(\vec{k}R - \omega t)\big)}{R} \int_V \rho_{atom}(\vec{r}) \exp(i\vec{q}.\vec{r}) d\tau \tag{2.10}$$

This relation can be recognized as a continuous Fourier transform. The integral in equation (2.11) represents the atomic form factor

$$f_0(q) = \int_V \rho_{atom}(\vec{r}) \cdot e^{(i\vec{q}.\vec{r})} d\tau \tag{2.11}$$

So far, the electrons were assumed to be entirely free and independent within the atomic cloud. In reality, electrons are bound to the nucleus according to discrete quantum energy levels. The Cromer-Mann parameters of the X-ray scattering factor $f_0(q)$ have been calculated for a wide range of materials using a Hartree-Fock relativistic approach [116]. In practice, the following adjustment function is used:

$$f_0\left(\frac{\sin(\theta)}{\lambda}\right) = \sum_{i=1}^{4} a_i \exp\left(-b_i \left(\frac{\sin(\theta)}{\lambda}\right)^2\right) + c \tag{2.12}$$

The parameters $a_i$and b_i for Zn and for O are listed in (Table. 2.1).

a	**Zn**	**O**	**b**	**Zn**	**O**	**c**	**Zn**	**O**
a1	14.6744	2.95648	**b1**	3.71486	13.8964	**c**	3.59838	0.30413
a2	5.62816	2.45240	**b2**	0.50033	5.91765	-	-	-
a3	3.92540	1.50510	**b3**	12.8862	0.34537	-	-	-
a4	2.16398	0.78135	**b4**	65.4071	34.0811	-	-	-

Table 2.1: Zn and O Cromer-Mann coefficients

When the energy of the incident X-rays is close to one of these energy levels, resonance phenomena occur. The "anomalous scattering factors" f' and f'' serve as corrective terms to the scattering factor.

$$f = f_0(q) + f'(E) + if''(E) \tag{2.13}$$

The real part of the anomalous scattering factor f' accounts for the phase shift in the scattering, while the imaginary part f'' is related to the absorption of the incident X-rays by the atom, which contributes to the scattering intensity. These terms are generally

negligible for elements with low atomic numbers because their effect on scattering is minimal. However, for X-ray energies close to an element's absorption edge, these factors become significant, especially for elements with higher atomic numbers.

2.1.1.3 Refraction, reflection, and absorption effects

Electrons in atoms or molecules exist in discrete bound states (characterized by a binding energy E_b) and their response to an incident electromagnetic field depends on the incident energy. The absorption of an X-ray photon with energy E by an electron at a certain atomic level (K,L,M..) results in the excitation to a higher level, leaving behind a vacancy. This initiates a cascade of processes aimed at filling this vacancy and releasing the excess energy from the atom where the interaction occurred (Figure 2.3). An electron from an upper level, designated as level $j-1$, undergoes de-excitation to the vacant level, designated as level j. This process results in the emission of a fluorescence photon with an energy equal to the difference between the energies of levels j and $j-1$, written as $E_j - E_{j-1}$.

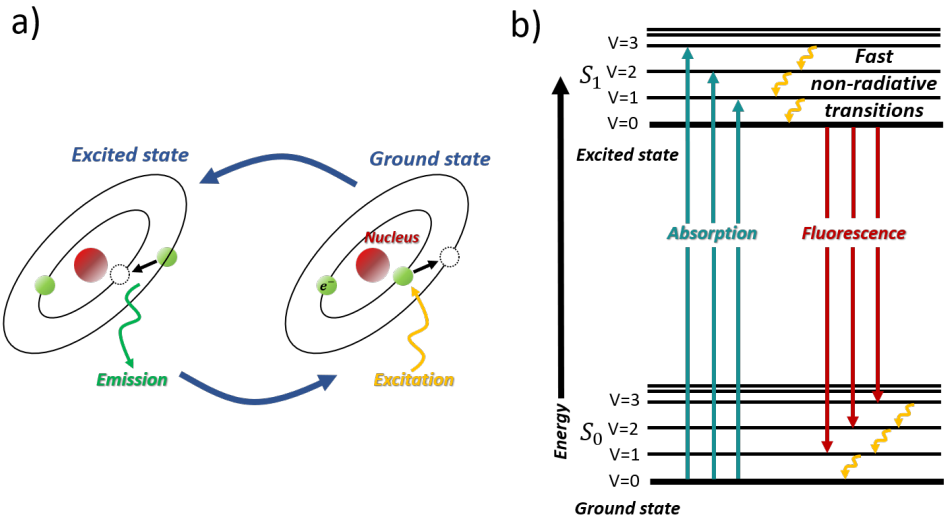

Figure 2.3: a) Schematic representation of the electron excitation and de-excitation processes. b) Energy level diagram illustrating absorption, non-radiative transitions, and fluorescence, where an excited electron returns to a lower energy state, emitting a photon with energy corresponding to the energy difference between the two levels.

The X-ray fluorescence energy depends strongly on the atomic number and the type

of emission line (K-line, L-line or M-line). The fluorescence lines for zinc and oxygen are presented in (Table 2.2).

Element	**Kα(eV)**	**Kβ(eV)**	**Lα(eV)**
Zinc (Zn)	8639	9572	1012
Oxygen (O)	525	-	-

Table 2.2: Fluorescence Energies of Zinc and Oxygen (in eV) [29][30]

2.1.2 Scattering by a crystal

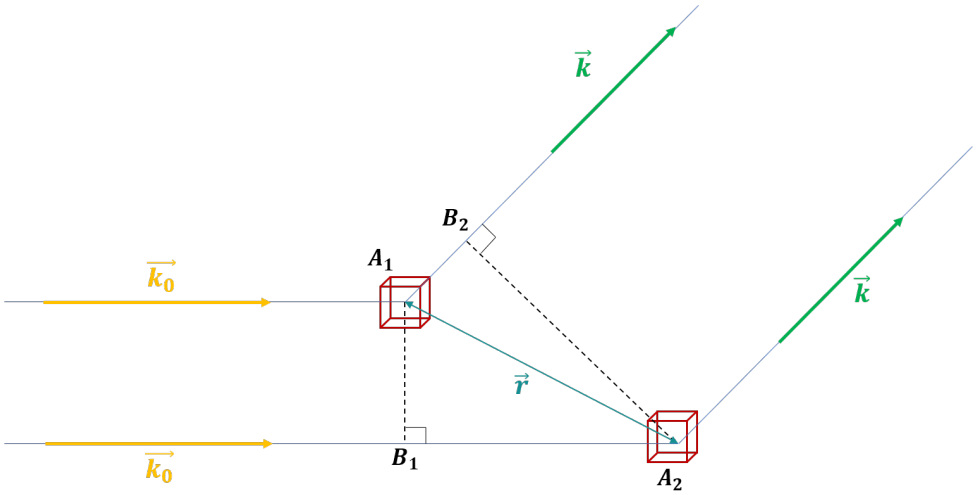

Figure 2.4: Scattering of a monochromatic beam with wavelength λ by two atoms, A and B, within an infinitesimal volume element d^3r.

While so far the scattering of X-rays was treated for a single atom, condensed matter typically exists in amorphous or crystallized form. Here, for simplification, a pair of identical atoms A_1 and A_2 (Fig. 2.4) is considered, which are distanced by $\vec{r}$. When an incident beam impinges on them, the difference in the optical path $|A_1B_2|$-$|A_2B_1|$ taken by the rays results in a phase difference $\Delta\Phi$:

$$\Delta\Phi = (\vec{k} - \vec{k_0}) \cdot \vec{r} = \frac{2\pi}{\lambda}(|A_1B_2| - |A_2B_1|) \tag{2.14}$$

The wave vectors for the incident beam and the diffracted beam are represented by $\vec{k_0}$ and $\vec{k}$, respectively, while $\vec{r}$ denotes the relative position of atom A_1 in relation to atom A_2. Given that E_0 represents the amplitude of the wave scattered by the scattering center A_1, the wave scattered by A_2 can be written as :

$$E_0 \cdot e^{(2\pi \cdot i(\vec{k}-\vec{k_0})\cdot\vec{r})} \tag{2.15}$$

Therefore, if N diffusing centers exist along the path of the incident plane wave:

$$E(r') = \sum_{j=1}^{N} E_j \cdot e^{(2\pi \cdot i\vec{q}\vec{r})} \tag{2.16}$$

with q being the scattering vector of the reciprocal space which can be written as:

$$\vec{q} = \vec{k} - \vec{k_0} \tag{2.17}$$

However, X-rays mainly interact with the electron cloud. Considering the N atoms as cubes with a volume of dr and taking into account the electron density of ρ(r), the scattered wave amplitude can be re-written as:

$$E(r') = \int_V \rho(r) e^{(2\pi i\vec{q}\vec{r})} dr \tag{2.18}$$

The equation above can be recognized as the Fourier transform of the electron density ρ(r). The diffracted intensity is proportional to the square of the scattered wave amplitude:

$$I \propto \left| \int_V \rho(r) e^{(2\pi i\vec{q}\vec{r})} dr \right|^2 \tag{2.19}$$

This intensity is also expressed as the product of the scattered wave's complex amplitude $A(\mathbf{q})$ and its complex conjugate $A^*(\mathbf{q})$:

$$I \propto A(\mathbf{q}) A^*(\mathbf{q}) \tag{2.20}$$

In the case of an infinite three-dimensional crystal, a discrete approximation model can be used to describe its characteristics. Every atom is viewed as a point of scattering distinguished by its atomic scattering factor. A perfect crystal is described as an infinite repetition of structural units aligned in space based on three vectors $\vec{a}$, $\vec{b}$, and $\vec{c}$. The position $\vec{r_n}$ indicates the position of the n-th atom within the lattice:

$$Crystal_{\infty} = lattice \otimes pattern \tag{2.21}$$

$$Crystal_{\infty} = \sum_{n}^{pattern} \rho_n(\vec{r} - \vec{r_n}) \otimes \sum_{u,v,w=-\infty}^{+\infty} \delta(\vec{r} - (u\mathbf{a} + v\mathbf{b} + w\mathbf{c})) \tag{2.22}$$

δ is the Dirac delta function while *u, v, and w* are integers. The amplitude of the wave scattered by the whole crystal can be written as :

$$E_{\infty}(r^*) = \frac{1}{V} E_M(H) \otimes \sum_{u,v,w=-\infty}^{+\infty} \delta(r - (u\mathbf{a} + v\mathbf{b} + w\mathbf{c})) \tag{2.23}$$

Let V represent the unit cell's volume and let $\vec{r}^* = h\vec{a}^* + k\vec{b}^* + l\vec{c}^*$ be the generic lattice vector in reciprocal space. $\vec{a}^*$, $\vec{b}^*$, and $\vec{c}^*$ are reciprocal lattice vectors that are mathematically defined to be orthogonal to the planes formed by pairs of real space lattice vectors, and their magnitudes are related to the spacing between those planes in the real lattice, where :

$$\vec{a}^* = 2\pi \frac{\mathbf{b} \wedge \mathbf{c}}{\mathbf{a} \cdot (\mathbf{b} \wedge \mathbf{c})} \qquad \vec{b}^* = 2\pi \frac{\mathbf{c} \wedge \mathbf{a}}{\mathbf{b} \cdot (\mathbf{c} \wedge \mathbf{a})} \qquad \vec{c}^* = 2\pi \frac{\mathbf{a} \wedge \mathbf{b}}{\mathbf{c} \cdot (\mathbf{a} \wedge \mathbf{b})} \tag{2.24}$$

which verifies $\vec{q} = h\vec{a}^* + k\vec{b}^* + l\vec{c}^*$

For non-periodic scatterers, the amplitude of the scattered wave $E_M(r^*)$ can assume non-zero values for any r^*. Conversely, if the scattering centers are periodic, a non-zero amplitude occurs only when r^* aligns with a point in reciprocal space so that $r^* = r^*_H$. By introducing the definition of $\vec{r}^*$ and multiplying the above equation by a, b, and c, one obtains:

$$a \cdot (s - s_0) = h\lambda \qquad b \cdot (s - s_0) = k\lambda \qquad c \cdot (s - s_0) = l\lambda \tag{2.25}$$

The relation mentioned above is known as Laue conditions. The directions $\vec{s}$ that satisfies these conditions are referred to as diffraction directions. In the context of crystal diffraction, the function E_H is termed the structure factor of the vectorial index H (or indexes h, k, l when referencing the components of r^*_H). It is represented as:

$$E_H = \sum_{j=1}^{N} f_j \exp\left(2\pi i \mathbf{r}^*_H \cdot \mathbf{r}_j\right) \tag{2.26}$$

where N is the number of atoms in the unit cell. The interplanar spacing d_{hkl} is perpendicular to the planes characterized by the Miller indexes (hkl). In cubic crystal systems, this spacing is given by the formula:

$$d_{hkl} = \frac{a_0}{\sqrt{h^2 + k^2 + l^2}} \tag{2.27}$$

where a_0 is the lattice parameter and h, k, and l are the Miller indices.

For a hexagonal structure like ZnO, the interplanar spacing d_{hkl} is expressed by the following equation:

$$d_{hkl} = \frac{1}{\sqrt{\frac{4}{3}\left(\frac{h^2+hk+k^2}{a^2}\right) + \frac{l^2}{c^2}}} \tag{2.28}$$

where a and c are the lattice parameters for the hexagonal structure and h, k, and l are the Miller indices of the crystal plane. In this expression, a and c are not equal, reflecting the anisotropy of the hexagonal structure in contrast to cubic crystals.

In hexagonal systems, the lattice vectors in the basal plane form a 120° angle (See Fig. 2.5), making the three-index notation difficult to work with. The $(hkil)$ notation, also known as the Miller-Bravais system, is a way to describe crystallographic planes and directions in hexagonal crystal systems. This notation uses four indices: h,k,i, and l. The indices h,k, and i represent the basal plane directions, whereas the index l corresponds to the c-axis direction. For index i the following condition has to be satisfied: $i = -(h + k)$

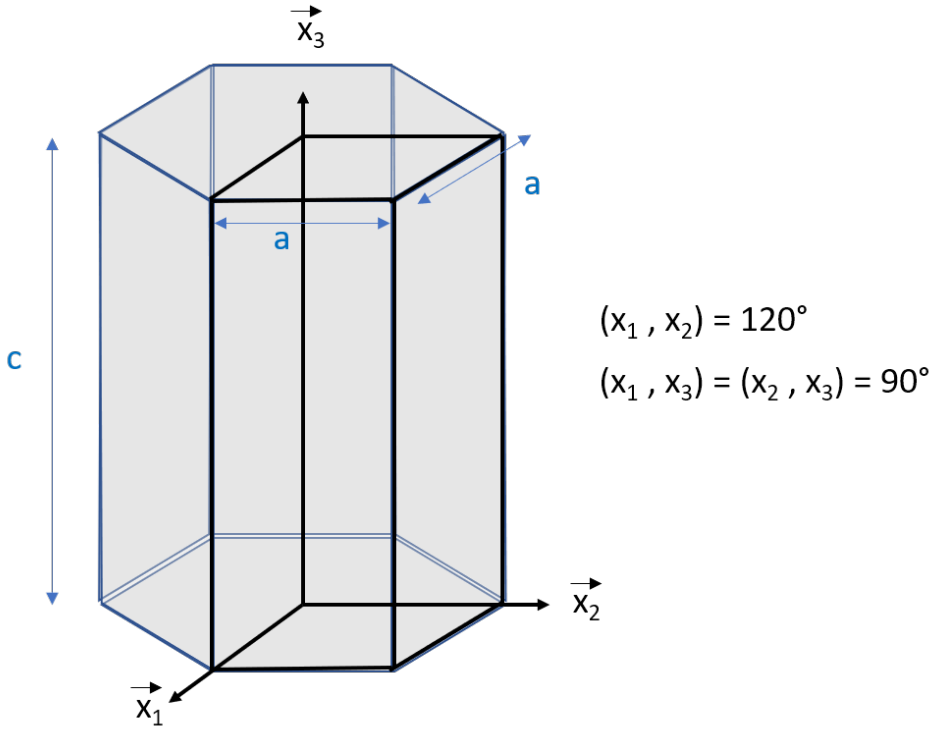

Figure 2.5: Schematic representation of a hexagonal crystal lattice system, showing the lattice parameters and orientations. The coordinate axes (x_1, x_2, x_3) are shown, where (x_1, x_2) form a 120° angle, characteristic of the hexagonal symmetry. Both (x_1, x_3) and (x_2, x_3) are orthogonal, forming 90° angles.

2.1.2.1 Bragg's law

A crystal can be described as a periodic arrangement of atoms forming a Bravais lattice. This structure enables diffraction phenomena when illuminated by X-rays. To study the diffraction pattern, let us consider two atoms A and B located at two lattice points of the Bravais lattice. The X-ray wave incident on the lattice has a wave vector $\vec{k}_i$, while the diffracted wave has a wave vector $\vec{k}_d$ (Fig. 2.6).

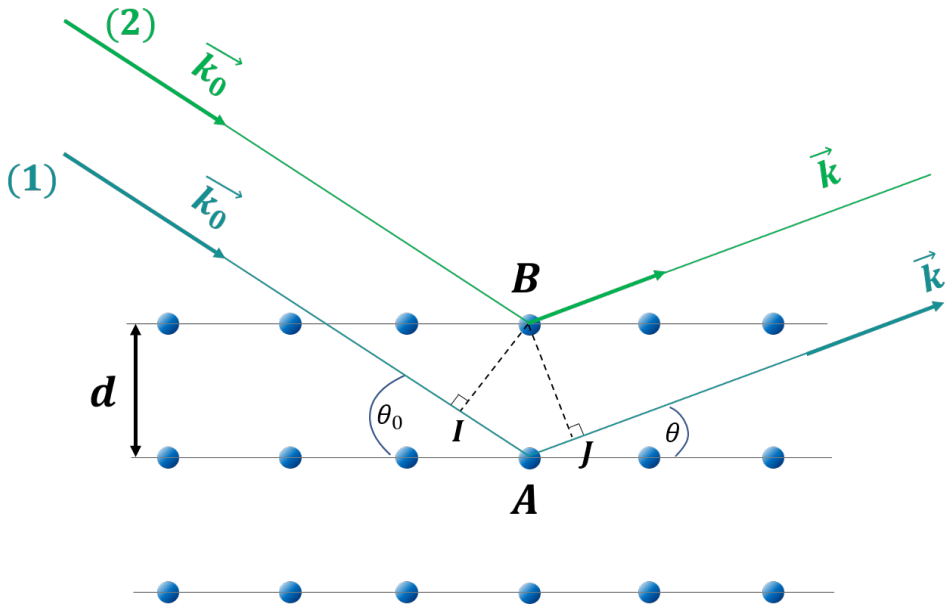

Figure 2.6: Schematic of the Bragg's law

The difference in the path length of the rays scattered by A and B can be expressed as:

$$\delta = IA + AJ = d(\sin\theta_0 + \sin\theta) \tag{2.29}$$

where θ_0 and θ represent the angles of incidence and diffraction, respectively. The phase difference associated with this path length difference is given by:

$$\Delta\varphi = \frac{2\pi}{\lambda}\delta = \frac{2\pi d}{\lambda}(\sin\theta_0 + \sin\theta) \tag{2.30}$$

where λ is the wavelength of the X-ray. For the waves to interfere constructively, this phase difference must be an integer multiple of 2π, leading to the condition:

$$\Delta\varphi' = 2\pi n \quad \text{with} \quad n \in \mathbb{N} \tag{2.31}$$

If the incident and diffracted waves are described by their wave vectors $\vec{k}_i$ and $\vec{k}_d$, then the difference in their wave vectors is defined as:

$$\vec{g} = \vec{k} - \vec{k}_0 \tag{2.32}$$

The scalar product of this vector with the lattice vector $\vec{d}$, connecting atoms A and B, must satisfy:

$$\vec{d} \cdot \vec{g} = n \tag{2.33}$$

Thus, the diffraction condition can be rewritten as:

$$n\lambda = 2d \sin\theta \tag{2.34}$$

where n is the order of diffraction.

2.1.2.2 Ewald's Sphere

A convenient visualization of the above-described diffraction conditions is the Ewald's sphere. To better understand its construction, a simplified, two-dimensional version of the Ewald's sphere is considered (see Fig. 2.7). This circle is depicted within the reciprocal lattice with its center O representing the location of diffraction and its radius being equal to the magnitude $k = 2\pi/\lambda$ of the wave vector. It is immediately apparent that the higher the energy of the incident X-ray beam, the larger the radius of this sphere. The origins of the incident vector $\vec{k}_{\mathrm{i}}$ and of the diffracted wave vector $\vec{k}_{\mathrm{d}}$ are placed at the center of the sphere. Subsequently, the diffraction vector $\vec{q}$ is constructed as $\vec{q} = \vec{k}_{\mathrm{d}} - \vec{k}_{\mathrm{i}}$. Each point in the reciprocal lattice that is intersected by the surface of the Ewald sphere represents a solution of Bragg's law. If multiple points are intersected by the sphere's surface for the same X-ray energy, it is possible to probe various inter-planar distances for different families of planes.

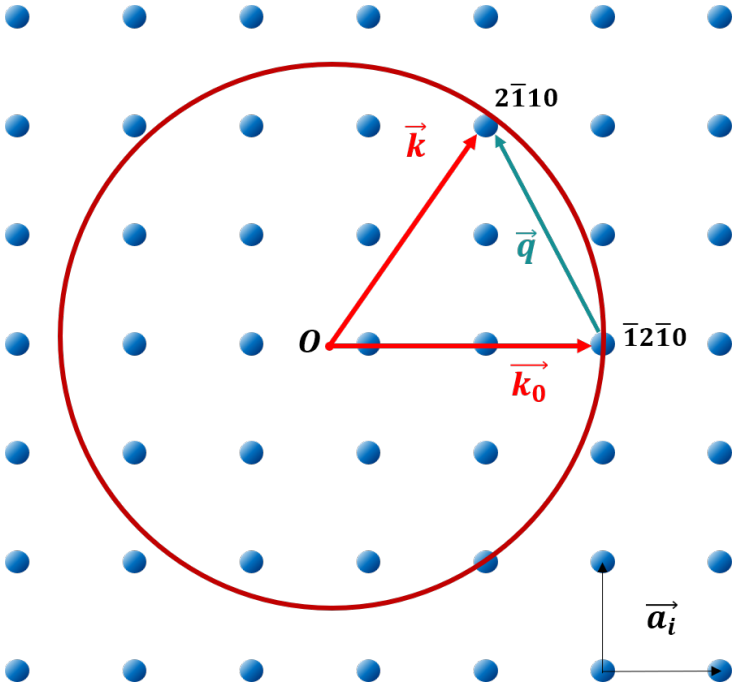

Figure 2.7: Schematic illustration of the Ewald sphere

When a monochromatic X-ray beam illuminates a single crystal, the Ewald sphere will intersect only few reciprocal lattice points. In order to measure the one or the other reciprocal lattice point that is intersected by the Ewald sphere, the sample has to be rotated accordingly to fulfill the Bragg condition. When varying the energy of the incident X-rays and thus the magnitude of the incident wave vector, the radius of the Ewald sphere is modified allowing to access other reciprocal lattice points that were not intersected before. As will be demonstrated further below, the use of a polychromatic X-ray beam provides access to a multitude of reciprocal lattice points at the same time without the need of sample rotations.

2.1.2.3 Crystal scattering factor

The electron density in a crystal can be formed by repeating the unit cell at each lattice point representing the periodicity and arrangement of the crystal. On the other hand, the crystal scattering factor $F_{crystal}$ in the reciprocal space is the Fourier transform of the electron density. The Fourier transform of a convolution is actually equal to the product of the Fourier transform of the individual functions. Therefore, the crystal scattering factor

can be written as the product of the Fourier transforms of the form factor F_{form} and the structure factor F_{uc}.

The form factor represents the periodic arrangement of the crystal lattice in Fourier space corresponding to the reciprocal lattice. It determines the positions and intensities of the diffraction peaks in the scattering pattern. The unit cell structure factor describes the distribution of the electron density within the unit cell of the crystal and modulates the scattered beam amplitude depending on the atoms that are present in the unit cell (amplitude) and their positions (phase).

Each diffraction peak corresponds to a specific Fourier component representing a sinusoidal wave of electron density with a particular frequency and direction determined by its scattering vector $\vec{q}$. The phase relationship between these Fourier components, which can be obtained from the measured diffraction pattern, allows for the reconstruction of the electron density within the unit cell. The superposition of these sinusoidal waves eventually recreates the original electron density distribution of the crystal.

The structure factor F_{uc} is the summation of the contribution of each atom j at the position $\vec{r_j}$ with the atomic form factor $f_j(\vec{q})$ in the unit cell for a given scattering vector $\vec{q}$. The position of each atom is defined in the unit cell by [117]:

$$F_{\text{Structure}}(q) = \sum_j f_j \cdot e^{i\mathbf{q}\cdot\mathbf{r}_j} \tag{2.35}$$

The form factor represents the contribution of the crystal lattice to the overall scattering amplitude taking into account the arrangement of atoms or scatterers within the crystal lattice and their interaction with the incident wave. The form factor is dependent on the electron density of the atom, as well as the geometry of the lattice, including its symmetry and the inter-atomic distances. The lattice form factor is denoted as :

$$F_{\text{form}}(q) = \sum_i f_i \cdot e^{i\mathbf{q}\cdot\mathbf{r}_i} \tag{2.36}$$

2.1.2.4 Crystal shape

When a perfect crystal is illuminated with X-rays, the diffraction pattern can be calculated by summing the scattered contributions from all atoms in the crystal. For an ideal infinite

crystal, the scattered amplitude would be proportional to the crystal's Fourier transform, where each point corresponds to reciprocal lattice points. However, in practice, crystals have finite sizes, and their shapes influence the diffraction. To model this, the crystal shape is represented as a function, $\Omega(\vec{r})$, which equals 1 inside the crystal and 0 outside. This shape function is multiplied with the atomic lattice positions. The Fourier transform of this product gives the diffraction amplitude, incorporating both the lattice and the sample shape :

$$\tilde{A}(\vec{q}) = F(\vec{q}) \cdot \mathrm{FT}(\Omega(\vec{r})) \tag{2.37}$$

where $F(\vec{q}) = \sum_j e^{i\vec{q}\cdot\vec{R}_j}$ is the Fourier transform of the infinite crystal lattice, which produces peaks only at reciprocal lattice points $\vec{G}_{h,k,l}$. It determines the positions of the main diffraction peaks in reciprocal space. $\mathrm{FT}(\Omega(\vec{r}))$ is the Fourier transform of the sample's shape function which describes the intensity distribution and introduces fringes in the pattern. These fringes result from the finite size and shape of the crystal and are visible near each reciprocal lattice point. For example, a crystal with flat surfaces will generate rods of intensity in reciprocal space perpendicular to the crystal surface. Fig. 2.8 shows examples of diffraction patterns for crystals with a tetragonal, a tetradecahedron, and a cubic shape. The shape of the diffraction patterns are directly related to the symmetry of the real space object and the fringes are related to the size of the objects. The distance between the fringes is inversely proportional to the lateral size of the real space object.

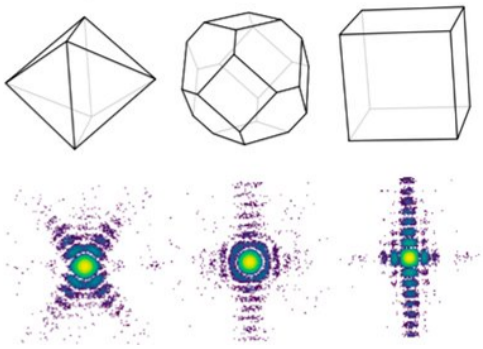

Figure 2.8: simulated diffraction patterns for three strain-free crystals. The recorded fringe pattern depends on the particle shape, with fringes seen in the directions of any surface facets.[12]

2.1.2.5 Coherence

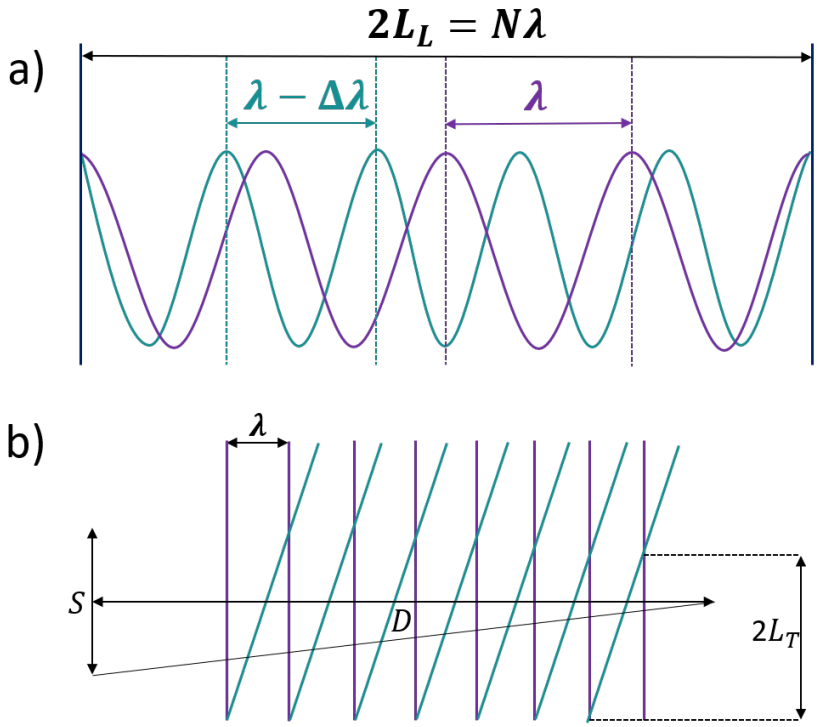

Figure 2.9: Diagram illustrating coherence lengths: (a) longitudinal coherence length and (b) transverse coherence length.

As mentioned above, an X-ray beam is composed of a set of electromagnetic waves represented by their electric field (Eq 2.1). A beam can be described as a sum of plane waves with wave vectors $\vec{k_i}$ (direction of propagation) and different angular frequencies ω_i. This is also referred to as a wave train. When this wave train interacts with matter, the dispersion of $\vec{k_i}$ and E plays an important role. The concept of beam coherence can then be introduced to characterize this beam.

Presently, huge efforts are undertaken at synchrotron sources to increase the coherent flux of the emitted X-ray beam which depends on both the brilliance and the spectral flux. Brilliance refers to the distribution of flux in both space and angular range and it depends on the photon flux, which is the number of photons emitted per second, the cross-sectional area of the emitted X-ray beam, and its angular divergence:

$$Brilliance = \frac{\text{Photon flux}}{\text{Beam cross-section area} \cdot \text{Angular divergence}} \tag{2.38}$$

The spectral flux is a function of the area over which the X-rays are distributed, the energy range of the X-rays measured in keV, and the time interval during which the photons are emitted.

$$Spectral\ Flux = \frac{\text{Number of photons}}{\text{Area} \times \text{Energy Bandwidth} \times \text{Time}} \tag{2.39}$$

Both **Brilliance** and **Spectral flux** are critical parameters for defining the performance of X-ray sources. Brilliance focuses on the spatial and angular distribution of the beam, influencing coherence and resolution, while spectral flux relates to the intensity of X-rays within specific energy bands.

The emission of photons is in general a random process, and thus the photons are not correlated. However, depending on the geometry used, it is possible to observe interference with such radiation sources. These interference effects are a signature of partial coherence. To characterize the coherence of a beam, longitudinal and transverse coherence lengths are defined.

The longitudinal coherence length ξ_l describes the distance in the direction of the beam after which two waves of slightly different wavelength $\Delta\lambda$ (or energy dispersion ΔE) are out of phase. Considering two waves that are initially in phase but having slightly different wavelengths will dephase with each oscillation n. They will eventually be out of phase when the phase difference reaches 2π resulting in an accumulated gap of $n\lambda = (n+1)(\lambda - \Delta\lambda)$. Defining ξ_l as the distance such that $2\xi_l/\lambda = 2\lambda/\Delta\lambda$ (Fig. 2.1a) leads to the following relation where the two waves are in opposition of phase:

$$\xi_l \simeq \frac{\lambda^2}{2\Delta\lambda} = \frac{\lambda}{2}\frac{E}{\Delta E} \tag{2.40}$$

At many synchrotron beamlines, Si(111) monochromators are typically used providing an X-ray beam with an energy dispersion of $\Delta E/E = 10^{-4}$. Considering an X-ray energy of 10 keV leads to a longitudinal coherence length ξ_l of about 0.6 μm. The energy resolution can be reduced, and thus the longitudinal coherence length increased by choosing other monochromators such as Ge(220), Si(331), *etc.*, but at the cost of a drastic reduction in flux.

On the other hand, the transverse coherence mainly depends on the size of the source as seen from the sample position. Two beams originating from different points of the source will not follow the same path to reach the point of observation. Equivalent to the temporal coherence length, the transverse coherence length $\xi_\perp$ is defined as the distance at which the two beams become out of phase by 2π (see Fig. 2.1b).

$$\xi_\perp \simeq \frac{\lambda}{2\Delta\theta} = \frac{\lambda R}{2\sigma_\perp} \tag{2.41}$$

The smaller the source size, the larger is the transverse coherence length. Asymptotically, a point source would result in infinite transverse coherence. This length can also be understood as the inverse of the angle subtended by the source as seen from the sample. In the case of synchrotron beamlines, the size of the source defined by undulators is on the order of few tens to few hundreds of micrometers. Typical lengths of synchrotron beamlines range from several tens of meters reaching up to 150 m for very long beamlines, thus reducing the apparent source size and giving transverse coherence lengths of the order of several tens to few hundreds of micrometer.

2.2 Experimental Techniques

In this chapter, the experimental methods used throughout this thesis will be presented. Particular emphasize will be given on micro- and nano-focused synchrotron X-ray diffraction methods as well as transmission electron microscopy. These techniques played a crucial role in the investigation of the mechanical and the electromechanical behavior of ZnO nanowires.

2.2.1 Focusing optics

The synchrotron X-ray diffraction techniques employed throughout this thesis base on hard X-ray beams focused down to few hundred nanometer in diameter. The refractive index for electromagnetic waves is given by $n = 1 - \delta + i\beta$, where the real part $1 - \delta$ and the imaginary part β define the critical angle of reflection and the absorption, respectively [118][119] . Unlike visible light, where refractive indices are typically larger than 1 (*e.g.*

1.33 in the case of water), the refractive index for X-rays is smaller than 1. In addition, for X-rays, δ is typically on the order of 10^{-6} while β is about 10^{-9}. This low refractive index necessitates specialized optics for focusing X-rays, unlike visible light which easily undergoes refraction through lenses. The refractive index being slightly less than 1 means that X-rays experience a phenomenon called *total external reflection* rather than internal reflection, which dominates visible light. Total external reflection occurs at very shallow grazing incidence angles, determined by a critical angle that depends on δ. This property forms the basis of mirror-based optics such as Kirkpatrick-Baez mirrors which will be introduced below and which allow X-rays to be focused via reflectivity rather than refractive lenses.

Focusing X-rays is challenging due to their negligible refraction and strong absorption in most materials. Over the past decades, tremendous progress on the fabrication of reflective, diffractive, and refractive focusing optics at 3rd and 4th generation synchrotron sources has been achieved.

2.2.1.1 Reflective optics

The real part of the refractive index $1 - \delta$ defines the critical angle for reflection α_c. Considering $\delta \approx 10^{-6}$ and $\alpha_c \approx \sqrt{2\delta}$, the critical angle is typically on the order of few milliradians. To reduce the astigmatism, Kirkpatrick and Baez[120] proposed the use of two spherical and cylindrical mirrors in a crossed configuration - one mirror focusing the beam horizontally and the other vertically (Fig. 2.10) a). A big advantage of mirrors as focusing optics is their achromaticity, *i.e.,* the focal length does not depend on the energy and respective wavelength of the incident radiation. Thus, they are used for focusing monochromatic beams as well as white beams.

2.2.1.2 Diffractive optics

A Fresnel zone plate (FZP) consists of alternating opaque and transparent rings, causing the X-ray beam to diffract through these rings and constructively interfere at the lens' focal point. Higher orders of diffraction are filtered out by placing a pinhole in front of the sample to retain only the first diffraction order. A "beam stop" is also located at the center of this lens to block the 0th diffraction order of the direct incident beam, which is

not focused by the FZP (Fig. 2.10) b). The minimal focal size achievable with a FZP is determined by its outermost zone width, Δr_N, because this parameter defines the spatial resolution of the FZP. The focal behavior of an FZP arises from constructive interference of light, where the zones guide the light waves to focus at a specific point. The width of the outermost zone directly influences how finely using the beam focused by the FZP can resolve spatial details. The focal length of an FZP is related to the outermost zone width Δr_N and the radius of the outermost zone r_N by the equation[121]:

$$f = \frac{2 r_N \Delta r_N}{\lambda} \tag{2.42}$$

where λ is the wavelength of the incident light. From this, we see that the focal properties depend critically on Δr_N.

The minimum focused beam size demonstrated by simulation is 0.87nm reported by C. Schroer[122] for an FZP focal length of 25.7µm and an energy of 20 keV.

2.2.1.3 Refractive optics

While refractive lenses for visible light are convex they actually have to be concave for X-rays due to the fact that n < 1. Since the refractive index is very close to unity refractive lenses are not very efficient resulting in focal lengths of few tens of meters for hard X-rays. In order to obtain focal lengths of the order of 1 m and below, multiple refractive lenses are stacked together to a compound refractive lens (CRL), which together act like a single, more powerful lens. To minimize absorption by the CRLs, materials with low atomic numbers like Be, Al, or Si are chosen (Fig. 2.10) c).

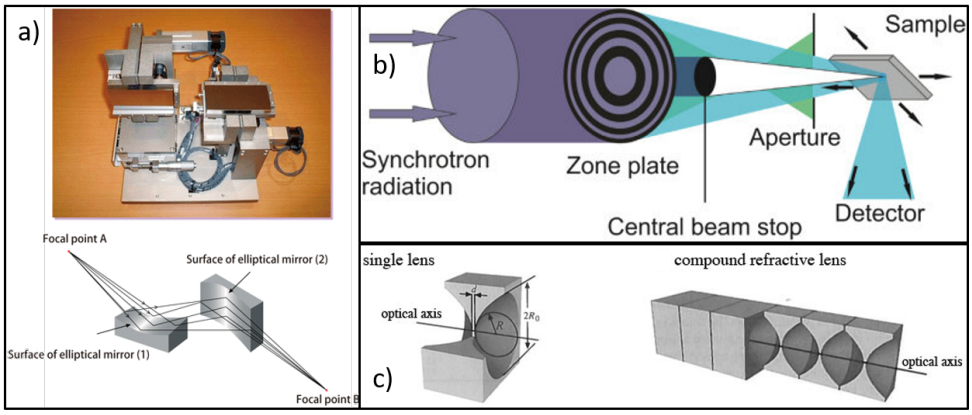

Figure 2.10: a) Picture and a schematic view of a Kirkpatrick-Baez (KB) system[13] b) Schematic of a Fresnel zone plate (FZP) setup which consists of the FZP itself, an order sorting aperture (OSA) for selecting one particular diffraction order, and a central beam stop (CBS)[14] c) Schematics of a biconcave lens with radius R and the arrangement of several lenses as compound refractive lens.[15]

It should be kept in mind that the synchrotron X-ray source, meaning the electron beam, is not a point source but it is extended. Typical source sizes are in the range of few tens to few hundreds of micrometer (e.g. 50 µm x 5µm at the ESRF BM32 beamline and 388 µm x 8.1 µm at Soleil SIXS beamline). Therefore, focusing optics only allow for a demagnification of the source size. The length of synchrotron undulator beamlines may vary from around 50 to more than 100 m (like ID01 at ESRF) and the distance of the focusing optics from the sample varies between few centimeter up to the meter range. Thus, demagnification ratios ranging from several tens to one thousand can be obtained. Nowadays, hard X-ray beams are routinely focused down to few hundreds of nanometer or even few tens of nanometer at very long beamlines. While focusing optics installed very close to the sample position offer very small foci, they limit the possibility of installing special sample environments such as heating stages, cryostats, atomic force microscopes etc.

2.2.2 Laue microdiffraction

Laue microdiffraction uses a white (polychromatic) X-ray beam. This technique, which dates back to the work of Laue and Knipping on ZnS crystals in 1912, has gained renewed

interest thanks to advancements in microfocused X-ray beams and achromatic focusing optics, particularly with the use of Kirkpatrick-Baez mirrors (introduced in 1948) [120].

For a polychromatic X-ray beam with an energy range between E_{min} and E_{max}, two Ewald spheres can be drawn for these extreme energies (see Fig. 2.11). In Laue diffraction, not only the reciprocal lattice points on the surface of an Ewald sphere are probed, but also those within the volume defined by λ_{min} and λ_{max}.

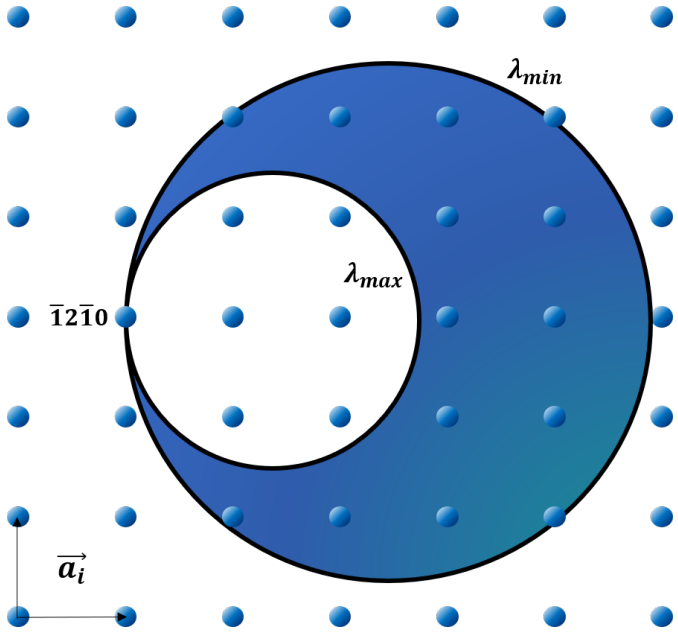

Figure 2.11: A 2D representation of the Ewald sphere is shown for a white beam, defined by two wavelength limits, the minimum and the maximum.

Recently, this method has seen significant development on different synchrotron beamlines around the world such as BM32 beamline at ESRF. Proving especially useful for analyzing polycrystalline materials[123]. When a 2D detector is positioned close to the sample under a white beam, numerous atomic planes fulfill the Bragg condition simultaneously. As a result, a diffraction pattern is then captured containing multiple reflections (Fig. 2.12) a).

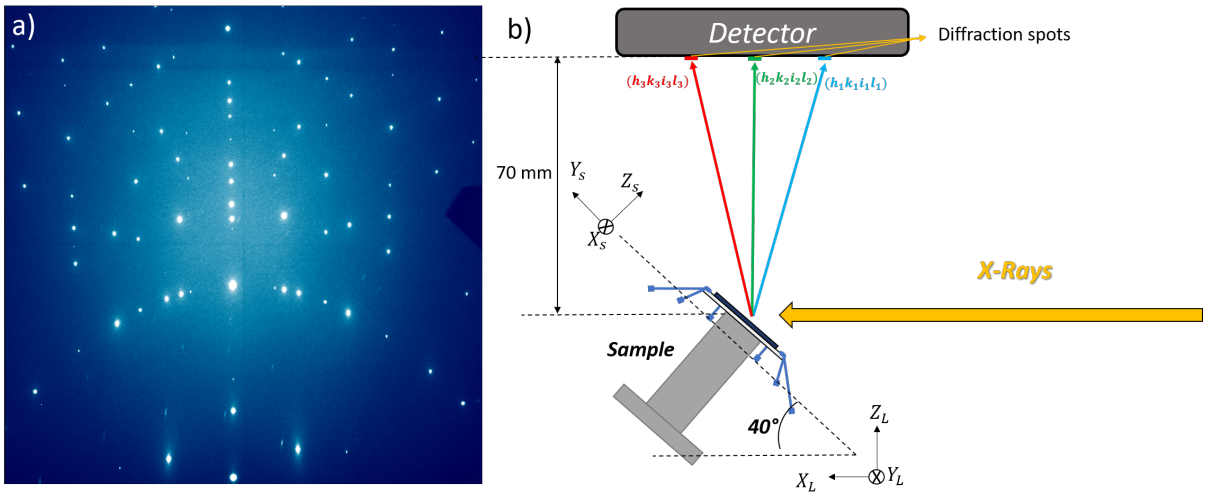

Figure 2.12: a) Example of a Laue diffraction pattern showing ZnO and Si diffraction spots. b) Diagram of the Laue microdiffraction setup at the BM32 beamline of the ESRF.

The diffraction peaks in Fig. 2.12 a) show up as distinct spots. By analyzing the positions of these Laue spots, the crystal orientation and deviatoric strain can be determined. Additionally, the streaking of these peaks is linked to uneven elastic strain distribution or geometrically necessary dislocations (GNDs). Lattice rotations often occur alongside strain gradients, such as those seen during a bending test.

Laue microdiffraction is highly sensitive to relative changes in lattice parameters and the orientation of the probed crystal, which means the deviatoric strain, enabling precise mapping of strain distributions and gradients within the material. Due to the experimental configuration with a fixed incident angle and a polychromatic X-ray beam the diffraction peaks of the same type of families of lattice planes like {**111**}, {**222**}...etc are superposed. Thus, Laue microdiffraction is not able to probe isotropic volume changes. However, it is highly sensitive to changes of the deviatoric strain (Fig. 2.13).

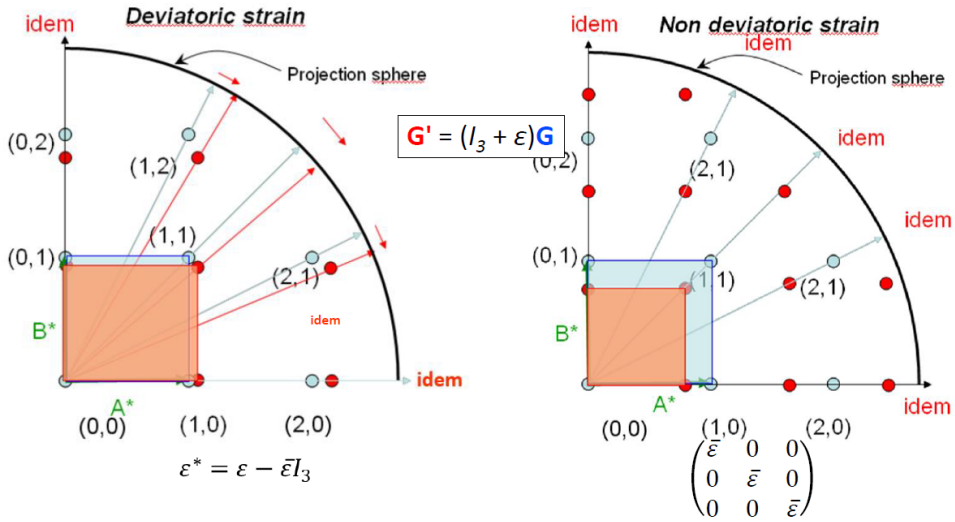

Figure 2.13: Laue diffraction sensitivity to deviatoric strain[16]

To overcome the shortcoming of Laue microdiffraction in measuring the absolute strain, the energy of the diffracted X-rays of at least one Laue spot has to be measured. This has been demonstrated using a fluorescence detector or an energy-dispersive pn-CCD [124].

As shown in (Fig. 2.13), a uniform lattice expansion changes the primitive reciprocal lattice vectors equally. This causes all reciprocal lattice points to move radially outward. Since the atomic planes $\vec{u}_q$ remain oriented the same way, these changes do not appear in the diffraction pattern. Therefore, in white-beam Laue diffraction, the unit cell volume (dilatation) cannot be uniquely determined. Instead, the strain tensor obtained is the deviatoric strain ε_{dev}, which excludes the hydrostatic term ε_{hyd}. The relationship is written as:

$$\varepsilon_{\text{dev}} = \varepsilon - \varepsilon_{\text{hyd}} = \begin{bmatrix} \varepsilon_{11} & \varepsilon_{12} & \varepsilon_{13} \\ \varepsilon_{12} & \varepsilon_{22} & \varepsilon_{23} \\ \varepsilon_{13} & \varepsilon_{23} & \varepsilon_{33} \end{bmatrix} - \begin{bmatrix} \Delta/3 & 0 & 0 \\ 0 & \Delta/3 & 0 \\ 0 & 0 & \Delta/3 \end{bmatrix} \tag{2.43}$$

Here, $\Delta = \varepsilon_{11} + \varepsilon_{22} + \varepsilon_{33}$, and ε represents the strain tensor of the material.

2.2.2.1 Strain and orientation

The Laue diffraction method using a white beam is highly sensitive to the orientation of a crystal. In order to obtain this orientation, the pattern of Laue spots that is projected

on a 2D detector is indexed using the Miller convention (h,k,l) with the help of different software packages such as LaueTools (used in this thesis), XMAS[125], or LaueGO[126]. When it comes to the coordinate systems, we take into consideration the lab coordinate system in reference to the real space units (a_1, a_2, a_3) with their corresponding angles (α_1, α_2, α_3) and the reciprocal space units of the crystal (b_1, b_2, b_3) with their corresponding angles (β_1, β_2, β_3) (Fig. 2.14).

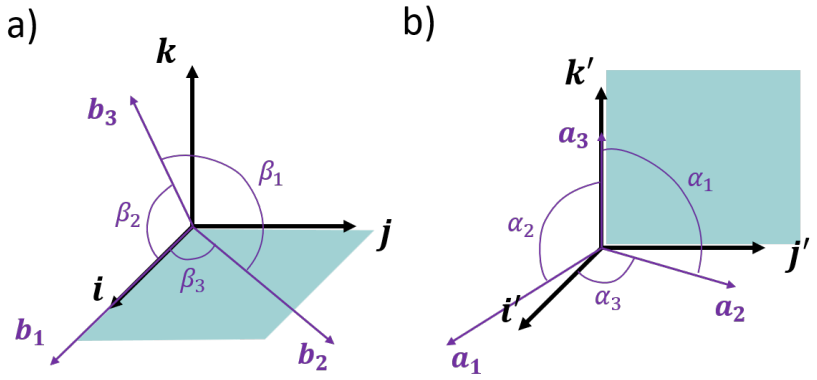

Figure 2.14: (a) Cartesian coordinate system representing the reciprocal lattice of the sample. (b) Cartesian coordinate system representing the real-space unit cell.

The origins of both the Cartesian system and the reciprocal space system are superimposed, which allows to transferring vectors described in the reciprocal space $\left(\vec{q}_r = h\vec{b_1} + k\vec{b_2} + l\vec{b_3}\right)$ into the Cartesian coordinates $\left(\vec{q}_c = u\vec{i} + v\vec{j} + w\vec{k}\right)$ using the transformation matrix $\mathbf{B}$ [Busing & Levy, 1957] :

$$\begin{pmatrix} u \\ v \\ w \end{pmatrix} = \mathbf{B} \begin{pmatrix} h \\ k \\ l \end{pmatrix} = \begin{bmatrix} b_1 & b_2 \cos\beta_3 & b_3 \cos\beta_2 \\ 0 & b_2 \sin\beta_3 & -b_3 \sin\beta_2 \cos\alpha_1 \\ 0 & 0 & \frac{1}{a_3} \end{bmatrix} \begin{pmatrix} h \\ k \\ l \end{pmatrix} \tag{2.44}$$

The transformation matrix B is connected to the material's lattice structure. By setting the values of h, k, and l to (1,0,0), (0,1,0), and (0,0,1), it can be demonstrated that each row in the B matrix corresponds to one of the primitive reciprocal lattice vectors in Cartesian space. The reciprocal Cartesian coordinate system can then be rotated into a laboratory Cartesian coordinate system using the matrix U, where the axis directions are aligned with the incoming beam and the detector.

$$q_{hkl} = \begin{pmatrix} u' \\ v' \\ w' \end{pmatrix} = U \begin{pmatrix} u \\ v \\ w \end{pmatrix} = UB \begin{pmatrix} h \\ k \\ l \end{pmatrix} \tag{2.45}$$

The matrix U is called the orientation matrix, which defines the crystal orientation relative to the laboratory frame. To express the directions of the reciprocal lattice vectors in the laboratory's Cartesian coordinate system, the Miller indices are multiplied by both the U and the B matrices.

In order to determine the crystal orientation, the U matrix has to be calculated. This involves measuring the angles between different Bragg peaks using the 2D detector's geometry. Then, an angle between two specific Bragg peaks is selected and compared to a list of angles calculated for the expected lattice structure. If there is a match within a certain tolerance, this angle is used to calculate a trial U matrix. Using this trial matrix, a Laue pattern is computed considering the white beam's energy bandwidth. By comparing the computed Laue diffraction pattern with the experimental one, the orientation matrix that matches the most points and has the smallest angular errors is chosen. Once the best-fitting trial matrix is selected, the Laue diffraction peaks are indexed, and the crystal's geometrical parameters in the experimental frame are set. Due to experimental errors and lattice strain, the B matrix from the perfect lattice structure may not fit the diffraction peaks perfectly. To improve the fit, the reciprocal lattice parameters $b_1, b_2, b_3, \beta_1, \beta_2, \beta_3$ are adjusted, and a new B matrix is calculated. This refinement minimizes the differences between theoretical and experimental angles, resulting in a matrix that describes the distorted reciprocal lattice parameters caused by crystal strain.

To calculate the deviatoric strain tensor, the primitive reciprocal lattice vectors are expressed in Cartesian coordinates using a transformation matrix A. In this new coordinate system, the origin is set at one lattice point, the z-axis is aligned with the lattice vector a_3, and the y-axis lies in the plane formed by a_3 and a_2. The matrix A is related to the matrix B by the following equation:

$$A^t B = I \tag{2.46}$$

where I is the identity matrix and t represents the transpose operation. Using a

transformation matrix Tr, the matrix A of the distorted crystal can be related to the matrix A_0 of the perfect lattice structure:

$$A = TrA_0 \tag{2.47}$$

The matrix Tr includes both distortion and rotation components. For small rotations, the rotation component is antisymmetric. Therefore, the distorted term can be determined by:

$$\varepsilon_{dev} = \frac{Tr^t + Tr}{2} - I \tag{2.48}$$

where ε_{dev} is the deviatoric strain tensor of the crystal. The average deviatoric strain tensor can be obtained from the Laue diffraction pattern by refining the fit of the diffraction data.

In summary, indexing Laue diffraction patterns involves the determination of two matrices, U and B. The matrix U describes the crystal orientation, while B relates to the lattice parameters. With these matrices, the direction of the diffraction planes and the deviatoric strain tensor can be determined.

For a grain with (111) orientation and Euler angles (φ, ψ) (Fig. 2.15), a Laue pattern can be simulated by calculating the normal vectors of several atomic planes. There is a specific energy at which a diffraction vector $\vec{q}_n$ aligns with this direction. The direction of the vector $\vec{k}_f = \vec{q}_n - \vec{k}_i$ can be easily determined since the incidence remains constant. These directions $\vec{k}'_f$ are then projected onto the 2D dectector, considering the sample position and precise angle. This method is highly sensitive to grain orientation within the plane and is based on a simplified model that ignores sample deformations and the superposition of harmonics $E, 2E, 3E$ that diffract at the same location. The positional accuracy of Laue diffraction can give us the deviatoric strain tensor.

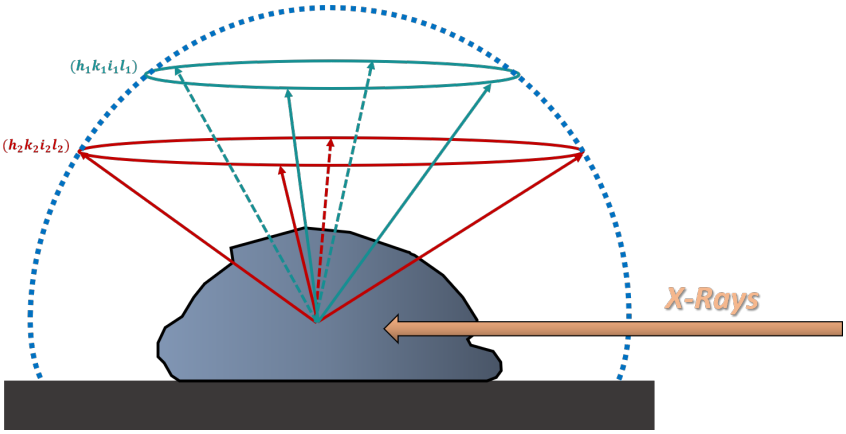

Figure 2.15: Schematic of Laue diffraction for a grain with (111) orientation. Incident X-rays interact with the crystal, diffracting different zone axis and projected onto a 2D detector.

Once the measurement is completed, a Laue pattern is obtained, showing the intensity and positions of the Bragg peaks on the camera. The energies of these peaks fall within the range of the incident white beam. This diffraction pattern is then indexed, *i.e.* each diffraction peak is associated with Miller indices h, k, and l. Here, the LaueTools software [127] is used, which was developed at the BM32 beamline at the European Synchrotron Radiation Facility (ESRF). For indexation, the position of at least 8 Laue spots in the diffraction pattern are needed as well as the crystal structure of the sample. For correct indexation and calculation of the UB orientation matrix of the sample and the deviatoric strain, the detector has to be calibrated employing a calibration sample. In most cases, a Ge single-crystal is used for calibration. In this thesis, Si is employed for calibration purposes since the ZnO nanowires were actually placed on patterned Si substrates. The calibration is performed by the superposition of the positions of the experimentally measured Laue spots and a theoretical diffraction pattern allowing for determining the camera-sample distance, pixel size, inclination angles of the detector, and the orientation of the detector's center. For indexation, the LaueTools software uses two coordinate systems where one is fixed to the detector (which is used for indexation), while the second one is fixed to the sample. Since there is a 40° rotation about the x-axis between these two systems, it is possible for the software to express the indexed diffraction vectors (u_{mc}, u_{df}, and $\mathbf{q}$) as a function of the diffraction angles 2θ and χ in the detector's reference frame (Fig. 2.16).

Knowing the material's type and its Bravais lattice, the material can be described in two systems of Cartesian coordinates. In real space, the lattice parameters are a, b, c, α, β, and γ, while in reciprocal space, they are a^*, b^*, c^*, α^*, β^*, and γ^*. Only the reciprocal space is of interest. The passage from the laboratory system to this new system is made using a matrix B_0, calculated according to the reciprocal lattice. This passage involves transforming the vectors in the detector's reference frame into the crystal's reference frame. The orientation matrix, commonly denoted as UB, can then be used to express the crystal's orientation in the laboratory reference frame:

$$\mathbf{q} = UB \cdot B_0 \cdot \begin{pmatrix} h \\ k \\ l \end{pmatrix} \tag{2.49}$$

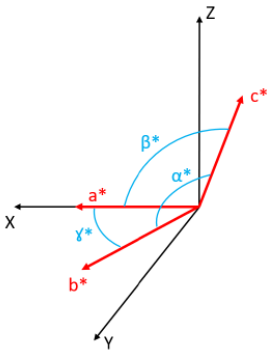

Figure 2.16: The coordinate system in reciprocal space is obtained by orthonormalizing the X, Y, and Z axes.

2.2.2.2 Experimental setup at beamline BM32 at ESRF

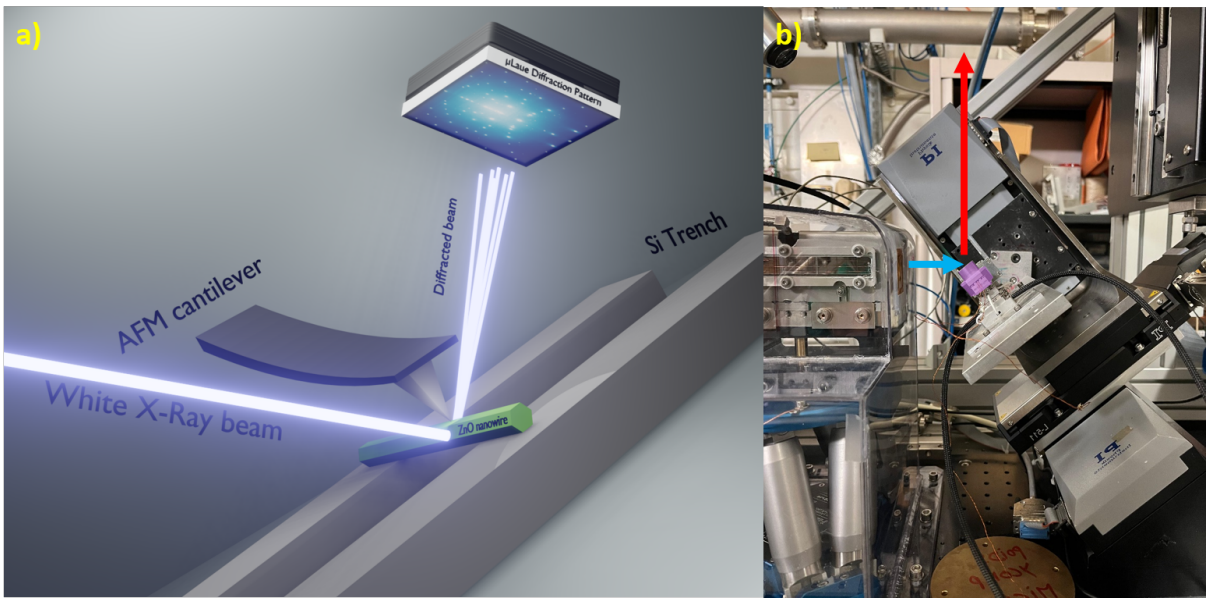

Figure 2.17: a) Schematic illustration of the experimental setup for in-situ three-point bending tests in combination with Laue microdiffraction. b) Photograph illustrating the sample mount and the incident and diffracted beam at the BM32 experimental hutch

During this thesis, Laue microdiffraction experiments were performed at the BM32 beamline at the European Synchrotron ESRF in Grenoble (France). This beamline operates within an energy range of 5 to 22 keV. The beam is focused down to a size of 300 nm x 300 nm using a pair of KB mirrors. The diffracted X-rays are recorded using a PhotonicScience quad sCMOS detector (73.4 µm x 73.4 µm pixel size) with a 0.5 s readout time[128], which is installed at 90° with respect to the incident X-ray beam at a distance of about 77 mm from the sample position. The sample stage consists of a stack of three perpendicular translation axes, each with a movement range of ±16 mm and a relative positioning accuracy of 0.1 µm (see Fig. 2.17). This configuration allows for sample movements within a standard coordinate system, referred to as the "sample stage (ss)" frame. In addition, a frame attached to the sample ("s") is defined, which is chosen to be identical to the sample stage frame. The movement directions in this frame are denoted as $\vec{x}_s$, $\vec{y}_s$, and $\vec{z}_s$. The sample is inclined by 40° relative to the incident beam (Fig. 2.17). The exact orientation

of the sample in this frame depends on the way it is mounted on the translation stage. It is important to note that this sample frame definition does not match the one used in LaueTools [129]. However, the small deviations in the alignment between the "ss" and "s" frames are not critical for our study. These discrepancies will result, for example, in an error in the absolute orientation of a grain in the sample but not in the misorientation within the same sample. An optical microscope, equipped with a zoom lens and a CCD camera, is used to observe the sample facilitating sample alignments. This microscope, mounted on translation stages, is pre-aligned with respect to the position of the incident X-ray beam on the sample surface so that it is in the center of the field of view when the zoom is at its maximum. The optical axis of the microscope approximately coincides with the $\vec{z}_s$ axis.

The unit vector parallel to the incident beam is denoted $\vec{y}_b$ and points in the direction of X-ray propagation. The intersection point between this beam and the geometric surface of the sample will be referred to as point O (see Figure 2.17). The reference frame attached to the detector will be denoted by the index "d". This will be the primary reference frame for the Laue microdiffraction experiments, in which all calculations are performed. The axes $\vec{x}_d$ and $\vec{y}_d$ are aligned with the pixel grid of the detector with $\vec{y}_d$ being close to the direction of the incident beam $\vec{y}_b$ and pointing in the same direction. The third vector, $\vec{z}_d$, is normal and inward to the surface of the detector. The direction of the incident beam relative to the detector frame is defined using the two angles β and γ as shown in (Fig. 2.17). Thus, in the detector frame, the vector $\vec{y}_b$ has the following coordinates:

$$\vec{y}_b = \begin{pmatrix} -\sin\gamma & \cos\beta & 0 \\ \cos\gamma & \cos\beta & 0 \\ \sin\beta & 0 & 0 \end{pmatrix} \tag{2.50}$$

To transform from the detector frame to the sample frame let's review the mathematical method used to transition between orthogonal bases.

Considering two orthonormal bases with $\vec{e}_i^{(1)}$ representing the unit vectors of the old basis (1), and $\vec{e}_i^{(2)}$ representing the unit vectors of the new basis (2). Here, i denotes the index of the basis vector. For example, $\vec{e}_1^{(1)}$ is the unit vector along the x-axis of basis (1), $\vec{e}_2^{(1)}$ is the unit vector along the y-axis of basis (1), and so forth.

We define the transition (or rotation) matrices $[P]$ and $[Q]$ with components P_{ij} and Q_{ij}, respectively. $[P]$ represents the components of the unit vectors of the new basis $\vec{e}_j^{(2)}$ expressed in the old basis $\vec{e}_i^{(1)}$ with $P_{ij} = \vec{e}_j^{(2)} \cdot \vec{e}_i^{(1)}$. $[Q]$ represents the components of the unit vectors of the old basis $\vec{e}_j^{(1)}$ expressed in the new basis $\vec{e}_i^{(2)}$ with $Q_{ij} = \vec{e}_j^{(1)} \cdot \vec{e}_i^{(2)}$.

If the reference frames are orthonormal, then $[P]$ and $[Q]$ are orthogonal matrices, i.e. $[P]$ is the transpose of $[Q]$ (and vice versa), meaning $[P] = [Q]^T$. The transpose of $[P]$ is equal to the inverse of $[P]$ (and the same for $[Q]$).

The relation between P_{ij} and Q_{ij} can be expressed as:

$$P_{ij} = Q_{ji} \tag{2.51}$$

with the additional properties:

$$[P]^{-1} = [P]^T, \quad [Q]^{-1} = [Q]^T \tag{2.52}$$

In the example shown in (Fig. 2.17), the matrices $[P]$ and $[Q]$ are:

$$[P] = \begin{pmatrix} \cos\theta & -\sin\theta & 0 \\ \sin\theta & \cos\theta & 0 \\ 0 & 0 & 1 \end{pmatrix}, \quad [Q] = \begin{pmatrix} \cos\theta & \sin\theta & 0 \\ -\sin\theta & \cos\theta & 0 \\ 0 & 0 & 1 \end{pmatrix} \tag{2.53}$$

The unit vectors $\vec{e}_i^{(1)}$ and $\vec{e}_j^{(2)}$ are related by the following expressions:

$$\vec{e}_i^{(1)} = P_{ij}\vec{e}_j^{(2)}, \quad \vec{e}_i^{(2)} = Q_{ij}\vec{e}_j^{(1)} \tag{2.54}$$

Here, we use implicit summation over repeated indices (e.g., summation over j). The index order in these relations is put into consideration. These are not scalar products but rather vectorial relationships that allow the expression of a vector like $\vec{e}_j^{(2)}$ as a linear combination of $\vec{e}_i^{(1)}$.

Given the properties discussed above, these relations can also be written as:

$$\vec{e}_j^{(1)} = Q_{ji}\vec{e}_i^{(2)}, \quad \vec{e}_j^{(2)} = P_{ji}\vec{e}_i^{(1)} \tag{2.55}$$

For the Euler angles ϕ_1, ϕ_2 (according to the "Bunge" convention[130]) are defined as follows: to transition from frame (1) to frame (2), the following rotations are performed, in sequence:

1. A rotation by angle ϕ_1 around the axis $\vec{e}_3^{(1)}$, which gives the new frame $\{\vec{e}_1^{(1')}\}$.
2. A rotation by angle Φ around $\vec{e}_1^{(1')}$, which gives the new frame $\{\vec{e}_2^{(1'')}\}$.
3. Finally, a rotation by angle ϕ_2 around $\vec{e}_3^{(1'')}$, which gives the new frame $\{\vec{e}_3^{(2)}\}$.

The transition matrix corresponding to this sequence of rotations is written as:

$$[Q_{\text{Bunge}}] = \begin{pmatrix} \cos\phi_2\cos\phi_1 - \sin\phi_2\sin\phi_1\cos\Phi & \sin\phi_2\cos\phi_1 + \cos\phi_2\sin\phi_1\cos\Phi & \sin\phi_1\sin\Phi \\ -\cos\phi_2\sin\phi_1 - \sin\phi_2\cos\phi_1\cos\Phi & -\sin\phi_2\sin\phi_1 + \cos\phi_2\cos\phi_1\cos\Phi & \cos\phi_1\sin\Phi \\ \sin\phi_2\sin\Phi & -\cos\phi_2\sin\Phi & \cos\Phi \end{pmatrix} \tag{2.56}$$

2.2.3 Bragg coherent X-ray diffraction imaging

Bragg Coherent X-ray Diffraction Imaging (BCDI) is a novel lensless imaging technique that measures the three-dimensional reciprocal space map relying on coherent illumination, as it also allows to determine and to image the displacement field in 3D.

In general, an electromagnetic wave is described by its amplitude A and its phase ϕ. However, diffraction experiments measure the intensity of the diffracted X-rays, which is the complex conjugated square of the amplitude ($I(q) = \tilde{A}^*(q)\tilde{A}(q)$) (See Eq. 2.19). Thus, the phase information, which is in the exponential function, is lost. Without any knowledge about the phase, the electron density cannot be directly reconstructed by means of an inverse discrete Fourier transform and obtain a detailed structural model of the object. During the last two to three decades, phase retrieval algorithms have been developed to numerically recover the phase. The retrieved diffraction amplitude is then subjected to inverse Fourier transformation (IFT), which generates a complex density function of the crystal. This reveals details about the crystal's shape, strain, and defect distribution.

The objective of this sub-section is to introduce the BCDI technique.Firstly, the method for recording the 3D intensity distribution in reciprocal space will be presented. Subsequently, the coherent properties of the illumination and the conditions required to observe fringes within the diffraction pattern with reasonable contrast are introduced. Thereafter, the basic principals of phase retrieval algorithms will be described. Finally, the general experimental setup for BCDI experiments will be presented.

2.2.3.1 Bragg Coherent Diffraction Imaging measurement process

In general, the three-dimensional intensity distribution in the vicinity of a given Bragg reflection is measured by rocking the sample on the order of about 1° (depending on the extension of the diffraction intensity in reciprocal space) around the incident angle of the X-ray beam. This rocking tilts the sample's corresponding Ewald's sphere allowing to probing different slices of the reciprocal space in the detector for each angular step as illustrated in Fig. 2.18.

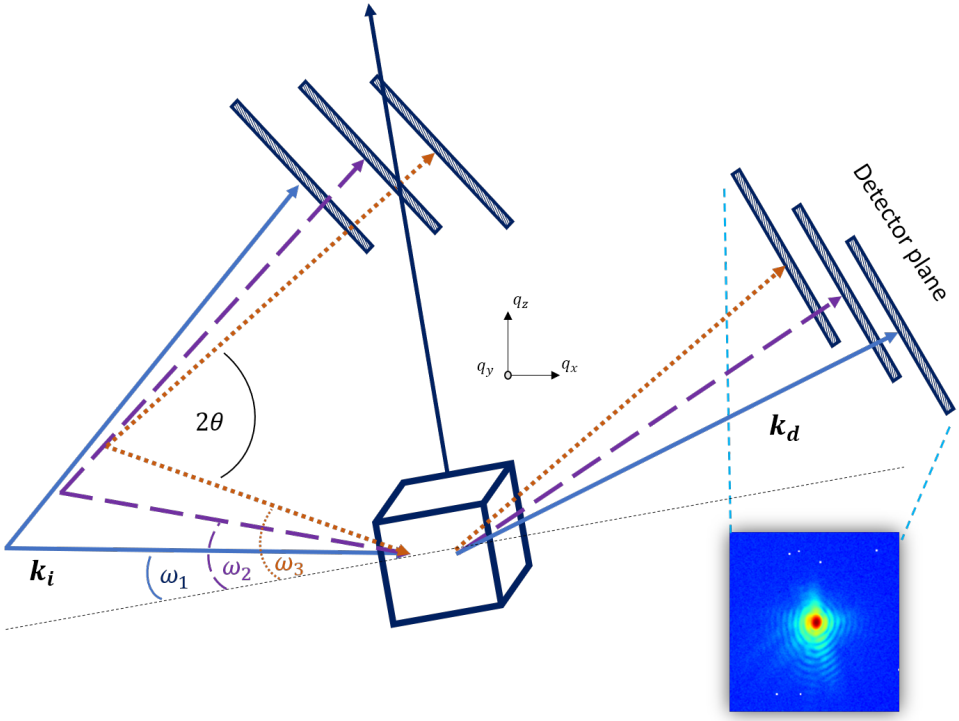

Figure 2.18: Illustration of the measured position in reciprocal space for a rocking scan

2.2.3.2 Phase relation to the displacement field and strain

As we explained in (Eq. 2.34), a crystal can be thought of as a repeating arrangement of unit cells on a lattice. The structure factor can be expressed as a combination of the lattice factor F_{lattice} and the unit cell structure factor F_{uc}. The shape of the scattering intensity around Bragg peaks is determined by F_{lattice}, which is the Fourier transform of the lattice, while F_{uc} represents the Fourier transform of the unit cell's electronic density[131].

For strained crystals, the structure factor can be rewritten as:

$$F_{\text{crystal}}(\vec{q}) = \sum_{j}^{N} f_j(\vec{q}) e^{i\vec{q}\cdot(\vec{r}_{0,j}+\vec{u}_j)} \sum_{k} e_k^{i\vec{q}\cdot\vec{R}} \tag{2.57}$$

where $\vec{r}_{0,j}$ is the ideal position of atom j in the unit cell, $\vec{u}_j$ is the displacement of atom j from its ideal position and $\vec{R}_k$ is the position of unit cell k.

Equation 2.57 simplifies the displacements by assuming all atoms in a unit cell share the same displacement. To simplify further, only the intensity near Bragg peaks is considered ($\vec{q} \approx \vec{G}$), where $\vec{G}$ is the reciprocal lattice vector corresponding to the Bragg peak[132, 133]. This leads to:

$$F_{\text{crystal}}(\vec{q}) = DFT[F_{\text{uc}}(\vec{G}) e^{i\vec{G}\cdot\vec{u}_k}]_{N_{\text{uc}}} \tag{2.58}$$

where DFT refers to the discrete Fourier transform. This approximation works when $(\vec{q} - \vec{G}) \cdot \vec{u}_k \ll 1$, but breaks down for highly strained crystals, requiring more detailed simulations[134].

For non-strained crystals, F_{lattice} is constant at each Bragg peak. In strained crystals, the additional phase factor modifies the symmetry of the Bragg peaks, reflecting the heterogeneous displacement field. These distortions reveal the displacement field but require collecting scattered intensity from at least three non-coplanar Bragg peaks to reconstruct the complete strain tensor over an orthogonal basis[135].

When we measure the diffracted intensity during a BCDI experiment, we record how much X-ray signal is scattered in different directions. However, this measurement only captures the intensity of the scattered X-rays, not their phase. The phase contains crucial information about the atomic displacements within the material, which are directly related to the displacement field. To overcome this issue, advanced computational algorithms, are used to estimate the missing phase information and reconstruct the displacement field indirectly.

2.2.3.3 Phase retrieval

The diffracted amplitude near a node in reciprocal space can be seen as a Fourier transform. Knowing the complex amplitude would therefore imply knowing the displacement field

within the object projected onto $\vec{G}$:

$$f_0(\vec{r})e^{i\vec{G}\cdot\vec{u}(\vec{r})} = TF^{-1}\{A(\vec{q})\} \tag{2.59}$$

The complex amplitude is the only experimentally accessible modulus. As a result, we don't have access to the information related to the deformation field. Nevertheless, Coherent X-ray Diffraction Imaging (CDI) is capable of overcoming this obstacle through the reconstruction of the phase of the diffracted wave using dedicated algorithms. In the Bragg condition, the displacement field can then be extracted from this phase of the scattered wave.

Phase reconstruction as a technique is originally a method used in signal treatment, which was adapted to diffraction. In the context of reconstruction, we refer to the term "Oversampling" which is the condition where the recorded diffraction pattern contains more data points than the number of independent variables in the object being reconstructed. This allows for unique recovery of the phase information by utilizing iterative reconstruction algorithms. In the case of fulfilling the oversampling condition, the lost phase is retrieved by using the **Shannon** or the **Sayre** oversampling criteria [136][137]. This concept can be extended to complex and multi-dimensional cases. Such signal reconstruction is possible if the oversampling condition, $\sigma_{\text{Over}} > 2$, is met. For 2D or 3D data, the oversampling ratio is defined as [138]:

$$\sigma_{\text{Over}} = \frac{\text{Number of measurements}}{\text{Number of points describing the object}} \tag{2.60}$$

Similarly, this ratio represents the number of measurement points to the number of unknowns. In some cases, it is possible for $\sigma^{3D}_{\text{Over}} = \sigma_x \times \sigma_y \times \sigma_z$ to be much larger than 2, but with one direction having $\sigma_i < 1$. In this scenario, the reconstruction will be partial, with overlapping information covering only part of the support in that direction.

2.2.3.4 Phase reconstruction algorithms

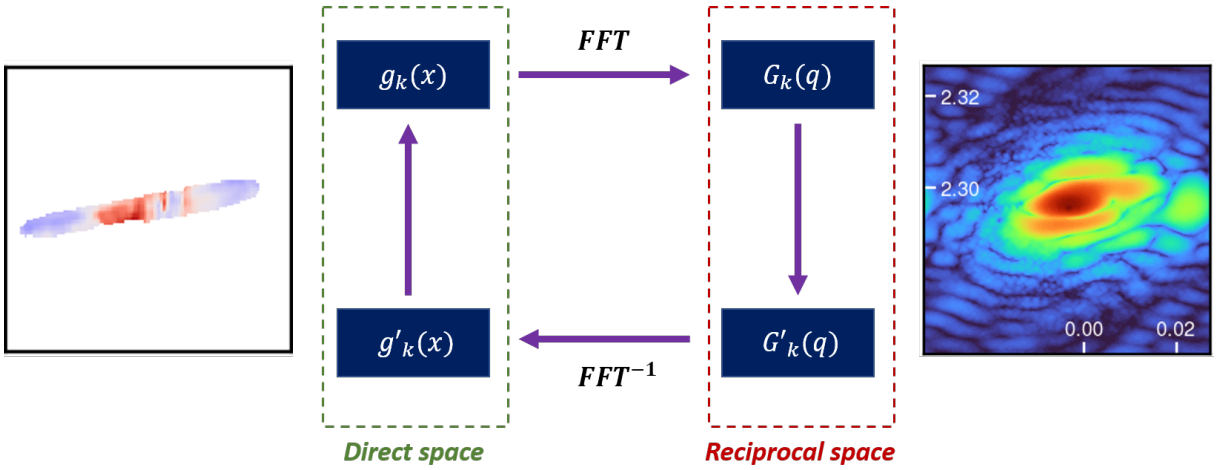

Figure 2.19: General functioning of the inversion algorithm

The basics of these phase retrieval algorithms were laid out by [139, 140]. It is an iterative process between the real space and the reciprocal space using Fast Fourier transforms (FFT) and inverse FFTs (FFT^{-1}) to reduce the errors. First, a random phase is assigned to the amplitude (i.e. the square root of the measured intensity). For the first loop of iteration, a complex object is calculated from the FFT^{-1}. This initial estimation or reconstructed amplitude does not necessarily have the form of the real object. An upper limit of the modulus is defined where the electron density on the outside is set to 0, also called "support", while the phase remains unchanged. With this corrected object, the reciprocal amplitude is recalculated by Fourier transform. The resulting diffracted amplitude often does not perfectly match the measured amplitude, so it is replaced by this measured amplitude. By iterating between the direct space and the reciprocal space, this error reduction (ER) algorithm seeks to reduce the error between the measured amplitude and the reconstructed amplitude. However, it does not always converge and it may also become stuck in a local minimum.

In order to improve the phase retrieval, other algorithms have been developed which will be briefly introduced below :

- **Shrink-wrap :** This algorithm dynamically adjusts the "support," or the region of

interest, during iterative phase retrieval. Initially, a rough estimate of the object's boundary is used as the support. As iterations proceed, the algorithm updates this boundary based on the reconstructed image to refine the region containing the object, effectively reducing artifacts[141]. It starts with an initial guess for the support (S). Then it uses a Fourier constraint to refine the object in reciprocal space and updates the support by thresholding the real-space amplitude of the object:

$$S_{n+1} = \{x || \psi(x)| > \alpha \max(|\psi(x)|)\} \tag{2.61}$$

where $\psi(x)$ is the reconstructed wavefield, and α is a threshold parameter.

- **Hybrid Input-Output (HIO) :** The HIO algorithm alternates between enforcing constraints in reciprocal and real space to iteratively refine the phase. It is an improvement over basic iterative Fourier transform algorithms, incorporating feedback to avoid stagnation[142]. The update rule in real space is:

$$\psi_{n+1}(x) = \begin{cases} \psi_n(x) & \text{if } x \in S \\ \psi_n(x) - \beta[\psi_n(x) - \psi_n^{\text{prev}}(x)] & \text{if } x \notin S \end{cases} \tag{2.62}$$

Here, $\psi(x)$ is the reconstructed field, S is the support, and β is a feedback parameter.

- **Relaxed Averaged Alternating Reflection (RAAR) :** The RAAR algorithm combines the features of HIO with additional stability by weighting real-space updates. It is useful for datasets with noise or imperfect measurements[143]. The update rule:

$$\psi_{n+1}(x) = (1-\beta)P_R(\psi_n(x)) + \beta P_S(\psi_n(x)) \tag{2.63}$$

where P_R is the projection operator in reciprocal space, P_S is the support projection, and β is a relaxation parameter.

2.2.3.5 Experimental setup

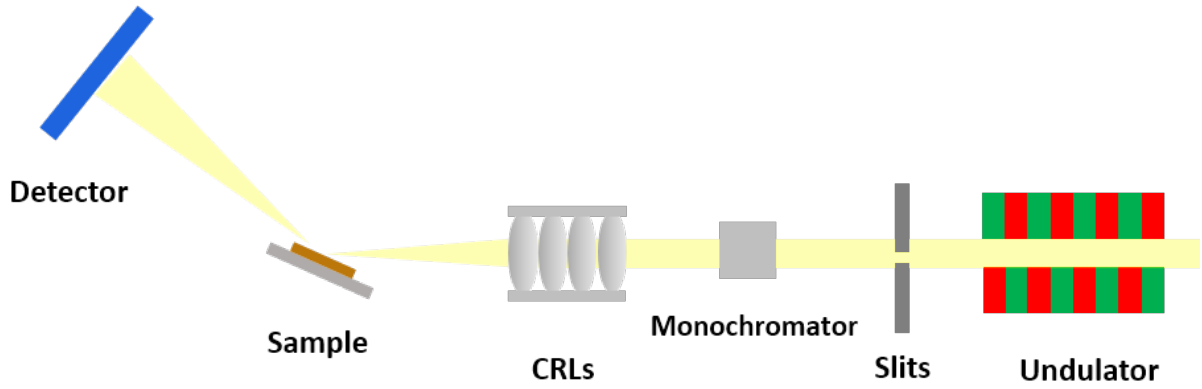

Figure 2.20: Simplified schematic of the Bragg coherent diffraction imaging setup

During this thesis, BCDI experiments were performed at three different beamlines, P10 at PETRA III, ID01 at ESRF, and SIXS at SOLEIL. The general setup for a coherent diffraction beamline is illustrated by the ID01 beamline at ESRF[144]. This beamline contains an undulator as source followed by a set of slits to collimate the incident X-ray beam (Fig. 2.20). The wavelength, respectively, the energy of the X-rays is selected using a Si 111 double-bounce monochromator with an energy resolution of approximately $\Delta E/E \approx 10^{-4}$. This setup provides a longitudinal coherence length of around 600 nm considering an X-ray energy of 10 keV. The transverse coherence length at this beamline is about 300 µm (V) x 60 µm (H). As focusing optics, Be compound refractive lenses are used focusing the X-ray beam down to about 480 nm. A pair of slits are installed right in front of the CRLs in order to select the coherent part of the incident X-ray beam, i.e. the slit aperture is set to for the horizontal and vertical coherence lengths. The sample is mounted on a piezoelectric stage allowing for translations of up to 100 µm with nanometric resolution. This stage itself is installed on top of a hexapod with a stroke of 15 mm. The hysteresis of the motors controlling these translations must be minimal, as it is crucial to keep the incident beam centered on the goniometer's rotation axis to maintain consistent illumination during measurements. Finally, the last component in the setup is a 2D pixelated Maxipix detector, located about 1 meter downstream from the sample. This

detector consists of 516 x 516 pixels with a size of 55 x 55 µm² and an energy detection range of 6 to 15 keV. To reduce air scattering, a "flight tube" can be positioned between the sample holder and the detector. The sample is observed using an optical microscope looking perpendicular on the sample surface.

2.2.4 Electron microscopy techniques

Throughout this study, various electron microscopy techniques, including Scanning Electron Microscopy (SEM), Transmission Electron Microscopy (TEM), and Focused Ion Beam (FIB) microscopy, were employed to characterize the structure and the morphology of ZnO nanowires.

2.2.4.1 Scanning electron microscopy (SEM)/Focused ion beam (FIB)

A scanning electron microscope provides images of the surface of a sample by scanning it with a focused electron beam. It is operated with acceleration voltages typically ranging from 1 to 30 kV. The intensity of the signal collected on various types of detectors is stored as a function of the scanning position. The images obtained can achieve magnifications up to ×500k. In an SEM, various cathodes such as a tungsten filament, a LaB6 crystal, or a Field Emission Gun (FEG) are employed as electron emitters. The emitted electrons are accelerated and focused onto the sample surface by electromagnetic lenses. The electron beam interacts with atoms at different depths within the sample (depth of electron penetration). Among the possible interactions between the electron beam and the sample, one distinguishes backscattered electrons which are scattered inelastically from the sample and thus lose a part of their incident energy, emission of low-energy secondary electrons from the outer layers of atoms, as well as the emission of X-rays, Auger electrons as well as UV and visible photons. Each of these emissions provides specific information about the sample. Here, we are particularly interested in secondary electrons, which enable the construction of an image of the sample's surface by providing information about its topography.

During this thesis, a Gemini SEM 500 70-04 (ZEISS) was used, capable of acquiring images with a spatial resolution of 0.6 nm at 15 kV and 1.1 nm at 1 kV. This SEM is

equipped with a variety of detectors tailored to specific information needs, including In-lens secondary electron (SE), Energy-Selective Backscattered (ESB), High-Energy Secondary Electron (HE-SE), Backscattered Electron Detector (BSD), Aberration-Corrected Scanning Transmission Electron Microscopy (aSTEM), and SE detectors.

Handling and/or bonding of the nanowires was performed in a FEI Nanolab Helios Mod. 600 focused ion beam microscope equipped with an Omniprobe micro-manipulator and a Pt gas injector system (GIS). In this microscope, a SEM column is coupled with an ion beam (Ga) column, allowing to combine ion micromachining with electron imaging. The stage on which the sample was fixed allows for tilted imaging up to 60°. This instrument was employed either to glue the nanowires by electron or ion beam induced deposition (EBID/IBID) of Pt onto specifically-designed nanostructured substrates for synchrotron experiments, or to prepare electron-transparent lamellae for TEM analyses.

2.2.4.2 Transmission Electron Microscopy (TEM)

Transmission electron microscopy (TEM) facilitates the investigation of the crystalline structure of materials and the analysis of volumic defects. Over the past few decades, TEM has benefited considerably from significant technical advancements, including the introduction of new electron sources, aberration correctors, and digital detectors. These improvements have notably enhanced spatial resolution, allowing the study of the local structure of thin samples at atomic resolution.

2.2.4.2.1 Basics of TEM

In this study, a FEI Titan 80-300 transmission electron microscope was employed which is equipped with a CEOS CETCOR geometric aberration corrector for imaging. Thanks to this aberration corrector, which can measure aberrations up to the 5th order and correct them automatically up to the 3rd order, this microscope has a spatial resolution limit of less than 1 Å (for an acceleration voltage of 300kV).

A transmission electron microscope consists primarily of five distinct parts (see Fig. 2.21). The first part is the electron gun, where electrons are generated and accelerated by a stabilized voltage (typically between 60 and 300 kV) to significantly increase their speed which by itself reduce the electron wavelength and thus the spatial resolution.

Various types of electron guns exist depending on the technique used to extract electrons: thermionic emission using tungsten filaments and LaB6 tips, and field emission (FEG, for Field Emission Gun). The microscope used in the present work has a FEG source, which offers the advantage of better spatial coherence and better temporal coherence (i.e. lower energy dispersion).

The second part is the illumination or condenser system, which consists of a set of electromagnetic lenses (C1, C2, mini condenser lens) and diaphragms (condenser diaphragm). This system allows for modification of the sample illumination mode (parallel or convergent beam). The condenser lenses C1 and C2 control the probe size (spot size) and the convergence angle ϑ of the beam on the sample. The role of the condenser diaphragm is to reduce the angular aperture, thereby increasing the coherence of the beam. To change the convergence angle of the beam without needing to switch the condenser diaphragm, the mini-lens is utilized. In some microscopes, including the one used in this study, a third condenser lens C3 is employed to adjust the convergence angle without altering the beam intensity or the size of the illuminated area.

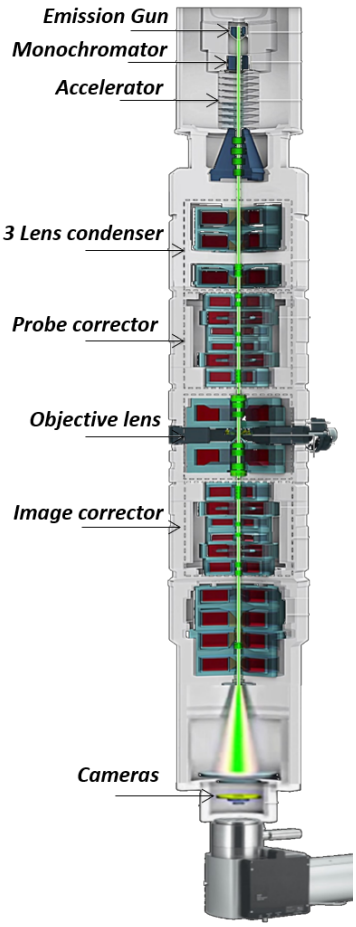

Figure 2.21: Schematic illustrating the FEI titan 80-300 components

Below the condensing system is located the objective lens, divided into two parts (upper and lower objective lenses) and a series of apertures: the contrast (or objective) apertures and the selected area apertures. The sample to be studied is placed in the object plane of the objective lens. By varying the current passing through this lens, the focal distance is slightly adjusted, allowing the desired focusing of the image to be obtained. For conventional TEM imaging, the selection of the electron beam (transmitted or diffracted) used to form the image is made through the contrast aperture, enabling bright-field imaging as well as dark-field imaging. For aberration-corrected high-resolution imaging, all the transmitted and diffracted beams are used to form the image. The selected area aperture allows for electron diffraction studies

of a desired region of the sample.

The following part of the TEM column is the projection system, which consists of intermediate and projection lenses. The intermediate lenses switch between image mode and diffraction mode, depending on whether the object plane of the projection lens coincides with the image plane or the focal plane of the objective lens, respectively.

The fifth and last part is the observation system, which enlarges and projects the image or diffraction pattern obtained by the projection lens. Various detectors can be used, such as a fluorescent screen or a CCD camera. As electrons pass through the sample, some of them lose energy because of inelastic interactions with the material. This information can be utilized for chemical analysis through Electron Energy Loss Spectroscopy (EELS). In the case of the Titan microscope used in this thesis, a magnetic sector spectrometer (GIF) is positioned below the observation screen. Additionally, another spectroscopic technique exists that utilizes the X-rays produced by the de-excitation of atoms excited by electron irradiation provides local chemical information called Energy Dispersive X-ray Spectrometry (EDS).

2.2.4.2.2 HRTEM image formation theory and simulation

In TEM, the formation of an image under the weak phase object approximation (WPOA) assumes that the electron wave interacts weakly with the sample, resulting in minimal changes to the wave's amplitude but significant changes to its phase. This approximation is widely used for thin samples where scattering is limited. The exit wave function of the electron beam after interacting with the sample is expressed as:

$$\psi_0(x,y) = 1 + i\phi(x,y) = 1 + i\sigma V(x,y)t \tag{2.64}$$

Where $\phi(x,y)$ represents the phase shift, σ: Interaction constant, $V(x,y)$: Projected electrostatic potential of the sample, and t: Sample thickness. The image contrast in TEM primarily arises from the phase modulation of the electron wave, which is converted to intensity variations due to the objective lens' transfer function. The final image intensity is a convolution:

$$I(x,y) = 1 + 2\sigma V(x,y)t \otimes s(x,y) \tag{2.65}$$

where $s(x, y)$ is the impulse response of the microscope, related to its phase contrast transfer function (PCTF) $S(u, v)$ in reciprocal space:

$$S(u, v) = A_\delta(u, v)A_\alpha(u, v)\sin(\chi(u, v)) \tag{2.66}$$

$A_\delta(u, v)$ is the temporal coherence damping function, $A_\alpha(u, v)$ is the Spatial coherence damping function and $\chi(u, v)$ is the phase aberration function. In summary, The exit wave function carries the phase information related to the sample's potential and thickness. The objective lens then modifies this wave using its transfer function, which depends on aberrations like defocus and spherical aberration. And finally, the resulting image intensity encodes structural information from the sample, which can be interpreted through simulations or comparison with theoretical models.

High-resolution TEM (HRTEM) imaging is an important part of understanding a material's structure and, more importantly, to study the dislocations in the material. However, it is very often hard to conclude on some types of dislocations and difficulties arise when a mixture of dislocations exists and also when there's a local bending of the sample. This is why the approach taken to help us complete the information, is trough simulating a HRTEM image, in order to conclude on what type of dislocations we are facing. Java Electron Microscopy Software (JEMS), is a simulation software widely used for simulating electron diffraction patterns and high-resolution images. Developed by Pierre STADELMANN [17], JEMS was initially created as an enhancement for understanding and interpreting transmission electron microscopy data, which has made it a reliable tool to visualize and predict electron diffraction patterns and TEM/STEM images.

The key steps in HRTEM image simulation in JEMS are :

- **Providing an object model :** The structure provided for HRTEM simulation is modeled as a crystal lattice (it can be perfect or include dislocations), defined by the lattice constants a, b and c and the atomic positions. *Atomsk* software [145] was used to create these crystal structures and introduce different types of dislocations with variable characteristics (line direction, Burgers vector) (see Fig. 2.22) a).

- **Wavefunction interaction with the model :** The software then simulates an electron wavefunction $|\chi\rangle$ incident on the sample, which interacts with the atoms

as it propagates through the crystal. The interaction is governed by the evolution operator $U(z,0)$, calculated using Schrödinger's equation. This operator evolves the wavefunction slice by slice through the thickness of the crystal, accounting for electron scattering and diffraction by atoms within each slice.

- **Multislice method :** For structures with large unit cells, the multislice approach divides the crystal into thin slices (see Fig. 2.22) b). The electron wavefunction is transmitted through each slice via a phase object approximation and then propagated to the next slice using a Fourier transform-based propagator. The resulting exit wavefunction is the cumulative effect of these sequential interactions.

- **Transfer Function and Image Formation :** After exiting the sample, the wavefunction is transformed by the microscope's Contrast Transfer Function (CTF). The CTF includes terms for defocus C_1 and spherical aberration C_3 and C_5, which affect image sharpness, contrast, and phase contrast in HRTEM images:

$$\chi(q) = \pi\left(C_1\lambda q^2 + \frac{C_3\lambda^3 q^4}{2} + \frac{C_5\lambda^5 q^6}{3}\right) \tag{2.67}$$

  where λ is the electron wavelength and q is the spatial frequency. The transfer function modulates the image contrast by introducing phase shifts in the electron wave. We decided to use the negative C_3 condition for the HRTEM imaging in order go reach the highest possible spatial resolution using our microscope[146].

- **Creation of the final image :** The modified wavefunction, after passing through the CTF, undergoes a Fourier synthesis to create the final HRTEM image (see Fig. 2.22) c). The image intensity is influenced by the specimen thickness, defocus, and other aberrations. In the Weak Phase Object Approximation (WPOA), the image intensity $I(\vec{x})$ is:

$$I(\vec{x}) \sim 1 - 2\sigma V_p(\vec{x}) \tag{2.68}$$

  where $V_p(\vec{x})$ is the projected potential and σ represents the electron-matter interaction constant. This intensity is calculated using the (Eq. 2.65) where the projected potential is deduced from the multislice calculations and the impulse response of the microscope from the phase shift given by the (Eq. 2.67). This approximation helps

in interpreting black and white contrasts based on positive and negative values of spherical aberration.

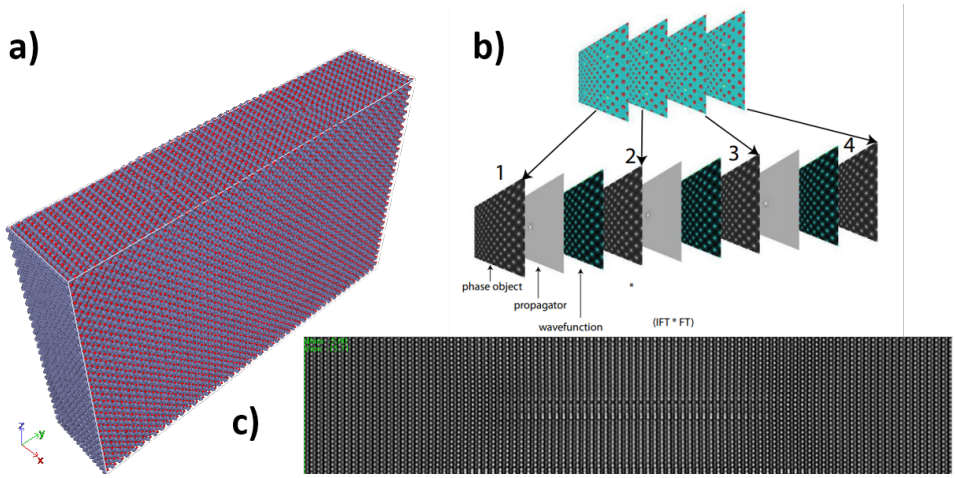

Figure 2.22: a) ZnO Crystal structure created in atomsk serves as an object model for the JEMS simulation. b) The solid is sliced into thin sub-slices [17]. c) Example image of a HRTEM image simulation of the ZnO crystal model with a dislocation loop at the center

2.2.5 AFM SFINX

2.2.5.1 Working principle of an AFM

The Atomic Force Microscope (AFM) is a type of Scanning Probe Microscope (SPM) that allows for the examination of local properties of a sample by scanning it with a mechanical probe. Developed by Gerd Binnig and Heinrich Rohrer at IBM Zurich in 1986 [147], the AFM is nowadays widely used to assess the surface topography of materials. Depending on the specific properties of interest for a given sample, different types of SPMs are used. The basic principle of each SPM bases on the local physical interaction between the probe and the sample: the AFM is used for dimensional/topographical properties, conductive AFM (C-AFM) and Scanning Tunneling Microscopy (STM) to characterize electrical properties [148][149], Magnetic Force Microscopy (MFM) to study the magnetic properties [150], and Piezoresponse Force Microscopy (PFM) to investigate the piezoelectric and ferroelectric properties at the nanoscale [151].

The basic principle of an AFM involves sensing the surface via the interaction between the atoms at the sample surface and a probe tip. This technique offers a resolution on the order of Angstrom [152]. A schematic of the general working principle of an AFM is given in Fig. 2.23. A typical AFM consists of a microfabricated Si cantilever with a pyramid-shaped tip. A laser beam is focused on the extremity of the Si cantilever from where it is reflected to a four-quadrant photodiode.

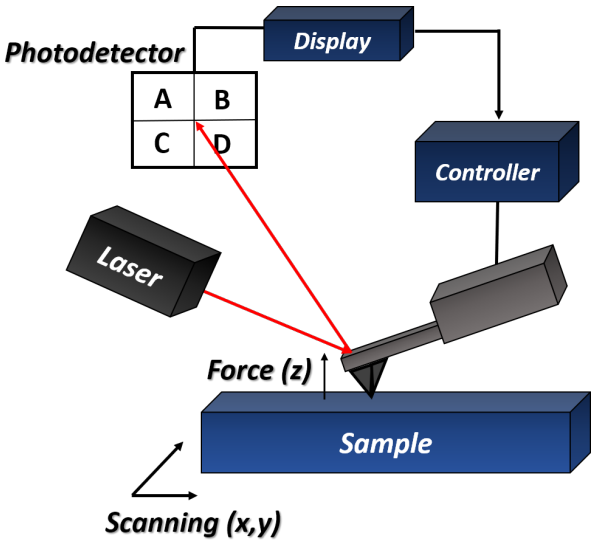

Figure 2.23: Diagram showing the basic working principle of an Atomic Force Microscope (AFM).

The measurement of the position of the laser beam on the photodiode by comparing the intensities between the different quadrants A, B, C, and D allows for determining deflection and torsion of the cantilever. The vertical deflection is given by the signal $(A+B)-(C+D)$, while the torsion (lateral deflection) is represented by $(A+C)-(B+D)$. Considering exclusively the vertical component, the force F acting on the Si-tip can be determined by the cantilever deflection taking into account its effective stiffness k:

$$F = kx \tag{2.69}$$

Therefore, the deflection of the lever reflects the variations in the tip-sample interaction forces. In the absence of an external field, the dominant forces are van der Waals interactions, electrostatic forces as well as capillary and adhesion forces:

- **Van der Waals forces** arise from electromagnetic field fluctuations due to thermal or quantum effects. Theoretical descriptions of these forces are approximated by a sphere-plane configuration with $r \gg z$. In this context, the van der Waals force contribution is given by [153]:

$$F(z) = -\frac{Hr}{6z^2} \tag{2.70}$$

where H is the Hamaker constant, r is the radius of curvature of the AFM-tip, and z is the tip-sample distance. This force is mostly attractive at short distances. For example, for a value of $H \approx 10^{-19}$ J, a tip radius of 15 nm, and a tip-sample distance of 1 nm, the van der Waals force on the tip is about 0.25 nN.

- **Electrostatic forces** are the second major contributor to long-range interaction forces. Depending on the material properties, the tip, and the experimental conditions, these forces can play a significant role. Many models describe the interaction between a tip and a metallic substrate. Additionally, in insulating samples, the presence of charge distributions on both the tip and the sample can lead to electrostatic interactions, which are often modeled using Coulomb's expression in a sphere-plane geometry.

  Consider a charged tip with radius r, represented by a point charge Q positioned above a surface region with a uniform charge density σ and the vacuum permittivity ϵ_0. The resulting electrostatic interaction, when the tip and sample are separated by a distance z, is given by:

$$F(z) = \frac{Q\sigma}{2\epsilon_0}\left[1 - \frac{z}{\sqrt{r^2 + z^2}}\right] \tag{2.71}$$

- **Capillary forces:** In ambient conditions, one of the most important contributing forces in the contact mode are capillary forces. This effect occurs in the contact region between the AFM-tip and the sample where the surface energy is elevated, which makes the vapor in the air condensate forming a capillary bridge.

  Given the orders of magnitude obtained, under ambient conditions the capillary and adhesive forces may dominate the molecular forces in the working range of the AFM.

The spatial extent of the tip's end and the distance between the tip and the sample are two parameters that determine the predominant forces in the AFM acquisition process. Tips generally have a radius of curvature on the order of tens of nanometers. Unlike in scanning tunneling microscopy, where the measured current largely corresponds to the tunneling current from the tip's last atom, in atom force microscopy the signal results from an averaging of interaction forces over hundreds or even thousands of atoms.

The precision of atomic force microscopy lies in the tip's sensitivity to variations in the force field depending on the distance. Constant-force operation guides the tip to follow isoforce contours. Depending on the tip-sample distance, different operating modes of the device are distinguished. On the one hand, the sample surface can be imaged in contact mode where the tip remains in continuous contact with the sample surface while being scanned across the surface. This technique can lead to a wear-out of the AFM-tip depending on the hardness of the sample. On the other hand, dynamic imaging modes where the cantilever oscillates while being scanned across the sample surface. For this purpose, a sinusoidal signal is applied to a piezoelectric actuator causing this cantilever to oscillate mechanically. When the tip approaches the sample surface, the interaction forces between tip and the sample lead to a damping of the oscillator, which results in a reduction of the oscillation amplitude and a shift of the resonance frequency. Within the dynamic modes, it exists the non-contact mode where the tip oscillates near the surface with small oscillation amplitudes (<1 nm) without actually touching the sample and the tapping mode where the oscillation amplitude is >1 nm causing the tip to contact the surface at the peak of each oscillation.

These three modes correspond to different operating regimes and involve different interactions. The tip-sample interaction potential can be roughly modeled by a Lennard-Jones potential, featuring a long-range attractive component, a very short-range repulsive component for tip-sample distances below the Bohr radius a_0, and a transitional region in between (see Fig. 2.24). The Contact Mode operates in the repulsive, short-range regime of contact forces, while the Non-Contact Mode operates in the long-range attractive potential region. The intermittent Contact Mode oscillates between the two aforementioned regimes.

Within the dynamic modes, one can distinguish between three different modes[154, 155]:

- **Amplitude modulation (AM) :** In AM-AFM, the cantilever oscillates near its

resonance frequency. The oscillation amplitude serves as the feedback parameter to maintain a constant interaction between the tip and the sample surface. This mode is widely used due to its ability to minimize damage to soft samples and provide a good resolution for surface imaging.

- **Frequency modulation (FM) :** FM-AFM operates without touching the sample and by detecting shifts in the cantilever's resonance frequency caused by tip-sample interactions. A phase-locked loop is utilized to continuously adjust the excitation frequency, ensuring the cantilever oscillates at its resonance frequency. This mode is particularly advantageous for achieving atomic-scale resolution and is effective in ultra-high vacuum environments.

- **Phase-locked loop (PLL) :** A PLL is an electronic control system that synchronizes the phase of the cantilever's oscillation with an external reference signal. In AFM, PLLs are important to FM-AFM operations, enabling precise tracking of resonance frequency shifts due to tip-sample interactions. This facilitates accurate measurements of surface properties, including potential variations and mechanical characteristics.

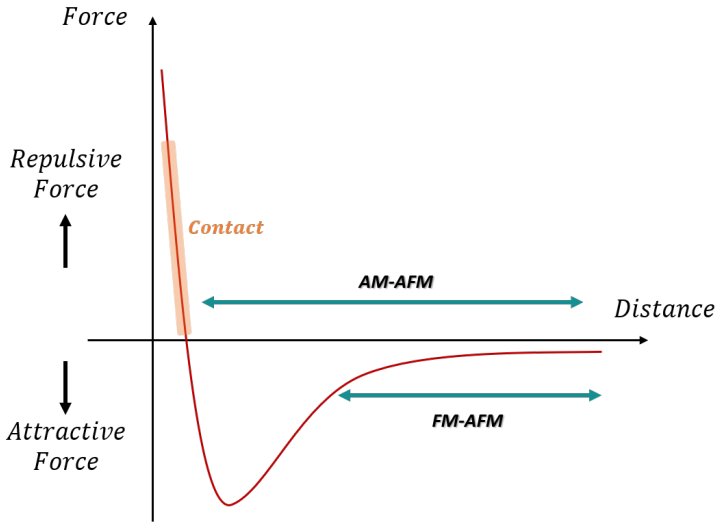

Figure 2.24: Contact mode AFM continuously operates in the repulsive force regime, where the tip of the AFM remains in physical contact with the sample. In amplitude modulation (AM) mode, the AFM lever oscillates with large amplitudes, sweeping across a wide range of distances, including both attractive and repulsive regimes. Conversely, frequency modulation (FM) mode typically uses small oscillation amplitudes, focusing on detecting force gradients, particularly in the attractive range near the sample surface.

2.2.5.2 SFINX setup

The Scanning Force Microscope for In Situ nano-focused X-ray (SFINX) was custom-designed by the MNO research team to be mounted on synchrotron goniometers, particularly on the ID01 and BM32 beamlines. It is both compact and lightweight, with dimensions of $10 \times 10 \times 10$ cm^3 and a weight of about 500 g. Beyond its small size, ease of use was a priority for integration into the crowded and constrained experimental environments typical of synchrotron end-stations. The microscope is operated using a Phase-Locked Loop (PLL), ensuring precise control and stability during imaging. To protect the sample, the tapping mode was chosen for imaging. This mode is significantly gentler than the contact-mode enabling detailed imaging while minimizing sample damage [156]. Non-contact mode is also less suitable because it provides lower resolution for for our samples, as its reliance on long-range forces makes it less effective for detailed topographical mapping.

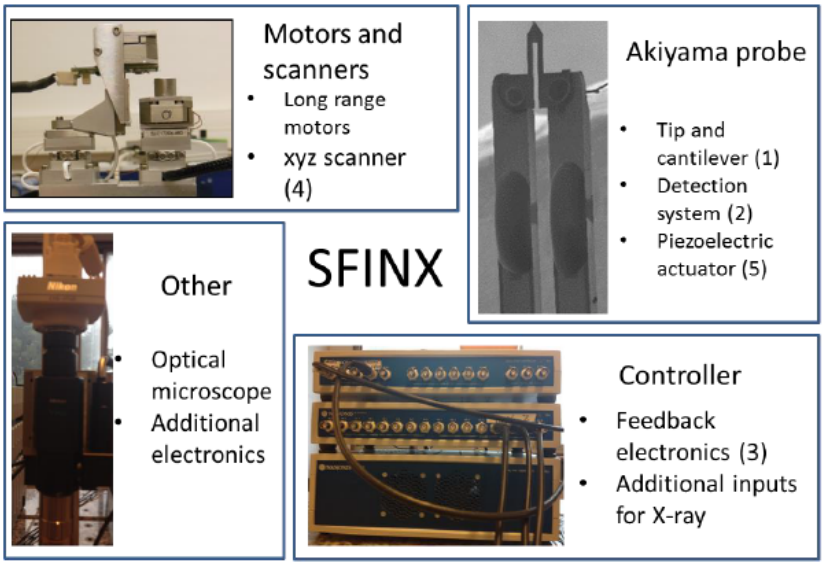

Figure 2.25: Parts of the SFINX AFM tool[18]

In the following the main parts of SFINX will be briefly introduced.

- **Piezoelectric motors:** A standard AFM consists of piezoelectric actuators in the x and y directions for the sample holder and a vertical scanner (z) for the AFM tip. In addition to these kinds of piezoelectric scanning stages with a stroke of 40 µm in x and y and 24 µm in z, SFINX features two long-range piezoelectric actuators for x and y translations (12 mm) beneath the sample holder, and two more identical x and y motors beneath the AFM-head, along with a third stage for vertical movements of the AFM-tip. These 5 long-range piezoelectric motors allow to separately aligning a selected nanostructure and the AFM-tip with an incident X-ray beam in case of *in-situ* synchrotron X-ray diffraction experiments.

- **Akiyama probe:** For reasons of compactness, the self-sensing and self-actuating Akiyama was chosen. This probe consists of a quartz tuning fork coupled with a silicon cantilever. Typically used in dynamic mode, the probe operates without a piezoelectric actuator. Instead, an electrical control signal is applied to the tuning fork's electrodes, causing its two prongs to vibrate horizontally in antiphase. This motion induces mechanical stress in the silicon cantilever, translating into vertical oscillations of the tip. When approaching a surface, interactions between the tip and

the sample alter the resonance characteristics of the entire system. These resonance changes are monitored by measuring the electrical impedance of the tuning fork, which serves as the feedback mechanism. Consequently, no additional detection system or piezoelectric actuator is needed for AFM imaging. This design not only makes the system compact but also facilitates the integration of SFINX with various diffraction techniques.

- **AFM calibration:** Each set of Akiyama probes comes with manufacturer-supplied specifications, such as resonance frequency and expected quality factor, while the stiffness constant is assumed to be the same for all probes. However, upon replacing the probe, it is essential to recalibrate the feedback loop by accurately determining the probe's specific resonance frequency. Achieving maximum precision in this frequency improves the quality factor, resulting in sharper and more accurate topographical images of the sample. To calibrate, the vertical oscillation amplitude and phase are analyzed over a broad frequency sweep of the tuning fork. Once the resonance frequency is roughly identified, narrower frequency sweeps are performed to refine the measurement. If the amplitude peak appears asymmetric, this is corrected to ensure a sharp phase jump, which is crucial for proper feedback performance. Adjustments are made manually using a small potentiometer on the preamplifier located on the AFM head, fine-tuning the parasitic capacitive resistance. Once the feedback loop is configured, the tip's oscillations can be excited effectively, allowing for accurate AFM imaging.

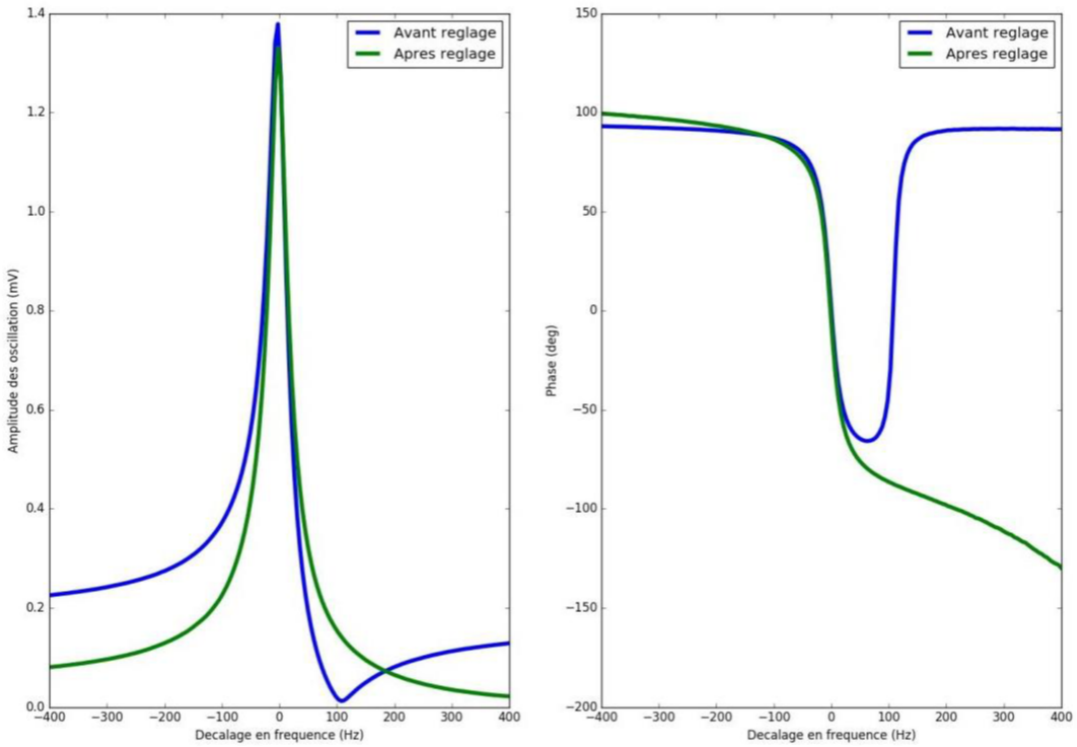

Figure 2.26: a) Oscillation amplitude and b) phase during a frequency sweep of ±400 Hz, measured before and after adjusting the parasitic capacitance.[19]

Chapter 3

In situ three-point bending tests on ZnO NWs

This chapter reports on the nanomechanical behavior of piezoelectric semiconductor ZnO nanowires (NWs) studied by three-point bending test using the custom-built atomic force microscope "SFINX" in combination with *in situ* Laue microdiffraction. Laue microdiffraction was performed at the French CRG-IF beamline BM32 at the European Synchrotron ESRF in Grenoble (France). The experimental setup at this beamline is described in detail in (chapter III 3.22). This chapter will describe the steps taken and analysis done in order to explore the nanomechanical behavior of ZnO NWs, highlighting the size effects observed in coherence with related studies and some interesting mechanical behavior on ZnO NWs.

3.1 Sample preparation

High-quality ZnO NWs with a diameter of about 200 nm and a length of 10 µm were provided by the FunSurf group of C. Ternon at the LMGP in Grenoble. The nanowires were fabricated by a hydrothermal process[99, 100]. Firstly, a ZnO seed layer was deposited on a Si (100) substrate using a sol-gel procedure that enables to selectively tune the mean grain size, surface coverage rate, and texture coefficient of the ZnO layer. Then, ZnO NWs were grown on this ZnO layer by hydrothermal synthesis at ambient pressure using

an optimized protocol. More details on the fabrication can be found elsewhere [101]. A scanning electron micrograph of a dense forest of ZnO NWs is presented in Fig. 3.1. The as-grown nanowires measure between 200 and 300 nm in diameter and are 1.5 to 4 µm long.

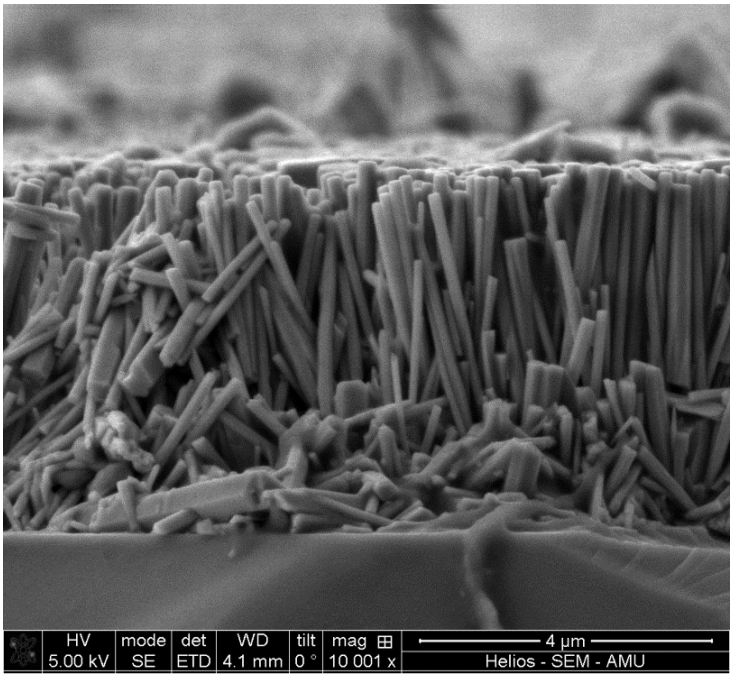

Figure 3.1: Scanning electron microscopy image of the cross-section of a sample containing a dense forest of ZnO NWs on top of a Si substrate.

The ZnO NWs were then detached from the growth substrate by submerging the sample in absolute ethanol and using ultrasonication which also lead to their fracture into few micrometer long sections and their dispersion in the ethanol solution. The solvent containing ZnO NWs was then drop-casted on a Si substrate patterned lithographically with 2 µm wide and 1 µm deep micro-trenches. Some of the NWs cross these micro-trenches forming suspended nanobridges (see Fig.3.2). These suspended NWs were then thoroughly attached at both ends by electron-beam-induced deposition of Pt in a focused ion beam (FIB) microscope (see Fig. 3.2).

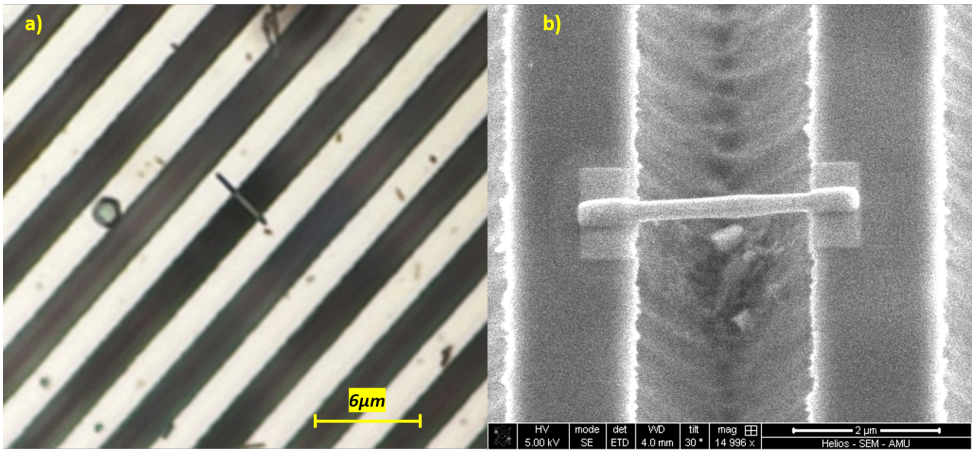

Figure 3.2: a) Optical microscope image of a drop-casted suspended ZnO NW across a Si microtrench. b) SEM image of a suspended ZnO NW embedded by Pt at the extremities.

3.2 Sample alignment

The sample was mounted so that the trenches were oriented parallel to the incident X-ray beam. Thus, the nanowires crossing the micro-trenches are oriented almost perpendicular to the X-ray beam direction. Considering the X-ray beam footprint on the sample surface, due to the inclination of 40° of the sample with respect to the incident beam, this configuration provides the best spatial resolution on the NW at this experimental setup. The AFM head is oriented perpendicular to the incident beam direction to minimize its interference with the incident or the diffracted X-ray beam. For *in situ* three-point bending experiments, the custom-built *in situ* AFM "SFINX", was installed on the *xyz*-translation stage of the conventional Laue microdiffraction setup. The SFINX Si-tip and the focused polychromatic X-ray beam were aligned with respect to a selected suspended ZnO NW by atomic force topography imaging in tapping mode and mapping of the $Pt - L_3$ and the $Zn - K_\alpha$ fluorescence yield, respectively. For a first coarse alignment, the AFM-tip is positioned close to the location of one of the suspended ZnO NWs using the optical microscope available at the BM32 beamline (see Fig. 3.3 a)). As can be seen on the Laue microdiffraction pattern displayed in Fig. 3.3(b), almost half of the sCMOS detector is shadowed by the AFM-head that blocks a part of the X-rays diffracted from the sample. Despite this partial shadowing, sufficient Laue spots of the ZnO NW are recorded allowing

for the eventual indexation of the Laue microdiffraction patterns (see Fig. 3.3) b).

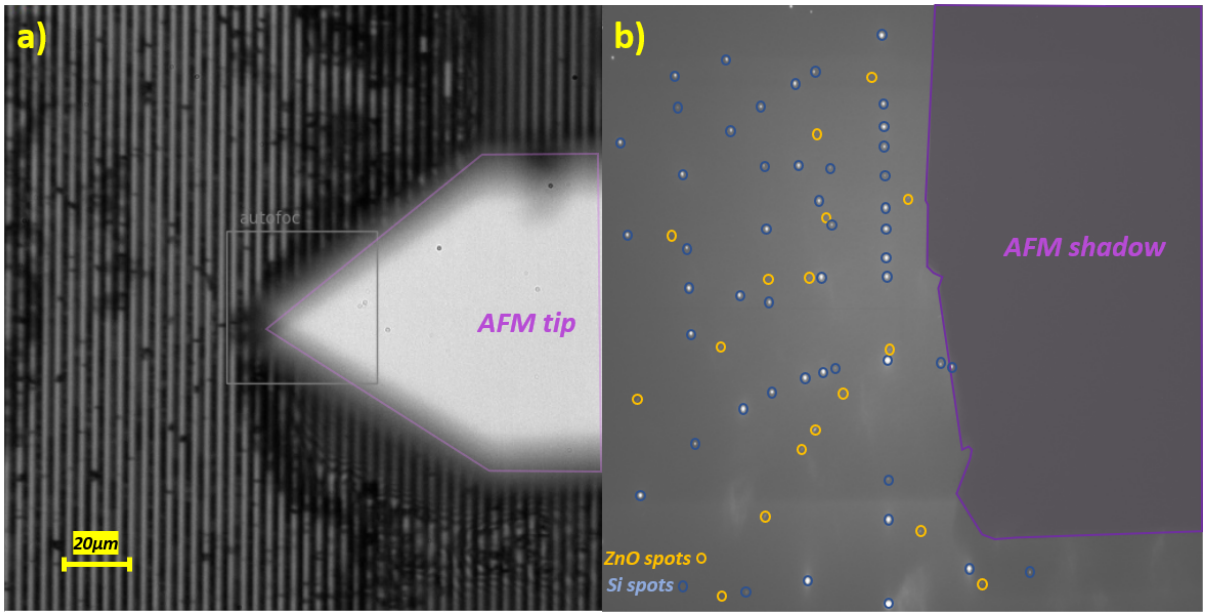

Figure 3.3: a) Optical microscopy image of the microstructured Si substrate with ZnO NWs and the AFM-tip close to the sample surface. b) Laue microdiffraction pattern of a ZnO nanowire on the Si substrate partially shadowed by the AFM-head. The Laue spots corresponding to the ZnO NW and the Si substrate are highlighted by orange and by blue circles, respectively.

While the AFM-head blocks a part of the diffracted X-ray beam, the absorption by the AFM-tip itself is negligible. The X-ray transmission of a similar AFM Si-tip was recorded by [21] using a monochromatic X-ray beam with an energy of 8 keV at the ID01 beamline at ESRF. As illustrated in Fig. 3.4, the Si cantilever absorption can be up to 35%, while the AFM-tip can be as low as 2%. Considering that the polychromatic X-ray beam used for Laue microdiffraction covers an energy range from 5 to 25 keV, the absorption by the AFM-tip can be neglected in particular for the higher energies.

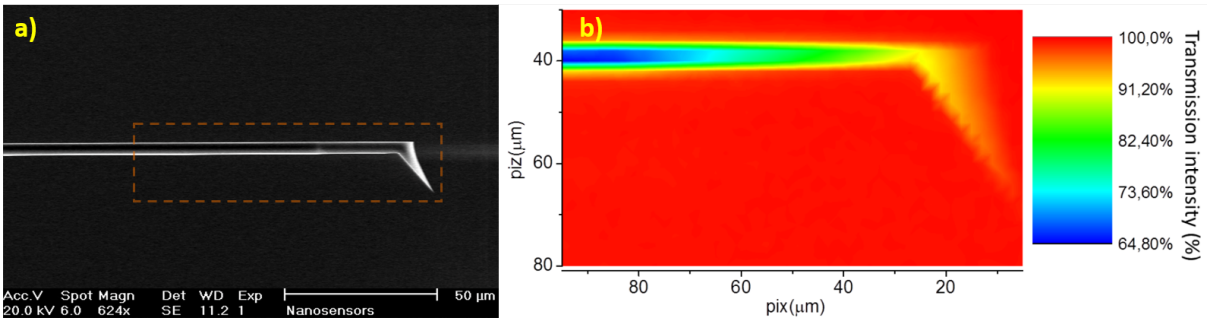

Figure 3.4: a) Side profile SEM image of the Akiyama probe tip [20]. b) X-Ray transmission mapping of the AFM cantilever side profile showing a high transmission at the tip [21]

.

For further alignment of the AFM-tip with respect to the selected ZnO NW shown in the SEM image presented in Fig. 3.5 a), an AFM topography image in tapping mode is recorded (Fig. 3.5) b). In order to align the focused X-ray beam with respect to the ZnO NW, an area of 10 µm x 10 µm is mapped in steps of 200 nm (corresponding to the X-ray beam focal size) in fluorescence contrast recording the $Zn - K_\alpha$ and $Pt - L_{III}$ fluorescence yield by means of the Röntec XFlash 1001 energy-resolved point detector. The fluorescence map is shown in Fig. 3.5(c) highlighting the ZnO NW and the Pt glue. This alignemnt process thus allows for positioning the AFM-tip in he center of the suspended ZnO NW and the focused X-ray beam close to it in order to follow the deformation of the NW during force application using the AFM-tip.

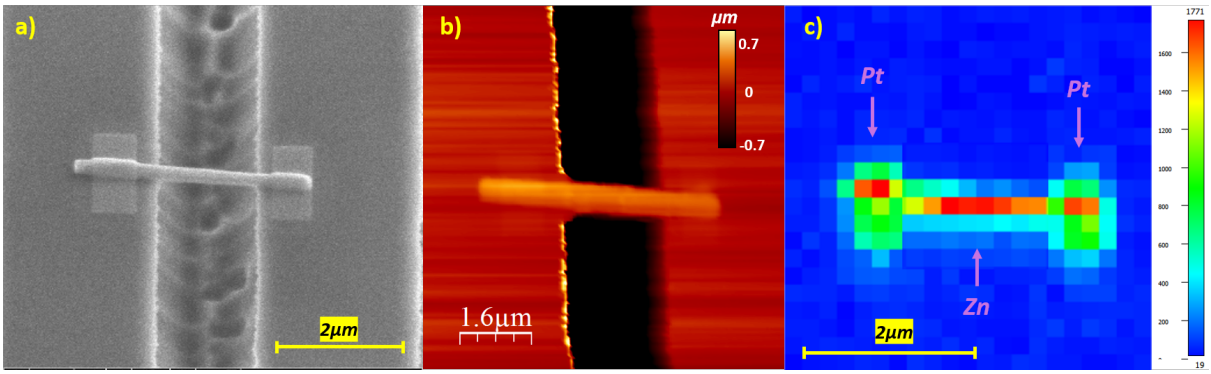

Figure 3.5: a) SEM image, b) AFM topography image, and c) fluorescence map of a ZnO NW. The arrows in part (c) mark the areas related to the $Zn - K_\alpha$ and $Pt - L_{III}$ fluorescence.

3.3 Laue microdiffraction mapping of as deposited ZnO NWs

Prior to any nano-mechanical testing, the as-deposited ZnO NWs were mapped by Laue microdiffraction allowing for determining the orientation of the NWs. As demonstrated by the Laue microdiffraction pattern displayed in Fig. 3.6, the central Laue spot corresponds to the $\{\mathbf{2\bar{2}00}\}$ lattice planes indicating that the NW lies on one of their $\{\mathbf{1\bar{1}00}\}$ side facets. This is coherent with the fact that the growth direction of the NW is along the [0001] axis, which is the characteristic c-axis of the ZnO wurtzite structure. It further gives access to possible deformations prior to mechanical tests. The Laue microdiffraction maps were done around each NW and were recorded in steps of 200 nm with an exposure time of 5 seconds at each step in order to obtain sufficiently intense ZnO Laue spots for the subsequent indexation of the Laue microdiffraction patterns. Fig. 3.7 a) displays a scanning electron microscopy image of a suspended ZnO NW overlaid with a grid representing the measurement positions.

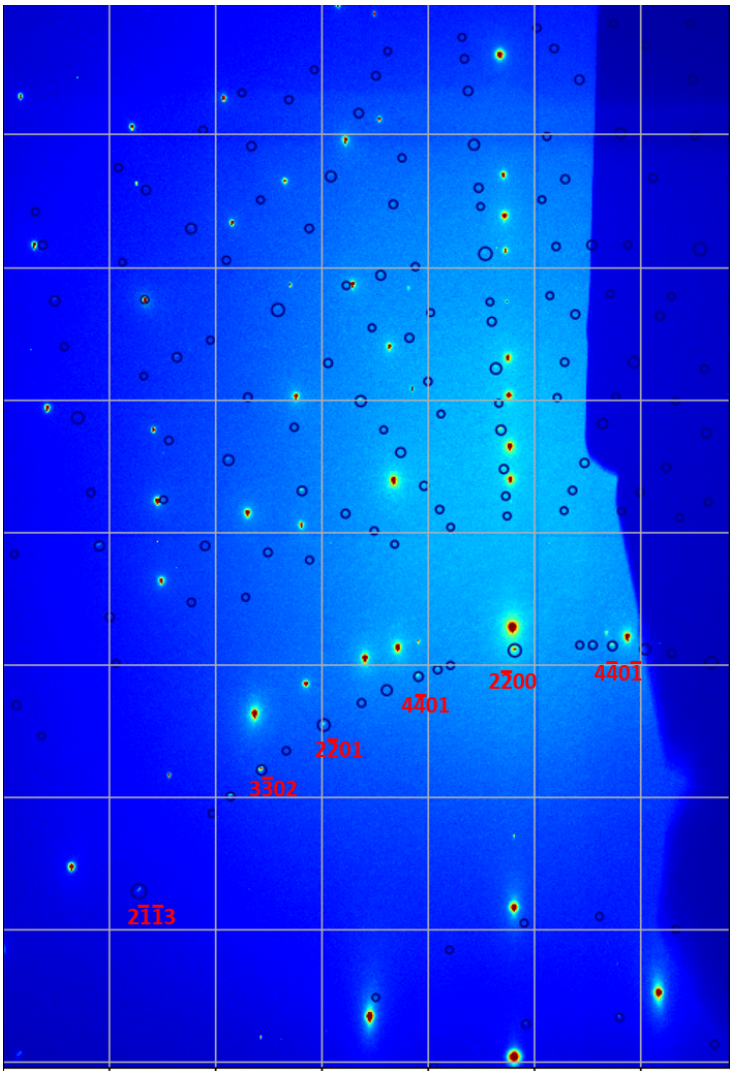

Figure 3.6: Laue diffraction pattern of a suspended ZnO NW on a Si substrate, showing Laue diffraction spots.

For the ease of visualization only one diffraction peak, here the ZnO $\mathbf{3\bar{3}02}$ Laue spot, is displayed in Fig. 3.7) c). The result is a spatial map that helps to illustrate the variation of the crystal orientation and the peak shape for different positions. This indicates variations either in strain gradients or in defect concentrations in different regions of the nanowires. Thus, specific orientations or strain in the scanned region can be interfered from the diffraction pattern, by indexing each diffraction pattern from each measurement position, per example the central ZnO spot is $\mathbf{2\bar{2}00}$ which is a facet of the NW.

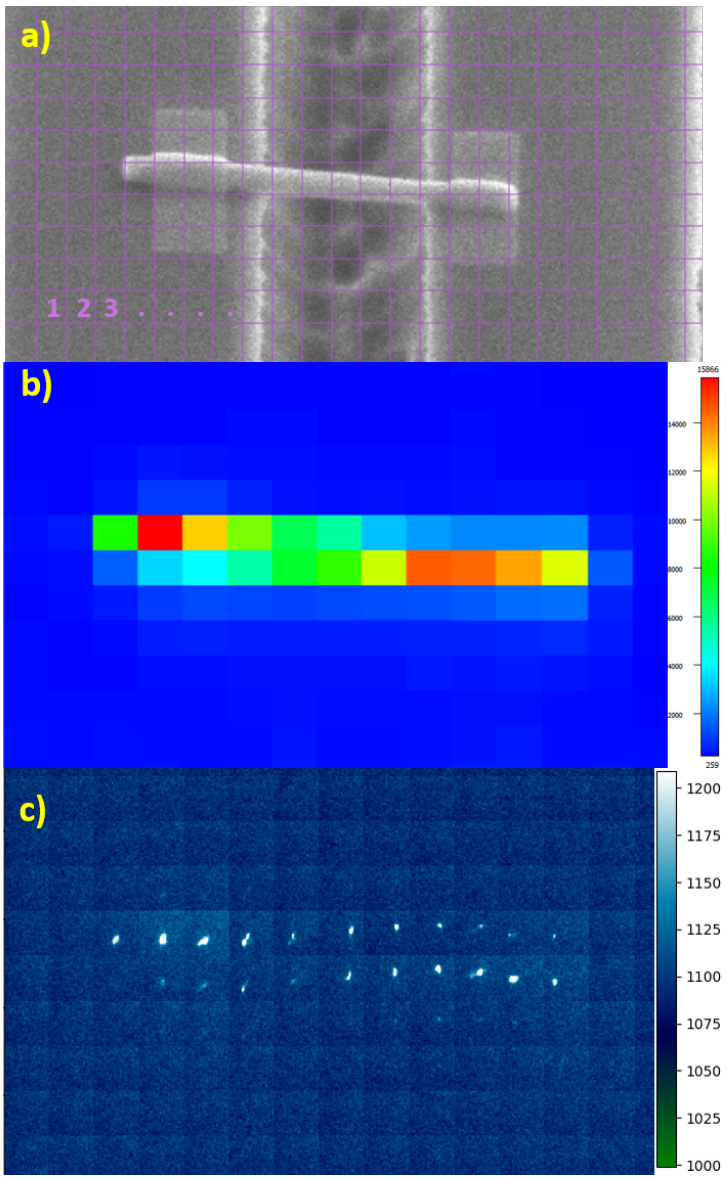

Figure 3.7: a) SEM image of a suspended ZnO NW before nanomechanical testing superposed with a grid representing the measurement steps during the mapping of the NW using the $Zn - K_\alpha$ fluorescence and Laue microdiffraction. b) Fluorescence mapping of a suspended ZnO NW c) Laue microdiffraction mapping of the $\mathbf{1\bar{1}01}$ diffraction spot of the same ZnO NW

The two lines of diffraction spots come from the fact that the step size of 200 nm between the different measurement positions is smaller than the beam focus of 300 nm and, thus the NW is actually measured twice.

3.4 In-situ three-point bending tests

The nano-mechanical properties of suspended ZnO NWs were investigated by *in situ* three-point bending tests using the "SFINX" AFM in combination with Laue microdiffraction. The diffraction patterns were recorded before, during, and after these tests in order to analyze the NW elastic, as well as plastic deformation. The diffraction patterns before the experiment serve as a reference. Laue microdiffraction during and after the mechanical test give access to the in-situ deformation and the post-mortem state of the ZnO NW, respectively. In addition, post-mortem SEM and TEM were performed to further analyze the mechanically deformed NWs and to further elucidate possible plasticity in ZnO at the nanoscale. In this section, the results of five different ZnO NWs will be discussed. As will be shown hereafter, these nanowires behaved differently showing fully elastic deformation, plasticity with the storage of dislocations, and brittle fracture.

Here, four ZnO NWs were studied which are called from here on NW (I, II, III, and IV). The NWs parameters length, suspended length, diameter and misorientation angle of the NW with respect to a perpendicular crossing of a trench are summarized in the table below.

Nanowire number	**length (µm)**	**suspended length (µm)**	**diameter (nm)**	**NW angle (°)**
I	3.8	1.8	213	3.7
II	5.27	2.5	195	18
III	6.2	2	265	5
IV	6.2	2.5	130	35

Table 3.1: The studied ZnO nanowires in this work and their parameters

3.4.1 Force calibration

The custom-built AFM "SFINX" lacks a direct measurement of the applied force due to the absence either of an optical laser feedback like in ordinary AFMs or a deflection sensitive Si cantilever. In order to circumvent this shortcoming the deflection of the Si cantilever of the Akiyama probe was determined directly by Laue microdiffraction [157] during the testing of the NW IV. Therefore, the incident polychromatic X-ray beam was

focused on the Si-tip during the three-point bending of the ZnO NW IV staying within the elastic regime of the nanostructure (see inset of Fig. 3.8). The displacement of the Si Laue spots on the detector was monitored and the rotation angle α of the Si lattice planes of the SFINX-tip (which coincides with the rotation of the lattice planes of the cantilever as a whole) during the mechanical loading was inferred from the UB orientation matrices obtained by the indexation of the Si Laue microdiffraction patterns.

To extract the applied force by the Si cantilever on the ZnO NW, the Euler-Bernoulli beam theory is employed, where the deflection (δ) of the cantilever beam under an applied force (F) is calculated using:

$$\delta = \frac{FL^3}{3EI} \tag{3.1}$$

Here, L is the length of the cantilever, E is its Young's modulus, and I is the moment of inertia.

The rotation angle of the Si cantilever, which is measured by Laue microdiffraction, is directly related to the applied force.

$$\alpha = \frac{FL^2}{2EI} \tag{3.2}$$

By substituting the deflection equation into the expression for rotation, we find a simple relationship between the rotation angle and the cantilever deflection:

$$\delta = \frac{2}{3} L \cdot \alpha \tag{3.3}$$

Considering the length of the cantilever of $L = 300$ µm and the cantilever stiffness of $k = 5$ N/m (as provided by NanoAndMore GmbH), the applied force F was inferred from the rotation angle of the Si-tip lattice planes as described in ref [157]:

$$F = \frac{2}{3} L \cdot \alpha \cdot k \tag{3.4}$$

Due to the fact that the piezoelectric stage is actually open-loop, the real speed of the loading and unloading varies by about 4%. This discrepancy was taken into account resulting in a loading-unloading curve that overlaps almost perfectly (in contrast to ref [157]) as presented in Fig. 3.8. The interaction of the SFINX-tip with the NW is

characterized by an intermediate contact during the first 500 nm of movement of the piezoelectric stage after the first interaction between NW and tip. Once a strong physical contact is established, the applied force increases linearly with the displacement z of the piezoelectric stage. During unloading the intermediate contact range is prolongated by about 250 nm due the adhesion of the SFINX-tip to the NW before the tip completely detaches from the nanostructure. The linear part of the loading-unloading curve with a slope of 5 µN/µm (which agrees very well with the stiffness value provided by the manufacturer) is used as calibration for the applied force for all following three-point bending experiments on NWs with similar diameters (considering similar NW stiffness) where solely the displacement of the piezoelectric stage after the first contact of the SFINX-tip with the studied NW is known. Considering both the intermediate contact regime and the intersection of the extrapolated linear part of the loading-unloading curve with the x-axis, leads to an uncertainty of the definition at which point the Si-tip is in hard contact with the NW. This uncertainty results in an error of 0.74 µN in the absolute value of the applied force while the relative variations of the force can be measured with a very high accuracy of 114 nN.

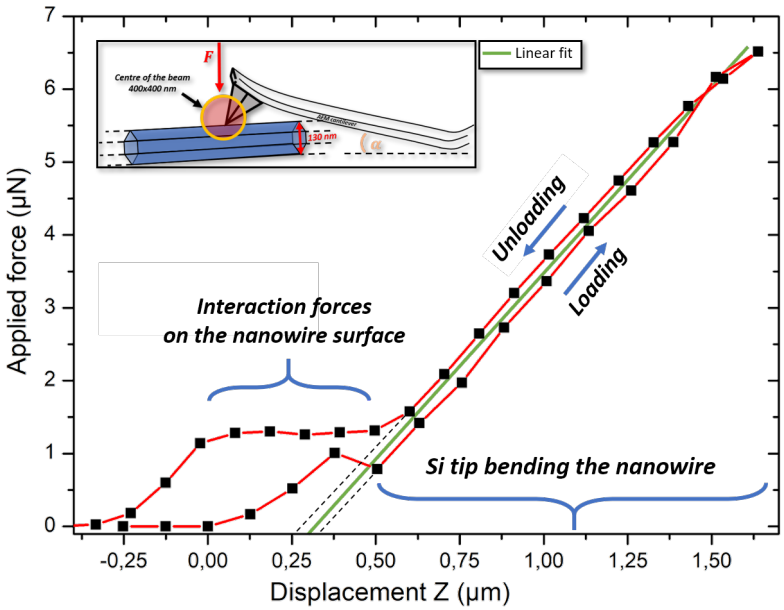

Figure 3.8: Applied force as a function of the displacement of the piezoelectric stage carrying the Si cantilever inferred from the rotation angle of the Si lattice planes of the SFINX-tip.

3.4.2 Three-point bending

To determine the deformation of ZnO NW I during three-point bending tests, the rotation angle of the three orthogonal lattice planes (0002), $(0\bar{1}10)$, and $(2\bar{1}\,\bar{1}0)$ were inferred from the Laue microdiffraction patterns recorded *in-situ* during the mechanical loading-unloading cycles (Fig. 3.9) in a suspended region of the NW of a width that corresponds to the beam size. While for a perfect three-point bending test solely the orientation of the (0002) and $(0\bar{1}10)$ lattice planes are affected, an additional rotation of the $(2\bar{1}\,\bar{1}0)$ lattice planes is detected indicating the presence of a NW torsion. This angle of torsion, which might originate from a non-central application of the force on the NW top facet or other factors, is about 4 times smaller than the NW bending angle itself. The fact that the rotation angles for all three lattice planes return to their initial values within the experimental error bars after complete unloading, indicates a fully elastic behavior. This is supported by the shape of the Laue diffraction spots which is the same before and after mechanical loading (as demonstrated per example for the ZnO $\mathbf{0\bar{1}10}$ Laue spot in Fig.

3.9), thus confirming that no defects were introduced and stored in the material in the probed volume.

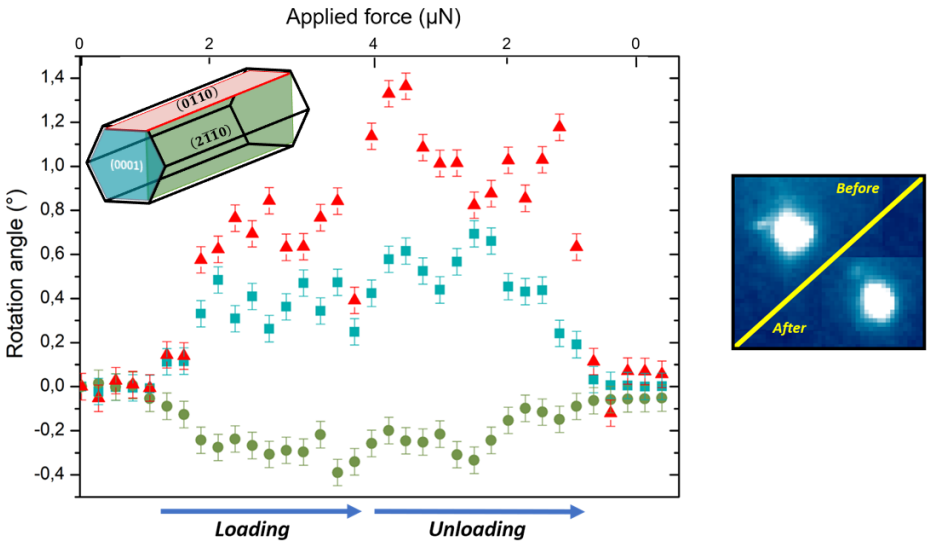

Figure 3.9: a) Rotation angles the three orthogonal lattice planes (0002) (□), $(0\bar{1}10)$ (△), and $(2\bar{1}\,\bar{1}0)$ (◯) in ZnO NW I during three-point bending. The inset shows the crystalline orientation of the NW with its growth direction along [0001] lying flat on one of its $(0\bar{1}10)$ side facets. b) The ZnO $(0\bar{1}10)$ Laue spot before and after the three-point bending test demonstrating that no plasticity was actually induced within the probed volume.

3.4.3 Comparison of calculations using classical Euler-Bernoulli beam theory and finite-element method simulations

The bending of the ZnO NWs was calculated using the Euler-Bernoulli beam theory for a double-clamped beam (equation 3.5) and compared to finite element method simulations using COMSOL Multiphysics, in the FEM simulations we took into account the elastic anisotropy.

$$\Delta_{\max} = \frac{FL^3}{192EI} \tag{3.5}$$

For the computations, a maximum force of $F = 2.50\mu N$, a suspended length of $L = 2.5\mu m$, a Young modulus of $E = 150GPa$, and a NW diameter of $d = 213$nm are taken

into account. The moment of inertia for a beam with a hexagonal cross-section amounts to $I = 0.06014 \cdot d^4$.

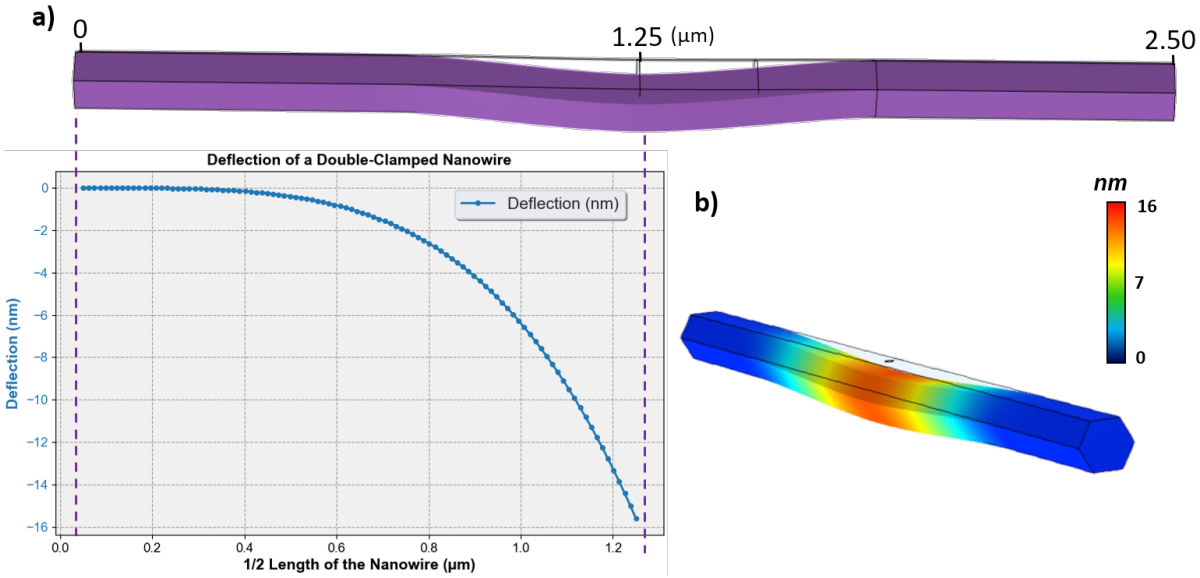

Figure 3.10: a) Theoretical calculation of the NWs deflection using Euler-Bernoulli beam equation b) FEM simulation in COMSOL showing the deflection value of a NW with same parameters

The beam deflection along the nanowire length is presented in Fig. 3.10. The maximum deflection was calculated to amount to 16 nm and 15 nm using the Euler-Bernoulli beam bending theory and FEM simulations, respectively.

The validity condition of the Euler-Bernoulli equation however stays correct only if we always assuming that the force applied by the AFM tip is roughly at the center, and that the deflection remains small compared to the radius of the nanowire to ensure linear elastic behavior. Significant deviations arise when these conditions are violated, requiring consideration of geometric nonlinearities or additional effects. Fig. 3.11 illustrates the beam deflection at the center of the suspended nanowire as a function of the applied force. While the Euler-Bernoulli theory provides a reasonable approximation under small deflections, FEM simulations capture more complex effects, highlighting the limitations of the simplified theoretical model.

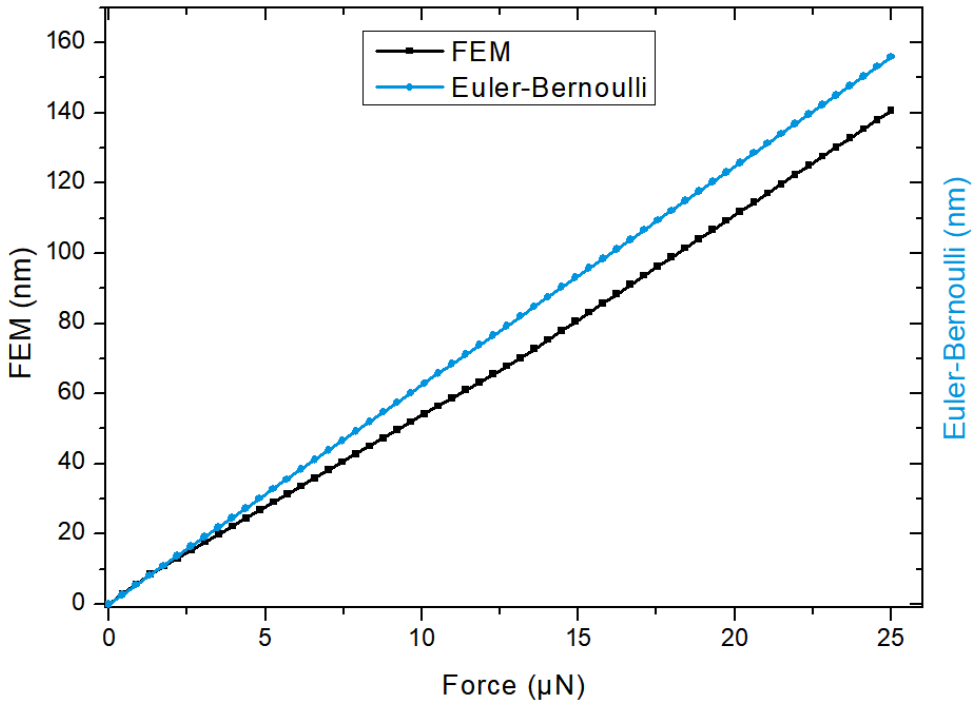

Figure 3.11: Comparison of FEM simulation and theoretical calculations using the Euler-Bernoulli beam deflection equation for an applied force of 25 µN. The theoretical model closely matches the FEM results for small deflections, after which it starts to diverge.

Considering the range of forces applied in the experiments and the resulting deflections of 4 to 15 nm, geometric nonlinearities are negligible although they were taken into account in all simulations described above.

3.4.4 Fracture

The fracture strength, defined as the maximum stress a material can withstand before failing, was determined for ZnO NW II using a three-point bending test until fracture occurred. As in the previous case, the three orthogonal lattice planes (0002), $(0\bar{1}10)$, and $(2\bar{1}\,\bar{1}0)$ rotate during mechanical loading indicating bending as well as NW torsion (Fig.3.12). Here, ZnO NW II was loaded up to a force of 5.79 µN (+/- 0.74 µN) before NW fracture occurred as confirmed by *post mortem* SEM imaging (see inset of Fig.3.12). Note that while the rotation angle of the $(0\bar{1}10)$ and the $(2\bar{1}\,\bar{1}0)$ lattice planes follow each other very closely, they actually deviate from each other for $F > 4.5$ µN. This deviation may

originate either from the slipping of the SFINX-tip on the NW facet or from plasticity in the NW before the actual fracture. Fig.3.12 (b) and (c) present the stress ε_{zz}, respectively, the strain (of the lower NW facet) along x, y and z at highest applied load just before fracture which were simulated by FEM. Here, the NW growth axis is oriented along the y-direction and the loading direction along z. For calculations a circular contact area with a diameter of 15 nm corresponding to the radius of curvature of the SFINX-tip was considered for applying the mechanical load. The maximum bending of the NW just before fracture amounts to 70 nm. The stress and strain are concentrated at the loading point in the center of the suspended NW and close to the two clamping points. The strain ε_{zz} ranges from -1.9 to +1.9%. The stresses σ_x and σ_y in the nanowire's lower facet are found to vary between -1.2 and +0.8 GPa while σ_z ranges from -2 to +3 GPa where 3 GPa corresponds to the fracture strength of the NW. The largest negative stresses for all three components are found close to the clamping positions while the maximum stress is located at the loading position. Inhomogeneous strain distributions in the NW on top of the Si supports close to their edges are visible which are induced by the non-orthogonal crossing of the NW via the micro-trench.

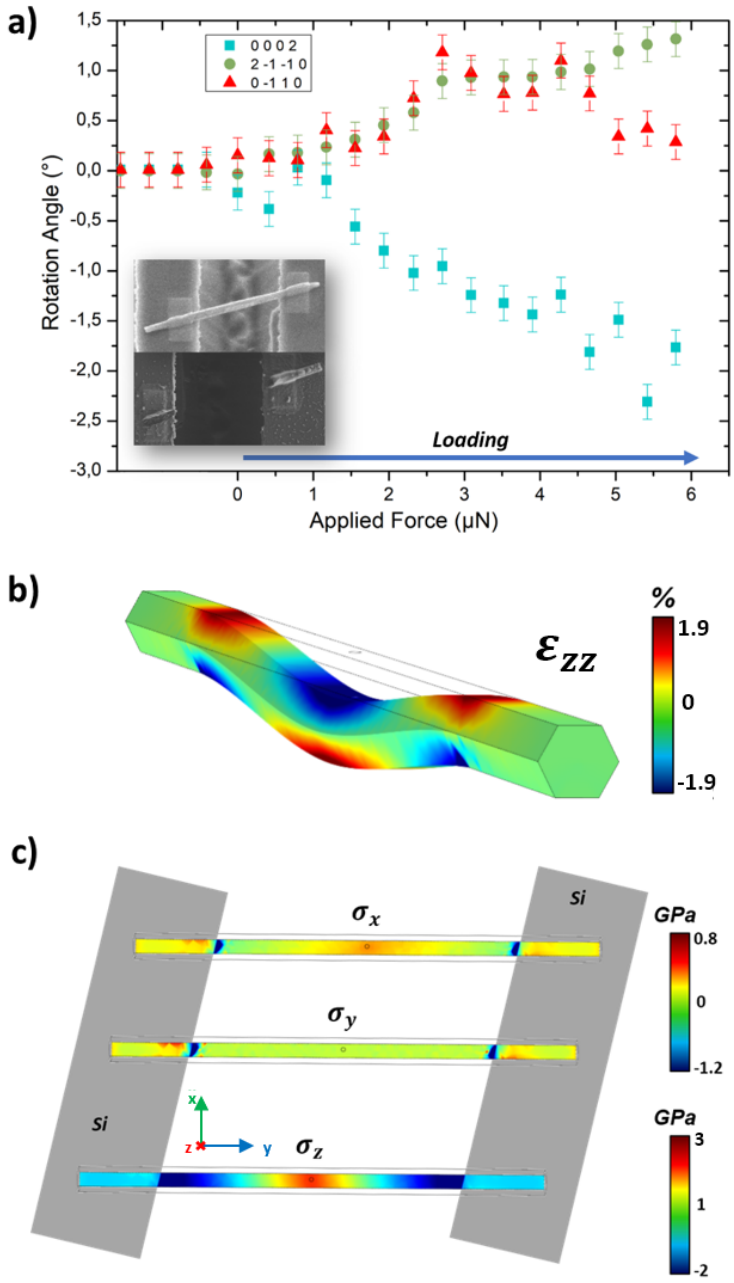

Figure 3.12: a) Rotation angle of the three orthogonal lattice planes (0002) (□), $(0\bar{1}10)$ (△), and $(2\bar{1}\,\bar{1}0)$ (◯) during three-point bending of a ZnO NW with a diameter of 200 nm and a suspended length of 2.5 µm until failure. The inset shows a *post-mortem* scanning electron microscopy image confirming NW fracture. b) Strain ε_{zz} and c) stress σ_x, σ_y, σ_z (of the lower NW facet) in the ZnO NW at highest applied load of 5.79 µN calculated by finite-element method simulations considering identical loading and positioning configuration as in the experiment. The z direction shows a high stress of 3 GPa at the loading point, while the x and y directions are clearly affected by the positioning of the NW along the trenches, where the stress near the embedded parts are highest in the opposite part of each region.

3.4.5 Plasticity

To further elucidate potential plasticity in ZnO at the nanoscale, ZnO NW III was mechanically loaded and unloaded with a maximum applied stress of 0.5 GPa at the loading point and a ε_{zz} of 0.15% both in the center and close to the clamping points. It shows the same behavior as the previous NWs with bending as well as torsion. The rotation angles for the three orthogonal lattice planes were found to return to their initial values indicating a fully elastic behavior (see Fig.3.13).

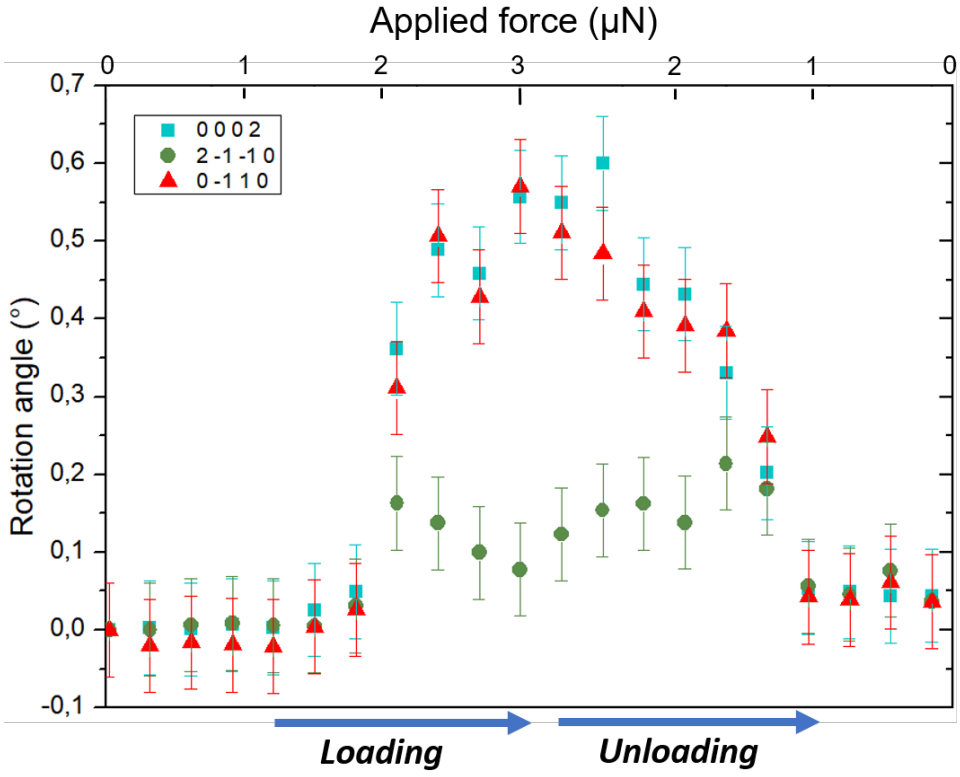

Figure 3.13: Rotation angle of the three orthogonal lattice planes (0002) (□), $(0\bar{1}10)$ (△), and $(2\bar{1}\,\bar{1}0)$ (○), during three-point bending of ZnO NW III

However, in this case, the shape of the Laue diffraction spot of the completely unloaded ZnO NW III changed in comparison to its initial shape implying the storage of defects and, thus the activation of plasticity in the NW. The irreversible deformation of the NW is confirmed by the *post mortem* SEM image presented in Fig. 3.14 showing a clear bending of the right part of the NW. Laue microdiffraction patterns were recorded all along the

NW after nano-mechanical testing. The $[5\bar{4}\bar{1}2]$ Laue spot is exemplarily displayed below the *post-mortem* SEM image. The Laue spot moves on the detector as a function of the position along the NW revealing a variation of the crystalline orientation. In addition, a splitting of the Laue spot is evident in the clamped part on the left-hand side of the NW while a pronounced streaking of the spot is visible in the suspended NW.

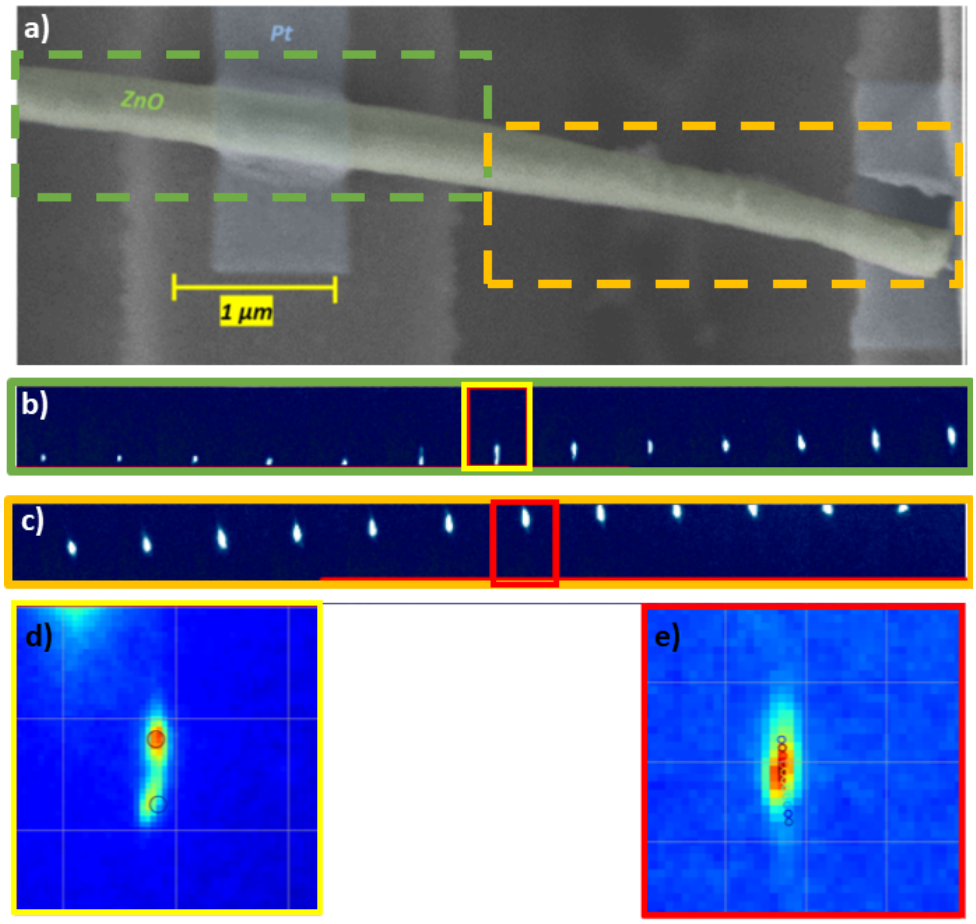

Figure 3.14: *Post-mortem* scanning electron micrograph of the ZnO NW III after three-point bending testing demonstrating irreversible deformation. The $[5\bar{4}\bar{1}2]$ Laue spot measured all along the NW after mechanical testing is exemplarily shown below the SEM image. A splitting of the Laue spot is apparent in the clamped area on the left-hand side of the NW while the Laue spot of the suspended NW part shows a pronounced streaking. Open circles indicate the simulation of the position of the same Laue spot considering a rotation of the crystal around the [0001] axis. In the case of the split Laue spot a rotation of 0.20° reproduces the splitting.

The splitting of the Laue spot as well as the streaking of the Laue spot are both oriented in a similar direction indicating that the crystal lattice rotates almost around the same axis at these two positions. The rotation axis corresponds to the [0001] direction (as illustrated by the simulated displacement of the Laue spot indicated by black circles) signifying a NW torsion. The splitting of the Laue spot in the clamped area is well reproduced by a local rotation $\Delta\Theta$ of the crystal by 0.20° around the [0001] axis. The Laue spot splitting is a clear indication of a subgrain formation which can be related with the aggregation of geometrically necessary dislocations in a geometrically necessary boundary (GNB). Considering Nye's law the number of stored GNDs n can be inferred from this local rotation of the crystal lattice.

This splitting indicates the storage of geometrically necessary dislocations (GNDs) in the probed volume.

$$\Delta\Theta = \rho_{GND} \cdot L \cdot b \tag{3.6}$$

Here, b is Burger's vector and L is the length of the probed volume along b. Considering the NW thickness t, the absolute number of GNDs within the probed volume is obtained:

$$n = \rho_{GND} \cdot L \cdot t \tag{3.7}$$

When substituting Eq.(3.6) in Eq.(3.7), the absolute number of stored GNDs is obtained:

$$n = \Delta\Theta \cdot \frac{t}{b} \tag{3.8}$$

Taking into account the NW thickness t of 260 nm and assuming dislocations in the basal plane with the Burgers vector of $b = 0.324$ nm, the number n of stored GNDs within the probed volume is about 3.

It should be noted that the simulation of a NW torsion does not perfectly reproduce the streaking of the second highlighted Laue spot in (Fig. 3.14). In addition, the streaking direction of the Laue spot varies along the NW and, as mentioned above, the Laue spot moves on the detector as a function of the position along the NW. The irreversible NW deformation is thus more complex than a simple torsion around the c-axis. From the

displacement of the Laue spots on the detector as a function of the position along the NW, the rotation of the three orthogonal lattice planes (0002), $(0\bar{1}10)$, and $(2\bar{1}\,\bar{1}0)$ was inferred (Fig. 3.22) demonstrating both bending and torsion of the NW. This irreversible rotation of the NW crystal may originate from both plasticity as well as residual elastic deformation considering that the NW may be attached to the Si support on the right-hand side by van der Waals forces.

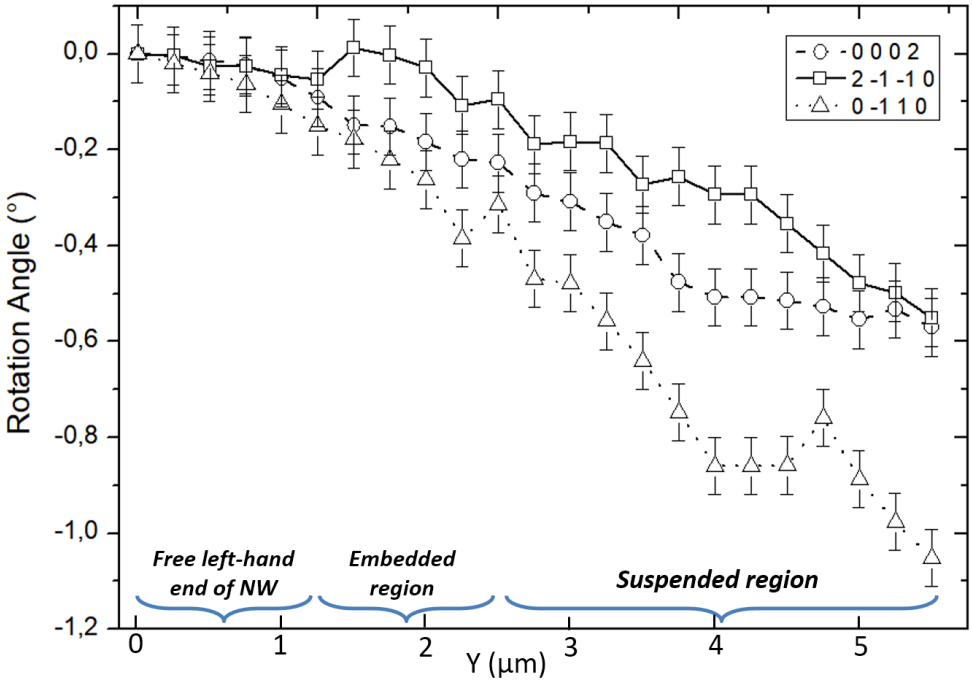

Figure 3.15: Rotation angle of the three orthogonal lattice planes (0002) (□), $(0\bar{1}10)$ (△), and $(2\bar{1}\,\bar{1}0)$ (○) measured along the length of ZnO NW III in steps of 200 nm after complete unloading.

3.5 TEM Analysis

Post mortem transmission electron microscopy (TEM) was performed on three-point bent NWs for further analysis of their microstructure using a Cs-corrected TEM (FEI TITAN 80-300) operated at 300 kV. Bright Field (BF), Dark Field (DF) and High resolution (HR)TEM images were taken using a negative spherical aberration coefficient to both improve spatial resolution and reduce delocalization effects [146].

3.5.1 Sample preparation

The NWs were harvested from the patterned Si wafer and electron transparent lamella for TEM analysis were prepared by focused ion beam (FIB) micromachining. For this purpose, a platinum protective shield was first deposited onto the NW by electron beam induced deposition (EBID) in a FIB microscope (FEI Helios 600 NanoLab). Using an acceleration voltage of 30 kV, a slice was then cut parallel to the axis of the NW to withdraw it together with the supporting Si substrate (See Fig. 3.16). Thinning of the lamella was performed using decreasing voltages and ionic currents down to 1 kV, respectively, 17 pA to minimize the sample damaging. Finally, the lamella was thinned down to a thickness of less than 20 nm by Ar^+ ion milling using a Fischione Nanomill device operating at a 500 V accelerating voltage.

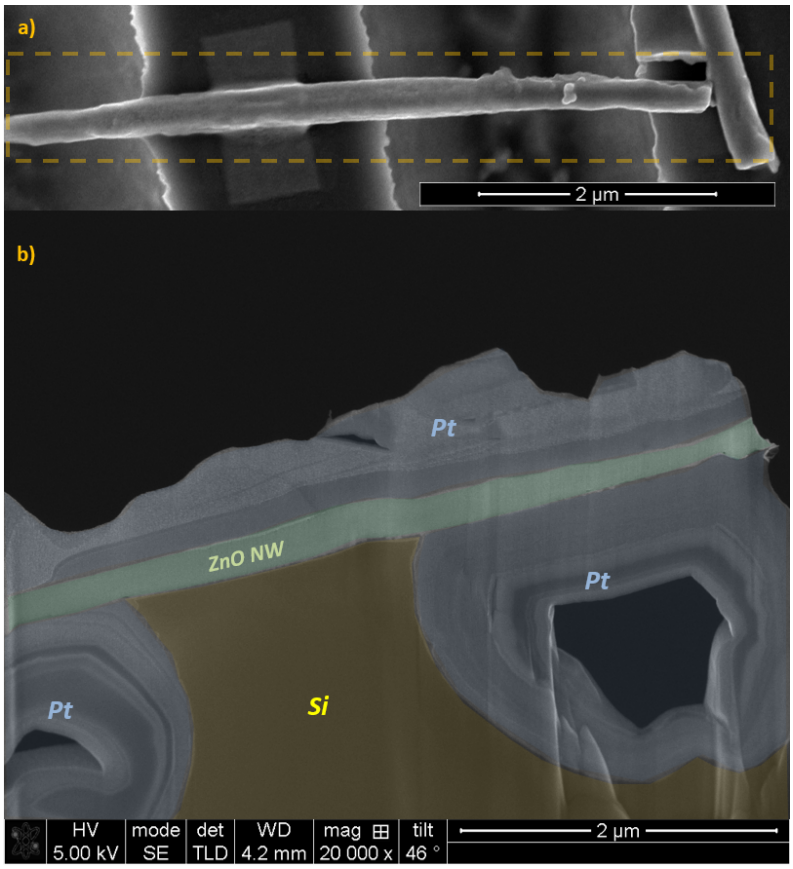

Figure 3.16: Scanning electron microscopy image a) of the plastically deformed ZnO NW III observed from the top and b) of a TEM lamella of the same NW prepared by FIB micromachining. Platinum was deposited prior to the milling process to avoid any damaging of the NW.

3.5.2 Defects observation

To further investigate the irreversible deformation of ZnO NW III and the nature of the defects involved in the above mentioned plastic deformation, the microstructure of this NW was analysed by *post mortem* transmission electron microscopy. For this purpose, an electron transparent lamella containing a $[2\bar{1}\bar{1}0]$-oriented slice was extracted from the NW using FIB micromachining and then thinned down by Ar^+ ion milling. It should be noted that, due to the pronounced bending of the NW at one of its extremities, this part was progressively eroded and disappeared during the thinning process of the TEM lamella. Observation of the NW cross-section by conventional TEM imaging (*cf.* Fig. 3.17) allowed to draw a general picture of the deformation: the main part of the NW is free of defects,

while the observed extended defects being concentrated in a very narrow region in the vicinity of one edge of the Si support. This is in agreement with the FEM simulations predicting high stress concentrations in this region. Circular bent contours just below the surface in the central part of the NW are notably visible, probably resulting from an unintentional nanoindentation by the SFINX-tip. Surprisingly, no defect was observed neither within the NW below this zone nor further towards the bent end of the NW.

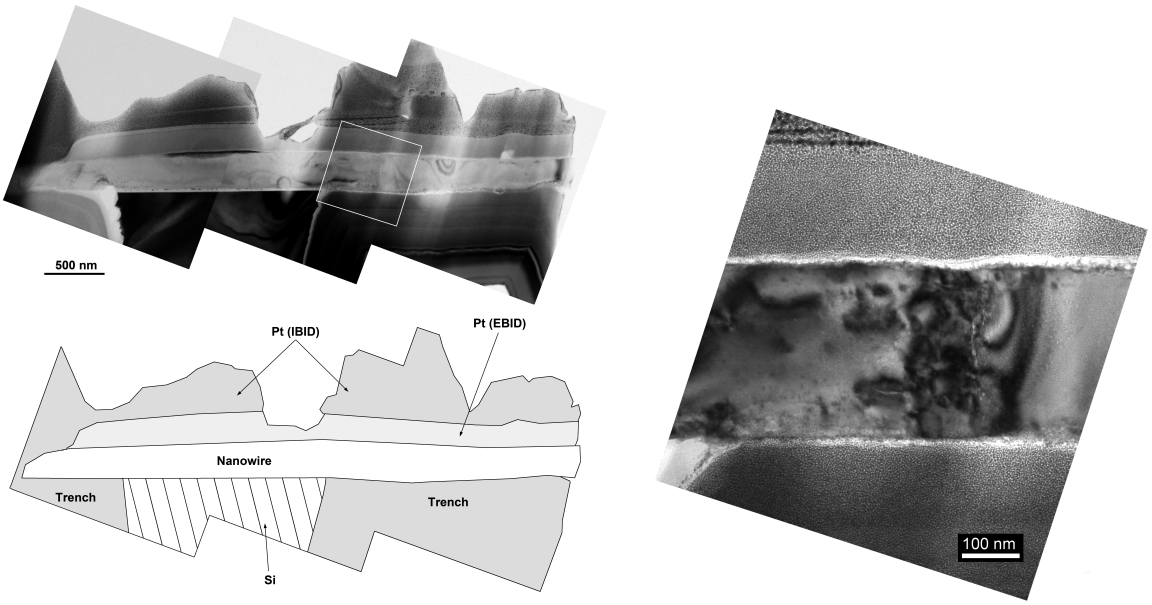

Figure 3.17: Left : Assembly of bright field (BF) TEM images of plastically deformed ZnO NW, observed in cross-section. Right: Higher magnification BF image of the area marked by a square in the left image. This zone, located at the edge of the trench, contains numerous extended defects.

High-resolution (HR) TEM imaging performed close to the edge of the trench (framed zone in figure 3.17) shows the presence of both microcracks and extended defects. In (Fig. 3.18), two differently-oriented portions of the NW are visible around a few microcracks. Both NW portions are being here observed parallel to the $[2\overline{1}\overline{1}0]$ crystallographic axis as evidenced by the fast-Fourier transform (FFT) of the image. The analysis of the FFT indicates that the two parts are rotated with respect to each other by an angle of 3.8° around the $[2\overline{1}\overline{1}0]$ direction (*i.e.* perpendicular to both the NW axis and the SFINX-tip displacement direction).

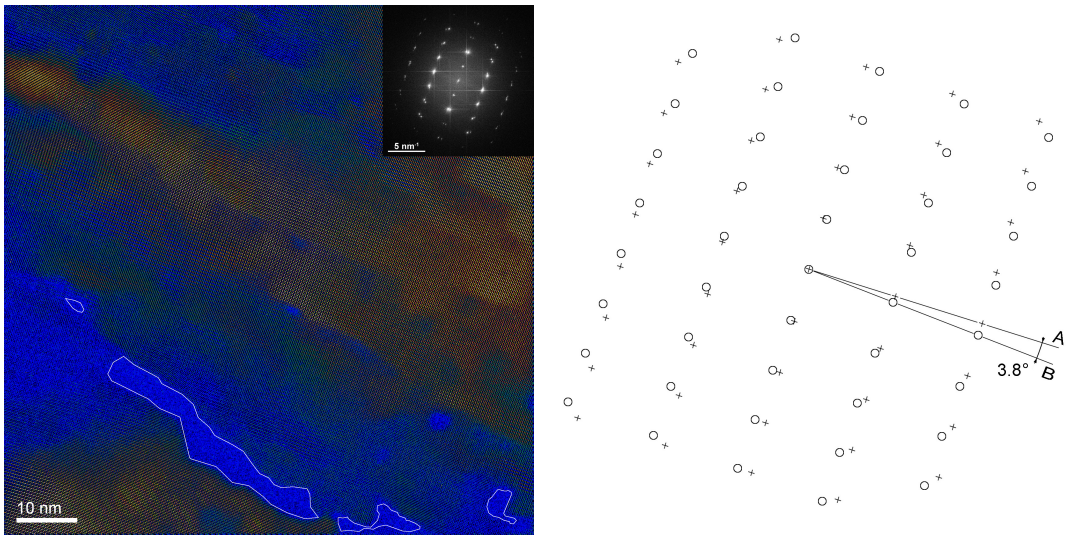

Figure 3.18: Left: HRTEM image filtered using the average background subtraction filtering (ABSF) method showing two differently-oriented crystalline parts of the NW separated by a disordered transition zone. Right: Schematic drawing of the spots observed in the FFT. The two crystalline parts are parallel to the $[2\overline{1}\overline{1}0]$ crystallographic axis and rotated by an angle of 3.8° with respect to each other.

In this region close to the corner of the Si support, numerous defects extending in (0001) planes are also observed (see Fig.3.19). As the presence of stacking faults has not been detected in the examined areas, these defects likely consist of perfect a/3 $<2\overline{1}\overline{1}0>$ dislocation loops. Depending on the local thickness of the observed zone, they appear as straight lines of variable length, parallel to the $[1\overline{1}00]$ direction. A defect with a short extension is exemplarily shown in Fig. 3.20. Filtering of the FFT of the HRTEM image evidences that this defect consists of a small dislocation loop which is partially or completely contained within the TEM lamella.

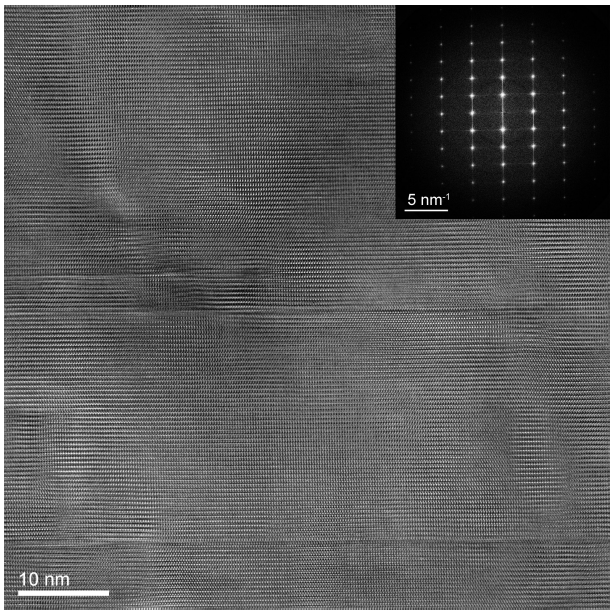

Figure 3.19: Average background subtraction filtered HRTEM image and the corresponding FFT of the area located at the corner of the trench. Numerous dislocations extend in the (0001) planes.

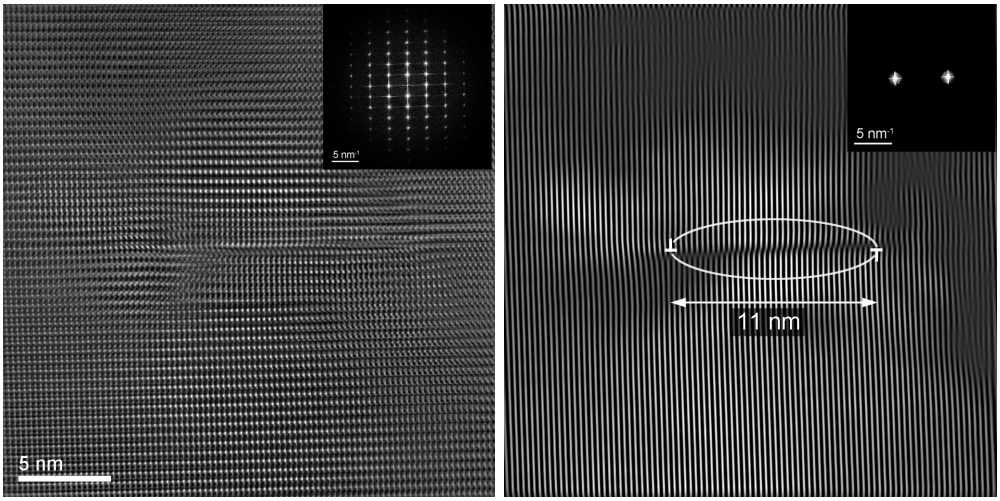

Figure 3.20: Left: ABSF-filtered HRTEM image and the corresponding FFT of a region containing an isolated dislocation loop. Right: image filtered using the $1\bar{1}00$ symmetrical reflections. A scheme showing the approximate positions of the two opposing 60° segments of the dislocation is superimposed on the image.

Although a very high defect density is observed in the studied region, it must be

emphasized that the experimental HRTEM images do not allow for a direct identification of the dislocations (*e.g.* Burgers vector, core structure) due to the continuous contrast variations in the basal planes containing the observed defects. An example of such a characteristic contrast is shown in Fig. 3.21 where the observed defective region is likely to contain two very close dislocation loops in parallel basal planes. It can therefore be assumed that the observed dislocations consist of small dislocation loops with a diameter not exceeding the thickness of the TEM lamella in the investigated regions (between 10 and 50 nm).

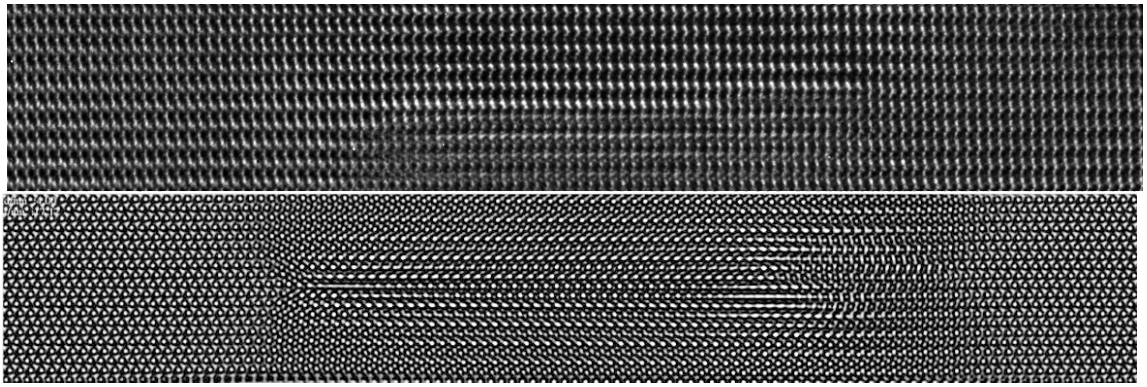

Figure 3.21: **Top**: Detail of a HRTEM image showing two small dislocation loops in close basal planes. The local thickness of the sample, derived from image simulation of a defect-free region of the sample close to the observed region (see Fig. 3.23), is estimated to be 17.2 nm. **Botttom**: Multislice simulation showing the local contrast variations produced by two dislocation loops with Burgers vectors $\vec{b} = 1/3[11\bar{2}0]$ in a similar configuration to that observed in the experimental image (t: 17.2nm, C1: -12nm, C3: -7μm). Note that the simulation does not take into account the slight misorientation of the sample with respect to the $<11\bar{2}0>$ crystallographic axis as seen in the experimental image.

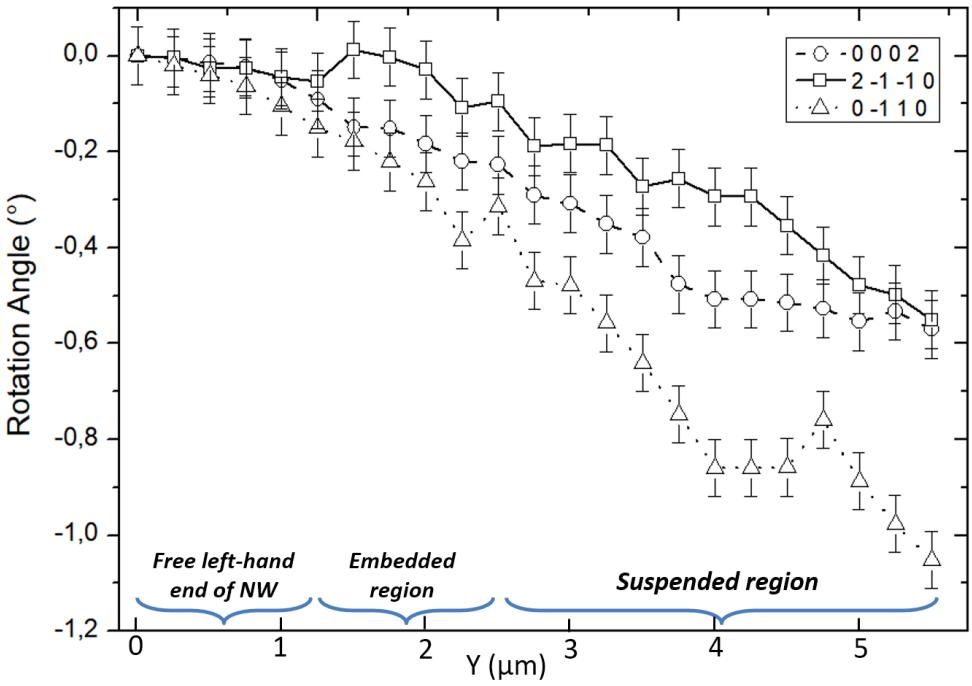

Figure 3.22: Rotation angle of the three orthogonal lattice planes (0002) (□), $(0\bar{1}10)$ (△), and $(2\bar{1}\,\bar{1}0)$ (◯) measured along the length of ZnO NW III in steps of 200 nm after complete unloading.

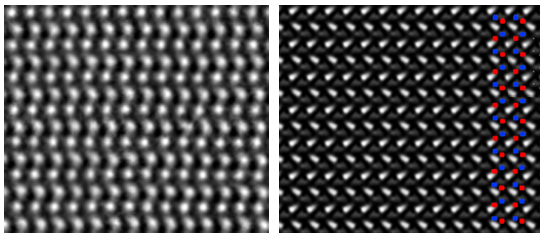

Figure 3.23: Experimental (left) and simulated (right) HRTEM images of the wurtzite structure observed along the $<2\bar{1}\bar{1}0>$ crystallographic axis. The thickness of the sample is estimated to 17.2 nm in this region (C1: -23nm, C3: -7μm). The atomic positions of Zn (blue) and O (red) atoms are superimposed to the right-part of the simulated image.

3.6 Appendix

The study of the plasticity and the electromechanical properties of individual ZnO NWs using transmission electron microscopy needs a very complex sample preparation which is briefly described below. We tested different approaches, the main one being individually manipulating a ZnO NW using a micro-probe in a focused ion beam (FIB). The first attempt involved picking it from the as-grown ZnO NWs sample (Fig. 3.24 a).

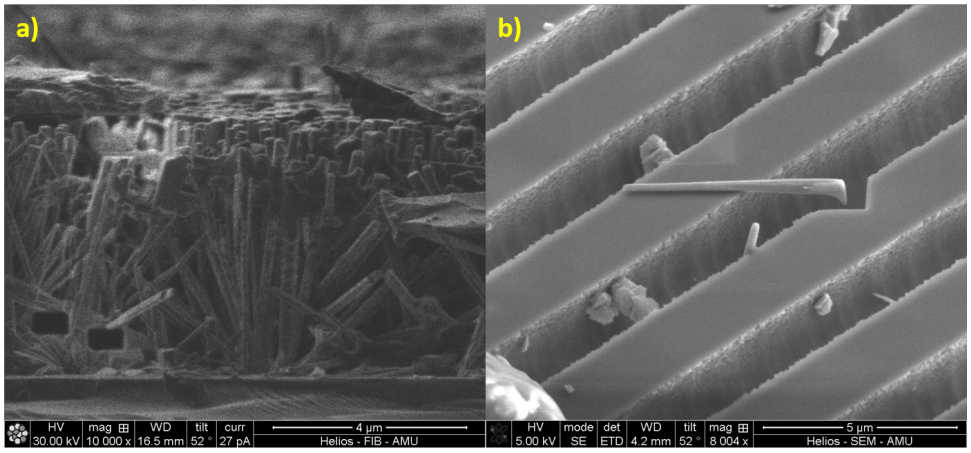

Figure 3.24: Scanning electron microscopy image a) of ZnO nanowires grown on a Si substrate b) of a single suspended ZnO nanowire.

However, this was found to be very difficult due to the high density of the NW forest and the relatively large size of the probe. We then decided to select a ZnO nanowire that was already suspended across a micro-trench on the micro patterned Si substrate.However, the NWs are very firmly attached to the Si supports by van der Waals forces that make it impossible to displace or to manipulate the NWs. Therefore, the Si supports below the NWs had to be cut using the focused ion beam without damaging or deteriorating the NWs. (Fig. 3.24.b).

The nanowire was then positioned between two copper electrodes connected to an e-chip (Fig 3.25.a) that can be inserted into a TEM holder. In theory, this would enable us to apply an electric field to the NW while observing it under HR-TEM.

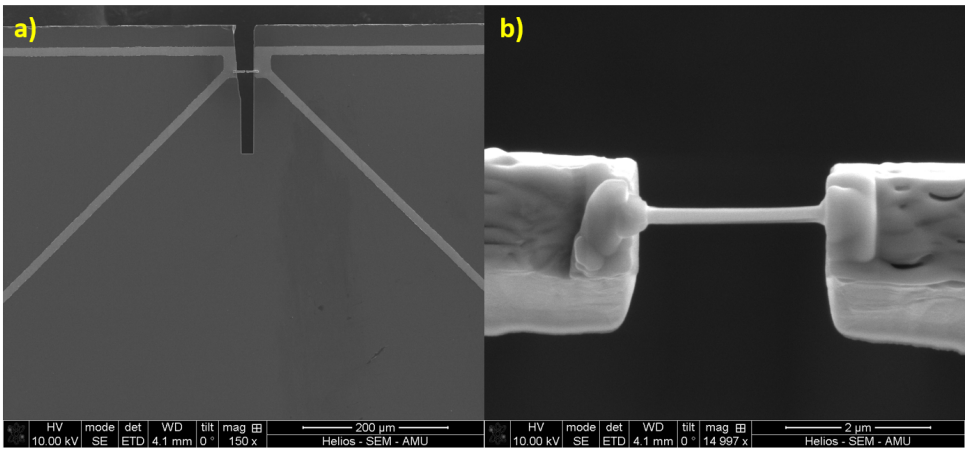

Figure 3.25: Scanning electron microscopy image a) of the electrically connected e-chip holding b) a single suspended ZnO NW between two electrodes.

Fig 3.25.b show the suspended single ZnO NW before the electrical tests involving the application of an electric field up to 40V. When manipulating the NW under FIB, some Pt contamination occurred, despite us taking all the necessary measures to minimise it. This caused the NW to short circuit and melt down (see Figure 3.26.

Although this method proved challenging and time-consuming, and did not yield successful results despite all precautions. It provided valuable insights that could guide improved strategies and approaches in future attempts.

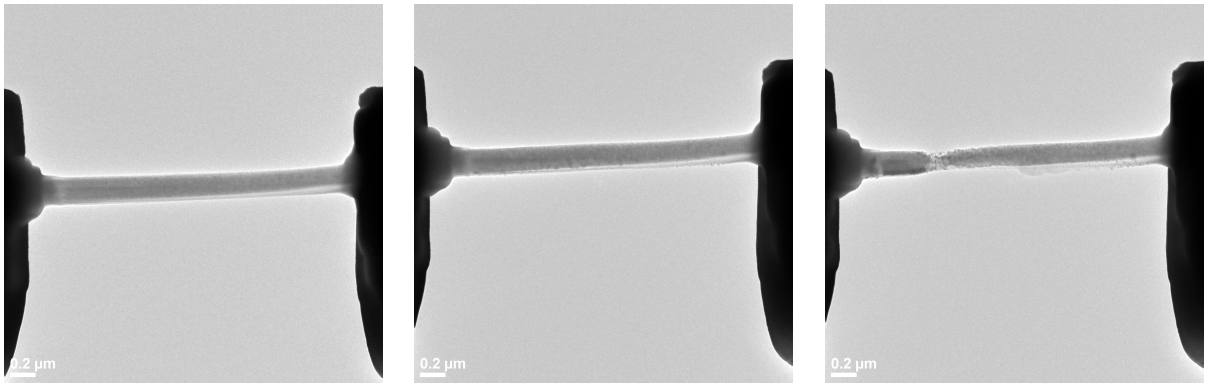

Figure 3.26: TEM images showing the morphology of a nanowire before biasing experiment (left), and after biasing experiments with V=2V (center) or 3V (right).

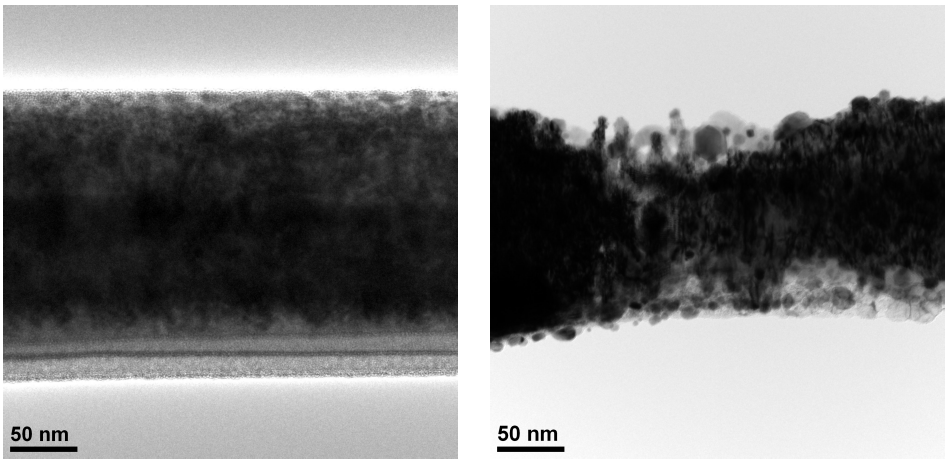

Figure 3.27: TEM images of the NW shown in Figure 3.26 performed at higher magnification before biasing experiment (left) and after (right). The partial melting of the NW is clearly visible on the right image.

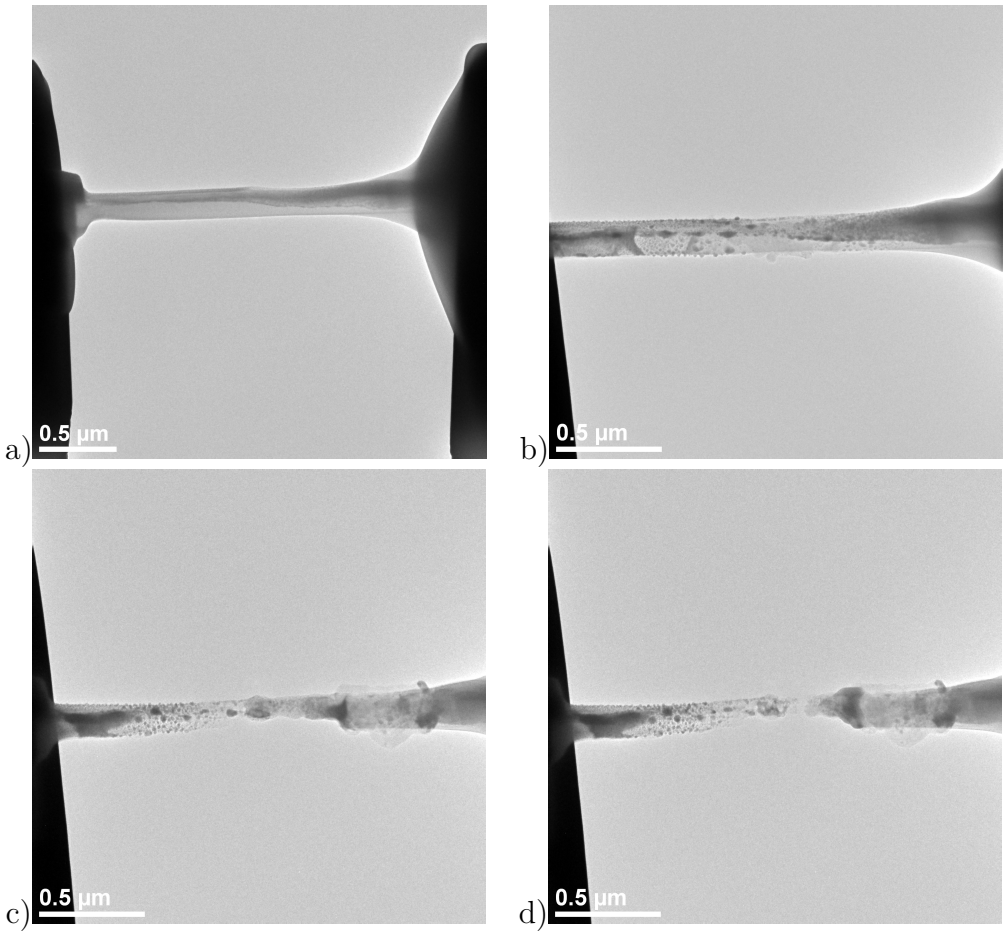

Figure 3.28: TEM images showing the damaging of a nanowire submitted to various voltages: a) 0V, b) 2V, c) 30V, d) 40V.

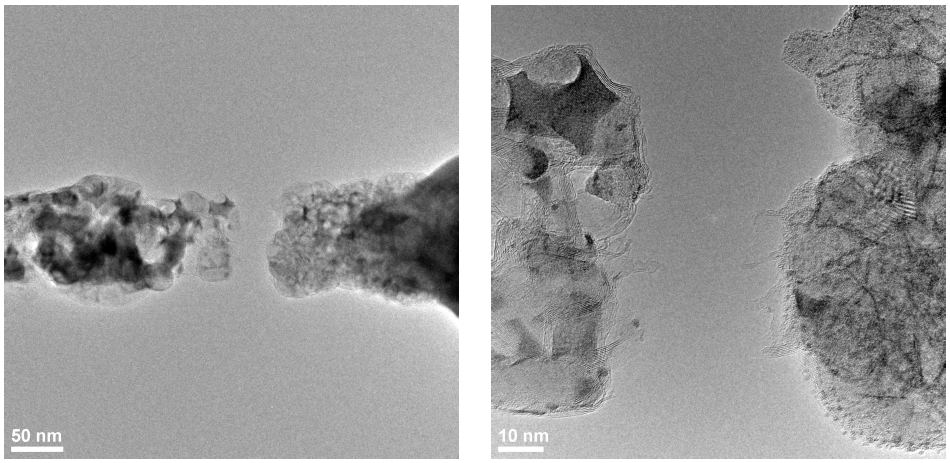

Figure 3.29: HRTEM images of the NW shown in Figure 3.28 showing the microstructure of the NW in the vicinity of the melted part.

3.7 Discussion

All ZnO NWs tested in three-point bending configuration in this work demonstrated a more or less significant torsion during loading. These findings can be explained by a misalignment of the SFINX-tip with respect to the center of the NW side facet, and the orientation of the NW with respect to the Si micro-trenches. As demonstrated by FEM simulations of ZnO NW II, the fact that the NW does not cross the micro-trench at a right angle induces inhomogeneous strain distributions in the NW which eventually may induce a rotary moment that leads to a NW torsion around its *c*-axis.

Fracture strengths of up to 3 GPa and maximum strain of about 1.9% were demonstrated for three-point bent ZnO NWs. These values are about one order of magnitude larger than in bulk ZnO and are comparable to other studies reporting on fracture strengths of 2 to 8 GPa and maximum strains of few percent for ZnO NWs [158, 159, 160].

The fracture strength represents the largest possible deformation of the NW before failure. Assuming that no plasticity occurred up to NW failure, the maximum NW bending corresponds to the maximum elastic strain that could eventually be converted into electrical energy by the piezoelectric effect in the piezoelectric semiconductor ZnO NW.

In order to estimate the maximum electrical potential generated in a bent NW, a cantilever beam instead of a three-point bending configuration is considered for simplification.

Here, the cantilever is fixed at its lower extremity and a lateral force is applied to the top of the cantilever. The generated electrical potential is calculated using the following equations [22]:

$$\varphi = \begin{cases} \frac{1}{8\kappa_r}\frac{f}{I_{xx}E}\left[2(1+\nu)e_{15}+2\nu e_{31}-e_{33}\right]\left[\frac{\epsilon_0+3\kappa_r\frac{r}{a}}{\epsilon_0+\kappa_r}\frac{r^2}{a^3}\right]a^3\sin\theta, & r<a, \\ \frac{1}{8\kappa_r}\frac{f}{I_{xx}E}\left[2(1+\nu)e_{15}+2\nu e_{31}-e_{33}\right]\left[\frac{2\kappa_r}{\epsilon_0+\kappa_r}\frac{a^2}{r}\right]a^3\sin\theta, & r\geq a, \end{cases} \tag{3.9}$$

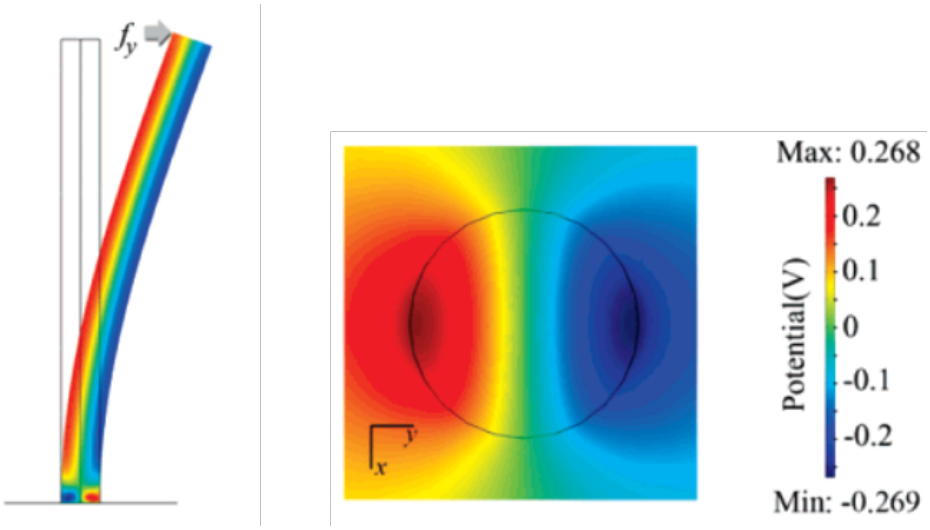

Figure 3.30: 2D FEM simulation of the electric potential distribution for a ZnO nanowire of a rectangular form with $D = 50nm$ and $L = 600nm$ at a lateral bending force of $F = 80nN$ [22]

The parameter r is the radial distance from the origin, while $a = 97.5nm$ is the radius of the nanowire. For calculations, an applied force of $F = 5.8\mu N$, this value of force is taken to find an approximation of the generated at electric potential at maximum strain before facture for our NW II. The moment of inertia for a hexagonal cross-section $I_{xx} = \frac{\pi}{4}a^4$, the Young's modulus of ZnO of $E = 129GPa$, the Poisson ratio of ZnO of $\nu = 0.349$, the piezoelectric coefficients of ZnO $e_{15} = -0.45C/m^2$, $e_{31} = -0.51C/m^2$ and $e_{33} = 1.22C/m^2$, and the relative dielectric constant of $\kappa_r = 7.77$ are taken into account.

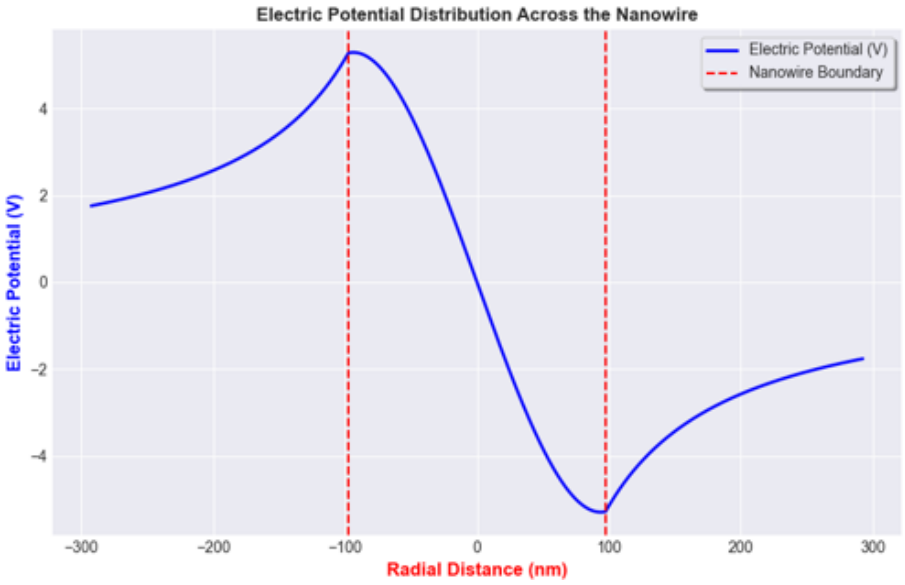

Figure 3.31: Electric potential profile of our ZnO NW extracted from equation 3.9.

Figure 3.31 b) shows the electric potential profile across the ZnO NW calculated using Eq. 3.9. The maximum potential is located at the surface of the NW. Considering the maximum applied force just before NW fracture, the electrical potential in the ZnO NW amounts to 5.3 V. It should be noted that these calculations are very simplified. They do not take into account the semiconductor properties and surface traps, which may significantly reduce the generated electric potential. In addition, a cantilever NW is considered although the actual bending experiment was performed in a three-point bending configuration where the deflection of the NW is significantly smaller amounting to few tens of nanometer only. The calculated value can thus be considered as an upper limit. The work from Wang et al. [161] takes this a step further, by using the same NW diameter and length as Fig. 3.30 and a Force of 0.8nN and with taking into account the other parameters such as the bending of the AFM tip during the tests as well as the flexoelectricity for which they found that the influence of flexoelectric effect on the carrier concentration redistribution increases with decreasing diameter. The electric potential was found to be one order of magnitude lower than that calculated simply using Eq. 3.9.

In the case of the irreversibly deformed ZnO NW III, split Laue spots as well as streaked Laue spots were evidenced. The splitting is a clear indication of the misorientation of two parts of the crystal within the probed volume which agrees with a geometrically necessary

boundary formed by GNDs at this probed region. The TEM microstructural analysis of the region close to the left-hand Si support revealed the presence of a high density of small basal dislocation loops, while local rotations of the basal planes were detected in the FFT of the HRTEM images. The dislocation configurations locally responsible for either a torsion or a bending of a crystal can be considered schematically as acting either as twist or as tilt sub-grain boundaries (SGB), respectively. In the former case a pure twist SGB is formed by screw dislocation segments extending in the plane perpendicular to the axis of rotation, whereas in the latter case a pure tilt boundary is formed by an array of edge dislocation segments with Burgers vectors perpendicular to the axis of rotation [162]. Between these two extremes, the presence of mixed SGBs produces both macroscopic torsion and bending of the crystal. Assuming that only basal dislocation slip has been activated in the studied nanowire, the two observed local mechanical responses (*i.e.* torsion around the [0001] axis or bending leading to the rotation of the nanowire planes) can result from the activation of the three types of perfect dislocations in the basal planes, depending on their respective proportions of screw and edge components.

The macroscopic deformation of the NW evidenced by both the Laue spot streaking and the *post-mortem* SEM images may result from the propagation of extended defects, some of which being stored in the NW after unloading, leading to the permanent deformation. However, no dislocations were found by TEM neither below the loading position nor in the right-hand part of the NW while another large part of the NW was lost during lamella preparation. This may indicate that the irreversible deformation may actually originate from an elastic bending where the NW right-hand end was displaced during loading (probably at the onset of plasticity) and then got stuck at the Si support being attached by van der Waal's forces.

Chapter 4

Influence of X-ray beam and beam damage

Beam damage is a critical issue, particularly when considering the ongoing upgrades of major synchrotrons and beamlines worldwide resulting in considerably higher flux levels. The influence of high-energy beams, whether X-rays or electrons, on a sample during experiments cannot be overlooked. In electron microscopy, phenomena like carbon deposition are well-documented examples of sample contamination. Similarly, synchrotron experiments, often conducted under ambient conditions, bring their own set of challenges. Hydrocarbons present in the air can lead to contamination of the sample surface. The intense X-ray beam can cause localized heating, while electrostatic charging may create additional complications, especially for insulating materials. These effects can significantly impact both the sample's integrity and the quality of the data obtained. At the initial BM32 setup, the impact of the X-ray beam on samples appeared minimal. However, the experimental setup underwent a significant upgrade during the course of these studies. The Laue setup was replaced with LaueMAX, which delivered an X-ray beam with an intensity more than one order of magnitude higher than the original system. This increase in beam intensity brought new challenges, as the higher energy density amplified the potential for beam-induced effects. The upgraded LaueMAX station presented both opportunities and challenges. While the higher beam intensity offered improved resolution and faster data acquisition, it also necessitated a more comprehensive understanding of beam damage

mechanisms. These insights are crucial for refining experimental protocols, minimizing sample damage, and ensuring the reliability of the results obtained from synchrotron-based studies.

4.1 Experimental conditions

The influence of the X-ray beam on the sample was investigated at the LaueMAX nd-station at the BM32 beamline at ESRF, which provides an incident flux that is more than one order of magnitude higher than at the previous installation. The general setup of the experiment remained the same as described above. The polychromatic X-ray beam was focused down to 200 x 200 nm^2 using a new pair of KB mirrors compared to about 300 x 500 nm^2 in the previous setup. While previous experiments at the initial Laue microdiffraction end-station at BM32 produced clean Laue diffraction patterns with a homogeneous background, the new installation revealed additional blurry signals on the detector, as illustrated by the Laue diffraction patterns presented in Fig. 4.1. The end-station was moved closer to the source, and due to the divergence of the incident beam, a larger portion of the beam now enters the KB mirror system to be focused on the sample. In between the exit of the vacuum system of the beamline and the entrance to the KB mirrors, the X-rays traverse a distance of about 3 m in air. The incident X-rays are scattered in the air and then interact with other materials within the experimental hutch. These scattered X-rays eventually reach the detector, causing the observed blurry signals. Although such scattering may have occurred in previous experiments, the significantly higher beam intensity in the upgraded setup amplifies these effects to a level where they can no longer be ignored. The fluorescence detector was shielded with lead tape to block excessive scattered radiation. This precaution effectively stopped any possible saturation of the fluorescence detector, further suggesting that the diffuse signals could be related to air scattering caused by the high-intensity beam. To address the problem of blurry signals, lead shielding was also applied around the beam path which later confirmed that this approach mitigated the issue, as the detector no longer showed signs of saturation, further supporting the hypothesis that the diffuse signals are caused by air-scattered radiation refracted onto the detector.

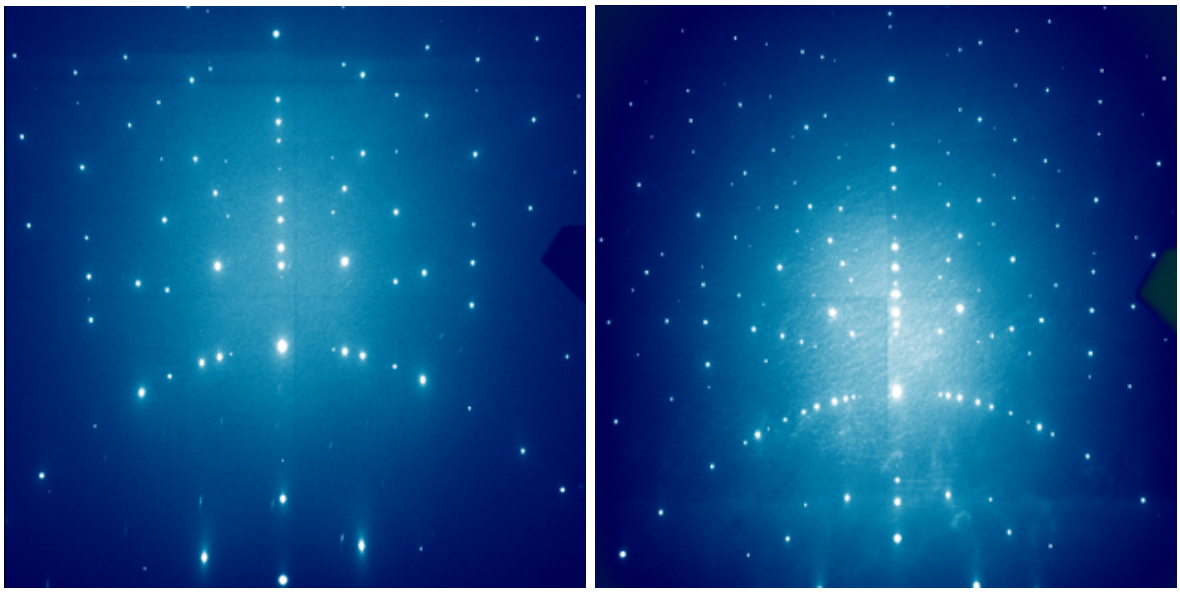

Figure 4.1: Diffraction pattern of a suspended ZnO NW on Si substrate of the old (left) and the new "LAUEMAX" (right) setup, showcasing a notable difference in clarity and background intensity

4.2 Sample damage

The influence of the highly intense polychromatic X-ray beam on ZnO nanowires was investigated by illuminating them for several seconds to perform fluorescence mapping, Laue microdiffraction mapping as well as AFM topography images. In the beginning, the slits in front of the KB mirrors were opened to 0.15 x 0.15 mm². Fig. 4.2 a) presents the $Zn\text{-}K_\alpha$ fluorescence map of the initial ZnO NW. After one X-ray fluorescence mapping of 10 µm x 4 µm with a time-step of 1 second and a step of 300 nm, the ZnO NW was found to be damaged by it as demonstrated in Fig. 4.2 b). This damage was confirmed by AFM topography imaging using SFINX showing that the NW was actually cut into half (Fig. 4.2 c)).

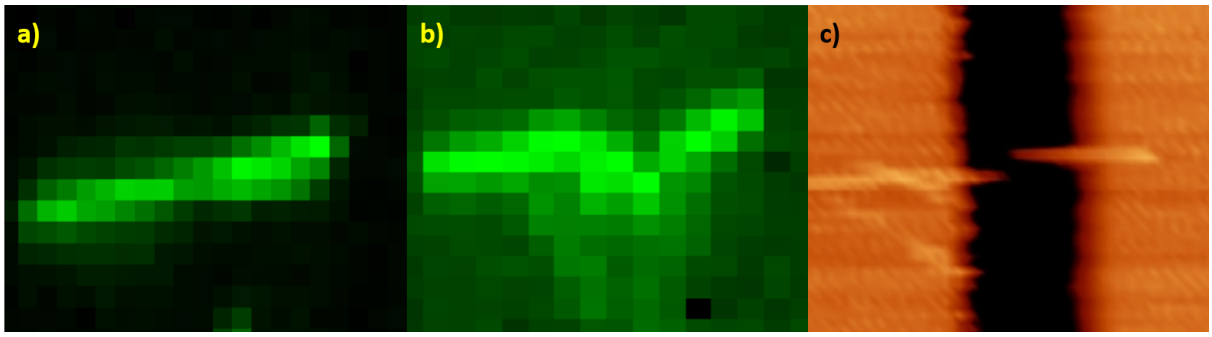

Figure 4.2: a) Fluorescence image of a ZnO NW before focusing the X-ray beam on it b) Fluorescence image of the same NW after focusing the beam for some seconds c) AFM image of the NW after breakage

Comparison of SEM images taken prior to the Laue microdiffraction experiment with *post mortem* SEM images further evidenced a large amount of residue deposition (see Fig. 4.3). The *post mortem* SEM image also confirmed the findings of the fluorescence mapping and AFM imaging that the suspended part of the NW was cut into half. The contamination observed on the sample surface extends over more than 1 µm in width around the NW while the size of the focused X-ray beam measures only about 200 nm. However, the focal size corresponds to the full width of half maximum of the X-ray beam. Considering a Gaussian profile of the X-ray beam, the actual spot size and, in particular, the tails of the X-ray beam can extend over several micrometer explaining the large extension of the contaminated area. The deposition is likely due to the interaction of the highly intense, focused X-ray beam with hydrocarbons present in the air. As the beam strikes the sample, it breaks molecular bonds in these hydrocarbons, leading to the deposition of carbon or carbon-containing materials on the surface. This process is comparable to electron beam and ion beam-induced deposition (EBID and IBID) observed in SEM, TEM, or FIB. The excitation of photoelectrons in the sample may further enhance the effect of local deposition of hydrocarbons.

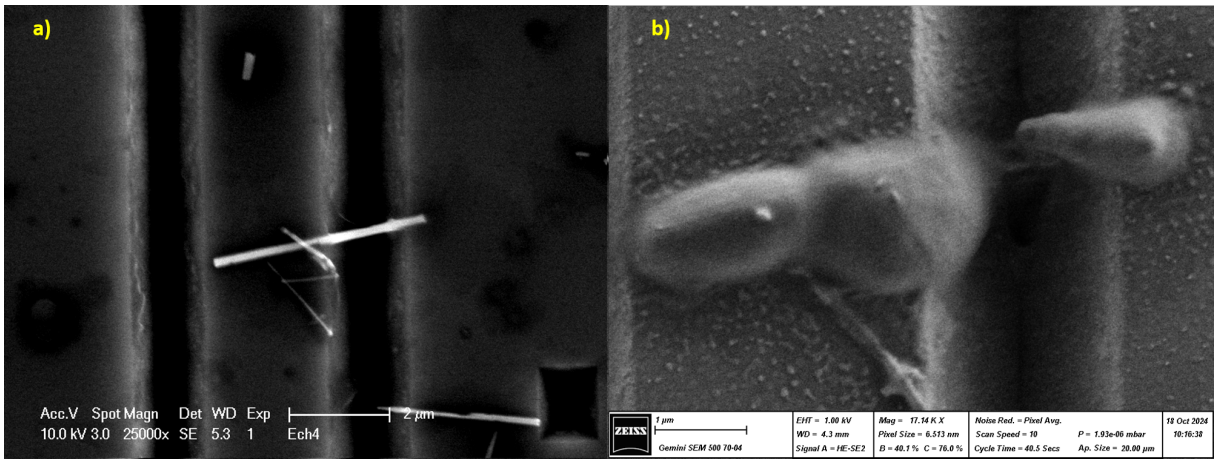

Figure 4.3: a) SEM image of the suspended ZnO NW before the beam damage b) SEM image of the same ZnO NW after the beam damage

In order to minimize the influence of the X-ray beam on the studied ZnO nanowires, the incident flux was reduced by closing the slits upstream from the KB mirror system from 0.15 to 0.05 mm. The beam intensity was thus decreased by almost one order of magnitude. A second ZnO nanowire was illuminated on one position along its suspended length. Despite the decrease of the incident flux by almost one order of magnitude, this second nanowire was also damaged. However, the nanowire was able to withstand for a longer period of time than the first nanowire illuminated by the full flux. The evolution of a ZnO Laue spot as a function of illumination time is exemplarily shown in (Fig. 4.4). While the Laue spot is streaked in the beginning, its shape evolves with time on a time scale of several tens of seconds and eventually splits into two separate Laue spots after more than 100 s of exposure. This behavior, as previously discussed, indicates that we have a generation of a deformation on the lattice level. While the overall shape of the ZnO nanowire remains largely unchanged before and after the experiment (see Fig. 4.5), apart from significant surface and surrounding depositions, other possibilities should be considered. The observed changes could be attributed to the formation of geometrically necessary dislocations (GNDs) or the induction of point defects in specific regions of the nanowire, leading to a reduction in diffracted intensity and the appearance of "holes" in the diffraction spots.

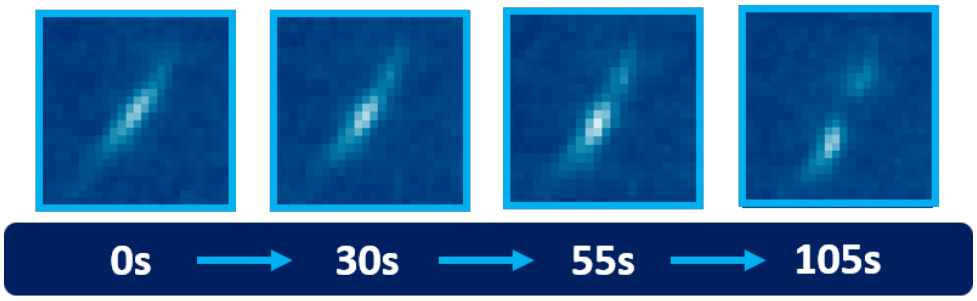

Figure 4.4: The Laue spot of the ZnO NW under the beam experiences a splitting in the course of time

Fig. 4.5 a) and b) present SEM images of a suspended ZnO nanowire taken before and after the Laue microdiffraction experiment, respectively. As for the NW above, surface contamination is observed that is, however, much less pronounced. Moreover, in contrast to the aforementioned NW, this one remains structurally intact. To further mitigate beam-induced damage, nitrogen gas flow was introduced during the experiment, which significantly improved the NW resistance to the beam, allowing it to withstand exposure for a much longer duration.

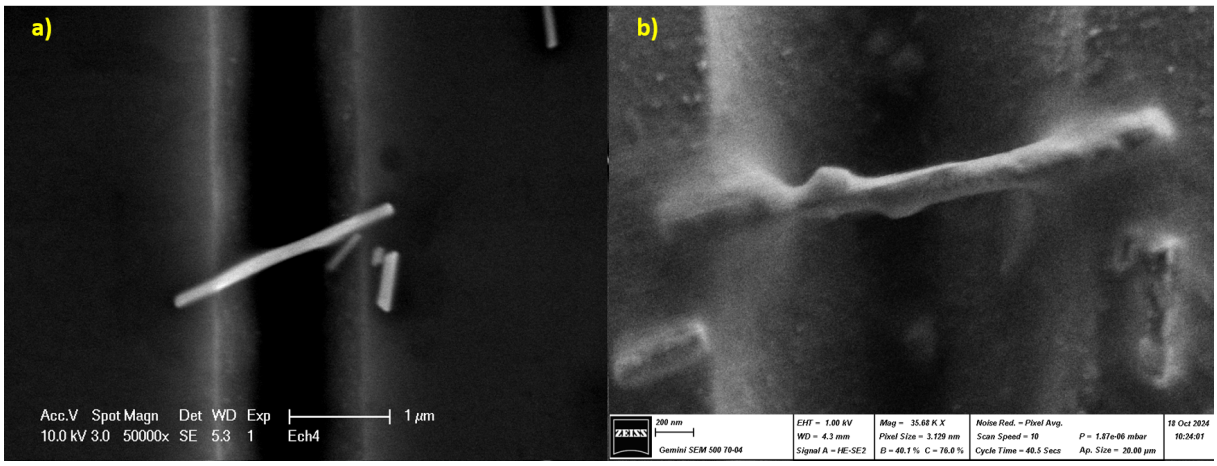

Figure 4.5: SEM images of the suspended ZnO nanowire a) before and b) after the Laue microdiffraction experiment at the LaueMAX end-station using a reduced incident flux.

This persistent effect of the beam can go back to different possibilities, from a heating effect in the NW induced by the beam, to a chemical reaction between ozone gas generated

by the beam interacting with O_2 molecules in the open air and the ZnO NW surface.

As for the heating effect, the power deposited in the ZnO nanowire can be calculated using the power equation from [128]:

$$P = \int_{E_{min}}^{E_{max}} \left(1 - e^{-\mu(E)\cdot D}\right) \cdot \rho(E)\, dE \tag{4.1}$$

Here, E_{min} and E_{max} are the minimum and maximum photon energies of the incident white X-ray beam which are 5 and 25 keV respectively, $\mu(E)$ is the linear attenuation coefficient of ZnO at an energy E, D is the diameter of the ZnO nanowire (200 nm), and $\rho(E)$ is the power spectral density extracted from the X-ray data booklet [163]. Considering the upgrade to LaueMAX, the averaged power spectral density, which was given as 10^{10} photons/s in reference [163] was multiplied by a factor of 10, when all slits were opened, resulting in $\rho(E) = 10^{11}$ photons/s.

As for the linear attenuation coefficient of ZnO $\mu(E)$, the National Institute of Standards and Technology (NIST) provides mass attenuation coefficients (μ/ρ) for various materials[164]. The mass attenuation coefficient μ/ρ can be converted to the linear attenuation coefficient μ using the density ρ of ZnO:

$$\mu(E) = \left(\frac{\mu}{\rho}(E)\right) \times \rho_{\mathrm{ZnO}} \tag{4.2}$$

The density of ZnO is approximately $5.606\,\mathrm{g/cm^3}$. Using the NIST data and by averaging between Zn and O atoms masses and values in ZnO, the ZnO mass attenuation coefficients at 5 keV and at 25 keV amounts to 179.82 $\mathrm{cm^2/g}$ and 30 $\mathrm{cm^2/g}$, respectively. This results in linear attenuation coefficients of $\mu(5\,\mathrm{keV}) = 1008\,\mathrm{cm^{-1}}$ and $\mu(25\,\mathrm{keV}) = 168\,\mathrm{cm^{-1}}$

Taking into account the above values, the power dissipation of the ZnO nanowire was calculated to be about **0.47** mW. By using the heat diffusion equation derived from Fourier's law of heat conduction and considering a sphere of radius a inside the illuminated zone of the nanowire, the thermal power that can be extracted by heat diffusion can be calculated using the following equation:

$$P = 4\pi \cdot a \cdot \kappa \Delta T \tag{4.3}$$

where $A = 4\pi a^2$ is the surface area of the sphere and κ is the thermal conductivity.

Taking into account the thermal conductivity of ZnO of $\kappa_{ZnO} = 50$W/m.K[165], the NW is heated up by about

$$\Delta T = \frac{P}{(4\pi \cdot a)\kappa} = \mathbf{14.96}\ \text{K} \tag{4.4}$$

This value corresponds to the temperature difference induced by the white beam in the BM32 on a ZnO NW with a diameter of 200 nm. As shown in the study conducted by Lawrence et al.[166], the heating effect induced by the beam depends strongly on the studied material and the beam flux. Their study shows that for the same incident flux and power on Cu and Al samples, the ΔT difference differs by one order of magnitude for these to materials due to their different absorption and heat conductivity. Considering the comparative small temperature increase of 15 K and the melting temperature of almost 2000 °C for bulk ZnO, the heating effect can be neglected for the studied ZnO NWs.

However, for all the samples, big surface depositions were observed, which suggested contamination or structural modifications of the randomly dispersed ZnO NWs caused by the beam. The presence of hydrocarbons in the ambient air likely played a significant role in contamination under high-intensity X-rays, as chemical reactions could be triggered on the sample surface.

Al Hassan et al.[23] demonstrated the possibility of a combination of both heating and a chemical reaction. This study that focused on the effects of a 9 keV X-ray beam with a photon flux of 10^{10} ph/s on core-shell GaAs NWs, demonstrated that there was a generation of ozone by the highly intense X-ray beam, and the subsequent formation of oxide layers on the NWs side, which leads to an oxidation process in the NWs that leads to its breakdown (See Fig. 4.6). In the case of ZnO NWs, this process may lead to a formation of ZnO_2 or even $Zn(OH)_2$ due to a combination of moisture present in the air and the irradiation by X-rays [167]. These hypotheses may explain the NW that broken-down in (Fig. 4.3) and the defects that have led to the observed splitting of the Laue spot (Fig. 4.4). As it also explain the large amount of depositions we see on the NWs such as in Fig. 4.5.

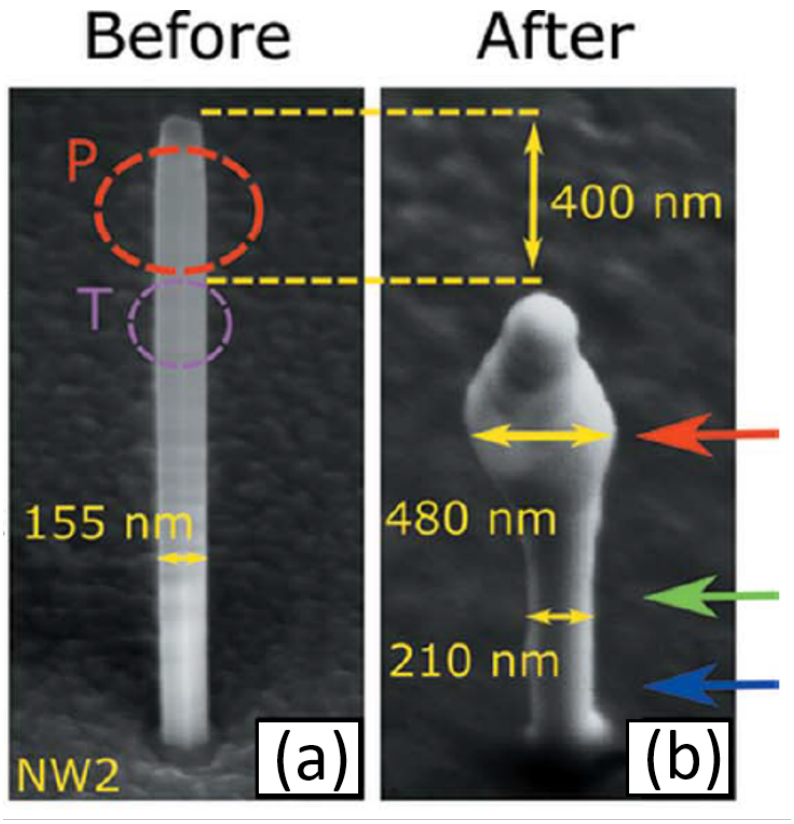

Figure 4.6: SEM images of a GaAs NW a) before and b) after exposure of 4 hours [23]

4.3 Discussion

While in-situ Laue microdiffraction is a very sensitive tool to study the mechanical behavior at the nanoscale, the influence of highly intense X-ray beams on the investigated nano-objects cannot be neglected. The results presented in this section highlight the significant impact of an intense polychromatic X-ray beam on ZnO nanowires. Prolonged irradiation, even at lower beam intensity, leads to structural alterations ranging from surface modifications to complete nanowire rupture. AFM imaging and fluorescence mapping unambiguously show that ZnO is particularly sensitive to X-ray exposure, leading to nanowire fragmentation under certain irradiation conditions. *Post-mortem* SEM images reveal substantial residue accumulation around the irradiated nanowires, extending well beyond the focused beam size. This contamination suggests a deposition effect induced by the interaction of the beam with hydrocarbons present in the ambient environment,

leading to carbonization similar to Electron Beam Induced Deposition (EBID) and Ion Beam Induced Deposition (IBID). Such contamination complicates the interpretation of structural modifications, as it may obscure intrinsic changes in the ZnO lattice. Moreover, the persistence of damage despite reducing the incident flux suggests that more complex mechanisms are at play. The evolution of the Laue diffraction spot over time highlights a localized deformation process, indicating the accumulation of crystal defects such as dislocations or vacancies. These defects could result from irradiation-induced strain or chemical reactions affecting the atomic structure of the nanowire.

The evaluation of the thermal effect induced by the X-ray beam showed that the temperature increase remains moderate (~15 K) and is insufficient on its own to explain the observed degradation. This supports the hypothesis of a chemical reaction involving ozone formation under X-ray irradiation, followed by a chemical attack on ZnO, potentially leading to the formation of secondary oxides such as ZnO_2 or $Zn(OH)_2$. This hypothesis aligns with previous studies on other semiconductor nanostructures exposed to intense X-ray beams. Finally, introducing a nitrogen gas flow during the experiment significantly improved the NWs resistance to irradiation, confirming the critical role of reactive species from the ambient air in the observed degradation process.

Chapter 5

In-situ electro-mechanical experiments

This chapter is dedicated to the study of the electromechanical behavior of individual ZnO nanowires (NWs). Although the technological development of nanogenerators has been largely explored, the enhancement of ZnO piezoelectric coefficients at small scales are still debated and values ranging from 20 pm/V to up to 1200 pm/V for 230 nm diameter ZnO NWs have been reported in literature. The uncertainty mainly originates from the difficulty to accurately measure piezoelectric strain in nanostructures due to the minute deformation induced in these small-scale objects. Considering a d_{33} close to the bulk value and an electric field of 100 kV/cm, a piezoelectrically-induced strain of 2 x 10^{-4} [168] is expected resulting in elongations of few angstroms in case of micrometer long NWs. In the case of AFM bending tests on single NWs, this absolute deformation of NWs can only be very roughly estimated and the piezoelectric coefficients can thus not be reliably extracted. In addition, transmission electron microscopy methods hardly give strain resolutions below 10^{-3}. Bragg coherent X-ray diffraction imaging, on the other hand, is highly sensitive to strain with resolution of 10^{-4}. Thus, by measuring the piezoelectrically induced strain as a function of an applied electric field, we aimed to determine the piezoelectric coefficient in a single nanowire. The 3D imaging of the strain field will further enable us to image for the first time the variation of the piezoelectrically induced strain within a NW (both along the NW long axis and within the NW cross-section) with a resolution of better than

10 nm [169].

5.1 Bragg Coherent Diffraction Imaging of ZnO NWs

This section focuses on Bragg coherent X-ray diffraction imaging of individual ZnO NWs performed at the ID01 beamline at the ESRF. Firstly, the preparation and the design of the samples for in-situ electrical actuation are introduced, followed by the experimental setup, and the measurements by BCDI as well as by scanning X-ray diffraction microscopy (SXDM).

5.1.1 Sample preparation

Similar to the in-situ nanomechanical experiments, we used ZnO nanowires (NWs) grown via the hydrothermal method described in Chapter III. For in-situ electro-mechanical testing, a custom-designed micro-patterned structure was used, consisting of a silicon (Si) substrate with aluminum (Al) interdigitated electrodes fabricated through photolithography. The electrodes have a width of about 2 µm and a length of 20 µm and they are spaced by about 2 µm from each other (see Fig. 5.1). These electrodes were connected to large crocodile clips outside the sample through thin Al wires. To prevent direct contact between the NWs and the electrodes and to eliminate any risk of short-circuiting, a thin insulating layer of Al_2O_3 with a thickness of 15 nm was deposited on the entire sample. The NWs were dispersed on top of the sample containing the Al contacts leading to an arbitrary dispersion of these NWs. This approach was chosen because depositing the NWs first and then fabricating electrodes on top of them would risk damaging or displacing the fragile NWs during the electrode deposition process. Additionally, ensuring the NWs remain undisturbed is critical to preserving their structural and piezoelectric integrity for subsequent electromechanical measurements. By dispersing the NWs after electrode fabrication, the experimental setup minimizes possible surface effects between the substrate and NWs, and provides better isolation of the NWs to exterior effects.

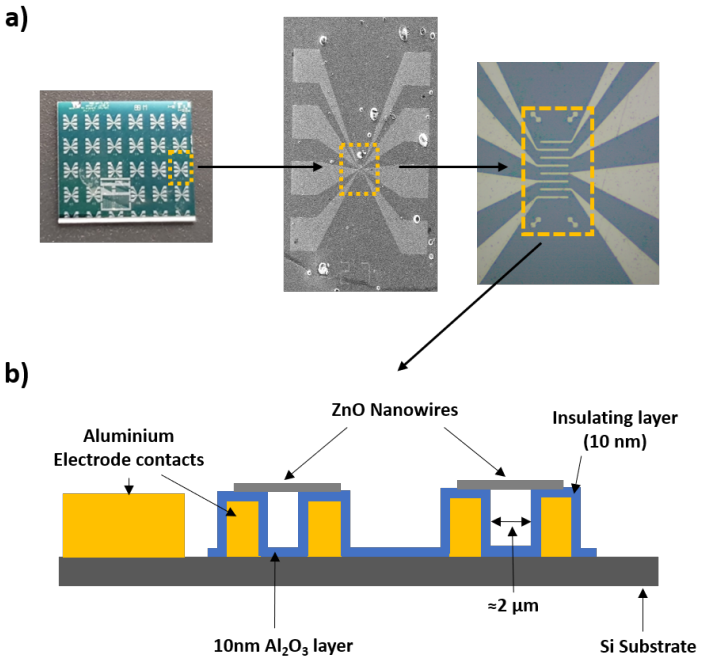

Figure 5.1: a) SEM images of the sample surface for in-situ electromechanical tests on ZnO NWs showing interdigitated Al contacts that were prepared by UV lithography. b) Schematic illustration of the Al electrical contacts including an Al_2O_3 insulating layer and a suspended ZnO NW.

The Figure 5.2 presents a SEM image of a ZnO NW crossing two Al contacts. This NW has a diameter of 133 nm and a suspended length of 1.83 μm

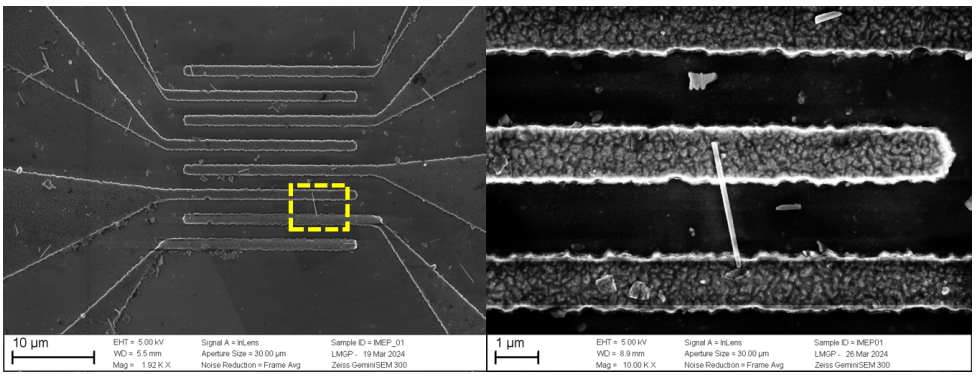

Figure 5.2: Scanning electron microscopy image of the sample studied using BCDI, showing a single connected ZnO NW.

5.1.2 Experimental conditions

The BCDI experiment was conducted on the ID01 beamline at the European Synchrotron ESRF in Grenoble (France). The incident X-ray beam was monochromatized to an energy of 9.7 keV which is above the Zn-K edge allowing for exciting the Zn-K_α fluorescence. The X-ray beam was focused down to a size of 480 nm using Be compound refractive lenses. A 2D Maxipix detector with an array of 516 x 516 pixels with a size of 55 x 55 µm^2 was installed at a distance of 1.5 m from the sample position (see Fig. 5.3).

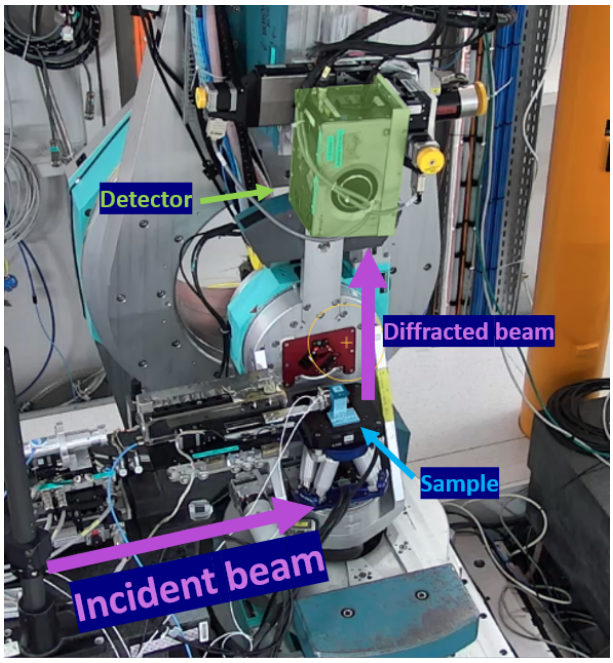

Figure 5.3: Image of the Maxipix detector positioned at δ=86° for the ZnO 3000 peak.

The sample was installed on a magnetic Thorlabs sample mount that allows for reproducible mounting and dismounting of the sample with an accuracy of a few micrometers. This sample holder is installed on top of a piezoelectric stage (Physik Instrumente) that is mounted on top of a hexapod, at an angle of η = 42.93° for the ZnO **3 0 0 0** peak and η = 33.14° for the Al **2 2 2** peak. An optical microscope enabled us to observe the sample and to pre-align it with respect to the incident X-ray beam.

5.1.3 Sample size

As mentioned in Chapter II (section 2.2.3), BCDI measurements provide a three-dimensional mapping of the diffracted intensity in reciprocal space. Figure 5.4 shows the ZnO **3 0 0 0** Bragg reflection, obtained by integrating 200 η scans over a range of $(\eta - 0.3)$ and $(\eta + 0.3)$, with an exposure time of 1 second per scan. The integration was performed along the η axis to enhance signal clarity while preserving angular resolution. The central region corresponds to the highest intensity, as expected for a Bragg peak, Although the gray-scale color-map in this image makes it appear dark.

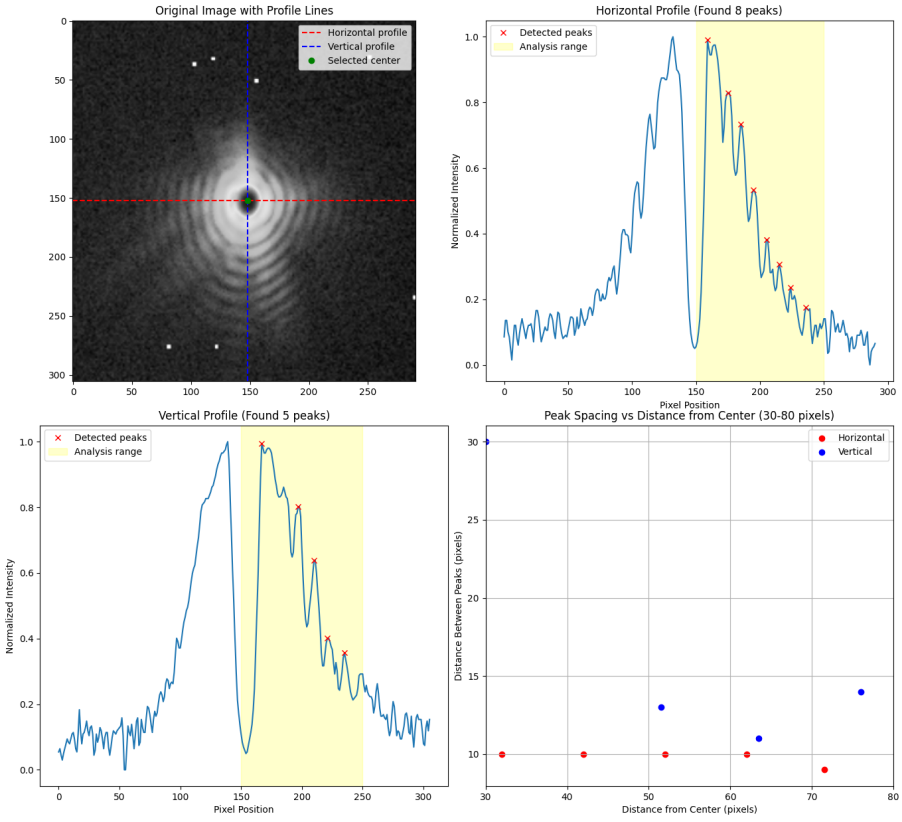

Figure 5.4: Top left : Superposition of 200 scans of the ZnO 3000 Bragg peak measured using BCDI, with vertical and horizontal lines showing the direction of the scan. Top right & Bottom left : Normalized intensity profiles along the horizontal and vertical directions, with detected peaks (red crosses) and analysis regions (yellow shading). Bottom right : Peak spacing as a function of distance from the pattern center, showing variations in fringe periodicity along both directions.

BCDI measurement is essentially the Fourier transform of the real-space electron density of the object. A well-defined, isolated nano-object produces a diffraction pattern with oscillatory fringes due to the sharp boundaries in real space, where the X-ray waves scattered from different points within the object interfere, forming a characteristic diffraction pattern. The intensity and spacing of these fringes are determined by the object's shape and size. Fig. 5.4 presents a diffraction pattern of a random ZnO nanostructure showing well-defined size fringes. The periodicity of the fringes is inversely related to the object's size - the smaller an object the larger is the distance between the size fringes, while larger objects yield more closely spaced fringes. Depending on the shape of an object, the periodicity of these fringes are not necessarily symmetric in all directions (as shown in Fig. 2.8 in Chapter II 2.1.2.4).

The object size L can be directly inferred from the distance between the size fringes, *e.g.* in Fig. 5.4, we use the following equation:

$$L = \frac{2\pi}{\Delta q} \tag{5.1}$$

Where Δq is the fringe spacing in pixels which can be converted into reciprocal space units using :

$$\Delta q = \frac{2\pi}{\lambda} \cdot \frac{\Delta x}{D} \tag{5.2}$$

Considering a sample-detector distance of 1.5 m, a wavelength of 0.128 nm, and an average inter-fringe distance horizontally of 10 pixels with a pixel size of 55 µm, the fringe spacing in reciprocal space amounts to

$$L = 349 \text{ nm} \tag{5.3}$$

While for the vertical inter-fringe direction, the average distance is of 14 pixels, which corresponds to a length of $L = 249$ nm. These values of L are coherent, due to the fact that most of our NWs aren't perfect hexagonals, with some asymmetry in one of the directions, and close to the size of our NWs diameters which are between 200 and 500nm.

5.1.4 Scanning X-Ray Diffraction Microscopy mapping

In order to locate ZnO NWs on the sample surface, scanning X-ray diffraction microscopy was employed, which allows for mapping an area of several 10 µm^2 with a spatial resolution given by the beam size in few minutes. Repeating the 2D imaging for several different incident angles allows to visualize orientation variations of ZnO NWs and to locate NWs that are bent or distorted.

Scanning X-ray diffraction mapping was performed on randomly deposited ZnO NWs lying on the bare Si substrate. Figure 5.5 shows a 5D SXDM mapping of multiple ZnO NWs at the **3 0 0 0** Bragg peak, where the mapping spans an angular range (η) of the sample between ($\eta - 1$) and ($\eta + 1$), with a total of 50 scans recorded in steps of 0.04°, each with an exposure time of 0.2 seconds. The mapped area covers a region containing multiple nanowires, By focusing on a single nanowire shown in Fig. 5.5 b), we observe that the SXDM map of its rocking angle as a function of the detector's ν-angle reveals significant movement of the diffraction peak. For a stationary, defect-free sample, a centered diffraction peak is expected. However, in our case, the diffraction peak exhibits substantial shifts along the x-axis of the detector. These irregularities indicate torsional effects within the nanowire structure. This behavior has been consistently observed for many randomly deposited nanowires that were measured.

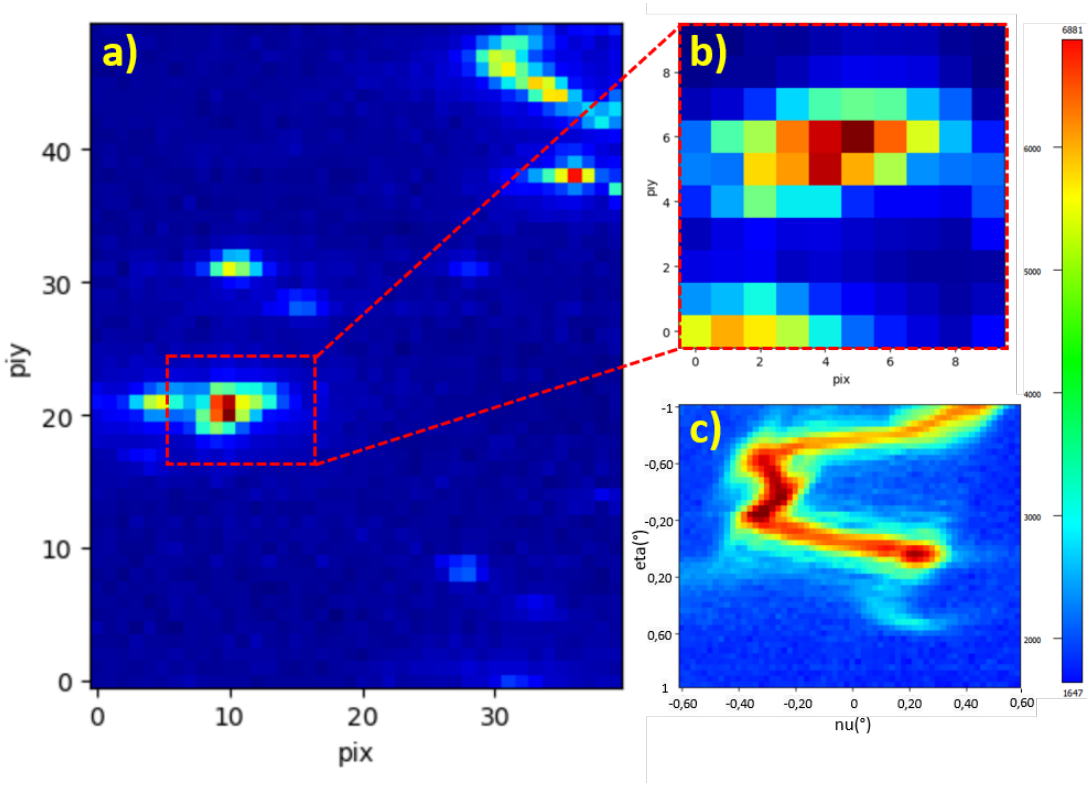

Figure 5.5: a) SXDM map of ZnO nanowires showing Bragg intensity distribution across the mapped area, highlighting several distinct diffraction spots corresponding to individual nanowires. b) Zoomed-in SXDM map focusing on a single nanowire. c) Mapping of the rocking angle as a function of the detector ν angle, demonstrating irregularities and significant twisting of the ZnO nanowire, resulting in the movement of the Bragg spot across the detector.

Figure 5.5 c), shows the variation of the Bragg peak intensity as a function of the rocking angle varying from $(\eta - 1°)$ to $(\eta + 1°)$ and the detector's x-axis which corresponds to the angle ν. This scan gives us important information about the NW as-deposited crystalline state, in which we can see that we have a movement along the ν angle for which it indicates that we observe an internal torsion of the NW. As for the movement along the η angle, it indicates a bending of the NW. Knowing detector angle and distance from the sample, we estimate a maximum bending angle of about 1° and an internal torsion of approximately 0.8°. It should be noted that both the bending and torsion do not vary monotonously along the nanowire.

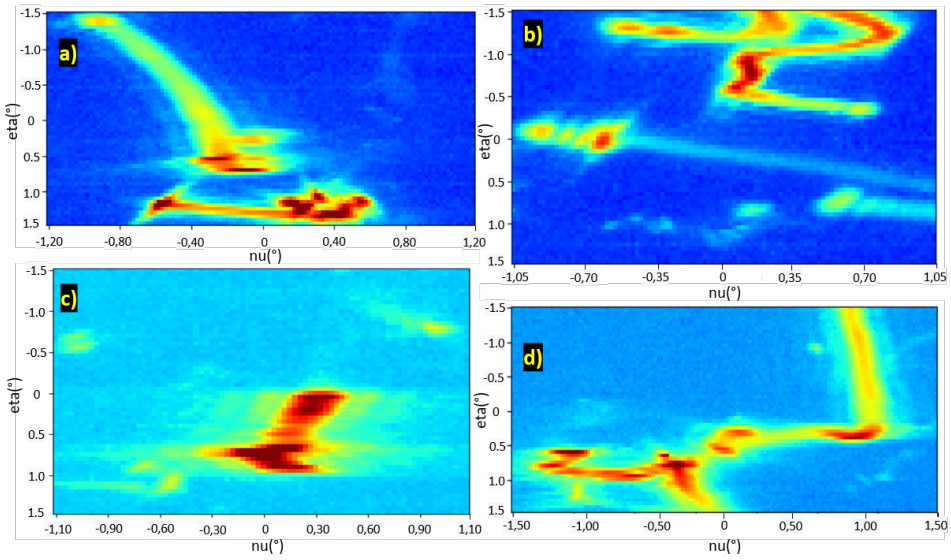

Figure 5.6: Bragg diffraction maps of ZnO nanowires, where the x-axis represents the detector position (ν angle) and the y-axis corresponds to the rocking scan range of $\eta - 1.5°$ to $\eta + 1.5°$. Movement along the x-axis corresponds to torsional deformation of the nanowire(s), while shifts along the y-axis indicate bending.

The different patterns observed in Figure 5.6 (a)-(d) reflect variations in bending, and twisting in the ZnO NWs. These variations likely arise due to surface effects that play a crucial role during the deposition phase. Specifically, residual stresses induced by deposition conditions, surface diffusion, and interactions with the substrate such as Van-der-waals forces that can lead to asymmetric strain distributions, causing the NWs to bend or twist.

5.1.5 BCDI on ZnO nanowires

BCDI was performed on randomly oriented ZnO NWs lying on the bare Si substrate. Figure 5.7 presents a series of diffraction patterns, each displaying clear size fringes. The symmetry of these patterns varies, indicating differences in the size and the shape of the nanowires. The diffraction patterns are generally asymmetric, indicating that the dimensions in the q_x/q_ydirections correspond to the nanowire length while those in the q_z direction corresponds to the nanowire thickness. The inter-fringe spacing differs among the NWs, reflecting variations in their size along the diffraction direction. A finer fringe

spacing suggests a larger nanowire dimension, while wider fringes correspond to smaller NWs. By analyzing these fringe spacings, it is possible to estimate the NW lengths in the direction perpendicular to the fringes. The presence of two or more diffraction signals as seen in Fig. 5.7 d), suggests either multiple crystalline domains within a single nanowire, strain-induced splitting of the Bragg peak, or the simultaneous illumination of distinct nanowires. The elongated horizontal diffraction feature may indicate a bending strain or an extended crystalline facet, while the secondary peak suggests the presence of a separate but nearby crystalline domain.

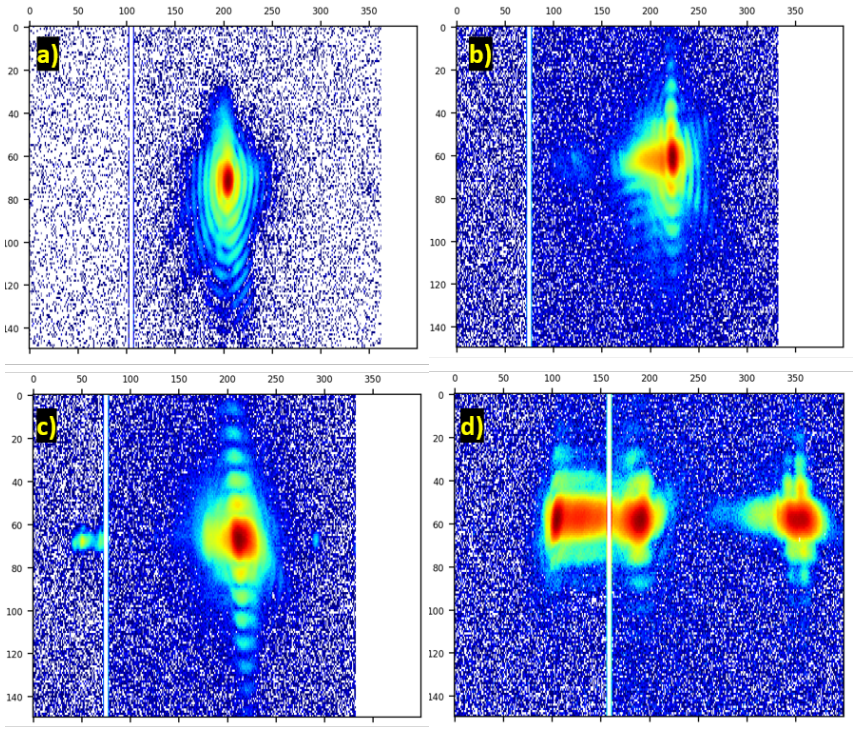

Figure 5.7: 4 examples of raw integrated diffraction patterns of full scans around different ZnO NWs.

The 3D intensity distribution in the vicinity of the ZnO **3 0 0 0** Bragg peak for each of the ZnO NWs was measured by rocking the sample by +/- 0.5° in steps of 0.005° and an exposure time of 5 seconds. To analyze these measurements and to obtain a 3D reconstruction of the sample, the first step involved a "pre-processing" of the data, where the raw ZnO Bragg diffraction patterns obtained during the measurements were assembled. A mask was applied to the four quadrants of the detector to exclude dead regions or noise,

ensuring clean data for the phase retrieval procedure Fig. 5.8, shows an example of the generated data after a "pre-process" procedure.

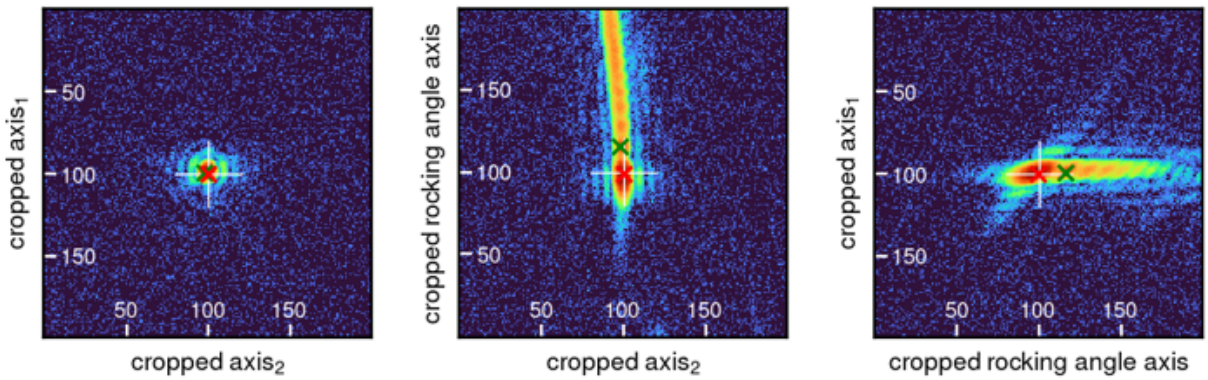

Figure 5.8: The stacking of all Bragg diffraction peaks of the 200-step rocking curve and creation of a signal clean of noise and dead regions. (X is the maximum intensity and X is the center of mass

The figure 5.9 represents a comparison between two diffraction patterns. The top row corresponds to the FFT of the reconstructed object, while the bottom row represents the experimental diffraction pattern that has been orthogonalized. Both sets of images exhibit a similar overall structure and sizes. Phase retrieval was performed using the PyNX software package, which implements several algorithms such as Gerchberg-Saxton, Hybrid Input-Output, Error Reduction, Difference Map etc. The phase retreival process was conducted using dedicated GPUs [170]. If the solution converges, we obtain a reconstructed image of the object's electron density and phase:

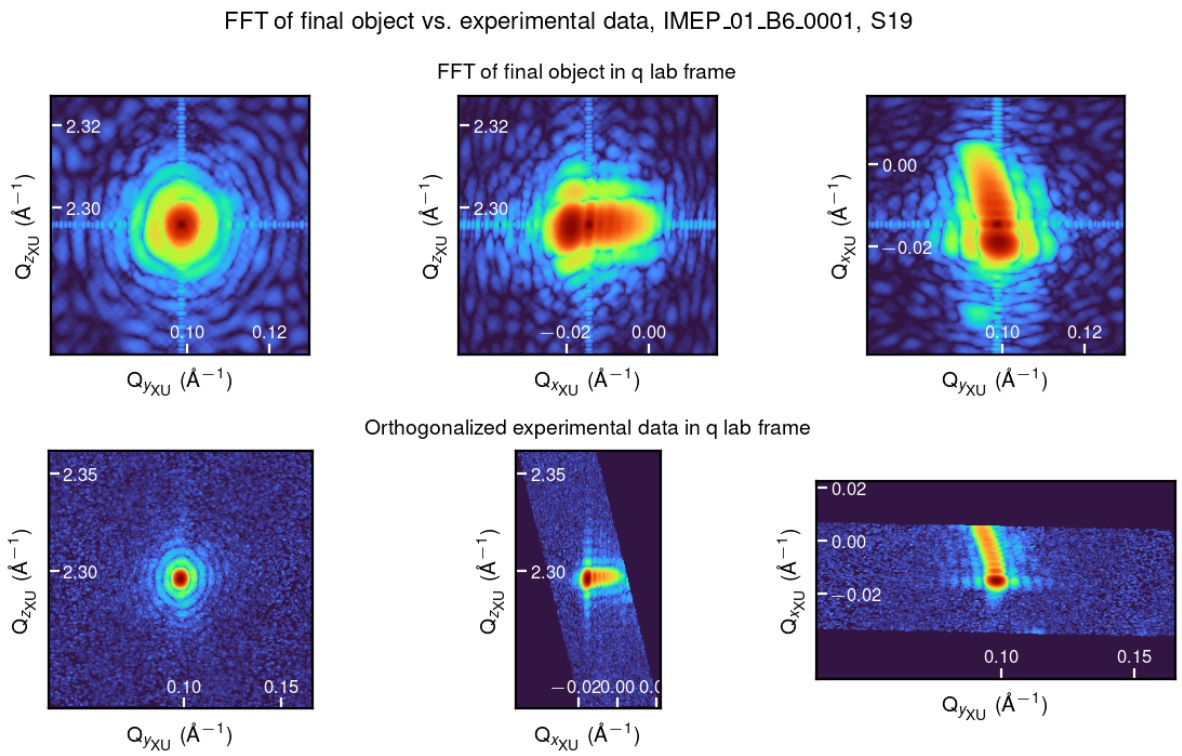

Figure 5.9: FFT of the original diffraction patterns during the phase retrieval step that display intensity distributions in reciprocal space.

For all reconstructions in our case, PyNX employed a sequence of iterative phase retrieval algorithms to refine the solution. The process began with 1000 iterations of the Error Reduction (ER) algorithm, a standard phase retrieval method that enforces constraints both in real space and in reciprocal space. This was followed by 150 iterations of the Hybrid Input-Output (HIO) algorithm, which helps to prevent stagnation by introducing a feedback parameter (β). To further refine the phase retrieval process, 10 iterations of Maximum Likelihood refinement were applied, optimizing the solution by minimizing a likelihood function. Additionally, 1000 iterations of the Relaxed Averaged Alternating Reflections (RAAR) algorithm were performed, striking a balance between convergence stability and aggressive updates by combining aspects of ER and HIO. Finally, 100 reconstruction trials were carried out with different initial conditions. From these 100 reconstructions, the 50 best reconstructions were selected to ensure robustness and

reliability. The algorithm also performed phase unwrapping, allowing for the retrieval of a continuous phase. This ultimately led to the reconstruction of the object, providing a three-dimensional representation of its electron density and phase distribution.

PyNX reconstructs the phase from Bragg diffraction data, which is then used to derive the displacement field. By computing its gradient, we obtain the strain distribution, revealing the mechanical deformations within the sample. The figure below 5.10 presents the reconstruction of the object from the Bragg diffraction data integrated along 3 different directions. The figure shows the variations of the phase (in radians), the displacement (in Å), and the strain field (in %) after the convergence of the reconstruction.

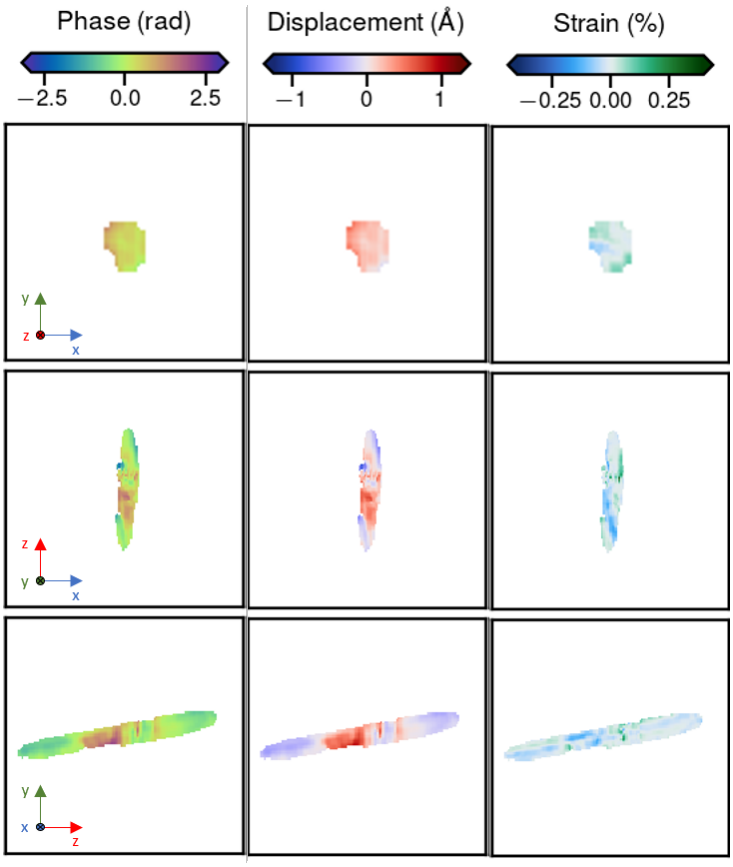

Figure 5.10: Post processing of a BCDI measurement showing the phase, the displacement, and the strain in the reconstructed object.

The reconstructed object represents a ZnO nanowire, with a length of approximately 1.2 µm and a diameter of approximately 200 nm. This size was captured using the large

vertical beam footprint, made possible by the sample surface being inclined at a 43° angle. The recovered phase varies from -2.5 to 2.5 radians, indicating local phase shifts within the structure. The displacement field, extracted from the phase, ranges from -1 to +1 Å. The strain field, computed as the spatial gradient of the displacement, varies between -0.25% and +0.25%, highlighting localized strain variations across the nanowire. These results provide insight into the internal mechanical deformations of the structure of the as-deposited ZnO NWs, likely influenced by growth conditions, defects, or external stresses.

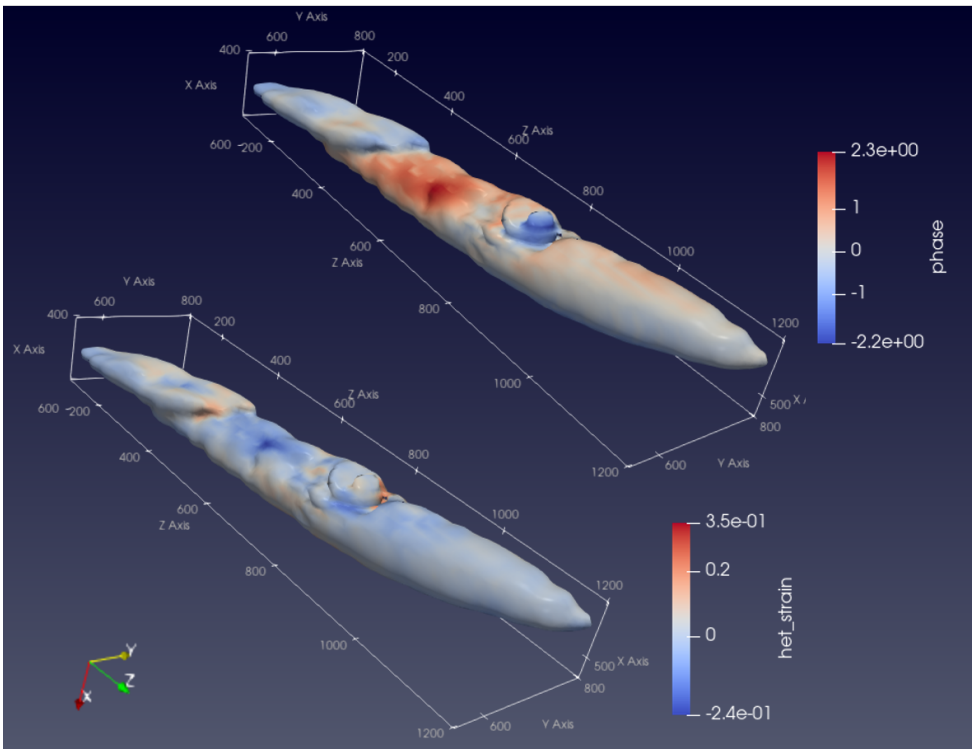

Figure 5.11: 3D representation of the reconstructed nanowire showing a) The distribution of the phase in the nanowire. b) The distribution of strain in the nanowire

A three-dimensional representation of the reconstructed object is presented in Fig. 5.11. The amplitude of this object gives its shape and electron density, while the calculated phase shown in bottom right of (Fig. 5.11). It represents the phase shift of the reconstructed object in radians. This phase shift is directly related to the atomic displacement field within the sample and can be interpreted in the context of strain analysis. The observed rounded morphology of the ZnO NW, rather than well-defined facets, may result from resolution

limitations in reciprocal space, phase retrieval artifacts, or strain-induced distortions.

In order to locate the electrically contacted ZnO NWs, the interdigitated Al contacts were firstly located by SXDM at the Al **2 2 2** Bragg reflection. As demonstrated by the detector image of the Al **2 2 2** Bragg reflection displayed in (Fig. 5.12) showing a section of a Debye-Scherrer ring, the Al contacts are actually polycrystalline. In order to prevent any misalignment when changing the incident angle from the Al **2 2 2** to the ZnO **3 0 0 0** Bragg reflection, the incident angle was set at the Bragg angle of the ZnO **3 0 0 0** Bragg reflection. This misalignment of the incident angle with respect to the η configuration of the Al **2 2 2** Bragg peak is possible thanks to the polycrystallinity of the Al contacts.

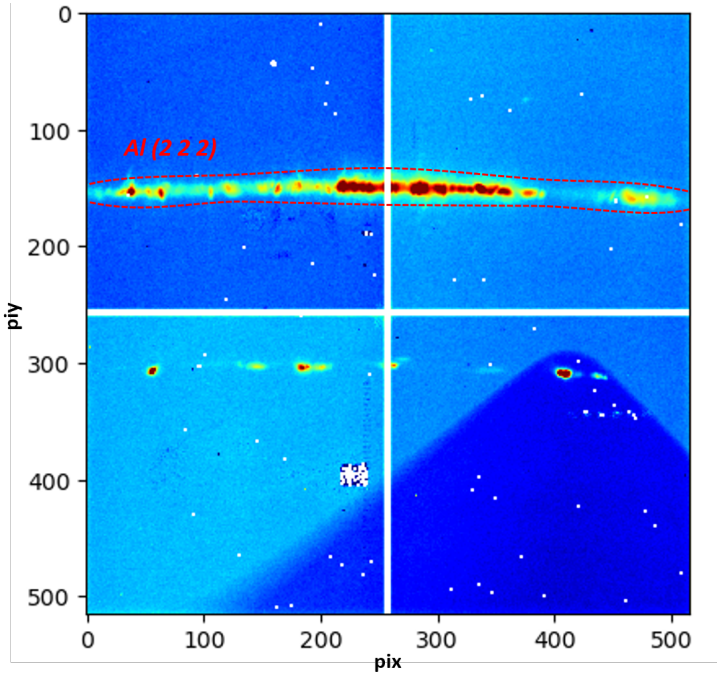

Figure 5.12: A diffraction pattern showing a part of the Al **222** Debye-Scherrer ring

The interdigitated Al contacts were mapped by SXDM. Fig. 5.13 a) presents a SXDM of the Al contacts recorded at the Al **222** Bragg reflection clearly revealing the interdigitated electrodes. Once the electrodes were located, a scanning X-ray diffraction map of the same area was recorded at the ZnO **3 0 0 0** Bragg reflection which is displayed in Fig. 5.13 b).

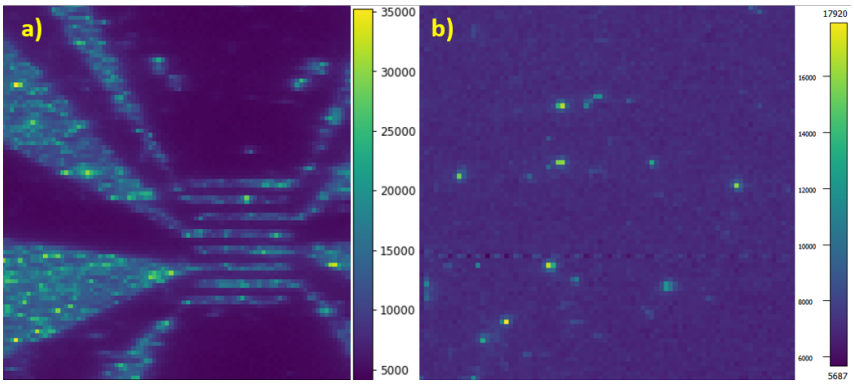

Figure 5.13: a) SXDM mapping of the Al showing the electrodes b) SXDM mapping of the ZnO showing some NWs that are in the diffraction conditions.

Three SXDMs were recorded at -3°, 0°, and 3° incident angles. These SXDM maps were superimposed together with the SEM image of the sample recorded prior to the experiment. By the superposition of these images, the electrically contacted ZnO NW was unambiguously identified (see Fig. 5.14).

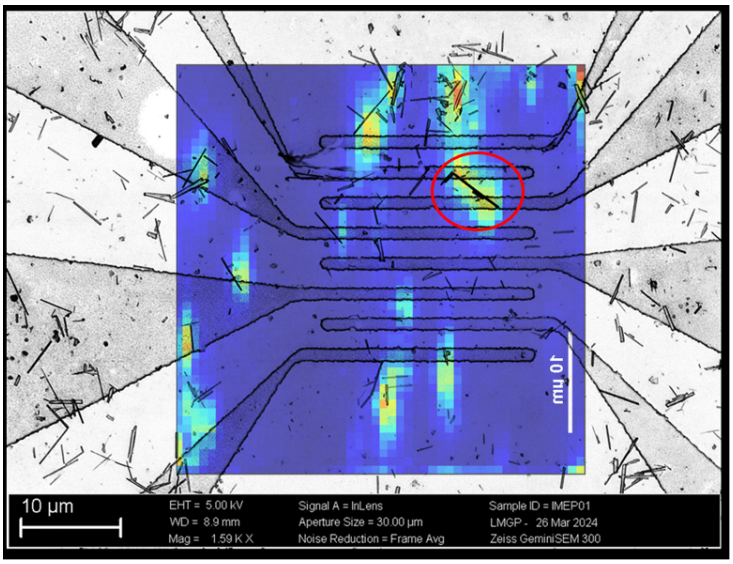

Figure 5.14: The superposition of an SXDM and a SEM map allowing us to correlate the positioning of our nanowires.

After aligning the beam and detecting the positions of the electrically contacted nanowire, the sample was dismounted from the goniometer in order to solder a wire to

the external electrical contacts for *in-situ*electromechanical measurements. However, after soldering, re-installation of the sample on the diffractometer goniometer, and repositioning of the sample, the ZnO NW was actually not on its position anymore as demonstrated by the SXDM maps taken before and after electrical contacting (see Fig. 5.15).

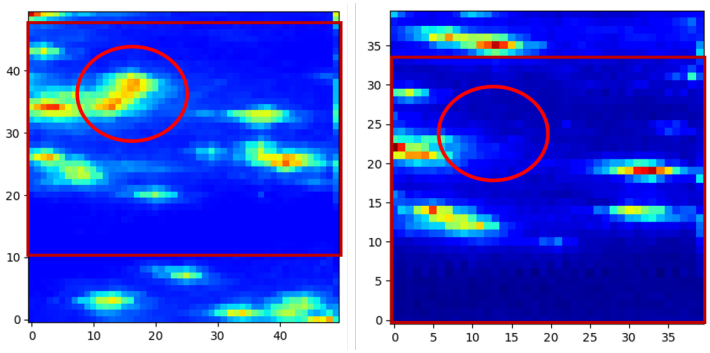

Figure 5.15: SXDM mapping before and after soldering the contacts on the sample, showing the disappearing of our last connected ZnO NW.

This finding was confirmed by optical microscopy. It may be attributed to several possibilities: an electrical discharge causing a direct current through the NW despite the insulating Al_2O_3 layer, an excessive current leading to Joule heating and subsequent damage, an electrostatic charging ejecting the NW from its position, or a general handling mistakes during the experiment resulting in the displacement of the NW.

5.2 Electromechanical testing by in-situ XRF

In this section, we will discuss a second *in situ* electromechanical experiment performed at the P10 beamline at PETRA III.

5.2.1 Sample preparation and alignment

A very similar sample design as in the experiment described above was employed. However, in order to avoid the damaging of an electrically contacted NW due to a direct current and Joule heating during a potential discharging, a slightly thicker Al_2O_3 layer with a thickness of 20 nm was deposited. In addition, wires were soldered to the external contacts of the

sample holder prior to the contacting of the Al electrodes. Thanks to the soldering of the wires before the synchrotron beamtime, the sample also did not have to be dismounted from the goniometer and reduced the amount of handling during the experiment.

The sample was then placed on a stub and held down using super glue. This stub was then positioned on a sample holder in a way that the connected nanowires are almost perpendicular to the beam direction. We then connected the electrodes to the sourcemeter inside the experimental hutch (Fig. 5.16).

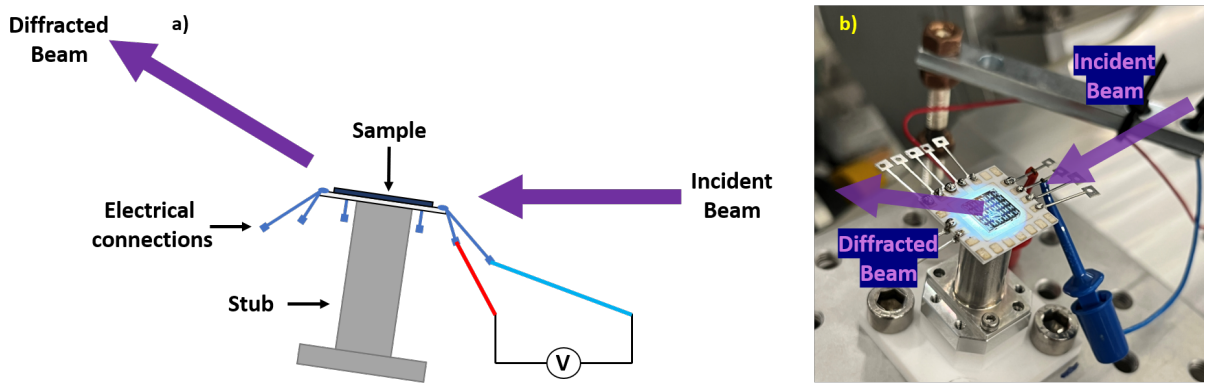

Figure 5.16: a) A schematic of the sample positioned on a stub while connected to a Keithley sourcemeter b) photo of the sample at the P10 beamline

5.2.2 Experimental conditions

This experiment was conducted on the P10 beamline at PETRA III at the Deutsches Elektronen-Synchrotron DESY in Hamburg (Germany). The X-ray beam was monochromatized to an energy of 10.57 keV and was focused down to 0.77 x 1 µm^2 using a series of Be CRLs. The diffratced X-rays were recorded using an Eiger 4M detector with an array of 2070 x 2167 pixels with a size of 75 µm which was installed at a distance of 1.82 m from the sample. The fluorescence yield was monitored using an energy dispersive XR-100SDD detector. In order to apply an electric voltage to the sample, a Keithley (model 6487) sourcemeter was employed.

5.3 X-Ray fluorescence mapping

In order to locate the Al interdigitated electrodes and the electrically connected ZnO nanowire, the sample was mapped by SXDM of the Al 222 Bragg peak and recording simultaneously the Zn (K_α) fluorescence yield as demonstrated by Fig. 5.17.

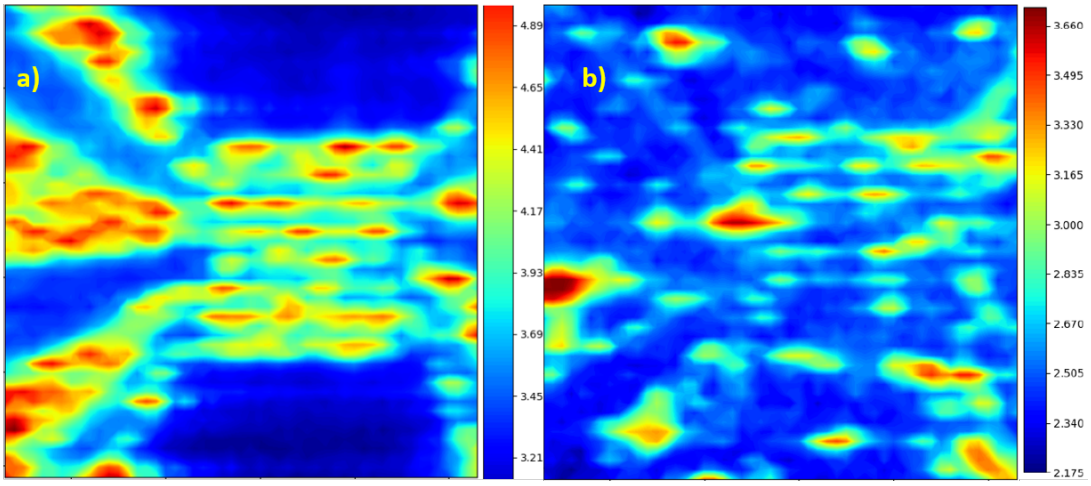

Figure 5.17: a) Diffraction mapping of the Al showing the electrodes b) XRF mapping of the Zn (K_α) line showing several nanowires.

The superposition of the SXDM map and the fluorescence map together with a SEM image taken prior to the experiment allows to identify the electrically NW as shown Fig. 5.19.

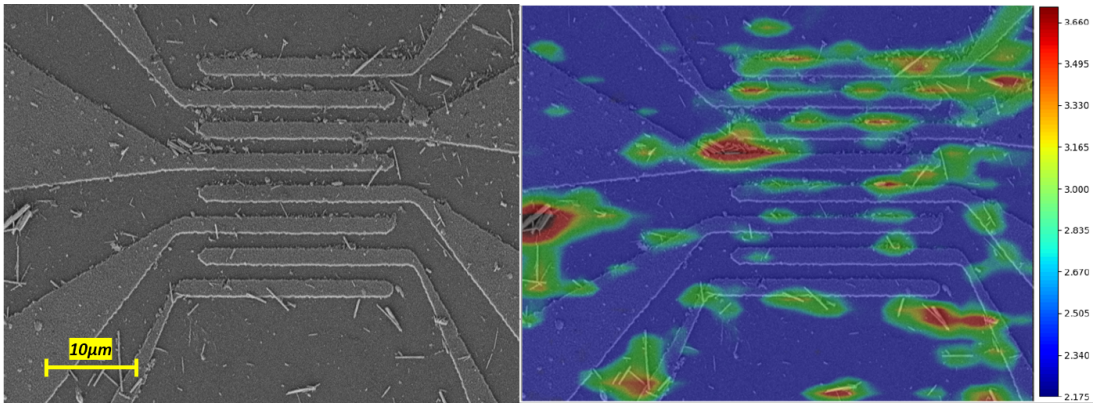

Figure 5.18: The superposition of a XRF and a SEM map allowing us to correlate the positioning of our nanowires.

After identification of the connected NW, an electric voltage was applied between the electrodes while performing fluorescence mapping at each voltage step, as shown in (Fig. 5.19). This image sequence shows XRF intensity maps of a ZnO nanowire under different applied voltages, transitioning from 0 to 6 V and then back to 0 V. The first image (0V) reveals a structured fluorescence pattern with intensities in regions along the nanowire. As the voltage increases to 1.2 V and to 3 V, the fluorescence intensity corresponding to the nanowire seems to decrease and to become more concentrated spatially. At 6V, the fluorescence intensity in the nanowire further reduces, with the intense regions centering even more in the same spot. When the voltage is reset to 0 V, the fluorescence slightly recovers, showing a more diffuse intensity distribution. This suggests some level of reversible change. The variation of the fluorescence signal as a function of the applied voltage may originate from a re-orientation of the ZnO NW within the applied electric field. This experiment demonstrates that the challenge of contacting ZnO NWs electrically has been overcome and that in-situ electromechanical measurements on individual ZnO NWs are actually feasible, although X-ray fluorescence does not give access to the piezoelectric-induced strain in the NWs.

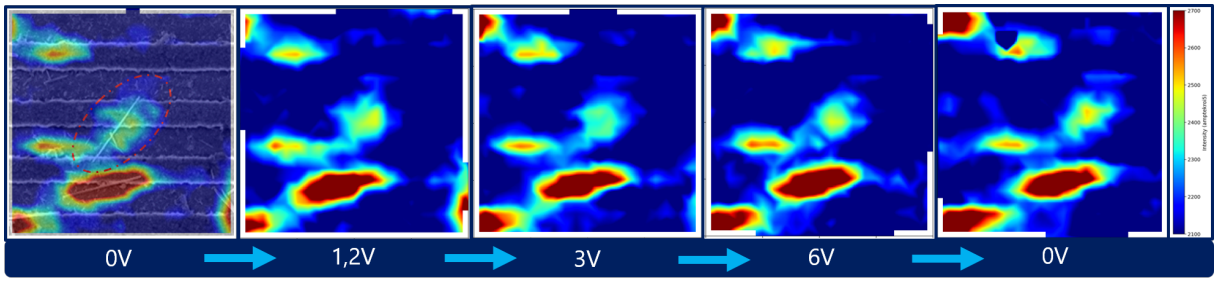

Figure 5.19: XRF map of an area containing a connected nanowire and its evolution when applying the electrical field from 0 to 6V.

5.4 Discussion

Scanning X-ray diffraction microscopy and Bragg Coherent Diffraction Imaging were employed to investigate the structural properties of as-deposited ZnO nanowires. SXDM revealed that the nanowires are bent and twisted on the order of few degrees. This

deformation may originate from the fabrication or being induced during the evaporation of the liquid used for the dispersion of the nanostructures on the substrate. This NW deformation complexified the measurements by BCDI. Any movement of the sample during the rocking scan, and thus displacement of the focused beam along the NW, would lead to the illumination of a part of the NW which is slightly bent or twisted with respect to the initial position. This movement along a deformed elongated object will result in a displacement of the Bragg reflection in reciprocal space. Hence, the phase retrieval process required for reconstructing the 3D electron density and displacement fields was hindered by the limited signal quality. In some cases, the reconstruction process was incoherent, either due to an insufficient diffraction intensity or due to a more pronounced deformation of the NW. One of the key objectives of these experiments was to study ZnO NWs under electrical actuation. However, significant challenges were encountered during sample preparation and measurement. Many electrically contacted NWs were lost during the soldering process. The high temperatures and potential electrical discharges during soldering may have led to mechanical or thermal degradation of the NWs, ultimately preventing successful in-situ measurements. These findings highlight the importance of optimizing contact fabrication techniques, to ensure stable electrical connections without compromising the structural integrity of the NWs. To further characterize the sample and verify the presence of ZnO NWs after soldering and beam exposure, X-ray fluorescence (XRF) mapping was performed. This technique provided elemental distribution maps, confirming the locations of the NWs and detecting possible material loss or contamination. The fluorescence data reinforced the observations from BCDI by indicating areas where the NWs either had remained intact or had been physically displaced during sample preparation. Given the difficulties encountered in the initial BCDI measurements, a follow-up experiment was conducted at the SIXS beamline to improve the experimental setup and optimize data collection strategies. The goal of this experiment was to refine the beamline configuration, enhance data acquisition methods, and explore new approaches to overcome the challenges faced during BCDI of small ZnO NWs. By leveraging insights from the SIXS experiment, improvements in beam focusing, exposure conditions, and sample environment control could be implemented in future studies to enhance the reliability of BCDI measurements. Overall, these experiments demonstrated the feasibility of BCDI

for studying ZnO NWs but also revealed significant experimental challenges, particularly for small NWs and electrically contacted structures. Future work should focus on refining measurement conditions, optimizing sample preparation techniques, and improving phase retrieval algorithms to enable more consistent reconstructions.

General discussion

The results presented in this thesis provide significant insights into the mechanical and electromechanical behavior of ZnO NWs, highlighting their potential for nanoscale applications in piezoelectric energy harvesting, sensors, and flexible electronics. A key motivation for this research was the theoretical prediction of a size-dependent enhancement in piezoelectric coefficients, which prompted experimental investigations using advanced characterization methods.

Through in-situ nanomechanical testing using the custom-built SFINX AFM system in combination with Laue microdiffraction, the mechanical properties of ZnO NWs were characterized in detail. The findings revealed remarkable elasticity and high fracture strengths reaching up to 3 GPa, with maximum strains around 1.9%, values an order of magnitude higher than those of bulk ZnO. While elastic deformation was observed in all tested NWs, some nanowires exhibited plastic behavior before failure. This plasticity is particularly noteworthy, as bulk ZnO is generally considered brittle. The observed plasticity is likely due to the nucleation of dislocations and its subsequent motion at the nanoscale, along with surface effects and defect structures unique to ZnO NWs. *Post-mortem* HRTEM studies of a three-point bent ZnO NW confirmed the presence of dislocation loops and sub-grain boundaries near the NW supports, correlating with high-stress regions predicted by finite element simulations. The use of the Euler-Bernoulli beam theory and FEM simulations allowed for a detailed understanding of NW deflection and stress distribution, with results aligning well with experimental observations. Notably, torsional effects were detected during three-point bending, likely due to slight misalignment between the NWs and the Si supports. These findings highlight the complexity of nanoscale mechanical testing and the interplay between elastic and plastic deformations in ZnO NWs. The

ability of ZnO NWs to sustain plastic deformation without immediate failure opens new possibilities for their use in flexible and resilient nanoscale devices where mechanical reliability is crucial.

The study then transitioned to investigating ZnO NWs using scanning X-ray diffraction mapping, Bragg Coherent Diffraction Imaging and X-ray fluorescence. SXDM revealed that the NWs are actually bent and twisted by few degrees. This deformation may originate from the fabrication process or from the dispersion of the NWs on the substrate. BCDI proved to be particularly advantageous due to its non-destructive, high-resolution 3D strain mapping capabilities. Unlike traditional X-ray diffraction techniques, which provide averaged strain measurements, BCDI allowed for the visualization of nanoscale strain variations and subtle structural deformations in individual NWs. This capability is essential for understanding the complex coupling between mechanical stress and electrical fields in ZnO NWs, particularly in the context of piezoelectric energy harvesting and sensing applications. However, in-situ BCDI during electrical actuation was not successful due to the loss of electrically contacted NW during the handling and soldering process. Modifications of the sample preparation eventually allowed for successful in-situ X-ray fluorescence experiments. The ability to combine electrical stimuli with advanced X-ray imaging techniques will enable the real-time tracking of strain evolution and defect formation at the nanoscale. Despite the challenges encountered, these experiments represent a significant step toward integrating in-situ electromechanical testing with high-resolution X-ray diffraction imaging. The insights gained from BCDI highlight the potential for real-time visualization of strain dynamics, defect evolution, and piezoelectric response, opening new avenues for optimizing the performance of ZnO NW-based devices.

This work represents a significant advancement in the understanding of nanoscale mechanics and electromechanical coupling in ZnO NWs, bridging theoretical predictions with rigorous experimental validation. The results provide a clear pathway for optimizing ZnO-based nanoscale devices, particularly for applications in piezoelectric energy harvesting, flexible sensors, and high-resolution electromechanical actuators. By combining in-situ nanomechanical testing, Laue microdiffraction, FEM simulations, and BCDI, this work demonstrates how advanced synchrotron techniques can reveal the fundamental properties of nanomaterials. Moving forward, further integration of theory, simulations,

and experimental methodologies will be essential for unlocking the full potential of ZnO and other 1D piezoelectric nanostructures, paving the way for the next generation of nanoscale electromechanical technologies.

The results of this thesis underscore the immense potential of ZnO NWs in nanoscale applications, particularly in piezoelectric nanogenerators, sensors, and actuators. The demonstrated size-dependent mechanical properties and defect-induced plasticity present opportunities for engineering NWs with tailored properties for specific applications. Future research should focus on further refining synthesis methods to control defect densities and optimize mechanical performance, which will enable the design of ZnO-based devices with superior performance and durability. Future research should prioritize refining synthesis methods to reach a greater control over defect densities during growth, which are crucial for achieving consistent mechanical and piezoelectric responses. The integration of advanced characterization techniques such as Laue microdiffraction, high-resolution transmission electron microscopy (HRTEM), and Bragg coherent diffraction imaging (BCDI) with in-situ actuation experiments represents a powerful approach for probing the coupled electromechanical phenomena. These methods enable a detailed understanding of strain distributions, defect interactions, and piezoelectric responses at the nanoscale. One promising perspective is to measure three independent Bragg peaks using BCDI to obtain a spatially resolved full strain tensor, which then provides direct insights into size effects and the intrinsic piezoelectric properties of ZnO nanowires. However, because these nanowires are elongated quasi-1D structures, they are not ideally suited for BCDI. In contrast, Bragg ptychography could allow for mapping the complete nanowire, offering a more comprehensive view of its structure while reducing the impact of pre-deformation on the measurements. However, the challenge lies in developing robust, reproducible, and well-characterized samples prior to performing such advanced in-situ measurements at synchrotron facilities. The samples for connected ZnO NWs need to be prepared with high precision, the ability to manually lift and connect a single ZnO NW, and suspend it on electrical contacts can make an optimal sample to study these properties for different NW diameters which can put into evidence the size-effect on the piezoelectric parameters of the ZnO NWs, while of course, taking all precautions against electrical discharge and better handling of the sample to avoid its destruction. Moreover, the implications of these findings

extend beyond ZnO nanowires. Future investigations could explore other one-dimensional piezoelectric materials, such as GaAs and GaN, to provide comparative insights into their piezoelectric performance at the nanoscale. Studying these materials in parallel with ZnO NWs would expand the material toolkit for n ext-generation nanoscale devices and shed light on the influence of material composition and structure on piezoelectric behavior. Efforts should also focus on understanding and mitigating beam-induced damage, which remains a persistent issue during synchrotron-based experiments. Implementing experimental setups under vacuum conditions, employing beam filters, intensity modulation, or using cryogenic environments could significantly minimize contamination and structural alterations.

Further advancements in synchrotron facilities and experimental setups could play a transformative role. Enhancing sample holders for stability during in-situ measurements, reducing beam sizes for higher spatial resolution, and incorporating faster detectors would improve data quality and allow for a broader range of experiments. Finally, this research highlights the importance of coupling experimental insights with theoretical models. Future work could incorporate more sophisticated simulations, including ab initio methods, to capture the electronic and piezoelectric responses of ZnO NWs under simultaneous mechanical and electrical stresses. Investigations into the role of surface states, flexoelectricity, and nanoscale charge dynamics would provide a more comprehensive understanding of these materials behavior.

In conclusion, this thesis represents a significant step toward unlocking the potential of ZnO NWs for next-generation nanoscale technologies. By bridging experimental validation with advanced theoretical modeling, it lays the groundwork for innovative applications that exploit the unique properties of ZnO and other piezoelectric nanomaterials. Through continued interdisciplinary efforts in synthesis, characterization, and simulation, the full potential of piezoelectric NWs can be realized, enabling transformative advancements in energy harvesting, sensing, and actuation technologies.

Bibliography

[1] Patrick Commins, Durga Prasad Karothu, and Panče Naumov. Is a bent crystal still a single crystal? *Angewandte Chemie International Edition*, 58(30):10052–10060, 2019.

[2] Joanna Moneta. *Mechanisms of strain relaxation in InGaN films grown on (0001)-oriented GaN substrates*. PhD thesis, Instytut Wysokich Ciśnień PAN, 10 2022.

[3] Bruker. https://www.bruker.com/fr/products-and-solutions/test-and-measurement/nanomechanical-instruments-for-sem-tem/push-to-pull-device.html, 2024.

[4] Yong Zhu and Horacio D Espinosa. An electromechanical material testing system for in situ electron microscopy and applications. *Proceedings of the National Academy of Sciences*, 102(41):14503–14508, 2005.

[5] Horacio D Espinosa, Yong Zhu, and Nicolaie Moldovan. Design and operation of a mems-based material testing system for nanomechanical characterization. *Journal of Microelectromechanical Systems*, 16(5):1219–1231, 2007.

[6] Sergei Vlassov, Dmitry Bocharov, Boris Polyakov, Mikk Vahtrus, Andris Šutka, Sven Oras, Veronika Zadin, and Andreas Kyritsakis. Critical review on experimental and theoretical studies of elastic properties of wurtzite-structured zno nanowires. *Nanotechnology Reviews*, 12(1):20220505, 2023.

[7] Sergei Vlassov, Boris Polyakov, Sven Oras, Mikk Vahtrus, Mikk Antsov, Andris Šutka, Krisjanis Smits, Leonid M Dorogin, and Rünno Lõhmus. Complex tribomechanical

characterization of zno nanowires: nanomanipulations supported by fem simulations. *Nanotechnology*, 27(33):335701, 2016.

[8] K. Momeni, Gregory M. Odegard, and Reza S. Yassar. Finite size effect on the piezoelectric properties of zno nanobelts: A molecular dynamics approach. *Acta Materialia*, 60(13):5117–5124, 2012.

[9] Zhong Lin Wang. Nanopiezotronics. *Advanced Materials*, 19(6):889–892, 2007.

[10] Zhong Lin Wang. Energy harvesting for self-powered nanosystems. *Nano Research*, 1:1–8, 2008.

[11] Sheng Xu, Yong Qin, Chen Xu, Yaguang Wei, Rusen Yang, and Zhong Lin Wang. Self-powered nanowire devices. *Nature nanotechnology*, 5(5):366–373, 2010.

[12] Rafael A Vicente, Itamar T Neckel, Subramanian KRS Sankaranarayanan, José Solla-Gullon, and Pablo S Fernández. Bragg coherent diffraction imaging for in situ studies in electrocatalysis. *ACS nano*, 15(4):6129–6146, 2021.

[13] SPring. Birth of x-ray beams of nanometer size, world's smallest diameter - extraordinary beam enabling ultrahigh resolution, November 2024.

[14] Andreas Schümmer, H-Ch Mertins, Claus Michael Schneider, Roman Adam, Stefan Trellenkamp, Rene Borowski, Larissa Juschkin, and Ulf Berges. Fast and easy fabrication methodology of fresnel zone plates for the extreme ultraviolet and soft x-ray regions. *Applied Optics*, 58(4):1057–1063, 2019.

[15] Bruno Lengeler, Christian G Schroer, Marion Kuhlmann, Boris Benner, Til Florian Günzler, Olga Kurapova, Federico Zontone, Anatoly Snigirev, and Irina Snigireva. Refractive x-ray lenses. *Journal of Physics D: Applied Physics*, 38(10A):A218, 2005.

[16] Jean-sebastien Micha. Laue microdiffraction. ESRF. Accessed on [07/01/2025].

[17] P Stadelmann. Image analysis and simulation software in transmission electron microscopy. *Microscopy and Microanalysis*, 9(S03):60–61, 2003.

[18] Zhe Ren. *Nanomechanics: combining mechanical testing in situ with focused X-ray diffraction on a synchroton beamline*. PhD thesis, Aix-Marseille, 2015.

[19] Florian Lauraux. *Etudes nano-mécaniques in situ de nanostructures métalliques utilisant le rayonnement synchrotron*. PhD thesis, Aix-Marseille, 2020.

[20] AdvancedTEC™. Nanosensors™ afm tips. https://www.nanosensors.com/, 2024. [Accessed 24-11-2024].

[21] Zhe Ren. *Nanomechanics : combining mechanical testing in situ with focused X-ray diffraction on a synchroton beamline*. PhD thesis, Aix-Marseille University, 2015.

[22] Yifan Gao and Zhong Lin Wang. Electrostatic potential in a bent piezoelectric nanowire. the fundamental theory of nanogenerator and nanopiezotronics. *Nano letters*, 7(8):2499–2505, 2007.

[23] Ali Al Hassan, Jonas Lähnemann, Arman Davtyan, Mahmoud Al-Humaidi, Jesús Herranz, Danial Bahrami, Taseer Anjum, Florian Bertram, Arka Bikash Dey, Lutz Geelhaar, et al. Beam damage of single semiconductor nanowires during x-ray nanobeam diffraction experiments. *Journal of synchrotron radiation*, 27(5):1200–1208, 2020.

[24] U.S. Geological Survey. Zinc statistics and information, 2023.

[25] Hadis Morkoç and Ümit Özgür. *Zinc oxide: fundamentals, materials and device technology*. John Wiley & Sons, 2008.

[26] K Tapily, D Gu, H Baumgart, G Namkoong, D Stegall, and AA Elmustafa. Mechanical and structural characterization of atomic layer deposition-based zno films. *Semiconductor science and technology*, 26(11):115005, 2011.

[27] KA Matori, MHM Zaid, HAA Sidek, MK Halimah, ZA Wahab, and MGM Sabri. Influence of zno on the ultrasonic velocity and elastic moduli of soda lime silicate glasses. *International Journal of Physical Sciences*, 5(14):2212–2216, 2010.

[28] I Vurgaftman and JR n Meyer. Band parameters for nitrogen-containing semiconductors. *Journal of applied physics*, 94(6):3675–3696, 2003.

[29] NIST. X-ray transition energies database : https://www.nist.gov/pml/x-ray-transition-energies-database, Oct 2024.

[30] eDisciplinas. X-ray absorption edges, characteristic x-ray lines and fluorescence yield, Oct 2024.

[31] Christopher J Frederickson, Jae-Young Koh, and Ashley I Bush. The neurobiology of zinc in health and disease. *Nature Reviews Neuroscience*, 6(6):449–462, 2005.

[32] Valentine Walsh, Tracey Chaplin, and Ruth Siddall. *Pigment Compendium: A Dictionary and Optical Microscopy of Historic Pigments*. Taylor & Francis, 2008.

[33] Amir Moezzi, Andrew M McDonagh, and Michael B Cortie. Zinc oxide particles: Synthesis, properties and applications. *Chemical engineering journal*, 185:1–22, 2012.

[34] Harvey E Brown. *Zinc oxide rediscovered*. New Jersey Zinc Company, 1957.

[35] RL Hoffman, Benjamin J Norris, and JF Wager. Zno-based transparent thin-film transistors. *Applied Physics Letters*, 82(5):733–735, 2003.

[36] Dae-Kue Hwang, Min-Suk Oh, Jae-Hong Lim, and Seong-Ju Park. Zno thin films and light-emitting diodes. *Journal of Physics D: Applied Physics*, 40(22):R387, 2007.

[37] CW Bunn. The lattice-dimensions of zinc oxide. *Proceedings of the Physical Society*, 47(5):835, 1935.

[38] Linus Pauling. Interatomic distances and bond character in the oxygen acids and related substances. *The Journal of Physical Chemistry*, 56(3):361–365, 1952.

[39] JC Phillips and Walter A Harrison. Bonds and bands in semiconductors, 1974.

[40] Xiang Yang Kong and Zhong Lin Wang. Polar-surface dominated zno nanobelts and the electrostatic energy induced nanohelixes, nanosprings, and nanospirals. *Applied physics letters*, 84(6):975–977, 2004.

[41] Chunguang Tang, Michelle JS Spencer, and Amanda S Barnard. Activity of zno polar surfaces: an insight from surface energies. *Physical Chemistry Chemical Physics*, 16(40):22139–22144, 2014.

[42] Zeshan Hu, Gerko Oskam, and Peter C Searson. Influence of solvent on the growth of zno nanoparticles. *Journal of colloid and interface science*, 263(2):454–460, 2003.

[43] Shuangxing Dai and Harold S Park. Surface effects on the piezoelectricity of zno nanowires. *Journal of the Mechanics and Physics of Solids*, 61(2):385–397, 2013.

[44] A Akhtar and A Teghtsoonian. Plastic deformation of zirconium single crystals. *Acta Metallurgica*, 19(7):655–663, 1971.

[45] Tapatee Kundu Roy. Assessing hardness and fracture toughness in sintered zinc oxide ceramics through indentation technique. *Materials Science and Engineering: A*, 640:267–274, 2015.

[46] Tapatee Kundu Roy. Estimation of fracture toughness in zno ceramics from indentation crack opening displacement measurements. *Measurement*, 137:588–594, 2019.

[47] Ümit Özgür, Ya I Alivov, Chunli Liu, Ali Teke, Michael A Reshchikov, S Doğan, VCSJ Avrutin, S-J Cho, Morkoç, and H. A comprehensive review of zno materials and devices. *Journal of applied physics*, 98(4), 2005.

[48] Hung-I Lin, Ray-Hua Horng, Kun-Ching Shen, and Dong-Sing Wuu. Zno nanowires embedded in epoxy resin separating from the substrate for wearable electronics applications. *IEEE Transactions on Nanotechnology*, 13(3):458–463, 2013.

[49] Mercedes Gabás, Angel Landa-Cánovas, José Luis Costa-Krämer, Fernando Agulló-Rueda, Agustín R González-Elipe, Pilar Díaz-Carrasco, Jorge Hernández-Moro, Israel Lorite, Pilar Herrero, Pedro Castillero, et al. Differences in n-type doping efficiency between al-and ga-zno films. *Journal of Applied Physics*, 113(16), 2013.

[50] Shou-Yi Kuo, Wei-Chun Chen, Fang-I Lai, Chin-Pao Cheng, Hao-Chung Kuo, Shing-Chung Wang, and Wen-Feng Hsieh. Effects of doping concentration and annealing temperature on properties of highly-oriented al-doped zno films. *Journal of crystal growth*, 287(1):78–84, 2006.

[51] SB Zhang, S-H Wei, and Alex Zunger. Intrinsic n-type versus p-type doping asymmetry and the defect physics of zno. *Physical Review B*, 63(7):075205, 2001.

[52] Kyoung-Kook Kim, Hyun-Sik Kim, Dae-Kue Hwang, Jae-Hong Lim, and Seong-Ju Park. Realization of p-type zno thin films via phosphorus doping and thermal activation of the dopant. *Applied Physics Letters*, 83(1):63–65, 2003.

[53] Anderson Janotti and Chris G Van de Walle. Fundamentals of zinc oxide as a semiconductor. *Reports on progress in physics*, 72(12):126501, 2009.

[54] Jacques Curie and Pierre Curie. Développement par compression de l'électricité polaire dans les cristaux hémièdres à faces inclinées. *Bulletin de minéralogie*, 3(4):90–93, 1880.

[55] BERNARD Jaffe, WILLIAM R Cook, and HJPC Jaffe. The piezoelectric effect in ceramics. *Piezoelectric ceramics*, pages 7–21, 1971.

[56] Gabriel Lippmann. Principe de la conservation de l'électricité, ou second principe de la théorie des phénomènes électriques. *J. Phys. Theor. Appl.*, 10(1):381–394, 1881.

[57] Qin and Qing-Hua. Introduction to piezoelectricity. *Advanced Mechanics of Piezoelectricity*, pages 1–19, 2013.

[58] Shuangzhe Zhang, Haiyan Yao, Wenliang Fan, Yu Hao, Xudong Wu, and Dongyuan Hou. Effects of flexoelectricity and surface elasticity on piezoelectric potential in a bent zno nanowire. In *IOP Conference series: materials science and engineering*, volume 167, page 012023. IOP Publishing, 2017.

[59] Gordon E Moore. Cramming more components onto integrated circuits. *Proceedings of the IEEE*, 86(1):82–85, 1998.

[60] Sidney S Brenner. Tensile strength of whiskers. *Journal of applied physics*, 27(12):1484–1491, 1956.

[61] Julia Deuschle, Susan Enders, and Eduard Arzt. Surface detection in nanoindentation of soft polymers. *Journal of Materials Research*, 22(11):3107–3119, 2007.

[62] Oliver A Bauchau and James I Craig. Euler-bernoulli beam theory. In *Structural analysis*, pages 173–221. Springer, 2009.

[63] Ali Vazinishayan, Shuming Yang, Dasaradha Rao Lambada, and Yiming Wang. Mechanical behavior enhancement of zno nanowire by embedding different nanowires. *Results in Physics*, 9:218–224, 2018.

[64] Michael D Uchic, Dennis M Dimiduk, Jeffrey N Florando, and William D Nix. Sample dimensions influence strength and crystal plasticity. *Science*, 305(5686):986–989, 2004.

[65] Rafael Soler, Jeffrey M Wheeler, Hyung-Jun Chang, Javier Segurado, Johann Michler, Javier Llorca, and Jon M Molina-Aldareguia. Understanding size effects on the strength of single crystals through high-temperature micropillar compression. *Acta materialia*, 81:50–57, 2014.

[66] Sharif Shahbeyk, George Z Voyiadjis, Vahid Habibi, Sarah Hashemi Astaneh, and Mohammadreza Yaghoobi. Review of size effects during micropillar compression test: Experiments and atomistic simulations. *Crystals*, 9(11):591, 2019.

[67] CR Mayer, LW Yang, SS Singh, J Llorca, JM Molina-Aldareguia, YL Shen, and Nikhilesh Chawla. Anisotropy, size, and aspect ratio effects on micropillar compression of alsic nanolaminate composites. *Acta Materialia*, 114:25–32, 2016.

[68] Yonghai Yue, Pan Liu, Ze Zhang, Xiaodong Han, and En Ma. Approaching the theoretical elastic strain limit in copper nanowires. *Nano letters*, 11(8):3151–3155, 2011.

[69] Wei Wu, Wanli Li, Fengzhou Fang, and Zong Wei Xu. *Microtool Fabrication by Focused Ion Beam Technology*, pages 1–33. Springer London, London, 2013.

[70] William D Callister and David G Rethwisch. *Fundamentals of Materials Science and Engineering: APS104S: Introduction to Materials and Chemistry*. John Wiley & Sons, 2009.

[71] P Pirouz, JL Demenet, and MH Hong. On transition temperatures in the plasticity and fracture of semiconductors. *Philosophical Magazine A*, 81(5):1207–1227, 2001.

[72] Fredrik Östlund, Karolina Rzepiejewska-Malyska, Klaus Leifer, Lucas M Hale, Yuye Tang, Roberto Ballarini, William W Gerberich, and Johann Michler. Brittle-to-ductile transition in uniaxial compression of silicon pillars at room temperature. *Advanced Functional Materials*, 19(15):2439–2444, 2009.

[73] Shanling Wang. *Brittle-to-ductile transition behavior of gallium arsenide*. Case Western Reserve University, 2006.

[74] A Merabet, M Texier, C Tromas, Sandrine Brochard, Laurent Pizzagalli, L Thilly, J Rabier, A Talneau, Y-M Le Vaillant, O Thomas, et al. Low-temperature intrinsic plasticity in silicon at small scales. *Acta Materialia*, 161:54–60, 2018.

[75] MA Haque and MTA Saif. In-situ tensile testing of nano-scale specimens in sem and tem. *Experimental mechanics*, 42:123–128, 2002.

[76] JA Brown and NM Ghoniem. Reversible–irreversible plasticity transition in twinned copper nanopillars. *Acta materialia*, 58(3):886–894, 2010.

[77] Subin Lee, Jiseong Im, Youngdong Yoo, Erik Bitzek, Daniel Kiener, Gunther Richter, Bongsoo Kim, and Sang Ho Oh. Reversible cyclic deformation mechanism of gold nanowires by twinning–detwinning transition evidenced from in situ tem. *Nature communications*, 5(1):3033, 2014.

[78] Suzhi Li, Xiangdong Ding, Junkai Deng, Turab Lookman, Ju Li, Xiaobing Ren, Jun Sun, and Avadh Saxena. Superelasticity in bcc nanowires by a reversible twinning mechanism. *Physical Review B—Condensed Matter and Materials Physics*, 82(20):205435, 2010.

[79] L Dai, WCD Cheong, CH Sow, CT Lim, and VBC Tan. Molecular dynamics simulation of zno nanowires: size effects, defects, and super ductility. *Langmuir*, 26(2):1165–1171, 2010.

[80] Ravi Agrawal, Bei Peng, Eleftherios E Gdoutos, and Horacio D Espinosa. Elasticity size effects in zno nanowires- a combined experimental-computational approach. *Nano letters*, 8(11):3668–3674, 2008.

[81] Ravi Agrawal, Bei Peng, and Horacio D Espinosa. Experimental-computational investigation of zno nanowires strength and fracture. *Nano letters*, 9(12):4177–4183, 2009.

[82] CQ Chen, Y Shi, Y St Zhang, J Zhu, and YJ Yan. Size dependence of young's modulus in zno nanowires. *Physical review letters*, 96(7):075505, 2006.

[83] XY Yan, JF Peng, SA Yan, and XJ Zheng. Electromechanical characterization of single gan nanobelt probed with conductive atomic force microscope. *Journal of Electronic Materials*, 47:3869–3875, 2018.

[84] M Pea, L Maiolo, E Giovine, A Rinaldi, Rodolfo Araneo, and Andrea Notargiacomo. Electrical characterization of fib processed metal layers for reliable conductive-afm on zno microstructures. *Applied Surface Science*, 371:83–90, 2016.

[85] Igor Beinik, Markus Kratzer, Astrid Wachauer, Lin Wang, RT Lechner, Christian Teichert, Christian Motz, W Anwand, Gerhard Brauer, XY Chen, et al. Electrical properties of zno nanorods studied by conductive atomic force microscopy. *Journal of applied physics*, 110(5), 2011.

[86] Min-Hua Zhao, Zhong-Lin Wang, and Scott X Mao. Piezoelectric characterization of individual zinc oxide nanobelt probed by piezoresponse force microscope. *Nano Letters*, 4(4):587–590, 2004.

[87] Andrés Jenaro Lopez Garcia, Thomas Jalabert, Manojit Pusty, Viktor Defoor, Xavier Mescot, Maria Montanino, Giuliano Sico, Fausta Loffredo, Fulvia Villani, Giuseppe Nenna, et al. Size and semiconducting effects on the piezoelectric performances of zno nanowires grown onto gravure-printed seed layers on flexible substrates. *Nanoenergy Advances*, 2(2):197–209, 2022.

[88] Keqiang Li, Yeqiang Bu, and Hongtao Wang. Advances on in situ tem mechanical testing techniques: A retrospective and perspective view. *Frontiers in Materials*, 10:1207024, 2023.

[89] Shize Yang, Lifen Wang, Xuezeng Tian, Zhi Xu, Wenlong Wang, Xuedong Bai, and Enge Wang. The piezotronic effect of zinc oxide nanowires studied by in situ tem. *Advanced Materials*, 24(34):4676–4682, 2012.

[90] Zhengkui Xu. In situ tem study of electric field-induced microcracking in piezoelectric single crystals. *Materials Science and Engineering: B*, 99(1-3):106–111, 2003.

[91] Wenzheng Jiang, Lei Zhu, Lingli Chen, Yumeng Yang, Xi Yu, Xiaolong Li, Zhiqiang Mu, and Wenjie Yu. In situ synchrotron xrd characterization of piezoelectric al1-xscxn thin films for mems applications. *Materials*, 16(5):1781, 2023.

[92] KK Korir, Giancarlo Cicero, and A Catellani. Piezoelectric properties of zinc oxide nanowires: an ab initio study. *Nanotechnology*, 24(47):475401, 2013.

[93] Nicola A Hill and Umesh Waghmare. First-principles study of strain-electronic interplay in zno: Stress and temperature dependence of the piezoelectric constants. *Physical Review B*, 62(13):8802, 2000.

[94] Sunandan Baruah and Joydeep Dutta. Hydrothermal growth of zno nanostructures. *Science and technology of advanced materials*, 10(1):013001, 2009.

[95] Thomas Cossuet, Hervé Roussel, Jean-Michel Chauveau, Odette Chaix-Pluchery, Jean-Luc Thomassin, Estelle Appert, and Vincent Consonni. Well-ordered zno nanowires with controllable inclination on semipolar zno surfaces by chemical bath deposition. *Nanotechnology*, 29(47):475601, sep 2018.

[96] Zhong Lin Wang. Zinc oxide nanostructures: growth, properties and applications. *Journal of physics: condensed matter*, 16(25):R829, 2004.

[97] Rudooh S Wagner and W Chadwick Ellis. Vapor-liquid-solid mechanism of single crystal growth. *Applied physics letters*, 4(5):89–90, 1964.

[98] N Caicedo, J-S Thomann, R Leturcq, and D Lenoble. Aspect ratio improvement of zno nanowires grown in liquid phase by using step-by-step sequential growth. *CrystEngComm*, 18(29):5502–5511, 2016.

[99] Thomas Demes, Céline Ternon, David Riassetto, Valérie Stambouli, and Michel Langlet. Comprehensive study of hydrothermally grown zno nanowires. *Journal of Materials Science*, 51:10652–10661, 2016.

[100] Thomas Demes, C Ternon, D Riassetto, H Roussel, L Rapenne, I Gélard, Carmen Jiménez, V Stambouli, and M Langlet. New insights in the structural and morphological properties of sol-gel deposited zno multilayer films. *Journal of Physics and Chemistry of Solids*, 95:43–55, 2016.

[101] Thomas Demes, Céline Ternon, Fanny Morisot, David Riassetto, Maxime Legallais, Hervé Roussel, and Michel Langlet. Mechanisms involved in the hydrothermal growth of ultra-thin and high aspect ratio zno nanowires. *Applied Surface Science*, 410:423–431, 2017.

[102] Ling Zhu and Wen Zeng. Room-temperature gas sensing of zno-based gas sensor: A review. *Sensors and Actuators A: Physical*, 267:242–261, 2017.

[103] Brijesh Kumar and Sang-Woo Kim. Energy harvesting based on semiconducting piezoelectric zno nanostructures. *Nano Energy*, 1(3):342–355, 2012.

[104] Sumit Vyas. A short review on properties and applications of zinc oxide based thin films and devices: Zno as a promising material for applications in electronics, optoelectronics, biomedical and sensors. *Johnson Matthey Technology Review*, 64(2):202–218, 2020.

[105] Guylaine Poulin-Vittrant, Christopher Oshman, Charles Opoku, Abhishek Singh Dahiya, Nicolas Camara, D Alquier, L-P Tran Huu Hue, and M Lethiecq. Fabrication and characterization of zno nanowire-based piezoelectric nanogenerators for low frequency mechanical energy harvesting. *Physics Procedia*, 70:909–913, 2015.

[106] Zhong Lin Wang and Jinhui Song. Piezoelectric nanogenerators based on zinc oxide nanowire arrays. *Science*, 312(5771):242–246, 2006.

[107] Zhong Lin Wang. From nanogenerators to piezotronics—a decade-long study of zno nanostructures. *MRS bulletin*, 37(9):814–827, 2012.

[108] Long Lin, Chen-Ho Lai, Youfan Hu, Yan Zhang, Xue Wang, Chen Xu, Robert L Snyder, Lih-J Chen, and Zhong Lin Wang. High output nanogenerator based on assembly of gan nanowires. *Nanotechnology*, 22(47):475401, 2011.

[109] James Dieffenderfer, Henry Goodell, Steven Mills, Michael McKnight, Shanshan Yao, Feiyan Lin, Eric Beppler, Brinnae Bent, Bongmook Lee, Veena Misra, et al. Low-power wearable systems for continuous monitoring of environment and health for chronic respiratory disease. *IEEE journal of biomedical and health informatics*, 20(5):1251–1264, 2016.

[110] Ran Tao, Mitesh Parmar, Gustavo Ardila, Paulo Oliveira, Daniel Marques, Laurent Montès, and Mireille Mouis. Performance of zno based piezo-generators under controlled compression. *Semiconductor Science and Technology*, 32(6):064003, 2017.

[111] ZH Chen, YB Tang, CP Liu, YH Leung, GD Yuan, LM Chen, YQ Wang, I Bello, JA Zapien, WJ Zhang, et al. Vertically aligned zno nanorod arrays sentisized with gold nanoparticles for schottky barrier photovoltaic cells. *The Journal of Physical Chemistry C*, 113(30):13433–13437, 2009.

[112] Ming-Cheng Kao, Hone-Zern Chen, San-Lin Young, Chen-Cheng Lin, and Chung-Yuan Kung. Structure and photovoltaic properties of zno nanowire for dye-sensitized solar cells. *Nanoscale research letters*, 7:1–6, 2012.

[113] DG Thomas. The exciton spectrum of zinc oxide. *Journal of Physics and Chemistry of Solids*, 15(1-2):86–96, 1960.

[114] M Pan, R Rondon, J Cloud, V Rengarajan, W Nemeth, A Valencia, J Gomez, N Spencer, and J Nause. Zno based light emitting diodes growth and fabrication. In *Zinc Oxide Materials and Devices*, volume 6122, pages 73–78. SPIE, 2006.

[115] Andreas Maier, Stefan Steidl, Vincent Christlein, and Joachim Hornegger. Medical imaging systems: An introductory guide. 2018.

[116] PA t Doyle and PS Turner. Relativistic hartree–fock x-ray and electron scattering factors. *Acta Crystallographica Section A: Crystal Physics, Diffraction, Theoretical and General Crystallography*, 24(3):390–397, 1968.

[117] Bertram Eugene Warren. *X-ray Diffraction*. Courier Corporation, 1990.

[118] Frank Schreiber and Alexander Gerlach. X-ray and neutron reflectivity for the investigation of thin films. *Website. www. physchem. ox. ac. uk/fs*, 2013.

[119] Paul Peter Ewald. *Fifty Years of X-Ray Diffraction: Dedicated to the International Union of Crystallography on the Occasion of the Commemoration Meeting in Munich July 1962*. Springer Science & Business Media, 2012.

[120] Paul Kirkpatrick and Albert Vincio Baez. Formation of optical images by x-rays. *JOSA*, 38(9):766–774, 1948.

[121] David Attwood. *Soft x-rays and extreme ultraviolet radiation: principles and applications*. Cambridge university press, 2000.

[122] Christian G Schroer. Focusing hard x rays to nanometer dimensions using fresnel zone plates. *Physical Review B—Condensed Matter and Materials Physics*, 74(3):033405, 2006.

[123] R Spolenak, WL Brown, N Tamura, AA MacDowell, RS Celestre, HA Padmore, B Valek, JC Bravman, T Marieb, H Fujimoto, et al. Local plasticity of al thin films as revealed by x-ray microdiffraction. *Physical review letters*, 90(9):096102, 2003.

[124] Ali AlHassan, A Abboud, TW Cornelius, Z Ren, O Thomas, Gunther Richter, J-S Micha, S Send, R Hartmann, L Strüder, et al. Energy-dispersive x-ray micro laue diffraction on a bent gold nanowire. *Journal of Applied Crystallography*, 54(1):80–86, 2021.

[125] N Tamura. Xmas: A versatile tool for analyzing synchrotron x-ray microdiffraction data, chapter-4 of strain and dislocation gradients from diffraction. *World Sci.*, 2014.

[126] Wenjun Liu, Gene E Ice, Bennett C Larson, Wenge Yang, Jonathan Z Tischler, and JOHN D Budai. The three-dimensional x-ray crystal microscope: A new

tool for materials characterization. *Metallurgical and Materials Transactions A*, 35:1963–1967, 2004.

[127] JS Micha. Lauetools: Open source python packages for x-ray microlaue diffraction analysis, 2014.

[128] O Ulrich, Xavier Biquard, P Bleuet, O Geaymond, P Gergaud, JS Micha, O Robach, and F Rieutord. A new white beam x-ray microdiffraction setup on the bm32 beamline at the european synchrotron radiation facility. *Review of scientific instruments*, 82(3), 2011.

[129] J Petit, Olivier Castelnau, Michel Bornert, FG Zhang, F Hofmann, AM Korsunsky, D Faurie, Christophe Le Bourlot, Jean-Sébastien Micha, O Robach, et al. Laue-dic: a new method for improved stress field measurements at the micrometer scale. *Journal of Synchrotron Radiation*, 22(4):980–994, 2015.

[130] H-J Bunge. *Texture analysis in materials science: mathematical methods*. Elsevier, 2013.

[131] Mark A Pfeifer, Garth J Williams, Ivan A Vartanyants, Ross Harder, and Ian K Robinson. Three-dimensional mapping of a deformation field inside a nanocrystal. *Nature*, 442(7098):63–66, 2006.

[132] William T Cochran, James W Cooley, David L Favin, Howard D Helms, Reginald A Kaenel, William W Lang, George C Maling, David E Nelson, Charles M Rader, and Peter D Welch. What is the fast fourier transform? *Proceedings of the IEEE*, 55(10):1664–1674, 1967.

[133] James W Cooley and John W Tukey. An algorithm for the machine calculation of complex fourier series. *Mathematics of computation*, 19(90):297–301, 1965.

[134] Satio Takagi. A dynamical theory of diffraction for a distorted crystal. *Journal of the Physical Society of Japan*, 26(5):1239–1253, 1969.

[135] Marcus C Newton, Steven J Leake, Ross Harder, and Ian K Robinson. Three-dimensional imaging of strain in a single zno nanorod. *Nature materials*, 9(2):120–124, 2010.

[136] Claude Elwood Shannon. Communication in the presence of noise. *Proceedings of the IRE*, 37(1):10–21, 1949.

[137] D Sayre. The squaring method: a new method for phase determination. *Acta Crystallographica*, 5(1):60–65, 1952.

[138] Jianwei Miao, David Sayre, and HN Chapman. Phase retrieval from the magnitude of the fourier transforms of nonperiodic objects. *JOSA A*, 15(6):1662–1669, 1998.

[139] James R Fienup. Reconstruction of an object from the modulus of its fourier transform. *Optics letters*, 3(1):27–29, 1978.

[140] James R Fienup. Phase retrieval algorithms: a comparison. *Applied optics*, 21(15):2758–2769, 1982.

[141] John H Van Drie. "shrink-wrap" surfaces: a new method for incorporating shape into pharmacophoric 3d database searching. *Journal of chemical information and computer sciences*, 37(1):38–42, 1997.

[142] Hiroaki Takajo, Tohru Takahashi, Ryuzo Ueda, and Makoto Taninaka. Study on the convergence property of the hybrid input–output algorithm used for phase retrieval. *JOSA A*, 15(11):2849–2861, 1998.

[143] Jolyon Browne and AB De Pierro. A row-action alternative to the em algorithm for maximizing likelihood in emission tomography. *IEEE transactions on medical imaging*, 15(5):687–699, 1996.

[144] Steven J Leake, Gilbert A Chahine, Hamid Djazouli, Tao Zhou, Carsten Richter, Jan Hilhorst, Lucien Petit, M-I Richard, Christian Morawe, Raymond Barrett, et al. The nanodiffraction beamline id01/esrf: a microscope for imaging strain and structure. *Journal of synchrotron radiation*, 26(2):571–584, 2019.

[145] Pierre Hirel. Atomsk: A tool for manipulating and converting atomic data files. *Computer Physics Communications*, 197:212–219, 2015.

[146] Michaël Texier and Jany Thibault-Pénisson. Optimum correction conditions for aberration-corrected hrtem sic dumbbells chemical imaging. *Micron*, 43(4):516–523, 2012.

[147] Gerd Binnig and Heinrich Rohrer. Scanning tunneling microscopy—from birth to adolescence. *reviews of modern physics*, 59(3):615, 1987.

[148] SJ O'shea, RM Atta, MP Murrell, and ME Welland. Conducting atomic force microscopy study of silicon dioxide breakdown. *Journal of Vacuum Science & Technology B: Microelectronics and Nanometer Structures Processing, Measurement, and Phenomena*, 13(5):1945–1952, 1995.

[149] Paul K Hansma and Jerry Tersoff. Scanning tunneling microscopy. *Journal of Applied Physics*, 61(2):R1–R24, 1987.

[150] D Rugar, HJ Mamin, P Guethner, SE Lambert, JE Stern, I McFadyen, and T Yogi. Magnetic force microscopy: General principles and application to longitudinal recording media. *Journal of Applied Physics*, 68(3):1169–1183, 1990.

[151] Sergei V Kalinin and Dawn A Bonnell. Imaging mechanism of piezoresponse force microscopy of ferroelectric surfaces. *Physical Review B*, 65(12):125408, 2002.

[152] Yang Gan. Atomic and subnanometer resolution in ambient conditions by atomic force microscopy. *Surface Science Reports*, 64(3):99–121, 2009.

[153] Jacob N Israelachvili. *Intermolecular and surface forces*. Academic press, 2011.

[154] Yaxin Song and Bharat Bhushan. Atomic force microscopy dynamic modes: modeling and applications. *Journal of Physics: Condensed Matter*, 20(22):225012, 2008.

[155] H Seo, D Goo, G Jung, R Stomp, and J Wei. Park nx-hivac: Phase-lock loop for frequency modulation non-contact afm. *Park AFM SYSTEMS*, 2019.

[156] Zhe Ren, Francesca Mastropietro, Anton Davydok, Simon Langlais, M-I Richard, J-J Furter, Olivier Thomas, Maxime Dupraz, Marc Verdier, Guillaume Beutier, et al. Scanning force microscope for in situ nanofocused x-ray diffraction studies. *Journal of Synchrotron Radiation*, 21(5):1128–1133, 2014.

[157] Florian Lauraux, Sarah Yehya, Stéphane Labat, Jean-Sébastien Micha, Odile Robach, Oleg Kovalenko, Eugen Rabkin, Olivier Thomas, and Thomas W Cornelius. In-situ force measurement during nano-indentation combined with laue microdiffraction. *Nano Select*, 2(1):99–106, 2021.

[158] Baomei Wen, John E Sader, and John J Boland. Mechanical properties of zno nanowires. *Physical review letters*, 101(17):175502, 2008.

[159] S Hoffmann, Fredrik Östlund, Johann Michler, HJ Fan, M Zacharias, SH Christiansen, and Christophe Ballif. Fracture strength and young's modulus of zno nanowires. *Nanotechnology*, 18(20):205503, 2007.

[160] Aditi Roy, James Mead, Shiliang Wang, and Han Huang. Effects of surface defects on the mechanical properties of zno nanowires. *Scientific Reports*, 7(1):9547, 2017.

[161] KF Wang and BL Wang. Electrostatic potential in a bent piezoelectric nanowire with consideration of size-dependent piezoelectricity and semiconducting characterization. *Nanotechnology*, 29(25):255405, 2018.

[162] Sandip Basu and Michel W Barsoum. Deformation micromechanisms of zno single crystals as determined from spherical nanoindentation stress–strain curves. *Journal of Materials Research*, 22(9):2470–2477, 2007.

[163] Albert C Thompson, Douglas Vaughan, et al. *X-ray data booklet*, volume 8. Lawrence Berkeley National Laboratory, University of California Berkeley, CA, 2001.

[164] NIST. X-ray mass attenuation coefficients, 2012. Accessed: 01/2025.

[165] Xufei Wu, Jonghoon Lee, Vikas Varshney, Jennifer L Wohlwend, Ajit K Roy, and Tengfei Luo. Thermal conductivity of wurtzite zinc-oxide from first-principles lattice

dynamics–a comparative study with gallium nitride. *Scientific reports*, 6(1):1–10, 2016.

[166] Eleanor Lawrence Bright, Carlotta Giacobbe, and Jonathan P Wright. Beam heating from a fourth-generation synchrotron source. *Journal of Synchrotron Radiation*, 28(5):1377–1385, 2021.

[167] Nicholas Rolston, Adam D Printz, Stephanie R Dupont, Eszter Voroshazi, and Reinhold H Dauskardt. Effect of heat, uv radiation, and moisture on the decohesion kinetics of inverted organic solar cells. *Solar Energy Materials and Solar Cells*, 170:239–245, 2017.

[168] Felix Hofmann, Nicholas W Phillips, Suchandrima Das, Phani Karamched, Gareth M Hughes, James O Douglas, Wonsuk Cha, and Wenjun Liu. Nanoscale imaging of the full strain tensor of specific dislocations extracted from a bulk sample. *Physical Review Materials*, 4(1):013801, 2020.

[169] Mathew J Cherukara, Wonsuk Cha, and Ross J Harder. Anisotropic nano-scale resolution in 3d bragg coherent diffraction imaging. *Applied Physics Letters*, 113(20), 2018.

[170] Jerome Carnis. BCDI: tools for pre(post)-processing bragg and forward coherent x-ray diffraction imaging data, 2023.